TURBULENT SHEAR-FLOWS NEAR IRREGULARLY

ROUGH SURFACES WITH PARTICULAR REFERENCE TO SHIPS' HULLS

Thesis submitted in accordance with the
requirements of the University of
Liverpool for the degree of Doctor in
Philosophy

by

ANTONY JOSEPH MUSKER

December 1977

TO MY PARENTS WITH MANY THANKS

STATEMENT OF ORIGINALITY

The work described in this thesis was carried out, except where otherwise indicated, by the author in the Fluid Mechanics division of the Department of Mechanical Engineering at the University of Liverpool between January 1975 and December 1977. No part of this thesis has been submitted for a degree in any other university or place of learning.

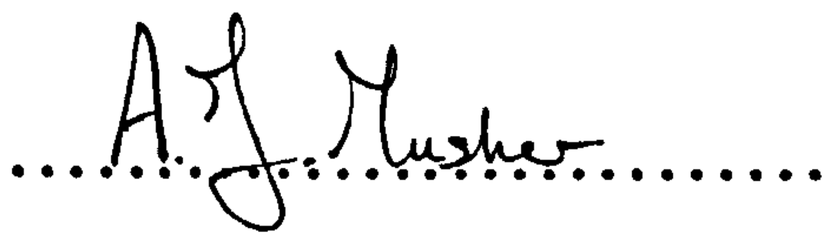

A.J. Musker

December 1977

ACKNOWLEDGEMENTS

I am indebted to the following for their co-operation during the period of my research:-

Dr. A.K. Lewkowicz, who supervised the work with much enthusiasm and offered many valuable suggestions. I am particularly grateful to him for providing me with the initial opportunity to become involved in the work;

Mr. F.J. Cummins, who undertook the detailed design of the pipe-lines;

Messrs. D. Sculthorpe, K. Fennah, D. Smith and J. Littler who manufactured the pipe-lines with great skill;

Messrs. M. Fisher and J. Patterson for their technical assistance;

Mrs. E. McKinley for the photographic work and

Miss D. Wright who was responsible for typing the thesis so painstakingly.

Financial support came from the Science Research Council (U.K.) and the British Ship Research Association to whom I am most grateful. Until his retirement in August 1976 I had the privilege to work with Professor J.H. Preston; his enthusiasm in the work was a constant source of encouragement to me.

Finally, I am especially grateful to my wife, Anne, for being so very patient during these last three years.

A.J. Musker

SUMMARY

This thesis concerns the effect of an irregularly-rough surface on the behaviour of turbulent shear-flows - such as exist in pipe and boundary-layer flows. Attention is focussed on the problem of ship-hull roughness which arises from natural corrosion, painting defects and biological growth. The economic importance of research into the effects of ship-hull roughness has been accentuated by the rises in fuel costs in recent years.

A novel feature of the work has been a method of replicating a sample area of hull-roughness while a ship is in dry-dock. This was accomplished using a thixotropic silicon rubber. By means of an additional stage of replication a plastic pipe-line can be manufactured whose inside surface is a positive copy of a real ship-hull roughness.

It is well established that surface effects are confined to the so-called 'inner region' of the mean velocity distribution - providing the longitudinal pressure gradient is not too severe. Moreover, for a given surface, the roughness function, arising from the inner-region velocity distributions, is a unique function of a 'roughness Reynolds number' formed by a typical height measurement relating to the surface. Hence, for identical surfaces, but regardless of the fluid media, the inner region velocity distributions for pipes and boundary-layers are related through the roughness function.

Six air pipe-lines were manufactured - one of which was smooth. The remaining pipe-lines were rough and corresponded to hull surfaces which were different in terms of both roughness-height and texture. At present hull roughness is measured in terms of the 'mean apparent amplitude' (M.A.A.), which is a form of peak-to-valley height based on

a surface wavelength of 50 mm. Measurements in the five rough pipes have shown, however, that no correlation exists between the roughness functions (and hence the wall friction) and the M.A.A.; this casts doubt on the validity of correlations between shaft horse-power and M.A.A. currently being employed by naval architects.

A hot-wire anemometry system was used to measure the turbulent normal and shear stresses. It has been found that the variation of these quantities across the pipe radius depends on the surface roughness - indicating the existence of a weak secondary flow. By Fourier-transforming the measured frequency spectrum function of the longitudinal normal stress, estimates were made of the size of a typical energy-containing eddy at various radial locations.

A digital method was used to analyse the topography of the surfaces in order to search for an 'effective roughness height' which would cause the measured roughness functions to collapse onto a single curve. The measured eddy size near the pipe wall was used as a guide to the longest surface wavelength which should be considered in the topography analysis. It has been found necessary to take into account the average slope of the surface and the average skewness and kurtosis of the height distributions, in addition to a one-dimensional measure of the roughness height, in order to produce a 'universal' roughness function.

Integral methods of predicting the development of two-dimensional turbulent boundary-layers, which can include the effect of surface roughness, have been developed. Predictions have been compared with published experimental data for boundary-layers developing over smooth and rough surfaces. The method based on the energy integral equation has been found to give good agreement with experimental measurements

for both smooth and rough surfaces in an arbitrary pressure distribution. This method has been used to investigate the effect of surface roughness on the separation of the two-dimensional boundary-layer developing over a flat plate with an external pressure distribution analogous to that found on a typical ocean-going vessel. For a fixed body-shape and plate Reynolds number it has been found that an increase in surface roughness causes the position of separation to move towards the leading edge.

The most important aspect of the proposed prediction methods, however, is that the roughness function for a particular surface can be incorporated directly into one of the governing equations (the wall friction relationship). Hence, using measurements in a pipe lined with a certain roughness, boundary layer predictions, over a surface with an identical roughness and in a specified pressure distribution, can be extended to arbitrarily high plate Reynolds numbers - providing the roughness function is adequately defined.

C O N T E N T S

NOMENCLATURE

		Equation or Section of first appearance*
a	empirical constant	(6.1)
a_1	coefficient appearing in shear-stress distribution	(4.22)
a_i	coefficients required to calculate R_T	(A5.1)
b	empirical constant	(6.2)
b_1	coefficient appearing in shear-stress distribution	(4.22)
b_i	coefficients required to calculate R_T	(A5.1)
c_1	coefficient appearing in shear-stress distribution	(4.22)
c_i	coefficients required to calculate R_T	(A5.1)
c_v	specific heat of air at constant volume	(A2.3)
d	roughness density	(2.28)
d_1	coefficient appearing in shear-stress distribution	(4.22)
e_1	coefficient appearing in shear-stress distribution	(4.22)
e_b	instantaneous anemometer bridge voltage	(3.9)
e'_b	fluctuating component of instantaneous linearised bridge voltage	(A4.4)
(f)	pipe friction coefficient = $8\tau_o/\rho U_{av}^2$	(2.29)
f_i	'function of'	(4.52)
(h)	measure of roughness height	[2.2]

* Curved brackets indicate equation of first appearance; square brackets indicate section of first appearance.

h_{MAA}	mean apparent amplitude of roughness based on maximum surface wavelength of 50 mm	[4.8]
h_o	stagnation enthalpy	(A2.3)
h_s	equivalent sand-grain roughness height	[2.2]
h_*	roughness Reynolds number = hu_o/ν	(2.25)
h_+	a Reynolds number, = hU_∞/ν	(4.15)
h'	effective roughness height	(6.1)
i	subscript used in analysis of surface profiles	[5.3]
j	subscript used in analysis of surface profiles	[5.3]
k	sensitivity coefficient	(3.8)
k_u	average kurtosis of surface height distributions	(6.2)
ℓ	value of x for onset of positive pressure gradient	(4.62)
ℓ_1	range of x for negative pressure gradient	(4.62)
m	calibration constant for hot-wire	(3.9)
$\dot{m}$	mass flow-rate through pipe	(A2.1)
n	frequency	(3.10)
p	static pressure	(2.6)
p_1	static pressure in pipe at distance L_1 upstream of exit plane	(A2.9)
p_a	static pressure at exit plane	(3.4)

p_2	static pressure at exit plane	(A2.9)
Δp	pipe pressure drop = $p_1 - p_2$	(3.4)
q_{eff}	instantaneous effective cooling velocity of hot-wire	(3.8)
q_m	mean effective cooling velocity of hot-wire	[App.4]
q_n	component of q_{eff} normal to wire	(3.8)
q_p	component of q_{eff} parallel to wire	(3.8)
q'	fluctuating component of effective cooling velocity of hot-wire	[App.4]
r	number of sampled height ordinates per surface profile	[5.3]
s	length of sampling interval	(5.2)
s_k	average skewness of surface height distributions	(6.2)
s_p	average slope of surface profiles based on sampling interval equal to correlation length	(6.1)
u	mean velocity in x direction	(2.3)
u_i	measured value of u in inner region	(3.5)
u_o	wall friction velocity = $\sqrt{\tau_o/\rho}$	(2.3)
$\Delta u/u_o$	roughness function	(2.23)
u_*	dimensionless velocity = u/u_o	(2.15)
u'	component of instantaneous fluctuating velocity in x direction	[2.2]
v	mean velocity in y direction	(2.8)
v'	component of instantaneous fluctuating velocity in y direction	[2.2]

w_k	wake function	(2.16)
w'	component of instantaneous fluctuating velocity in z direction	(2.49)
x	Cartesian co-ordinate in longitudinal direction	(2.6)
$\overline{x}$	dimensionless x co-ordinate such that $dx/d\overline{x} = \delta_*$	[2.3]
Δx	separation distance for R_T	(3.11)
x_{sep}	value of x at which separation occurs	(4.62)
y	Cartesian co-ordinate perpendicular to wall	(2.3)
y_i	value of y corresponding to u_i	(3.5)
y_*	dimensionless wall distance = yu_o/ν	(2.12)
y_o	length of order of sub-layer thickness	(4.2)
y'	arbitrary value of y in logarithmic overlap region	(2.47)
y''	limit of inner sub-range	(4.20)
z	Cartesian co-ordinate	-
A	constant	(A2.8)
A_1	constant in forced-convection law	(3.9)
A_2	constant in forced-convection law	(3.9)
A_e	intermediate parameter required to measure χ	(A3.7)
A_L	gain setting of lineariser	(A4.3)
B	constant in logarithmic region of mean velocity distribution	(2.5)
B_e	intermediate parameter required to measure χ	(A3.8)

B'	constant	(4.3)
C	constant of proportionality	(2.13)
C_1	universal constant for uniform sand-grain roughness	(2.26)
C_2	constant for roughness function for fully-rough region	(2.27)
C_e	intermediate parameter required to measure χ	(A3.9)
C_f	total wall friction coefficient = total resistance/(wetted area x $\frac{1}{2}\rho U_\infty^2$)	(2.1)
ΔC_f	C_f allowance for roughness effects	[2.1]
C_j	auto-correlation coefficient	(5.3)
C_r	constant in rate equation	(4.50)
C'	constant for given roughness	(4.4)
C'_f	local wall friction coefficient $\tau_o/\frac{1}{2}\rho U_\infty^2$	(2.32)
D	mean diameter of pipe	(3.4)
D_e	intermediate parameter required to measure χ	(A3.10)
E_b	mean anemometer bridge voltage	(A4.4)
E_e	intermediate parameter required to measure χ	(A3.11)
E'	energy dissipation parameter	(2.47)
F_e	intermediate parameter required to measure χ	(A3.12)
$F(n)$	frequency spectrum function	(3.10)
F'	term appearing in dissipation integral	(2.48)

$G_1, G_2 \ldots G_{11}$	functions of Π	(4.9)
G_e	intermediate parameter required to measure χ	(A3.13)
G_L	lineariser constant = u/E_b	[App.4]
G'	Clauser's shape factor	(2.37)
G_e'	equilibrium value of G'	(2.43)
H	shape factor	(2.32)
L	length of ship (see definition for R_s)	-
L_1	length of pipe over which pressure drop is measured	(3.4)
L_T	macro-scale of turbulence	(3.13)
M	Mach number	(A2.5)
R	pipe radius	(3.2)
R_e	pipe Reynolds number $U_{av}D/\nu$	(2.29)
R_s	ship Reynolds number = LU_∞/ν	(2.1)
R_T	longitudinal spatial correlation coefficient	(3.11)
R_x	plate Reynolds number = xU_∞/ν	(2.33)
R_θ	a Reynolds number, = $\theta U_\infty/\nu$	(4.60)
$\overline{R}$	gas constant	(A2.2)
T	absolute temperature	(A2.2)
U_{av}	pipe average-velocity	(3.2)
U_c	pipe centre-line velocity	(3.3)
U_∞	free-stream velocity	(2.4)
U_{∞_o}	free-stream velocity in constant pressure region	(4.62)
X	Cartesian co-ordinate for roughness analysis	(5.3)

ΔX	lag distance for roughness auto-correlation coefficient	(5.2)
Y	Cartesian co-ordinate for roughness analysis	(5.3)
α	eddy viscosity parameter in outer region	(2.51)
α_{eq}	equilibrium value of α	(4.50)
β	generalised constant in law of the wall	(4.1)
γ	ratio of specific heats = C_p/C_v	(3.4)
δ	boundary-layer thickness	(2.4)
δ_*	displacement thickness	[2.3]
δ_{**}	energy thickness	(2.44)
ε	error in origin of mean velocity distribution	(3.1)
η_o	$\alpha(1+\Pi)/\kappa^2$	(2.53)
η	y/δ	(4.22)
η_*	value of η at which ν_t is maximum	(4.23)
θ	momentum thickness	(2.32)
κ	von Karman constant	(2.5)
λ_T	micro-scale of turbulence	(3.14)
μ	molecular viscosity	(2.9)
ν	molecular kinematic viscosity	(2.3)
ν_t	eddy kinematic viscosity	(2.8)
ν'_t	local maximum value of ν_t	(4.50)
ξ_1, ξ_2	'function of'	[4.7]
ρ	fluid density	(2.2)
ρ_a	density of air at exit plane	(3.4)
ρ_2	density of air at exit plane	(A2.11)

σ_1	residuals in regression analysis of velocity profile	(3.6)
σ_r	average standard deviation of surface height distributions	(6.1)
τ	shear stress	(2.31)
τ_o	wall shear stress	[2.2]
ϕ_i	'function of'	[2.2]
χ	roughness function	(2.24)
ψ	angular co-ordinate measured about pipe axis	(3.18)
ω	u_o/U_∞	(2.53)
Γ	wake modification function	(2.19)
Δ	dimensionless pressure-gradient parameter	(2.7)
Π	wake-strength parameter	(2.4)
Φ	angle between hot-wire and mean flow direction	[App.4]
Ω	pressure-gradient term in wall-friction equation	(2.36)

NOTATION

$\sim$	varies as
$\hat{}$	spatially-averaged value of
$\fallingdotseq$	approximately equal to

CHAPTER 1

INTRODUCTION

1.1 General Outline of the Problem

The flow characteristics of a fluid moving past a solid boundary are known to change with the roughness of the boundary surface. In some circumstances surface roughness is negligible, in which case the boundary may be considered to be smooth. This, of course, is a limiting case; in practice most engineering surfaces exhibit roughness, which may be due to manufacturing processes, deterioration or surface coating. It is perhaps surprising that the problem of surface roughness on ship-hulls was appreciated as long ago as the middle of the seventeenth century and documented in The Philosophical Transactions of The Royal Society (1666):

> "There is in the Indian Seas a kind of small worms that fasten themselves to the timber of the ships, and so pierce them that they take in water everywhere; and so weaken the wood, that it is almost impossible to repair them. Many things have been tried to prevent this evil, but without success. Some have lined their ships with deal, hair and lime, but, besides that this does not altogether prevent the worms, it much retards the ship's way".

To this day the role of hull-roughness in the prediction of overall ship resistance is not understood. For very large tankers,

sea trials have established that surface roughness is a major consideration from the point of view of performance and economy. Lackenby (1962) has reported differences of 20% in power requirements between sister ships with different surface finishes, and has noted that for the vast majority of the world's mercantile fleet between 80% and 90% of the total ship resistance can be attributed to wall friction.

On modern aircraft, streamlining has reduced the form drag to such an extent that wall friction constitutes more than half of the total drag. Contributions to the wall friction come not only from surface protusions, such as rivets and spot-welds, but also from the surface micro-geometry. The effect of the latter is highlighted when a military aircraft is coated with camouflage paint, which can alter the aerodynamic characteristics of the wings (see Bertelrud (1976)).

Although a great deal of experimental research has been done over the last two decades on the problem of flow over rough surfaces, almost all of it has been concerned with regular roughness, by which is meant that the excrescences are uniform both in shape and distribution. This is extremely valuable from an academic standpoint since the experiments can be considered to be controlled, but the results of the research are of limited use to the engineer who is confronted with a flow problem associated with a naturally-rough surface, as might be found on a corroded plate or on the inside surface of a concrete pipe-line. What little work has been done relating to these irregularly-rough surfaces is mainly confined to pipe flows.

1.2 Reasons for the Present Investigation

From the engineer's point of view there is a dearth of knowledge in three main areas concerning hydraulic roughness. Firstly, there is the obvious problem of how the rough surface interacts with the fluid moving over it. It is doubtful whether this problem will ever be solved in its entirety in a mathematically-closed form, and so recourse must be made to semi-empirical modelling. For an irregularly rough surface, there is the difficulty of adequately describing the topographical features not only geometrically but also statistically. Nearly all flows over rough surfaces are turbulent, and so it is important to know how the turbulence structure is affected by the presence of the roughness. What is particularly challenging is to ascertain whether the length scales of the turbulence field and the surface micro-geometry are in any way correlated. If such correlations do exist, it should be possible to make flow predictions without the need for intermediate experimentation other than an investigation of the micro-geometry of the surface.

Secondly, there is the problem of how boundary layer predictions can be made, in relation to a particular rough surface, using data from flow experiments performed in a laboratory. It is quite clear that in order to carry out such experiments for a complex irregular roughness, such as is found on ship-hulls, some method of replicating the surface is required.

Thirdly, there is the important problem of boundary layer separation and to what extent it is affected by surface roughness. This has particular applications to aerofoil behaviour with reference to the stall and associated hysteresis characteristics. In the after-

body of large ships, where large pressure rises occur due to the contracting streamlines, separation of the flow, with the resultant formation of large-scale eddies, can cause very significant increases in resistance and can even affect the handling of the ship and the performance of the propeller.

1.3 The Present Investigation

In view of the rapidly rising cost of fuel in recent years, much effort has gone into improving the surface finish of large ship-hulls. However, the hull condition quickly deteriorates after dry-docking. This is due to poor surface preparation before painting, the formation of corrosion products, and organic fouling in the form of weeds and barnacles. It is most important, therefore, to be able to quantify these roughness effects in terms of the total ship resistance. Ideally, this should be done in a laboratory, since the only alternative is to have regular sea-trials which are both costly and time-consuming.

In order to investigate the feasibility of such a laboratory method funds were sought from the U.K. Science Research Council to establish the necessary facilities. These funds were provided and the author was employed to carry out the investigation. Work commenced on 1st January 1975, and this original work has been documented in a report to the Science Research Council by Musker, Lewkowicz and Preston (1976). The British Ship Research Association provided the necessary financial support to continue with the work for a further two years commencing 1st January 1976.

Some of the original work (which has already been reported as

mentioned above) is included in this thesis because it is considered to be an essential prerequisite for the understanding of the subsequent work. A discussion of the basic concepts and a review of the relevant literature is presented in Chapter 2 of the thesis. This chapter is divided into four sections. The first section concentrates on the particular areas of concern to the naval architect. The second section describes the physical modelling of a turbulent flow over both smooth and rough walls in the light of more recent knowledge about the turbulent mean velocity profile. A review of two-dimensional prediction methods for rough-wall boundary layers is given in the third section together with descriptions of the turbulent shear stress distribution. The last section describes the problem of obtaining profile records of a rough surface - an area which is becoming increasingly important to the production engineer.

Chapter 3 describes the methodology for the present investigation and the flow experiments which have been performed for a variety of irregularly-rough surfaces. A novel method of experimentation is used which relies on manufacturing a replica of a given roughness using a moulding process. In this way, copies of ship-hull roughness can be transferred onto the inside surface of a pipe-line which is subsequently used for flow studies. A smooth-pipe experiment serves to check the instrumentation and methodology employed in the main investigation. Apart from the mean-flow measurements, the turbulence field is studied, using a hot-wire technique. In particular, the integral length-scales of turbulence are measured for all of the six surfaces under scrutiny, and the turbulence results are compared with others reported in the literature.

Integral prediction procedures for turbulent boundary layers usually rely on an accurate knowledge of the distributions of both turbulent shear stress and mean velocity. Chapter 4 shows how the experimental data relating to the rough-wall mean velocity profiles leads to a modified wall-friction relationship which can be incorporated into two-dimensional boundary layer equations. The use of entrainment methods obviates the need for empirical shear stress distributions, and such concepts have been successfully used by other workers to predict flows over uniformly-rough surfaces. Semi-empirical modelling of the turbulent shear stress in terms of the mean velocity is necessary if use is to be made of the auxiliary equations derived from the boundary layer momentum equation. These points are discussed and a new, improved version of the Lewkowicz-Horlock family of integral prediction methods is presented, together with comparisons between theory and experiment for known test cases. This is done for both smooth and rough walls. Additionally, a numerical experiment is described which investigates the effect of hull-surface roughness on the onset of separation.

Chapter 5 deals with the analysis of surface topography. The analysis is necessarily restrictive and does not attempt to answer such philosophical questions as whether a profile peak is synonymous with a surface summit. Three-dimensional surface description is in its infancy and it must be assumed that the statistical geometry of surface profiles adequately represents the true topography. The roughness parameters used in the analysis are defined and the experimental technique used to measure them is described.

Chapter 6 shows how the length scales associated with the turbulence field and the surface topography can be used to search for a universal velocity distribution in terms of the surface statistics. This is one of the ultimate goals of rough-wall boundary layer work. It is important to realise that a waveform corresponding to a surface profile contains a wide spectrum of frequencies, and it is by no means clear which frequencies are responsible for the observed change in flow characteristics.

Long wavelengths will certainly not influence the flow in the immediate vicinity of the surface, since they may be regarded as being equivalent to body curvatures. Included in the topography analysis, therefore, is a technique for filtering the profiles and thus rejecting wavelengths above a certain quantity determined by the turbulence measurements.

The conclusions drawn from the investigation, together with recommendations for future work, are presented in Chapter 7.

CHAPTER 2

BASIC CONCEPTS AND A REVIEW OF THE LITERATURE

2.1 The Problem of Roughness in Naval Architecture

It is instructive to examine the nature of ship resistance in terms of its constituent components. For a smooth ship, immersed in a hypothetical frictionless fluid, the net longitudinal component of normal pressures arising from the streamline flow around the hull is zero. At the breaking surface, waves are created against gravity which give rise to normal pressures on the hull. Hence the resistance to motion is confined to these normal pressures. For a real fluid, of course, the situation is far more complicated.

For an infinitely thin flat plate of wetted-area equivalent to the submerged hull-form and at zero incidence to the flow, surface shear stresses arise, due to the viscosity of the fluid.

The viscosity creates a boundary layer which grows in thickness along the length of the plate. This flat-plate analogy is still used as a basis on which the wall friction is calculated. Because the plate is infinitely thin there can be no form drag. For a real ship-hull, of course, the wall friction is slightly different from its equivalent flat plate due to the stream-line flow around the hull-form. The true wall friction is the integration of the longitudinal components of the surface shearing stresses. Because of the displacement effect of the boundary layer a form drag arises which manifests itself in the form of a net pressure force in the longitudinal direction. Finally, the presence of the waves at the breaking

surface not only creates a further drag force in the form of normal pressures, but also produces its own viscous forces. It is apparent, therefore, that the wave-making and viscous forces are not entirely independent of each other.

The presence of surface roughness on the hull not only changes the wall friction, but also modifies the development of the boundary layer and consequently alters the form drag. The geometry of the aft end of the hull can, in some circumstances, give rise to another type of drag caused by the separation of the boundary layer from the hull surface. The pressure distribution is largely determined by the hull geometry, and if this is such as to cause large decelerating flow regions in the after-body, then reverse-flow can occur which creates large-scale eddies leading to a significant loss of energy. In situations where separation occurs it is usual to include the extra resistance in the form drag, since it is of viscous origin and is to be distinguished from the wall friction.

The effect of separation has been quantified by Lackenby (1962) for the particular case of a mercantile ship-form. Model tests were carried out in order to study the variation of resistance with the position of the longitudinal centre of buoyancy (L.C.B.). It was found that a 1% change in the L.C.B. resulted in a 20% change in the overall resistance. Flow visualisation using cotton tufts confirmed the suspicion that separation had occurred. It is important to be able to relate these model experiments on separation to full-scale ships, and to this end it is necessary to take into account the different relative thicknesses of the boundary layers. Sachdeva

(1973) examined this problem for a smooth surface, using a numerical method, and concluded that the scale effect is favourable in going from model tests to the full-scale ship. Hence, in so far as the effect of separation on ship resistance is concerned, model tests tend to be pessimistic. To the author's knowledge no theoretical work has been done on the influence of ship-hull roughness on separation.

The nature of wall friction in relation to ships was first investigated by Froude (1872 and 1874). He assumed that the wave-making and viscous components of resistance are separable. He further assumed that the wall friction of the ship and the model would be equivalent to that of a plane surface with identical length and wetted-area as the ship and model respectively. By measuring the wall friction on a series of planks towed in a tank he was able to isolate this particular component of resistance. A rather crude method of extrapolating Froude's results to ship-lengths of approximately 400 metres was described by Payne (1936). Lackenby (1937) pointed out that Froude had been unaware, at the time of his experiments, that there existed different flow regimes depending on the Reynolds number based on the plank length, towing-speed and kinematic viscosity. He re-analysed Froude's results and concluded that the smaller planks exhibited a substantial amount of laminar flow. A unique turbulent friction line was established from the data and this was corroborated by the measurements on painted steel surfaces by Kempf (1929 and 1937).

Theoretical work by Prandtl and von Kármán lent support to the

empirical correlations of wall friction in terms of Reynolds number, and Schoenherr (1932) published a wall friction formula based on this work which is still in use today. The formula relates the total wall friction coefficient, C_f, to the ship Reynolds number, R_s (these parameters are defined in the list of symbols):

$$C_f = \left[0.242/\log_{10} (R_s C_f)\right]^2 \qquad (2.1)$$

The formula is valid for smooth ship-hulls. To allow for the surface condition of clean new ships a standard allowance, $\Delta C_f = 0.0004$, is added to the Schoenherr value of C_f. This supposedly takes into account both the structural roughness of the hull in the form of rivets, plate overlaps and welding seams, and also the micro-geometry of the hull-plates. The latter depends on the surface preparation and the paint finish.

Although this roughness allowance seems rather crude it was arrived at after extensive sea-trials performed on the 'Lucy Ashton' by Conn, Lackenby and Walker (1953). One of the main problems associated with the measurement of the resistance of full-scale ships is that the thrust of the propellers is not equal to the ship resistance, due to interaction with the hull. To overcome this difficulty the 'Lucy Ashton' was fitted with aircraft jet engines whose combined thrusts could be accurately measured. Initially, tests were made with the hull in a clean condition and coated with red-oxide paint. The resistance was found to be 16% higher than the smooth ship prediction, based on model experiments, and this figure corresponds to the previously-mentioned roughness allowance. A similar allowance

was arrived at on the basis of sea-trials of the vessel 'Meteor' as reported by Grothues-Spork (1968). A slight Reynolds number dependence was noticed, resulting in the value of ΔC_f rising to 0.0005 at low speeds. Various other wall-friction correlations have been suggested for clean new ships; for example, by Schultz-Grunow (1940), Hughes (1954) and Telfer (1960). The formula most favoured by naval architects, however, is the one arising from the International Towing Tank Conference held in 1957, the so-called I.T.T.C. (1957) line:

$$C_f = 0.075/(\log_{10}R_s-2)^2 \qquad (2.2)$$

This formula renders wall friction coefficients somewhat higher than the Schoenherr line at lower ship Reynolds numbers.

Returning to the 'Lucy Ashton' trials, a systematic study was made to relate the surface finish of the hull to the wall friction. Differences of 3% on total resistance and 5% on wall friction were observed between red-oxide paint and a smoother aluminium paint. The ship was then allowed to become biologically fouled by barnacles, measuring a few millimetres in height, and fine grasses clinging to the sides of the hull. Increases of 30% and 50% were recorded for the total and wall friction resistances respectively. These trials drew attention to the underlying importance of hull-roughness from the point of view of performance and economy.

The British Ship Research Association (B.S.R.A.), who were responsible for the 'Lucy Ashton' trials, began to study the relationship between the hull-roughness and the total resistance. The roughness was quantified by means of a wall-gauge specially manu-

factured for use on ship-hulls. The details of the instrument can be found in the paper by Lackenby (1962), but essentially the gauge produces a 5 centimetre-long trace of a local surface-roughness profile on the hull. Envelope curves are drawn through points of maxima and minima and the area contained within them is calculated. The 'mean apparent amplitude' (M.A.A.) is defined to be this area divided by the profile length. Some fifty samples are used, corresponding to different locations around the hull, and an average M.A.A. is assumed to describe the magnitude of the hull-roughness.

Although this one-dimensional measure of surface roughness may seem rather arbitrary, it has proved immensely popular and is still widely used. The M.A.A. cannot take into account the structure of the surface roughness,which undoubtedly is a controlling factor in the generation of wall friction. It is claimed by Lackenby (1962) that an increase in M.A.A. of 100 microns results in an increase of approximately 10% in total resistance for large single-screw ships. However, this correlation only applies to new ships recently wire-brushed and painted in dry-dock, and highlights the importance of careful surface preparation and painting. Canham and Lynn (1961) have attributed the deterioration of a hull, after several years service, largely to corrosion rather than organic fouling, and this has been confirmed by Aertssen (1960) who noted a 17% increase in power requirements, due to the effects of corrosion, over a five-year period.

It is doubtful whether violations of all the rules of good painting practice occur anywhere else as frequently as they do in

dry-docks. This is accentuated by economic pressures on the ship-owners to minimise the dry-docking time, resulting often in the anti-fouling coating being applied over anti-corrosive paints which have not had time to dry fully. Indeed the anti-corrosive paints are often applied before even the ship has had time to dry out following descaling and fresh-water hosing. It is unfortunate that this problem persists in spite of the recent advances in the quality of marine paints.

Faced with these problems, therefore, it is clear that the naval architect is in need of a method which will give accurate correlations between the micro-geometry of a corroded hull-surface and the associated frictional resistance.

A systematic laboratory study of hydraulic roughness was presented by Nikuradse (1933) in his now classic paper. Using tightly-packed sand-grains glued onto the inside surface of a pipe-line he measured the wall friction coefficients in terms of the pipe Reynolds number for differently-sized grains. Prandtl and Schlichting (1934) later used these results to calculate the friction line of a flat plate with uniform, tightly-packed sand roughness in a constant pressure flow such as occurs for the major part of the length of a large ship. These calculations were confirmed experimentally by Allan and Cutland (1955) using different grades of emery powder glued to a plank. However, these friction lines do not agree in shape with earlier observations by Todd (1951), who used an equivalent sand roughness to describe simulated ship-hull roughness on his test-plates.

In attempts to relate the surface finish to wall friction, manufacturers of marine paints often use rotating drum and disc methods. These involve coating the drum or disc,which is then rotated in sea water in a concentric housing under laboratory conditions. The torque is related to the relevant roughness parameter, and the peripheral speed is set equal to a chosen ship speed. Although such experiments are useful to the designers of new paints they are of limited use to the naval architect. This is because the flows are subject to centrifugal forces which are absent in the case of pipes and flat plates. This causes a destabilising influence in the case of the rotating drum, for example, which may alter the roughness effects. In addition, there is the problem of end-effects caused by the three-dimensional nature of the apparatus, requiring corrections to the measured wall friction before extrapolations can be made to the full-scale ship. Despite the above objections these methods will still be in use for some time to come and the interested reader is referred to papers by Roy (1975) and Granville (1972).

Before leaving this section mention should be made of various drag-reducing chemicals which have been available in recent years. Firstly, there are the 'self-polishing' polymer paints, which rely for their efficacy on their resilient nature. The drag reduction claimed is attributed to the paint's ability to conform to the roughness topography while the ship is at sea, in such a way that the paint effectively 'smoothes over' the roughness excrescences. The compliant properties of the paint may well alter the character of the flow, in a manner similar to that recorded by Kramer (1960 and 1961) in his experiments to elucidate the drag-reducing properties

of a dolphin's skin, first noted by Gawn (1950). A theoretical treatment of this problem is given by Brooke-Benjamin (1960). There has been much controversy about the actual amount of drag reduction obtained using these paints, but it is now generally accepted that there are gains to be had by using them although they tend to be short-lived. Secondly, there are the long-chain polymers, such as polyethylene oxide. Solutions containing minute amounts of these chemicals exhibit drag-reducing properties. It is known that the associated drag-reducing properties of these polymers are not connected with a reduced fluid viscosity, but rather by the tendency to inhibit the production of turbulence. A complete review of the subject is given by Hoyt (1972).

The inclusion of the effects of these paints and chemicals is beyond the scope of this thesis. For the work which follows, it is assumed that the surface has originated from a conventional paint finish or from a drag-reducing paint which has aged sufficiently for it to have lost its effectiveness. It is also assumed that the contribution to the wall friction from the small amount of laminar flow near the leading edge is negligible, which is certainly the case for most ocean-going vessels.

2.2 The Turbulent Velocity Distribution Over Smooth and Rough Walls

Before discussing the effects of wall-roughness, it is important to recapitulate the state-of-the-art in relation to the representation of the turbulent mean velocity distribution over a smooth wall. Near to the wall this has the classical functional form

$$\frac{u}{u_o} = \phi_1 \left(\frac{yu_o}{\nu}\right) , \tag{2.3}$$

where u = the velocity at a distance y, $u_o = \sqrt{\tau_o/\rho}$ where τ_o = the wall shear stress and ρ = the fluid density, and ν = the fluid kinematic viscosity. Away from the wall, where viscous shear stresses are considered entirely negligible, the velocity distribution depends on the wall shear stress and a pressure gradient parameter, Π:

$$\frac{U_\infty - u}{u_o} = \phi_2 \, (y/\delta, \Pi) \, . \tag{2.4}$$

Here, δ refers to the boundary layer thickness or, in the case of a pipe, the pipe radius, and U_∞ refers to the free-stream velocity. Millikan (1938) showed that the region of simultaneous validity of these two laws must have a logarithmic form and this leads to the well-known law of the wall:

$$\frac{u}{u_o} = \frac{1}{\kappa} \log_e \frac{yu_o}{\nu} + B \, , \tag{2.5}$$

where κ and B are universal constants.

This representation of the velocity distribution near the wall implies an insensitivity to the external pressure gradient. For cases where the wall shear stress approaches zero, however, Townsend (1960) and Szablewski (1955) have shown that the velocity distribution near the wall assumes the limiting form:

$$\frac{u}{\left(\frac{\nu}{\rho}\frac{dp}{dx}\right)^{1/3}} = \phi_3 \left(\frac{y^3}{\nu^2}\frac{1}{\rho}\frac{dp}{dx}\right) \, , \tag{2.6}$$

where dp/dx is the longitudinal pressure gradient. Thompson (1967) has suggested the following modification to (2.3) to take the pressure gradient into account:

$$\frac{u}{u_o} = \phi_4 \left[\frac{yu_o}{\nu} , \Delta \right] , \qquad (2.7)$$

where

$$\Delta = \frac{\nu}{u_o^3} \frac{1}{\rho} \frac{dp}{dx} .$$

However, Rotta (1962) has shown, in an analysis of experiments by Ludwieg and Tillmann (1949) on the effects of a very strong positive pressure gradient on the flow in a diverging channel, that the influence of the pressure gradient term Δ on the universality of (2.3) was negligible. For flows very close to separation, the extent of the law of the wall ceases to be significant, as has been observed by Stratford (1959). Patel (1965) has also noted this in relation to the separating aerofoil-flow of Schubauer and Klebanoff (1951).

An analysis by Coles (1968) of hundreds of velocity profiles, submitted at the Stanford University Conference on turbulent boundary layers, has produced irrefutable evidence that the law of the wall adequately describes the overlap region between the inner and outer flows for the vast majority of engineering situations. In the light of this evidence it is interesting to see how the concepts of mixing length and eddy viscosity can usefully be used to describe the velocity distribution from the wall right up to the logarithmic overlap region. Following a suggestion by Professor J.H. Preston,* the author proposes

---

* Emeritus Professor, University of Liverpool.

the following analysis.

Denoting the eddy kinematic viscosity by ν_t, the equation of motion for two-dimensional turbulent flow in the x direction is (using conventional notation):

$$u\frac{\partial u}{\partial x} + v\frac{\partial u}{\partial y} = -\frac{1}{\rho}\frac{dp}{dx} + \frac{\partial}{\partial y}\left[(\nu+\nu_t)\frac{\partial u}{\partial y}\right] . \qquad (2.8)$$

At the wall, the pressure gradient is balanced by the laminar shear stress gradient,

$$\frac{dp}{dx} = \mu\frac{\partial^2 u}{\partial y^2} , \qquad (2.9)$$

which leads to

$$u\frac{\partial u}{\partial x} + v\frac{\partial u}{\partial y} = \frac{\partial}{\partial y}\left(\nu_t \frac{\partial u}{\partial y}\right) , \qquad (2.10)$$

for the region very close to the wall. Here, the viscous shear stresses predominate, which means that the velocity profile is linear. The continuity equation therefore implies that $v \sim y^2$, and hence from equation (2.10)

$$\nu_t \sim y^3 , \qquad (2.11)$$

which was first derived by Reichardt (1951).

Use is now made of the experimentally-observed fact that very near the wall the longitudinal turbulence intensity, $\sqrt{\overline{u'^2}}$, when non-dimensionalised with respect to the wall-friction velocity u_0, varies linearly with the dimensionless wall distance yu_0/ν. This has been

verified by Laufer (1954). Hence, as before, $\sqrt{\overline{v'^2}} \sim u_o \times y_*^2$, where $y_* = yu_o/\nu$. Since $\nu_t \frac{\partial u}{\partial y} = \overline{u'v'}$ it follows that

$$\frac{\nu_t}{\nu} \sim y_*^3 \qquad (2.12)$$

as $y_* \to 0$. Away from the wall, $\frac{\nu_t}{\nu} = \kappa y_*$, which results in the familiar derivation of equation (2.5). The following interpolation formula incorporates these two limiting flow regions in a compact form, as is readily confirmed by inspection:

$$\frac{1}{\nu_t/\nu} = \frac{1}{Cy_*^3} + \frac{1}{\kappa y_*} , \qquad (2.13)$$

where C is the constant of proportionality in (2.12). Remembering that in the near-wall region:

$$\frac{\tau_o}{\rho} = (\nu+\nu_t) \frac{\partial u}{\partial y} , \qquad (2.14)$$

and putting $u_* = u/u_o$, there results the final expression for the dimensionless velocity gradient which is continuously valid from the wall to the logarithmic-overlap region:

$$\frac{du_*}{dy_*} = \frac{\kappa+Cy_*^2}{\kappa+Cy_*^2+C\kappa y_*^3} . \qquad (2.15)$$

This will be referred to again shortly.

The outer region function, ϕ_2, has been found by Coles (1956), by analogy with wake flows, to take the following form:

$$\frac{U_\infty - u}{u_o} = \frac{\Pi}{\kappa}(2-w_k) - \frac{1}{\kappa}\log_e \frac{y}{\delta} , \qquad (2.16)$$

where w_k is a universal function which has since been endorsed at the Stanford conference. An analytical fit to this wake function has been given by Hinze (1959), and is often used in the literature:

$$w_k = 1 - \cos\left(\frac{\pi y}{\delta}\right) \quad . \tag{2.17}$$

A more convenient and equally accurate expression, however, is the polynomial due to Moses (1964):

$$w_k = 6\left(\frac{y}{\delta}\right)^2 - 4\left(\frac{y}{\delta}\right)^3 \quad . \tag{2.18}$$

Unfortunately, incorporation of the universal wake function into (2.16) and subsequent combination with (2.5) leads to a discrepancy in the slope condition at the edge of the boundary layer, as discussed by Cornish (1960), Bull (1969) and others. The effect of this discrepancy is most noticeable in cases of strong negative pressure gradient. The problem is overcome by introducing a modification function, r, into equation (2.16):

$$\frac{U_\infty - u}{u_o} = \frac{\Pi}{\kappa}(2-w_k) - \frac{1}{\kappa}\log_e\frac{y}{\delta} - \frac{r}{\kappa} \quad . \tag{2.19}$$

A polynomial representation for r leads to a unique solution which satisfies all the boundary conditions, as first shown by Finley (1966) and later by Granville (1975):

$$r = \left(\frac{y}{\delta}\right)^2 \left(1 - \frac{y}{\delta}\right) \quad . \tag{2.20}$$

Combining equations (2.5), (2.19) and (2.20) results in the familiar 'two-layer' velocity profile with the new wake function:-

$$\frac{u}{u_o} = \frac{1}{\kappa} \log_e \frac{yu_o}{\nu} + B + \frac{\Pi}{\kappa} \left[6\left(\frac{y}{\delta}\right)^2 - 4\left(\frac{y}{\delta}\right)^3\right] + \frac{1}{\kappa} \left(\frac{y}{\delta}\right)^2 \left(1 - \frac{y}{\delta}\right) \quad . \qquad (2.21)$$

Returning now to equation (2.15), this can be integrated analytically for known values of κ and C. C is found by trial and error by performing a Simpson integration of (2.15) in order to match equation (2.5) in the limit as $\frac{yu_o}{\nu} \to \infty$. The value of C is found to be 0.001093 for $\kappa = 0.41$ and $B = 5.0$. The values assigned to the latter two constants are the ones recommended by Coles at the Stanford Conference. After integrating (2.15) and combining with (2.19) and (2.20), a good deal of algebra yields the following closed-form expression for the velocity distribution over a smooth wall which is valid continuously from the wall up to the free-stream:

$$u_* = 5.424 \tan^{-1}\left[\frac{2y_*-8.154}{16.704}\right] + \log_{10}\left[\frac{(y_*+10.593)^{9.603}}{(y_*^2-8.154y_*+86.38)^{1.992}}\right]$$

$$- 3.52 + 2.44 \left\{\Pi \left[6\left(\frac{y}{\delta}\right)^2 - 4\left(\frac{y}{\delta}\right)^3\right] + \left[\left(\frac{y}{\delta}\right)^2 \left(1 - \frac{y}{\delta}\right)\right]\right\} \quad . \qquad (2.22)$$

As far as the author is aware there is no other explicit expression available for the smooth-wall velocity distribution which satisfies both the momentum and continuity equations at the wall. Dean (1976) has recently published a formula which combines Spalding's (1961) well-

known relationship for eddy viscosity near the wall with Finley's (1966) expression for the wake region. However the dimensionless velocity is implicit in Dean's final equation, making it difficult to use.

The description of the mean velocity distribution afforded by equation (2.22) is in excellent agreement with experimental data near the wall as Fig. 2.1 shows. Here, the equation is compared with the data of Laufer (1954). Away from the wall, as $y_* \to \infty$, equation (2.22) asymptotically approaches (2.21) so the outer region is adequately described.

The two-layer concept of mean velocity distribution is extremely useful for taking into account the effects of the introduction of surface roughness. Although in absolute terms the outer region velocity profile is augmented by the increased wall shear stress, it is essentially independent of viscous effects near the wall. Assuming, for the moment, that the roughness can be characterised by a one-dimensional roughness height, h, the logarithmic law becomes

$$\frac{u}{u_o} = \frac{1}{\kappa} \log_e \frac{yu_o}{\nu} + B - \frac{\Delta u}{u_o} \quad , \tag{2.23}$$

where $\frac{\Delta u}{u_o}$ is a roughness function uniquely related to the roughness Reynolds number $\frac{hu_o}{\nu}$. Nikuradse (1933) used the logarithmic law in a slightly different form thus defining an alternative roughness function, χ, such that

$$\frac{u}{u_o} = \frac{1}{\kappa} \log_e \frac{y}{h} + \chi \quad , \tag{2.24}$$

hence forming the identity

$$\chi \equiv B + \frac{1}{\kappa} \log_e h_* - \frac{\Delta u}{u_o} \quad , \tag{2.25}$$

where $h_* = hu_o/\nu$.

The experimental verification by Hama (1954), Perry and Joubert (1963) and others that the roughness effects are independent of the external pressure gradient has been perhaps one of the most significant contributions to the roughness problem. This means, for example, that roughness functions measured in a pipe are valid in a boundary layer for a particular surface.

Reverting to equation (2.23) the value of y needs defining in the case of a rough wall. The origin for y can occur anywhere between the top and bottom of the protuberances or may even occur outside of these limits. This does not, of course, mean that u = 0 at this point since (2.23) is only valid in the overlap region. The correct origin for y is the one which produces the best fit to equation (2.23) as first pointed out by Clauser (1956), and later by Perry and Joubert (1963).

It is important to understand the nature of the wall friction for a rough surface. For extremely low roughness Reynolds numbers the wall friction is largely of laminar origin. As the roughness Reynolds number, h_*, increases, however, pressure forces act on the individual excrescences. The wall friction now originates from a laminar shear gradient and a form drag associated with the protuberances. The flow is disrupted still further, with increasing h_*, until eventually the viscous forces may be negligible in relation

to the pressure forces. This is the fully-rough flow region which is characterised by the wall-friction coefficients being independent of Reynolds number.

Much work has been done on this fully-rough region with respect to the behaviour of the roughness functions. Schlichting (1936) showed how any roughness geometry could be assigned a value of equivalent sand-grain roughness, h_s, in order to compare the fully-rough frictional effects of different surfaces. The procedure is simply to find a value of h such that χ (whose value is dependent on the choice of h) is equal to 8.5, which corresponds to Nikuradse's measurements for uniform sand-grain roughness in this region. Here the roughness function is described by equation (2.25) which now takes the form:

$$\frac{\Delta u}{u_o} = \frac{1}{\kappa} \log_e \frac{h_s u_o}{\nu} + C_1 \ . \qquad (2.26)$$

Hama (1954) showed that when a uniform roughness is described by a typical length dimension, h, the roughness function in the fully-rough region (if it exists) becomes:

$$\frac{\Delta u}{u_o} = \frac{1}{\kappa} \log_e \frac{h u_o}{\nu} + C_2 \ , \qquad (2.27)$$

where C_2 is a constant depending on the roughness geometry and is to be compared with C_1 in (2.26) which is a universal constant. Using the wire-screen data of his co-workers, Rand and Sarpkaya, and the square-bar results of Moore (1951), Hama demonstrated the universality of equation (2.26) for roughnesses of similar geometries but different

absolute dimensions, and for identical roughnesses in different fluid mediums.

Betterman (1965) introduced the concept of roughness density in attempting to quantify C_2. Defining d to be the ratio of the total projected surface area to the projected roughness area, for uniformly-rough cases he found that the following correlation adequately described the available experimental data in the range $1 \leqslant d \leqslant 5$:-

$$C_2 = 17.35(1.625 \log_{10} d - 1) \quad . \tag{2.28}$$

Beyond this range C_2 is found to decrease with increasing d, which implies that the departure from the smooth law of the wall, $\Delta u/u_o$, reaches a maximum value for constant hu_o/ν at a critical spacing of the roughness elements. A little thought will show that this must be the case. Considering a roughness geometry in the form of regularly-spaced bars of rectangular cross-section, it is obvious that in the limiting cases of d approaching one and infinity the surface becomes smooth. A single roughness element, at low values of d, is subjected to a wake-flow created by the nearby upstream element. As d is increased, the frontal area exposed to the flow must increase due to the diminishing extent of the oncoming wake flow, and consequently the form drag predominates, producing a fully-rough region. The critical value of d must occur when the spacing is such as to allow reattachment of the flow immediately upstream of the element, since increasing the spacing still further then allows laminar shear gradients to be formed near the wall.

In view of the above comments, it is perhaps not surprising that

attempts to find expressions for C_2 in the range $d > 5$ have met with limited success. Such correlations have been proposed by Dvorak (1969), Simpson (1973) and Dirling (1973), but recent measurements by Furuya, Miyata and Fujita (1976) highlight the importance of taking into account the shape of the elements.

The effect of depression roughness was examined by Ambrose (1954). His roughness consisted of holes and cylinders uniformly distributed over the inside surface of a pipe. He found that a fully rough flow region occurred at high Reynolds numbers and he calculated the contribution to the wall friction arising from the presence of the holes alone by a process of interpolation. He deduced that $\Delta u/u_o$ was essentially constant, having a value determined only by the roughness density. The assumption he made was that the presence of the cylindrical roughness did not affect the flow over the depressions, but this seems a reasonable one in view of the roughness distributions used. Ambrose observed, however, that in the intermediate region (often called confusingly 'the transition region') between smooth and fully-rough flows $\Delta u/u_o$ also depended on the roughness Reynolds number.

Encouraging support for these observations comes from Townes and Sabersky (1966) in their highly informative flow-visualisation studies. They observed steady vortex patterns in square-section slots for values of hu_o/ν greater than 150, where in this instance h represents the slot depth. For lower values of hu_o/ν, however, the flow was observed to disrupt periodically. This was attributed to large-scale disturbances from the external boundary layer, rather than an instability in the vortex flow itself, because simultaneous disruptions

were observed in neighbouring slots. The fact that these two regions of slot-flow can be defined in terms of a roughness Reynolds number goes a long way towards explaining Ambrose's results in the intermediate region.

Perry, Schofield and Joubert (1969) have also demonstrated the redundancy of the roughness Reynolds number for depression-type roughness in the fully-rough region. They have proposed that a characteristic length scale which can be identified with $\Delta u/u_o$ is the 'virtual origin error', measured from the top of a slot, which produces a best fit to the logarithmic velocity distribution (as described earlier in this section). There is no obvious physical reason why the virtual origin error should feature as a significant flow variable, however, and in any case the expression which the authors propose in their paper introduces a constant which must be related to the slot geometry.

What emerges, therefore, is a distinct lack of hard experimental facts with respect to the behaviour of roughness functions for uniformly-rough surfaces. The different flow regions are well-defined in a qualitative sense, but what is particularly striking is the difficulty of adequately describing the intermediate region between effectively-smooth and fully-rough flows. The situation will now be examined for irregularly-rough surfaces.

Among the early investigations in this direction are the ones carried out by Colebrook and White (1937) shortly after Nikuradse's work. Using a pipe-flow they tested the effect of distributions of differently-sized sand grains on the roughness functions. They

found that the roughness functions differed from Nikuradse's curves which applied to tightly-packed sand grains of equal diameter. This led them to test naturally-occurring surfaces such as cast iron and galvanised steel. These surfaces displayed equally different characteristics as Fig. 2.2 shows (only the trends are shown here and not the actual data points). Later, Colebrook (1939) published his well-known formula describing the intermediate flow region, for natural surfaces, in terms of the pipe friction coefficient, f, and the equivalent sand-roughness:-

$$\frac{1}{\sqrt{f}} = 1.74 - 2 \log_{10} \left[\frac{h_s}{R} + \frac{18.7}{R_e \sqrt{f}} \right] , \qquad (2.29)$$

where R_e is the pipe Reynolds number. This can be transformed into an expression for the roughness function $\Delta u/u_o$. Musker, Lewkowicz and Preston (1976) derived the following expression using the two-layer velocity profile:-

$$\frac{\Delta u}{u_o} = 5.66 \log_{10} \left[\frac{h_s u_o}{\nu} + 3.31 \right] - 2.72 \ . \qquad (2.30)$$

A similar expression is given by Hama (1954).

The validity of equation (2.29) has been confirmed by Rouse (1942), and later by Bradley and Thompson (1951), despite earlier objections to its universal use by O'Brien, Folsom and Jonassen (1939). However, the Colebrook formula certainly does not apply to all irregular surfaces, and there are many instances of artificially-produced irregular roughnesses which exhibit Nikuradse's trend in

the intermediate region.

Millionshchikov et al. (1974) observed this phenomenon, for example, with irregularly-shaped elements distributed at random in a pipe. Hama (1954) performed experiments on simulated paint-surfaces. A typical surface consisted of fine glass beads which had been air-blasted onto a tacky surface which was subsequently painted with several coats of varnish. He found a considerable departure from Colebrook's intermediate region, even more so than for Nikuradse's results, and he found that this could not be related to the size-frequency distribution of the beads within the range investigated. The concrete pipe investigated by Straub, Bowers and Pilch (1960) showed a very limited intermediate region which became fully-rough at a value of $h_s u_o/\nu$ of about 15. This contrasts with a value of about 60 for Nikuradse's sand-grains and about 45 for the natural surfaces measured by Colebrook and White.

It should be pointed out that equation (2.29) does not relate to pipe-flows for which the equivalent sand-roughness is greater than about one tenth of the pipe radius. These flows are difficult to describe because of the non-existence of a well-defined logarithmic overlap-region. The two-layer concept of velocity distribution consequently breaks down for these macro-roughnesses, and the problem of relating these pipe measurements to a boundary layer flow cannot be tackled in the usual way, if at all. Monzavi (1972) has presented a method of calculating the pipe friction coefficients in such cases in terms of surface statistics. This resulted from his work on distributions of large pebbles on the inside of a pipe. He found that the

significant surface parameters were the averaged surface slope, standard deviation and an autocorrelation-length (this will be defined in Section 2.4). This work resulted in a formula from which estimates can be made of head-losses in extremely-rough pipes.

The above review points to the need for identifying a particular surface with its associated roughness function. It is clearly dangerous to predict the behaviour of the roughness function knowing only the equivalent sand-roughness. Nomograms exist for estimating this equivalent roughness for a range of different surfaces (see Moody (1944)), but their use inevitably relies on the intuition of the engineer. The criteria for applicability of the Colebrook formula in the intermediate region have not been investigated in terms of the surface micro-geometry and it is this region which is of major importance to the naval architect.

2.3 Two-Dimensional Boundary-Layer Flows and Prediction Methods

Methods of predicting turbulent boundary-layer flows fall into two broad categories: differential methods and integral methods. In both methods the transient details of the flow are of no consequence and instead the time-averaged properties of the turbulence field are considered.

The differential methods make use of the partial differential equations of momentum, continuity and energy. To obtain mathematical closure the various turbulence terms occurring in these equations must be related to each other. Bradshaw, Ferriss and Atwell (1967), for example, assumed that the ratio of the turbulent shear stress to

the turbulent kinetic energy is a constant. Alternatively, the turbulent shear stress can be accounted for using mixing-length or eddy-viscosity relationships, such as the popular van Driest (1956) model used in the methods of Patankar and Spalding (1970), Cebeci et al. (1970) and Pletcher (1970). When wall-roughness is present these models require modification. There are indications that Bradshaw's constant, as defined above, does not apply to rough walls, or at least needs modification (see El-Samanoudy (1974)). The van Driest model does not agree with experimentally-determined velocity profiles even in the fully-rough region, and does not account for the different types of behaviour observed in the intermediate region.

The differential methods cannot make direct use of empirical roughness functions because they do not assume any form of velocity profile. Other ways of describing the roughness effects are obviously needed and it would seem that a modified molecular viscosity is the most appropriate, such as proposed by Perry and Joubert (1963). They generalised the logarithmic overlap region, described by equation (2.5), by postulating that roughness modified the value of ν depending on the roughness Reynolds number. The differential methods can then calculate rough-wall flows, for a particular surface, by linking the viscosity to the wall shear-stress and thereby changing its value in accord with experimental observations. Singhal and Spalding (1975) have used this Couette-flow analogy near the wall with reasonable success.

Integral methods rely on cross-stream integration of the boundary-layer equations using an assumed velocity distribution. They lead to

a set of ordinary differential equations which can be numerically integrated very quickly by a computer. They are in general less superior to the differential methods, unless the turbulence structure changes slowly in the direction of the flow. Head (1970) has demonstrated that for such flows over smooth walls there is no noticeable difference in accuracy between the two methods.

What is required, for the purpose of the present work, is a method which can be incorporated as a subroutine into a three-dimensional calculation procedure for ship-hulls, such as the one due to Gadd (1971). In view of the above comments, it was decided to use an integral procedure for the numerical experiment described in Chapter 4. Accordingly, the following discussion and review is orientated towards integral methods of calculation.

The boundary-layer momentum equation for steady incompressible flow is (in the usual notation):-

$$u\frac{\partial u}{\partial x} - \frac{\partial u}{\partial y}\int_0^y \frac{\partial u}{\partial x}\,dy = U_\infty \frac{dU_\infty}{dx} + \frac{1}{\rho}\frac{\partial \tau}{\partial y} - \frac{\partial}{\partial x}\left(\overline{u'^2} - \overline{v'^2}\right) \quad . \qquad (2.31)$$

where u' and v' denote the instantaneous values of the fluctuating components of velocity in the x and y directions respectively, and the over-bar denotes time-averaged values. (This convention will be used throughout the thesis.) After defining the usual integral thicknesses, this becomes (after integrating across the stream):-

$$\frac{d\theta}{dx} + (H+2)\frac{\theta}{U_\infty}\frac{dU_\infty}{dx} = \frac{C'_f}{2} + \frac{d}{dx}\int_0^\infty \frac{\overline{u'^2} - \overline{v'^2}}{U_\infty^2}\,dy \quad , \qquad (2.32)$$

where θ = momentum thickness = $\int_0^\infty \frac{u}{U_\infty}\left(1 - \frac{u}{U_\infty}\right) dy$,

δ_* = displacement thickness = $\int_0^\infty \left(1 - \frac{u}{U_\infty}\right) dy$,

H = shape factor = δ_*/θ

and C'_f = local wall-friction coefficient = $\frac{\tau_o}{\frac{1}{2}\rho U_\infty^2}$.

The last terms in equations (2.31) and (2.32) are known to be negligible except near separation and will be ignored for the moment. It is clear that for constant pressure flows only one other equation is needed for closure, and a wall-friction relation provides this.

Prandtl and Schlichting (1934) carried out predictions for the case of a flat plate covered with uniform sand-grains in a zero pressure-gradient. They assumed that the logarithmic overlap region (to use the present terminology) applied right up to the free-stream and they ignored discontinuities there arising from a finite velocity gradient. Using the pipe data of Nikuradse (1933) they incorporated the roughness function into their calculations and produced charts of wall-friction coefficients, plotted against plate Reynolds number (based on free-stream velocity and distance from the leading edge), for a range of non-dimensional roughness heights.

Granville (1958) performed similar calculations for engineering roughness on flat plates (for constant pressure) and produced a formula which can be likened to Colebrook's (1939) expression for pipes:

$$\frac{0.544}{\sqrt{C_f}} - 5.61\sqrt{C_f} + 0.638 = -\log_e\left[\frac{1}{R_x C_f} + \frac{1}{4.84\frac{x}{h_s}\sqrt{C_f}}\right] \quad , \qquad (2.33)$$

where C_f is the total wall-friction coefficient and R_x is the plate Reynolds number. The above formula has been used by Harrison (1967), together with an assumed relationship between shape factor and local wall friction coefficient, to calculate the development of displacement thickness. This shape factor relationship has been found by Clauser (1954) to apply to both smooth and rough walls in constant pressure flows:

$$\frac{H - 1}{H\sqrt{\frac{C'_f}{2}}} = 6.7 \quad . \qquad (2.34)$$

For the more general case of variable pressure another equation is required and the effect of pressure gradient needs to be taken into account in the wall-friction equation. In the past these modifications to the friction equation have often not been directly related to the assumed form of the velocity distribution. For example Arndt and Ippen (1967) proposed the following friction law for constant pressure:

$$\sqrt{\frac{2}{C'_f}} = \frac{1}{\kappa}\log_e\frac{U_\infty \delta_*}{\nu} + B - \frac{\Delta u}{u_o} \quad . \qquad (2.35)$$

This is a direct consequence of the universality of the velocity defect law (equation 2.16) for such flows. For variable pressure they proposed a modified form:

$$\sqrt{\frac{2}{C'_f}} = \frac{1}{\kappa} \log_e \frac{U_\infty \delta_*}{\nu} + B - \frac{\Delta u}{u_o} + \Omega \quad , \tag{2.36}$$

where Ω is the additional pressure gradient term. Following the arguments of Section 2.2 this term must be independent of roughness effects,and relationships derived from smooth wall experiments can therefore be used. Arndt and Ippen used

$$\Omega = 1.253\ (G'-6.7) \quad , \tag{2.37}$$

for $G' \geqslant 6.7$, corresponding to positive pressure gradients, and

$$\Omega = 0.404\ (G'-6.7) \quad , \tag{2.38}$$

for $G' < 6.7$, corresponding to negative pressure gradients, where G' is related to a pressure gradient parameter $(\delta_*/\tau_o)dp/dx$ (see eqn. (2.42)). These are in good agreement with alternative expressions offered by Nash and MacDonald (1967), but they are strictly only applicable to equilibrium boundary layers (see Clauser (1956)). This will be discussed shortly.

It seems more desirable to avoid such empiricism by including the effect of pressure gradient in terms of the two-layer concept of velocity distribution. After inserting the free-stream boundary conditions into equation (2.21) the following results:

$$\sqrt{\frac{2}{C'_f}} = \frac{1}{\kappa} \log_e \left[\frac{\delta U_\infty}{\nu} \sqrt{\frac{C'_f}{2}} \right] + B + \frac{2\Pi}{\kappa} \quad , \tag{2.39}$$

which is the smooth-wall friction law used by Lewkowicz, Horlock et al. (1970). (It should be mentioned that equation (2.39) does

not depend on the form of the law of the wake except in so far as this in turn governs the absolute magnitude of the wake parameter, Π, defined at the free-stream. Hence, for the outer region velocity profile proposed in Section 2.2 (equation (2.19)) the normalising procedure of Coles (1956) is satisfied, but the quantitative definition of Π is necessarily different from that of Coles. The differences become smaller for increasingly positive pressure gradients. Lewkowicz et al. used the original Coles law in conjunction with Hinze's (1959) curve fit.)

Equation (2.39) is easily modified for the case of rough-walls by including the roughness function corresponding to the surface:

$$\sqrt{\frac{2}{C'_f}} = \frac{1}{\kappa} \log_e \left[\frac{\delta U_\infty}{\nu} \sqrt{\frac{C'_f}{2}} \right] + B - \frac{\Delta u}{u_o} + \frac{2\Pi}{\kappa} \quad . \tag{2.40}$$

El-Samanoudy (1974) used this relationship (for the fully-rough region only) in a method to be described shortly.

Returning now to the problem of closure, the third so-called 'auxiliary' equation can originate in two different ways. Firstly, there are the empirical equations which, in the older methods, related the x-wise derivative of the shape factor H to suitable flow variables. A full account of these older methods is given by Rotta (1962). A good empirical equation is the one proposed by Nash (1965) who proposed that the departure from equilibrium conditions could be quantified in terms of Clauser's (1956) shape factor G'. Head's (1960) entrainment method (and the later improved version by Head and Patel (1970)) also comes under this category. Secondly, there are the energy and moment of momentum methods which are derived by

multiplying equation (2.31) by u and y respectively and then integrating across the stream. These methods usually require a knowledge of the shear-stress distribution.

Brief mention will be made here of Nash's (1965) method. Reference has already been made to Clauser's (1956) shape factor G' in relation to equations (2.37) and (2.38). This is now defined:

$$G' = \int_0^\infty \left(\frac{U_\infty - u}{u_o}\right)^2 \, d\left(\frac{yu_o}{\delta_* U_\infty}\right) \quad , \tag{2.41}$$

and is to be distinguished from the geometrical shape factor H. For equilibrium layers (which can be defined as those layers for which the pressure gradient forces and the shear-stress forces, acting on a stream-wise element, are in constant ratio) Clauser showed that G' could be related to the pressure gradient parameter $(\delta_*/\tau_o)dp/dx$. After analysing available experimental data for equilibrium boundary-layers Nash proposed the following relationship:

$$G' = 6.1 \left[\frac{\delta_*}{\tau_o}\frac{dp}{dx} + 1.81\right]^{\frac{1}{2}} - 1.7 \quad . \tag{2.42}$$

Nash further proposed that this equilibrium relationship could be applied to non-equilibrium flows by introducing a new differential equation for the shape factor. His argument was that for these non-equilibrium flows the distribution of shear stress across the layer is not related to the local velocities in the layer but to their x-wise derivatives (see equation 2.31)). Hence, two flows with identical initial velocity profiles and downstream pressure distri-

bution will develop in a different manner unless the initial shear stress distributions are also identical. To take account of the upstream history of the flow, therefore, he proposed that the x-wise derivative of G' should be an additional initial condition. Of necessity this led to a second-order differential equation for G' and the departure from equilibrium $(G'-G_e')$, where G_e' is the local equilibrium value. It took the following form:

$$\frac{d^2G'}{d\bar{x}^2} = \phi_5 \left[\frac{d}{d\bar{x}} (G'-G_e'), (G'-G_e') \right] \quad , \tag{2.43}$$

where $\bar{x}$ is a non-dimensional distance defined by $dx/d\bar{x} = \delta_*$. Predictions of non-equilibrium flows using this equation gave significantly better agreement with experimental data than older equations. The non-equilibrium boundary layer has also been studied by McDonald and Stoddart (1965), Nash and MacDonald (1966), Goldberg (1966) and McDonald (1966).

Dvorak (1969) used Head's (1960) entrainment method as the auxiliary equation, together with Arndt and Ippen's (1967) wall friction relationship (equation (2.36)), and found satisfactory agreement with the limited experimental data available for rough-wall boundary layers in the fully-rough region. A significant finding was that the rough-wall data of Betterman (1965) collapsed onto the same entrainment curve as Head had originally proposed for smooth walls. This is not surprising in view of the fact that the entrainment is related to the outer part of the boundary layer.

Referring to the second class of auxiliary equations, the

energy and moment of momentum equations are:-

$$\tfrac{1}{2}\frac{d}{dx}\left(U_\infty^{\,3}\,\delta_{**}\right) = \frac{1}{\rho}\int_0^\infty \tau\,\frac{\partial u}{\partial y}\,dy \qquad (2.44)$$

and

$$\frac{1}{U_\infty^{\,2}}\frac{d}{dx}\left[U_\infty^{\,2}\int_0^\infty y\left(1-\frac{u}{U_\infty}\right)\frac{u}{U_\infty}\,dy\right] + \frac{1}{U_\infty}\int_0^\infty\left(1-\frac{u}{U_\infty}\right)\frac{d}{dx}\left[U_\infty\left(y+\int_0^y\frac{u}{U_\infty}\,dy\right)\right]dy$$

$$= \frac{1}{\rho U_\infty^{\,2}}\int_0^\infty \tau\,dy \qquad (2.45)$$

respectively, where

$$\delta_{**} = \int_0^\infty \frac{u}{U_\infty}\left[1-\left(\frac{u}{U_\infty}\right)^2\right]dy\ .$$

The use of the energy equation requires an expression for either the shear-stress distribution or the integral of the shear work (corresponding to the last term in equation (2.44)). Expressions for the shear-work integral have been proposed, based solely on experimental observations. A well-known one is due to Truckenbrodt (1952):

$$\frac{1}{\rho}\int_0^\infty \tau\,\frac{\partial u}{\partial y}\,dy = \frac{0.0056\,U_\infty^{\,3}}{\left(\frac{\theta U_\infty}{\nu}\right)^{1/6}}\ ; \qquad (2.46)$$

but it is only reliable for a very restricted range of shape factor. Rotta (1962) argued that the major contribution to the integral must

come from the wall region where most of the energy is dissipated. Denoting the energy dissipation by E', and an arbitrary point in the logarithmic region of the velocity distribution by y', the dissipation integral can be written as:

$$\int_0^\infty E'\,dy = \int_0^{y'} E'\,dy + \int_{y'}^\infty E'\,dy \quad . \tag{2.47}$$

Using the turbulent energy equation (and a convenient algebraic identity) the following results:

$$\int_0^\infty E'\,dy = u_o^2\left[U_\infty + u_o F'\right] \quad , \tag{2.48}$$

where

$$F' = \frac{-v'\left[\frac{1}{2}(u'^2+v'^2+w'^2) + P/\rho\right]}{u_o^3} + \frac{1}{u_o^3}\int_{y'}^\infty (E' - u_o^2\,\frac{\partial u}{\partial y})\,dy. \tag{2.49}$$

The first term (representing the transport of energy to the wall region by turbulent diffusion) is evaluated at y' so that F' should be independent of roughness. Rotta assumed that F' depended only on the shape factor for a given pressure distribution and after analysing available experimental data he proposed the following relationship for the shear work integral in terms of Π:

$$\frac{1}{\rho}\int_0^\infty \tau\,\frac{\partial u}{\partial y}\,dy = u_o^2\left[U_\infty + u_o\,(1.84\Pi^2 + 1.5\Pi - 5.55)\right] \quad . \tag{2.50}$$

Fediaevsky (1937) suggested that a polynomial could represent the shear-stress distribution subject to its satisfying certain boundary conditions. The method was improved by Ross and Robertson (1950), but agreement with available measurements was generally poor.

Tetervin and Lin (1951) showed that the boundary layer equation could be transformed into an expression for the shear-stress distribution by assuming a one-parameter family of mean velocity profiles. No theoretical support can be given for the existence of such a family, however, so that the final equation for the shear stress is only as good as the assumption that was made.

For equilibrium boundary layers Clauser (1956) showed that the eddy viscosity in the outer region was essentially constant and proportional to the free-stream velocity and the displacement thickness. The variation in the inner region follows from the universality of the logarithmic overlap region. Hence,

$$\nu_t = \alpha U_\infty \delta_* \quad , \tag{2.51}$$

for the outer region, where α is a constant and is equal to 0.018, and

$$\nu_t = \kappa y u_0 \tag{2.52}$$

for the inner region. These expressions are valid for both smooth and rough surfaces. Lewkowicz, Horlock et al. (1970) combined these simple relationships with the two-layer velocity distribution (using Hinze's approximation for the outer velocity distribution) and derived the following analytical expressions for the shear and shear-work integrals respectively:

$$\frac{1}{\rho U_\infty^2}\int_0^\infty \tau\, dy = \delta\omega^2\left[\eta_o\left(1+\Pi-\log_e\eta_o\right)+\frac{\Pi}{\pi}\sin(\pi\eta_o)\right] \qquad (2.53)$$

and

$$\frac{1}{\rho U_\infty^3}\int_0^\infty \tau\frac{\partial u}{\partial y}\,dy = \omega^2+\frac{\omega^3}{\kappa}\left\{1+\log_e\eta_o-\eta_o+2\Pi\left[1-\cos(\pi\eta_o)+\pi\eta_o\sum_{n=1}^{n=\infty}\frac{(-1)^{n-1}\,\pi^{2n-1}\,(1-\eta_o^{2n-1})}{(2n-1)(2n-1)!}\right]+\frac{\Pi^2}{2}\left[\pi^2\eta_o\left(1-\frac{\eta_o}{2}\right)+\frac{\sin^2(\pi\eta_o)}{4}\right]\right\}, \qquad (2.54)$$

where $\eta_o = \alpha(1+\Pi)/\kappa^2$, and $\omega = u_o/U_\infty$. The quantity η_o defines the value of y/δ at the join between the inner and outer regions. These equations were incorporated directly into equations (2.44) and (2.45) and the use of these auxiliary equations (which strictly apply to equilibrium flows) resulted in satisfactory agreement with a variety of measured boundary-layers.

The above method was extended by El-Samanoudy (1974) to include the effects of an irregularly-rough surface. This was done by incorporating the roughness function (corresponding to his sand-paper roughness) into the friction equation (see equation (2.40)). Unfortunately, El-Samanoudy's measurements covered only the fully-rough region corresponding to low values of plate Reynolds numbers; consequently, the computer predictions could not be extended to arbitrarily

high Reynolds numbers. The ability to do this is essential if laboratory measurements of roughness functions corresponding to ship-hull roughness are to be of any practical use.

2.4 The Acquisition of Roughness Records

The method currently in use for specifying hull roughness has already been mentioned in Section 2.1. It will be recalled that the M.A.A. is a one-dimensional parameter which represents the distance between the highest and lowest points along a profile of length five centimetres. Accepting, for the moment, that the M.A.A. does not correlate well with hydrodynamic drag, the naval architect will require to know the answers to three questions:

a) What roughness parameters need to be measured?

b) How can they be measured in a practical way?

c) What accuracy is necessary?

It is likely that the answer to (a) involves parameters which are related to the high-frequency structure of the roughness, rather than to single height measurements associated with long wavelengths (such as M.A.A.). Accordingly, a brief review of the literature is presented relating to methods of obtaining records of roughness profiles. The questions which have been posed will be dealt with in later chapters.

Specification of surface finish has become an important topic in the manufacturing industry due to the decreasing tolerances of high-precision components. Attempts were made in the early 1930's to assess roughness using optical amplification of surface profiles

obtained either by sectioning the specimen or by tracing the surface with a stylus whose vertical displacement could be mechanically amplified. One rather bizarre scheme involved listening to a loud-speaker connected (via anamplifier) to a phonographic pick-up which was travelling over the surface.

The first quantitative assessment of roughness was performed by Abbott and Firestone (1933) using a stylus-instrument.

The significance of Abbott and Firestone's work lies in the fact that the stylus was connected to a transducer which (after suitable electronic processing) was used to trace an amplified version of the original profile. Furthermore, the input and output devices were linked via a gearbox so that the profile could be deliberately distorted. Most stylus-instruments still use these principles.

Early transducers used piezoelectric crystals and moving-coil elements, but these suffer from poor low-frequency response due, respectively, to high leakage rates (of electric charge) and the need for integrating circuits. Modern instruments use linear variable differential transformers (L.V.D.T.'s) which rely on an inductance effect to produce a linear output voltage throughout the frequency range - even for static displacements (see Reason (1956)).

It is customary to mount the transducer on a skid so that the actual signal corresponds to the distance between the stylus and the skid. In this way a datum is not required, but Reason (1944) has pointed out a serious disadvantage in that the skid acts as a mechanical filter, so that the final profile record does not exhibit the original low-frequency components.

Diamond styli which can resolve wavelengths less than ten microns are commercially available. However, the ultimate fidelity of the profile record also depends on the traverse speed and the stylus tracking force. The latter cannot be too great, due to the danger of the stylus delving into the surface, and if the traverse speed is too high the stylus will 'hop' over the surface features. This problem has been treated by Guerrero and Black (1972).

The actual signal can be processed in one of two ways (assuming that quantitative information is required rather than a graphical record). Firstly, there are the analogue techniques which employ electronic circuits to measure the surface statistics. The difficulty here is that the signals are generally of low frequency (because of the low traverse speeds) and there are inherent electronic complications concerning such signals. Oonishi (1966) introduced a simple method of overcoming these problems, which involved recording the signal on a tape recorder and replaying it at a higher speed. Examples of analogue techniques can be found in the papers by Myers (1962) and Kubo (1964).

Secondly, there are the digital techniques which use an analogue-to-digital converter to produce a digital record of the surface profile. The availability of such a record has clear advantages. Almost any statistical parameter can be calculated on a computer simply by altering the program, whereas new hardware is required if analogue methods are used. Of course such hardware might not exist for complicated measurements.

Objections to the use of stylus instruments have come from Tarasov (1945) and Shaw and Peklenik (1963). Deep undercuts cannot

be recorded by the stylus, and the accuracy with which the roughness 'valleys' are tracked by the stylus is limited by the tip dimensions. Williamson, Pullen and Hunt (1969) demonstrated that for a bead-blasted aluminium surface the cumulative height distribution was Gaussian except near the valley bottoms. Although such a surface need not necessarily be Gaussian, the same effect could be explained in terms of lack of fidelity in the roughness record.

To summarise, therefore, it is desirable to have digital records of roughness profiles so that computers can be used to investigate the more complicated aspects of the surface microgeometry. If stylus instruments are to be used, then an analogue-to-digital converter is required. Moreover, the dimensions of the stylus tip must be smaller than the lowest wavelengths under consideration. Alternatively, if optically-amplified traces are to be used, then the method of sectioning the roughness must be such as to preserve the high-frequency components of the surface. A method must then be found of digitising the roughness records into a form suitable for input to a computer. These points will be discussed further in later chapters.

CHAPTER 3

THE PIPE-FLOW EXPERIMENTS

3.1 Introduction

The discussions in Sections 2.2 and 2.3 have demonstrated the need for empirical data concerning the behaviour of the roughness function for a particular rough surface. For the case of a ship-hull roughness it is proposed to make an accurate full-scale copy of a representative sample of the surface micro-geometry while the ship is in dry dock.

A two-dimensional flow is required to measure the roughness function, and a flat plate or pipe seems the obvious choice. Since the roughness function is uniquely related to the roughness Reynolds number, it is important to ensure that the range of Reynolds numbers being measured coincides with the actual ship. Clearly, flumes are not suitable for this purpose. Of course the fluid medium need not be water; it is the Reynolds number per unit length which is the important parameter (since the one dimensional roughness height is the same for both the experiment and the ship). A flat plate in a high-speed wind-tunnel poses measurement problems, which would undoubtedly affect the accuracy of the measured roughness functions.

Pipes provide a steady, two-dimensional flow whose associated wall friction can easily be found from the measured pressure drop. Since air compressors were readily available at Liverpool University it was decided to use air as the fluid medium. At high Reynolds numbers small corrections to the pressure drop are required, to take into account slight

changes in fluid density (this does not invalidate the assumption of a unique relationship between the roughness function and the roughness Reynolds number. Goddard (1957) has demonstrated that the only observable effect of compressibility is in the reduction of the fluid density term appearing in the roughness Reynolds number) and a simple one-dimensional analysis is adequate for this purpose. Finally, the use of air has a useful spin-off in that the measurements of turbulence quantities are made easier.

3.2 The Method of Surface Replication

The aim of copying a sample area of hull-roughness in dry dock is to obtain a nominally flat positive replica which shall be referred to as the 'master copy'. It is the master copy which will subsequently be used in order to manufacture a pipe-line containing the original surface roughness.

Ships were visited in dry dock and their hulls were inspected. A representative sample area was chosen for replication subject to its satisfying the following requirements:-

a) The sample area must measure approximately
   0.7m x 0.6m
b) The sample area must not contain double curvatures (it must be either flat, or curved about a single axis)

A thixotropic (free-flowing) silicon rubber paste was applied to the hull, using either a fine-quality paint brush or a squeegee. All moulding materials were subjected to lengthy tests and field trials before they were finally accepted for use in the experimental programme.

Experience showed that the problem of minute air-bubbles did not arise if the paste was applied correctly. This conclusion was drawn after measurements of both the original and the replicated test surfaces were compared. Qualitative examination under a microscope also confirmed the accuracy with which this moulding compound could reproduce features measuring down to approximately 20 microns.

A fine nylon mesh, applied over the paste, gave the final rubber negative some reinforcement. The time taken for the paste to cure was found to vary with the ambient temperature (cold weather tending to prolong the cure time considerably). A simple wooden framework was used to secure the rubber patch whilst it was curing.

After several hours the rubber could be removed from the hull and taken to the workshop. The rubber was then laid out face downwards so that the required rough surface was in contact with a smooth flat horizontal board. A wooden frame was placed in position around the board and filled with dental plaster. After the plaster had set, the whole arrangement was turned over and the board could be removed, thus exposing the original negative rubber copy, which was now nominally flat. This plaster backing was found necessary because it was not possible to apply a perfectly even coating of rubber to the hull.

The master copy was made by applying a coat of epoxy resin to the rubber, followed by alternate layers of medium-grade glass-fibre matting and resin. The choice of the resin which was used resulted from the field trials mentioned earlier. After the resin had catalysed, the master copy was removed and cut to size - the exact dimensions depending on the circumference and length of each pipe section. The details of all the chemicals used can be found in Appendix 1.

3.3 Manufacture of the Pipe-Sections

Two types of pipe were used in the investigation and they may conveniently be referred to as the 'large' and 'small' pipes. The nominal inside diameters of these were 130 mm and 60 mm respectively. The two different designs arose from the experience gained with the initial large pipes. It was decided that for the particular measurements under consideration a smaller pipe diameter could be used with very little loss in accuracy and it will be seen, in this section, that this resulted in a considerably simpler method of manufacture.

Each pipe was divided into a number of flanged sections whose inside surfaces were positive replicas of a particular master copy. Two large pipes were manufactured, one of which was smooth and the other corresponded to a ship which had recently dry-docked but had not received any treatment to its hull (this was the roughest surface in the range under consideration). Four small pipes were fabricated using the same basic method but with differences in detail. They corresponded to different ships - all of which had received surface preparation of one form or another (the samples were taken shortly before the ships were due out of dry-dock). The degree of roughness for these four samples was deliberately staggered (within the limits imposed by the availability of co-operative shipping companies) so that a continuous range of roughness could be tested. Details of the manufacture of the pipe lines can be found in Appendix 1.

3.4 Apparatus and Instrumentation

The large pipes in the series were the first to be tested and their dimensions were chosen after a thorough design study. Since

there was ample power available in the 750 kW 'Reavell' compressor, the two main constraints on the pipe diameter were imposed firstly by the need for a fully-developed flow and secondly by the limitations on pipe length set by the size of the laboratory.

The length-to-diameter ratio required for a fully-developed pipe-flow is generally accepted to be about 50 for a smooth surface and somewhat lower for a rough surface, although the actual figure does depend on the inlet conditions. Walklate, Heikal and Hatton (1977) have shown, using theoretical predictions supported by experimental measurements in a smooth pipe, that the turbulent shear stress distribution in the radial direction reaches its fully developed state after approximately 30 pipe diameters. Logan and Jones (1963) have reported one instance where turbulence quantities became fully developed in as few as 15 pipe diameters following an abrupt increase in surface roughness. The figure of 50 is thus a fairly pessimistic one when applied to rough surfaces.

In order to ensure a fully-developed flow a smooth P.V.C. inlet-pipe was connected between the supply line and the working sections (containing the test surfaces). The inlet-pipe was common to both systems and had an internal bore of 150 mm and a length-to-diameter ratio of 52.

At the junction between the supply-line and the inlet-pipe a 0.2m Wiseman valve was fitted to control the flow-rate. A 50 mm layer of honeycomb was housed 12 diameters downstream of the valve to eliminate any swirl which might have been present in the flow. In addition to the 750 kW compressor a 'Sturtevant' fan was connected to the supply duct. This was powered by a 15 kW English Electric motor which was

wired to an Allenwest control unit. A series of valves allowed the flow to be directed to the inlet-pipe and these were set according to the power requirements.

The particular test-pipe under consideration was connected to the end of the inlet-pipe via a matching fairing section to ensure a gradual change in cross section. The lengths of these sections were approximately 0.23m and 0.6m for the large and small pipes respectively. In the case of the small pipes an additional honeycomb housing was placed immediately after the fairing section to eliminate any disturbances which may have been set up. The diameter of the test-pipe was determined by filling a section with water at room temperature and weighing it. A mean diameter was calculated from the weight of the empty section and its length. A total of 12 sections was used for each type of pipe, giving working lengths of 56 diameters and 100 diameters for the large and small pipes respectively. These figures for working length do not include the inlet-length. Neoprene gaskets were incorporated in all the flanged joints to ensure an air-tight seal.

The whole apparatus was mounted on wooden cradles which could be adjusted to ensure perfect alighment of each pipe-line. Air was discharged to atmosphere and an open-ended collector duct served to divert the flow away from the working area. This was situated approximately two metres downstream of the exit so that the exit static pressure was essentially atmospheric. Figures 3.4 and 3.5 show the general layouts for the two types of pipes.

For the large smooth pipe a total of six static pressure tappings was made. Each tapping had an internal bore of 1.6 mm and great care

was taken to ensure that there were no burrs remaining on the insides of the liners resulting from the drilling operation (see Shaw (1960)). The tappings spanned a distance of 34 pipe diameters upstream of the exit plane (their exact locations are indicated in Fig. 3.4).

Although wall tappings have been used in the past for measurement of static pressure in rough pipes (see, for example, Townes, Gow et al. (1972)) it was felt that conventional probes immersed into the stream would provide more accurate measurements. According to Hinze (1959) accurate measurements of absolute static pressure are almost impossible to achieve in a turbulent flow, due to the lack of correlation between the hole size (of the probe) and the length scales of the turbulence field. For measurements of pressure drop in a pipe, however, the difference in readings between two probes of identical dimensions and at the same radial positions is all that is required - providing the turbulence structure is similar at both measuring stations. This latter condition is satisfied if the flow is fully developed.

For the large rough pipe a single static pressure probe was inserted to a depth of 25 mm and at a distance of 25 pipe diameters from the exit plane. The probe, which measured 3.2 mm in diameter, is shown in Fig. 3.6. Calibrations were performed in a wind tunnel, using a standard N.P.L. ellipsoidal probe as a reference. The static pressure was also measured at a distance of 10 mm from the exit plane and at the same radial location as the upstream station, using a similar probe mounted on a traverse gear. The static pressure recorded at this station was found to be signficant only at high Reynolds numbers.

A 'Mitutoyo' dial gauge, mounted on the traverse gear, could locate the radial distance from a datum position with an accuracy of

± 15 microns. The traverse gear could rotate through steps of 45 degrees in order to check for flow symmetry and could accommodate a variety of probes.

It is known that the maximum variation in static pressure across the radius of a pipe is of the order of one percent of the wall static pressure for a fully-developed flow. For a smooth pipe the radial static pressure distribution can be derived from the equations of motion (see Goldstein (1958)) but the analytical expression which results probably requires modification for rough pipes. In view of the very small variations involved it was decided to follow the example of Laufer (1953) and measure mean velocity (for the rough pipes) using a total head tube in conjunction with the static pressure measured at a fixed radial location.

All mean velocity profiles and turbulence measurements were made at a distance of 10 mm upstream of the exit plane. This applied to all the pipes. The pitot tube was square-headed, with an outer diameter of 0.9 mm and an inner-to-outer diameter ratio of 0.6.

For the small pipes two static pressure probes whose dimensions are shown in Fig. 3.6 were used (the same design was used for both types of pipe). The probes were positioned at 19 and 44 diameters upstream of the exit plane and at a distance of 10 mm from the wall. A special traverse gear, which incorporated a stream-lined shaft to minimise blockage effects, was manufactured for use with the small pipes. In addition, the whole assembly could be rotated about the pipe axis to enable traverses to be made along any radius. A photograph of the instrument is shown in Fig. 3.7.

Measurements of stagnation temperature were made, using a con-

ventional thermocouple probe, at the exit plane and also at the beginning of the inlet pipe. These measurements were needed to calculate the static temperature when compressibility effects became noticeable.

An inclined multi-tube manometer or a null-reading micromanometer was used for measurements of pressure. The choice of instrument and manometric fluid (methylated spirit or mercury) depended on the magnitude of the pressure. Head measurements could be read to within accuracies of $\pm$ 0.1 mm and $\pm$ 0.02 mm for the multi-tube instrument and the micromanometer respectively.

Turbulence quantities were measured using a two-channel hot-wire system. Platinum-coated tungsten wires were used throughout the investigation to reduce the problem of oxidation. A 'Disa' miniature X-probe (type 55P61) was connected via a 25m cable to two constant temperature anemometers ('Disa' type 55A01) whose output signals were processed, if required, by two linearising units ('Disa' type 55M25). The summing and differencing circuits of a random signal indicator and correlator ('Disa' type 55A06) were connected to the outputs of the linearisers for measurements of traverse normal stresses. Voltages were read from a digital voltmeter ('Weir' type 500, mk. 3) which had a variable integration time.

The signals from both channels were displayed on a double-beam storage oscilloscope ('Telequipment' type DM64). This was particularly necessary during the calibration and alignment of the instrumentation in order to minimise spurious oscillations in the anemometer bridge circuitry. The oscilloscope also enabled the frequency characteristics of the probe to be determined.

A frequency analyser and level recorder ('Brüell and Kjaer' types 2107 and 2305 respectively, with a frequency response of 20Hz to 20kHz) were used to calculate the frequency spectrum of the signals. The two instruments were mechanically-synchronised by means of a drive-cable. The interconnections for the electronic equipment are shown in Fig. 38.

In order to establish a datum from which wall distances were measured for the rough pipes, a flat-headed copper pin was introduced among the roughness excrescences in the measuring plane. The top of the pin was allowed to assume a position approximately 0.5 mm above the local peaks in the roughness. The other end of the pin was connected to one side of a transistorised continuity tester. The other side of the tester was wired to the traverse gear so that when the pitot tube just made contact with the pin a small light came on. For the smooth pipe a short-focus telescope was used to visually determine the point of contact between the wall and the pitot tube.

The datum for the hot-wire traverses could not be established using the above contact methods because of possible damage to the probe. A cathetometer, with a vernier scale accurate to within $\pm$ 10 microns, was used in order to measure the distance between a pre-arranged datum just above the surface and either the surface itself (in the case of the smooth pipe) or the top of the contact pin. Once the datum had been established the wall distances were measured using the dial gauge mounted on the traverse gear.

3.5 Experimental Measurements and Procedure

Each pipe was thoroughly checked for flow symmetry before any of

the experimental measurements were taken. For the smooth pipe, peripheral variations in longitudinal mean-velocity for a fixed wall distance were found to be of the order of one percent. This figure rose to approximately 1½ percent for all the rough pipes.

The air supply was switched on at least 30 minutes before the start of a measurement session for the apparatus to reach equilibrium conditions. The values of air density and kinematic viscosity were corrected for daily variations in barometric pressure and air temperature. Since methylated spirit is hygroscopic it was discarded every fortnight and the manometers were replenished with fresh fluid.

The velocity distribution was measured across the radius of the smooth pipe for pipe Reynolds numbers of approximately 9.5×10^4 and 3.5×10^5 and the corresponding pressure drops were determined from the static pressure distribution. It was found that any departure from a linear pressure gradient was negligible, except at high Reynolds numbers when changes in air density became appreciable. The friction curve for the smooth pipe was found by measuring the pressure distribution for Reynolds numbers ranging from 5.0×10^4 to 1.5×10^6.

The mean-flow measurements for all the rough pipes concentrated on the velocity profile in the wall region. For each profile the static pressure and centre-line velocity were recorded. It was found from experience that the logarithmic overlap region extended to about 15% of the pipe radius from the wall and that it could be adequately defined by five measurements. Due to the high turbulence levels near the wall particular care was necessary when reading the manometers. The meniscus was observed, using a magnifying glass, and after a period of sometimes three or four minutes an estimate of the average head

reading was made. The number of inner-region distributions per pipe measured in this way averaged about fourteen and covered the maximum range of Reynolds numbers possible with the equipment available. Mean velocity distributions across the radius of each pipe were also measured at three different Reynolds numbers.

A smooth perspex pipe with a diameter of approximately 35 mm and a length-to-diameter ratio of 120 was used to calibrate the hot-wire probe. The pipe was connected to a low-power fan which was controlled by means of a variac.

The response of the wire to a square-wave input was observed on the oscilloscope so that any necessary adjustments to the bridge balance of the anemometers could be made. The upper frequency limit of the probe was found to be approximately 20 kHz and the frequencies above this were rejected using the filtering unit on the anemometers - thus ensuring a good signal-to-noise ratio.

Frequency analysis was performed at a constant 6% bandwidth. The unfiltered signal was fed to the level recorder which was than adjusted to coincide with a datum recommended by the manufacturers. Filtered signals were recorded on the pen chart relative to an internally-generated reference voltage.

The probe was operated at a constant overheat ratio corresponding to a temperature of approximately 250^{o}C which is sufficiently low to prevent oxidisation at the surface of the wire. After initial calibration the distribution of the turbulence shear stress $-\rho\overline{u'v'}$ was measured in the calibration pipe and compared with the theoretical distribution based on the measured pressure gradient. The pressure gradient was determined using three static pressure holes. The direc-

tional sensitivity coefficient (see Section 3.6) was found by matching these two distributions. This procedure was repeated for each test-pipe before any measurements were taken.

Correct alignment of the probe with respect to the axis of the test-pipe was ensured by the judicious design of the probe holder on the traverse gear. For the rough pipes the dial gauge was set to zero corresponding to a distance of 1.29 mm measured from the top of the copper pin to the mid-point between the prongs of the probe. The true wall distance, measured from the geometric mean of the surface, was calculated from a knowledge of the surface geometry. Measurements were made of the transverse normal stresses and the shear stress $-\rho\overline{u'w'}$ in the conventional manner by rotating the probe through 90^{o}.

Measurements were taken of the three components of turbulence normal stresses and the above mentioned shear stresses for a pipe Reynolds number which, for all the test-pipes, was within a few per-cent of 9.5×10^{4}. The corresponding pressure gradients were also measured. Spectograms of the longitudinal normal stress were recorded at wall distances of y/R equal to 0.02, 0.08 and 1.0 - the first two stations representing extreme values of the wall distance in the loga-rithmic overlap region. For the small pipes these measurements were repeated at a Reynolds number of 4.5×10^{4}. Although the air intakes for both compressors were supplied with filters to remove dust particles the probe was regularly cleaned in acetone during the experimental sessions. After cleaning, the probe was returned to the pipe centre-line and the anemometer bridge d.c. voltage was compared with its value at the start of the experimental session. If these voltages differed appreciably the results were discarded and the probe was

examined for damage or contamination under a stereo-microscope. A replacement was available in the event of the original probe needing repair.

3.6 Reduction of Data

The main objective of the mean flow measurements was to determine the relationship between the roughness functions and the roughness Reynolds number, for all the rough surfaces. As a starting point, the roughness Reynolds number was defined in terms of the M.A.A. for the particular surface (these values were found using the B.S.R.A. wall gauge - see Lackenby (1962)).

Before discussing the procedure which was used for calculating the roughness functions from the experimental measurements, some definitions will be made. Whereas in Chapter 2 the wall distance, y, was generalised to give the best fit in the logarithmic overlap region (see equation (2.24)), it will now be defined as the wall distance measured from the geometric mean of the surface (this interpretation has already been used in the previous section in connection with the position of the hot-wire probe). A distance ε is defined such that the equation described by

$$\frac{u}{u_o} = \frac{1}{\kappa} \log_e \frac{(y+\varepsilon)}{h} + \chi \quad , \tag{3.1}$$

gives the best fit to the experimental values of u and y in the inner region (with y now assuming its new meaning). This distance will be referred to as the 'origin error' after Perry and Joubert (1963), although this is something of a misnomer.

At high Reynolds numbers the value of u_o in equation (3.1) cannot be determined directly from the pressure drop because of changes in air density along the pipe. It should be pointed out that the compressibility effects encountered in the investigation are too insignificant to invalidate the law of the wall. Walz (1961), in his discussion of compressible turbulent boundary layers, has demonstrated that the inner-region velocity distribution assumed in this investigation applies up to a Mach number of at least 9. The effect of compressibility on the roughness function was mentioned in Section 3.1. Relationships will now be established from which accurate values of χ can be determined from the experimental measurements.

The pipe average-velocity can be related to the wall friction velocity, u_o, centre-line velocity U_c and wake-strength parameter Π. Defining the pipe average-velocity, U_{av}, in the usual way:

$$U_{av} = \frac{2}{R^2} \int_0^R u(R-y)dy \quad , \tag{3.2}$$

where R is the mean radius determined from the weighing experiment, and using the velocity distribution described by equation (2.21), the following expression results:

$$\frac{U_{av}}{U_c} = 1 - \frac{u_o}{\kappa U_c} \left(\frac{43+42\Pi}{30}\right) . \tag{3.3}$$

Furthermore, the same result occurs when the roughness function is introduced into equation (2.21), so that (3.3) is valid for fully-developed flow in smooth and rough pipes. This relationship was

tested in both the large pipes and the resulting values of pipe average-velocity agreed with the integrated velocity profiles to within one percent. Preston and Norbury (1960) proposed a method of measuring the average velocity by means of a single measurement at the three-quarter radius position. Although this method was found to yield the same accuracy it can be shown that a small correction is required whose magnitude depends on Π. The correction becomes zero with Π is approximately 0.3 (assuming the effects of turbulence on the readings of the instruments are negligible). It was decided to use equation (3.3) for the present investigation.

Assuming a one-dimensional, adiabatic flow with friction, it can be shown that the wall friction velocity at the exit plane, u_o, is related to the pressure drop, Δp, measured over a length, L_1, by the following equation:

$$u_o^2 = \frac{\Delta p D}{4\rho_a L_1}\left[1 - \frac{\rho_a U_{av}^2}{\gamma p_a}\left(\frac{\gamma+1}{2} - \frac{\Delta p \gamma}{2\rho_a U_{av}^2}\right)\right] , \qquad (3.4)$$

where U_{av} is the pipe average velocity at the exit plane, p_a is the static pressure at the exit plane and γ is the ratio of specific heats. The above formula reduces to the incompressible form as U_{av} tends to zero. Details of the derivation of equation (3.4) can be found in Appendix 2.

A regression analysis (in the least squares sense) of equation (3.1) leads to the following expression for χ:

$$\chi = \frac{1}{5}\sum_{i=1}^{5}\left[\frac{u_i}{u_o} - \frac{1}{\kappa}\log_e\left(\frac{y_i}{h} + \frac{\varepsilon}{h}\right)\right] , \qquad (3.5)$$

where u_i and y_i represent the five inner-region measurements of mean velocity and wall distance respectively. The analysis assumes that u/u_o and y/h are expressed in semi-logarithmic co-ordinates. The sum of the squares of the residuals σ_1, is given by:

$$\sigma_1 = \sum_{i=1}^{5} \left[\frac{u_i}{u_o} - \left(\frac{1}{\kappa} \log_e \left(\frac{y_i}{h} + \frac{\varepsilon}{h} \right) + \chi \right) \right]^2 \quad . \tag{3.6}$$

Finally, combining equations (2.25) and (2.40), for the case of pipe-flow, leads to a relationship between χ, Π, and the centre-line velocity, U_c:

$$\frac{U_c}{u_o} = \frac{1}{\kappa} \log_e \frac{R}{h} + \chi + \frac{2\Pi}{\kappa} \quad . \tag{3.7}$$

Hence equations (3.3) to (3.7) lead to the solution set:

$$(\chi, u_o, \varepsilon, \Pi, U_{av}) \quad ,$$

for known values of:

$$(\kappa, \gamma, h, R, L_1, \rho_a) \quad ,$$

and for experimentally-determined values of:

$$(y_i, u_i, U_c, \Delta p, p_a) \quad ,$$

subject to σ_1 being minimised. A PDP8 computer was programmed in 'BASIC' to perform the necessary calculations. Details of the method are given in Appendix 3.

For the smooth pipe, equations (3.3), (3.4) and (2.39) form a closed system from which u_o, Π and U_{av} can be found from the measured

values of U_c, Δp and p_a. For all total head measurements the Young and Maas (1936) correction for the displacement of the effective centre of the pitot tube was applied.

The interpretation of the signals from a hot-wire anemometer depends on the assumed law for the effective cooling of the wire. For an infinitely-long wire the components of velocity along the wire does not influence the cooling. For finite wire-lengths, however, Hinze (1959), Champagne (1965) and others have shown that the instantaneous effective cooling velocity, q_{eff}, is given by:

$$q_{eff}^2 = q_n^2 + k^2 q_p^2 , \qquad (3.8)$$

where q_n and q_p are the instantaneous components of velocity normal and parallel to the wire and k is a directional sensitivity coefficient. The value of k depends mainly on the length-to-diameter ratio of the wire and a value of 0.2 was found for the probe used in the present investigation. Kjellström and Hedberg (1970) observed a tendency for k to decrease for increasing flow velocities but this could not be detected within the range of flow velocities encountered in the present calibration experiments.

The forced-convection law takes the well-known form:

$$e_b^2 = A_1 + A_2 q_{eff}^m , \qquad (3.9)$$

where A_1, A_2 and m are calibration constants and e_b is the instantaneous anemometer bridge voltage. The constant m is assumed to be universal and was found to be 0.465. This compares with the original value due to King (1915) of 0.5 and the value of 0.45 chosen by Collis and

Williams (1959). Details of the determination of the turbulence normal and shear stresses from the electronic measurements are given in Appendix 4. The influence of wall proximity on the hot-wire measurements, as reported by Oka and Kostic (1971), was found to be negligible, even at the smallest wall distances encountered in the investigation. Oka and Kostic found that a correction becomes necessary for values of yu_o/ν less than 5. However, the smallest value encountered in the investigation was approximately 25.

The frequency spectrum of the longitudinal turbulence normal stress was calculated from the spectograms. Denoting the frequency spectrum function at a frequency n by F(n) then the quantity $\overline{u'^2}\,F(n)dn$ is defined to be the fraction of the total unfiltered value of $\overline{u'^2}$ associated with the frequency interval dn. It follows that:

$$\int_0^\infty F(n)dn = 1. \qquad (3.10)$$

The signal voltage-ratios could be read from the level-recorder charts in units of decibels and these ratios were then used to calculate the spectrum function at different frequencies.

For two points in a turbulent flow, separated by a distance Δx in the x direction, the longitudinal spatial correlation coefficient, R_T, is defined to be:

$$R_T = \frac{\overline{u'(x)u'(x+\Delta x)}}{\overline{u'^2}}\ , \qquad (3.11)$$

where u'(x) represents the instantaneous value of the longitudinal

fluctuating velocity at a particular value of x. This is difficult to measure accurately using hot wires because the wake of the upstream probe is bound to affect the flow near the downstream probe. Taylor (1938) postulated that the sequence of changes in u' at a fixed point is due to the passage of a 'rigid' turbulent eddy past the point. This simplified model becomes less accurate as the fluctuating component of velocity increases in relation to the mean velocity. The advantage of the model lies in the fact that space correlations can be deduced from time correlations. The latter can be measured either directly, using a time-delay unit such as a frequency-modulated tape recorder, or indirectly by calculating the Fourier transform of the measured frequency spectrum function (as first shown by Taylor (1938) and later by Stewart and Townsend (1951)). Taylor's hypothesis of rigid convection of turbulent eddies has been investigated by Favre, Gaviglio and Dumas (1958) for a turbulent boundary layer on a flat plate. Their results show good agreement between direct measurements of space correlations and calculated values, using time correlations, for values of y/δ as low as 0.03. The Fourier transform method was used throughout the present investigation. The required relationship between the spatial correlation coefficient and the frequency spectrum function is:

$$R_T = \int_0^\infty F(n) \cos \frac{2\pi n \Delta x}{u} \, dn \quad . \tag{3.12}$$

The above correlation coefficient was calculated by numerically-integrating a set of curves which were fitted piece-wise to the measured spectrum function. The PDP8 computer was programmed to carry out the

necessary calculations; details can be found in Appendix 5.

An integral length scale of the turbulence field can be defined in terms of the longitudinal spatial correlation coefficient by:

$$L_T = \int_0^\infty R_T \, d(\Delta x) \quad . \tag{3.13}$$

This will be referred to as the 'macro-scale' of the turbulence and is a measure of the size of a typical energy-containing eddy. Taylor (1938) defined a length-scale, λ_T, in terms of the curvature of the R_T curve at its vertex:

$$\frac{1}{\lambda_T^2} = 2 \lim_{\Delta x \to 0} \left(\frac{1-R_T}{(\Delta x)^2} \right) \quad . \tag{3.14}$$

Taylor showed that a series expansion for the cosine term in equation (3.12), as $\Delta x \to 0$, leads to:

$$\frac{1}{\lambda_T^2} = \frac{4\pi^2}{u^2} \int_0^\infty n^2 F(n) dn \quad . \tag{3.15}$$

Hence λ_T can be calculated from the second moment of the frequency spectrum function. The length λ_T will be referred to as the 'micro-scale' of the turbulence; its value lies between the macro-scale and the length scales associated with the dissipation of the turbulence energy. Details of the calculation procedures for the two length scales are given in Appendix 5.

3.7 Presentation and Discussion of Results

Each rough surface was given a code number for identification purposes. These numbers were related to the 'mean apparent amplitude' of the surface as measured using the B.S.R.A. wall gauge (see Section 2.1). Hence the code number R345 refers to the rough surface with an M.A.A. of 345 microns. The five rough surfaces have the following code numbers which will be used throughout the thesis:

R550 - large pipe

R420 - small pipe

R345 - small pipe

R253 - small pipe

R173 - small pipe

The experimental data havebeen compiled in tabulated form by Musker (1977).

The mean velocity distributions for the smooth pipe are shown in Fig. 3.9 in the 'law-of-the-wall' co-ordinates of equation (2.5). In addition to the corrections outlined in the previous section, the raw data were corrected for the effect of turbulence on the pitot tube and the variation of static pressure across the pipe radius. These corrections are described by Goldstein (1938) and are of the order of one percent near the wall. Away from the wall these corrections become negligible. Excellent agreement is obtained with equation (2.5) if the constants $\kappa = 0.41$ and $B = 5.0$ are selected. The extent of the logarithmic overlap region is seen to be about 15% of the pipe radius. The value of the wake-strength parameter Π in equation (2.21) was found to decrease slightly from 0.31 at the low Reynolds number to 0.27 at the high Reynolds number.

The variation of pipe friction coefficient with Reynolds number for the smooth pipe is shown in Fig. 3.10. Good agreement is obtained with the universal friction law for smooth pipes due to Prandtl (1933). This law has been validated by many experimenters up to arbitrarily high Reynolds numbers. There is some discrepancy at the lowest Reynolds number which is probably due to inaccuracy in the measurement of mean velocity. The highest Reynolds number corresponds to a Mach number of about 0.45. It is clear that equation (3.4), which was used to calculate u_o and hence f, adequately takes into account the effects of compressibility.

Figs. 3.11 to 3.15 show the mean velocity distributions for the smooth and rough surfaces plotted in the 'velocity-defect' form of equation (2.4). When plotted in this way the distributions, according to the two-layer concept of velocity distribution, should be independent of surface roughness. A universal curve would be expected if Π were independent of the pipe Reynolds number. However, measurements indicated that Π decreased from approximately 0.3 to 0.1 as the respective Reynolds numbers increased from the lowest to the highest values. Despite this weak dependence on the value of Π a near-universal curve is obtained for all the pipes tested.

The inner-region velocity distributions for the rough pipes are shown in Figs. 3.16 to 3.20. Superimposed on each diagram are the points relating to the inner-region for the smooth surface taken from Fig. 3.9. For low roughness Reynolds numbers the profiles were close to the smooth logarithmic region. However, it proved to be impossible to measure a profile, for any of the surfaces, which merged with the smooth region. This indicates that even for extremely low roughness

Reynolds numbers the roughness excrescences inhibit the formation of a viscous sub-layer. For the sake of clarity some of the plots at the highest Reynolds numbers for the surface R550 are not shown in Fig. 3.16.

The roughness function $\Delta u/u_o$ is the amount by which the logarithmic region is displaced from the smooth line, measured along the u/u_o axis, in accordance with the definition given by equation (2.23). Using the M.A.A. to form a roughness Reynolds number the roughness functions for all the rough surfaces are plotted in Fig. 3.21. All the surfaces exhibit increasing values of $\Delta u/u_o$ with increasing roughness Reynolds number. The surface R253 does appear, however, to have an extensive region at low roughness Reynolds numbers where $\Delta u/u_o$ does not vary significantly. Despite the scatter of the data it seems that the general trends of the curves are similar to those of Colebrook and White (1937) as shown in Fig. 2.2. It is apparent that the M.A.A. is quite incapable of producing a universal curve for the roughness function. This is exemplified by Fig. 3.22 which shows the variation of χ in terms of the same roughness Reynolds number. This non-universality of the roughness functions, when expressed in terms of a roughness Reynolds number formed by the M.A.A., highlights the importance of taking into account the topography of the surfaces in attempts to find a more representative one-dimensional height. This problem will be dealt with in Chapter 6.

In the fully-rough flow regime the value of χ is constant. This regime was attained for the surface R550. The roughness functions for the surfaces R345 and R420 extend well into the intermediate flow regime and appear to fall just short of the fully-rough regime. Sur-

prisingly, the data for the surface R173 extend into the intermediate regime more so than the surface R253; however, the roughness Reynolds numbers for both sets of data are too low to show an approach to a plateau region.

The distributions of the three R.M.S. components of the velocity fluctuations are shown in Fig. 3.23 for the large pipes at a Reynolds number of 9.5×10^4. The velocity fluctuations have been non-dimensionalised with respect to the wall-friction velocity u_o. The results for the smooth pipe are in good agreement with those of Laufer (1954). Due to the damping influence of the wall the radial fluctuations are significantly lower than the peripheral fluctuations - the difference becoming smaller as the wall distance increases. The fact that they become equal at the pipe centre-line is a good indication that the flow is symmetric about the axis. The flow at the centre-line of the smooth pipe is very nearly isotropic, whereas the longitudinal fluctuating velocity for the R550 pipe is too high at the centre-line for isotropy to occur. Most noticeable is the fact that the longitudinal fluctuating velocity near the wall is higher for the rough surface.

The corresponding results for the small pipes are given in Figs. 3.24 to 3.27 for the two Reynolds numbers considered in the investigation. It appears that the Reynolds number has little effect on the distribution of the longitudinal component within the ranges of R_e and $y+\varepsilon/R$ considered. This is probably not the case very near the wall, however, because here the correct non-dimensional wall distance must involve u_o and ν, with hu_o/ν featuring as a parameter. A feature which is present for all the small pipes is that the increase in Reynolds number is associated with a marked decrease in the components

of the radial and peripheral fluctuating velocities. This was not observed by Laufer (1954) in his investigation of a smooth pipe.

Fig. 3.28 shows the distributions of the turbulent shear stresses $-\rho\overline{u'v'}$ and $-\rho\overline{u'w'}$ for the smooth and R550 surfaces. Starting with the time-averaged Navier-Stokes equation, Pai (1953) and Laufer (1954) independently derived the following expressions for the above turbulent shear stress distributions in a smooth pipe:

$$\frac{-\rho\overline{u'v'}}{\tau_o} = 1 - \frac{y}{R} - \frac{\mu}{\tau_o}\frac{\partial u}{\partial y} \qquad (3.16)$$

and

$$\frac{-\rho\overline{u'w'}}{\tau_o} = 0 \quad . \qquad (3.17)$$

The derivations are straight-forward and they assume that the mean velocity components, v and w, and all partial derivatives with respect to ψ, an angular co-ordinate measured about the pipe axis, are zero. Except for a region very close to the wall the term involving the mean-velocity gradient in equation (3.16) is negligible. The smooth-pipe data agree well with both the above equations; however, the rough-pipe data exhibit significant departures from the theoretical distributions.

The corresponding data for the small pipes arepresented in Figs. 3.29 to 3.32. The effect of an increase in Reynolds number is to increase the departure from the smooth distributions. At the low Reynolds number the measured values of $-\rho\overline{u'v'}/\tau_o$ tend to merge with the smooth distribution as the pipe centre-line is approached. Since non-zero values of the correlation $\overline{u'w'}$ imply a transport of longi-

tudinal momentum in the peripheral direction, it is clear that the above-mentioned partial derivatives with respect to ψ cannot be ignored for rough pipes. Also, amongst the roughness excrescences there must exist mean velocities in the transverse directions in addition to the longitudinal component.

Townes, Gow, Powe and Weber (1972) reported anomalous measurements of turbulent shear stresses in rough pipes similar to those mentioned above. In an attempt to model the flow in rough pipes they proposed spatially-averaging all the terms appearing in the governing equations. The spatial average of any variable, say u, is defined to be:

$$\hat{u} = \frac{1}{2\pi} \int_0^{2\pi} u \, d\psi \quad . \tag{3.18}$$

The spatial average of the mean radial velocity must be zero, by continuity, and, similarly, partial derivatives with respect to ψ must also be zero. Using the same analysis as Pai (1953) and Laufer (1954), Townes, Gow et al. derived the following expression for the spatially-averaged turbulent shear stress $-\rho\overline{u'v'}$:

$$-\rho\frac{\hat{\overline{u'v'}}}{\tau_o} = 1 - \frac{y}{R} - \frac{\mu}{\tau_o}\frac{\partial \hat{u}}{\partial y} + \rho\frac{\hat{uv}}{\tau_o} \quad , \tag{3.19}$$

where, strictly,

$$\tau_o = -\frac{R}{2}\frac{\partial \hat{p}}{\partial x} \, . \tag{3.20}$$

According to equation (3.19) an average value of v of less than ten centimetres per second would be sufficient to explain the maximum observed departures in the $\overline{u'v'}$ correlation in relation to the smooth-

pipe distribution described by equation (3.16). Unfortunately it proved impossible to confirm the existence of such a weak secondary flow with the apparatus available. The experimental difficulties here are two-fold. Firstly, there is the problem of measuring the transverse mean velocities. This can be done, using a single inclined wire, by referencing the hot-wire signal to the pipe centre-line where it can be assumed that the mean velocity vector is along the pipe axis. A single inclined-wire probe, which can be rotated 180^{o} above the probe axis, is necessary for this purpose since there is a danger of a significant disturbance to the flow caused by the introduction of an X probe. Secondly, it can be shown that the generalised response equations for an inclined hot-wire in the x-y plane, when the probe axis is not aligned with the direction of the mean flow, involve not only the correlation $\overline{u'v'}$ and the angle between the mean velocity vector and the hot-wire, but also the normal fluctuating components $\overline{u'^2}$ and $\overline{v'^2}$. Since only two equations are available relating the three unknowns $\overline{u'^2}$, $\overline{v'^2}$ and $\overline{u'v'}$ (the equations corresponding to the sum and difference of the squares of the two anemometer signals when the probe orientations are 180^{o} apart) it is necessary to measure $\overline{u'^2}$ independently, using another wire approximately normal to the flow. The experimental errors in such a procedure become unacceptably large in view of the low order of magnitude of the transverse mean velocity v. This itself could not be measured so that its effects on the true value of $\overline{u'v'}$, as determined from the generalised response equations, remains uncertain.

The frequency spectra of the longitudinal fluctuating velocity are shown in Figs. 3.33 to 3.38. The results are displayed in terms of the wave-number, $2\pi n/u$, which is inversely proportional to the eddy wave-length. The wave-length is thus related to the frequency, n, and the local mean velocity, u, by Taylor's hypothesis (see Section 3.6). Various theoretical studies have been performed on the nature of the wave-number spectrum in turbulent flow. A sub-range of turbulence production can be identified, within which energy is extracted from the mean flow. Tchen (1953) predicted that this sub-range should have a -1 power law. Hence $(u/2\pi)\,F(n) \sim (2\pi n/u)^{-1}$. Abell (1974) derived the same power law using a dimensional argument. For the sub-range corresponding to the smallest eddy sizes (high wave-numbers) Heisenberg (1948) proposed that the energy received from lower wave-numbers is dissipated by the action of molecular viscosity. He showed that a -7 power law should exist at high wave-numbers. An intermediate sub-range was proposed by Kolmogoroff (1941) (and later by Heisenberg (1948)) which must, from dimensional arguments, obey a -5/3 power law. In this sub-range energy is transferred from large to small eddies without being influenced significantly by either the production or dissipation mechanisms.

The experimental data show that the -7 law is approached asymptotically in all cases. The last couple of data points, corresponding to the highest wave-numbers, are probably an artefact of the instrumentation since they approach the upper frequency limit of the hot-wire. All three sub-ranges are clearly defined at $y+\varepsilon/R = 0.08$, particularly at the higher Reynolds number. At the pipe centre-line the production sub-range is non-existent at both Reynolds numbers. This is not surprising

in view of the fact that the energy production term in the turbulent energy equation (see Rotta (1962)) is $\overline{u'v'}\ \partial u/\partial y$, which is zero at the pipe centre-line. The results for the low Reynolds number at $y+\varepsilon/R = 0.02$ show a gradual change from the -1 to the -7 laws with a rather ill-defined intermediate sub-range. At the higher Reynolds number (Fig. 3.34), however, it is evident that the -5/3 power law does apply over a range of wave-numbers which, by close inspection, depends on whether the pipe is large (corresponding to the smooth and R550 surfaces) or small. Unfortunately, there is considerable scatter in the data for the low wave-number range due to the high turbulence levels associated with the near-wall region. Also, since the equipment did not respond to frequencies less than 20 Hz it is possible that the largest eddies were not detected by the equipment. The production sub-range for the smooth pipe, for example, is defined by only five points, starting at a wave-number of unity (per cm).

The second moments of the frequency spectra are shown in Figs. 3.39 to 3.45. These have been plotted in the form of a product of the wave-number and the first moment of the spectrum function against the wave-number. It is believed that this emphasises the near-universality of the second moments at a given non-dimensional wall distance, as can be inferred from Figs. 3.40 to 3.45. It will be recalled that the micro-scale of the turbulence is related to the area beneath the second-moment curve (see equation (3.15)). Fig. 3.39 shows a poor collapse of data for the smooth and R550 pipes at $(y+\varepsilon)/R = 0.02$. This indicates that the micro-scale is affected by surface roughness very near the wall, particularly at high Reynolds numbers. This latter qualification seems justified in view of the more perfect

collapse of data evident in Fig. 3.40 (at a low Reynolds number) when compared with Fig. 3.41 (which applies to a high Reynolds number).

The macro-scales of the turbulence are calculated from the spatial correlation coefficients (see equation 3.13)) which are shown in Figs. 3.46 to 3.48. Referring to the smooth and R550 results, it can be seen that the effect of the surface roughness in the wall region ($y+\varepsilon/R$ = 0.02 and 0.08) is to increase the macro-scale. However, at the pipe centre-line surface roughness has little effect, although the shapes of the correlation curves appear to be slightly different. The results for the small pipes in the wall region indicate increasing values of the macro-scale with increasing pipe Reynolds number. The Reynolds number dependence appears to diminish at the pipe centre-line. A detailed inspection of the data has shown that the macro-scale does not relate to the M.A.A. (given by the surface code-numbers) in any obvious way. This is not surprising in view of the results concerning the measured roughness functions (see Figs. 3.21 and 3.22).

The ratios of the macro-scale to the micro-scale are shown in Fig. 3.49. At the centre-line the ratio is equal to approximately 4 at both Reynolds numbers and for all the surfaces investigated. The data for the small pipes indicate that the ratio reaches a maximum value at some distance from the wall and subsequently decreases to its centre-line value. This trend is not followed, however, for the R253 pipe or, at the high Reynolds number, for the R173 pipe. For the large pipes the R550 surface shows the same behaviour, whilst the smooth-surface results are quite different. Similar results have

been reported by Robertson, Burkhart and Martin (1965). The experimental accuracy associated with the ratio, however, is no better than about 20% based on tests of repeatability. Consequently,more experimental data is required before unequivocal conclusions can be reached.

CHAPTER 4

THE PREDICTION OF TWO-DIMENSIONAL TURBULENT BOUNDARY-LAYERS ALONG AN IRREGULARLY-ROUGH SURFACE

4.1 Introduction

Two-dimensional turbulent boundary-layers, developing over a smooth or rough surface, can be conveniently divided into two classes: those in a region of constant pressure and those subject to a pressure gradient. For Reynolds numbers (based on distance from the point of transition to turbulent flow,and the free-stream velocity) which are not too low, the constant-pressure case can be dealt with by assuming that the wake-strength parameter, Π, is a constant. If the surface is rough then the measured roughness function must be incorporated into the wall friction equation.

It will be recalled from Section 2.3 that for flows with a pressure gradient at least three equations are required for prediction purposes (if a two-layer concept of velocity distribution is used). Furthermore, the auxiliary equation must be able to take into account the effects of roughness. In this respect the eddy-viscosity concept due to Clauser (1956) is appropriate if the energy or moment of momentum equations are to be used, since Clauser's model applies to both smooth and rough surfaces. An entrainment equation offers an alternative approach. Such an equation is applicable regardless of the nature of the surface because entrainment is essentially an outer-region phenomenon.

Clauser's eddy-viscosity model is strictly applicable only to equilibrium boundary-layers. Flows with moderately high negative (favourable) pressure-gradients approximate quite well to equilibrium flows. Flows with positive (unfavourable) pressure gradients, however, are usually associated with a departure from equilibrium conditions. Equilibrium pressure distributions are, of course, an exception to the above comments. A method is required, therefore, of extending Clauser's model to non-equilibrium flows.

4.2 A Semi-Empirical Formula for the Roughness Function χ

Although the measured roughness function could be curve-fitted to provide the numerical information required in a calculation procedure, it is desirable that the formula should be semi-empirical in nature. A continuous expression for χ can be determined by considering the law of the wall in its simplest form

$$\frac{u}{u_o} = \frac{1}{\kappa} \log_e y + \beta, \qquad (4.1)$$

where β is a constant. This may be rewritten as:-

$$\frac{u}{u_o} = \frac{1}{\kappa} (\log_e y - \log_e y_o) \qquad (4.2)$$

where, for a smooth wall, y_o is of the order of the sub-layer thickness which, by dimensional arguments, is of the order ν/u_o. Hence, for a smooth wall:-

$$y_o = \frac{B'\nu}{u_o} \quad , \qquad (4.3)$$

where B' is a constant. For fully-rough flow (when χ is constant), y_o must be of the order of the roughness height:-

$$y_o = C'h \quad , \tag{4.4}$$

where C' is a constant.

A simple interpolation formula for y_o can be found by adding the two quantities appearing in equations (4.3) and (4.4):-

$$y_o = \frac{B'\nu}{u_o} + C'h \quad ;$$

which may be rewritten as:-

$$y_o = h\left[\frac{B'}{h_*} + C'\right] \quad , \tag{4.5}$$

where h_* is the roughness Reynolds number hu_o/ν. Substituting equation (4.5) into (4.2) and comparing with equation (2.24) results in the following expression:-

$$\chi = \frac{1}{\kappa} \log_e \left[\frac{h_*}{B'\left(1 + \frac{C'}{B'} h_*\right)}\right] \quad . \tag{4.6}$$

The addition of a damping term to 'accelerate' the effect of the roughness at low roughness Reynolds numbers is found to give better agreement with experimental data:-

$$\chi = \frac{1}{\kappa} \log_e \left[\frac{h_*}{B'\left(e^{-0.005h*} + \frac{C'}{B'} h_*\right)}\right] \quad . \tag{4.7}$$

The value of C' for a particular surface depends on the choice of the roughness height used to describe the surface. If the Mean Apparent Amplitude (see Section 2.1) of 550 microns is used to describe the surface R550 then C' is found to be 0.00747. B' has a universal value of 0.129. The comparison between the measured data and equation (4.7) is shown in Fig. 4.1. It can be seen that the equation adequately describes the limiting cases of $h_* \to 0$ and $h_* \to \infty$, but more importantly it also describes the intermediate region between smooth and fully-rough flows.

4.3 The Development of Flows in a Zero Pressure Gradient

The boundary-layer momentum equation for the case of a constant pressure flow is given by (see equation 2.32):

$$\frac{d\theta}{dx} = \frac{C'_f}{2} \quad , \tag{4.8}$$

where the term involving the normal stresses has been neglected. The momentum thickness, θ, is found by integration of the velocity profile. Using the new wake function embodied in equation (2.21), it can be shown that

$$\theta = \omega\delta(G_1 - \omega G_2) \quad , \tag{4.9}$$

where $\omega = u_0/U_\infty$, δ = the boundary-layer thickness, and G_1 and G_2 are given by:-

$$G_1 = \frac{1}{\kappa}(\Pi + 0.9167) \tag{4.10}$$

and

$$G_2 = \frac{1}{\kappa^2} (1.4857\Pi^2 + 3.0428\Pi + 1.9123) \quad . \qquad (4.11)$$

It should be noted that the evaluation of equations (4.10) and (4.11) is independent of the roughness function. For values of the Reynolds number R_x greater than about 10^5 the value of Π is approximately constant and equal to about 0.55.

Equation (4.8) can be written in the following form:-

$$\omega^2 = \frac{d\left(\frac{1}{\omega}\right)}{d\left(\frac{x}{h}\right)} \cdot \frac{d}{d\left(\frac{1}{\omega}\right)} \left[\frac{\theta}{\delta} \cdot \frac{\delta}{h}\right] \quad . \qquad (4.12)$$

The quantity δ/h can be expressed, using the wall-friction relationship, equation (2.40), and equation (2.25), as:-

$$\frac{\delta}{h} = \exp\left[\kappa\left(\frac{1}{\omega} - \chi - \frac{2\Pi}{\kappa}\right)\right] \quad . \qquad (4.13)$$

The quantity θ/δ is given by equation (4.9). Inspection of equations (4.12) and (4.13) shows that an expression is required for $d\chi/d(1/\omega)$. Since $h_* = \omega\, hU_\infty/\nu$, it is easily shown that for a constant value of hU_∞/ν:-

$$\frac{d\chi}{d\left(\frac{1}{\omega}\right)} = -\omega^2 \frac{hU_\infty}{\nu} \frac{d\chi}{dh_*} \quad . \qquad (4.14)$$

The value of $d\chi/dh_*$ is found by differentiating equation (4.7).

For convenience, the term x/h in equation (4.12) is written as $xU_\infty/\nu \big/ hU_\infty/\nu = R_x/h_+$. Equation (4.12) becomes, after combining with

equations (4.7), (4.9), (4.13) and (4.14):-

$$\frac{dR_x}{d\left(\frac{1}{\omega}\right)} = h_+ \exp\left[\frac{\kappa}{\omega} - 2\Pi - \log_e\left(\frac{\omega h_+/B'}{\exp(-0.005h_+\omega) + \frac{C'}{B'}h_+\omega}\right)\right]\left\{2\omega G_2\right.$$

$$\left. - G_1 + \left(\frac{\kappa G_1}{\omega} - \kappa G_2\right)\left[1 + \frac{1}{\kappa}\left(\frac{[1 + 0.005\omega h_+]\exp(-0.005\omega h_+)}{\frac{C'h_+}{B'} + \frac{1}{\omega}\exp(-0.005\omega h_+)}\right)\right]\right\} . \quad (4.15)$$

For a constant value of h_+, the above equation can be integrated numerically using Simpson's method. For flow over a flat plate it is convenient to assume fully-rough flow near the leading edge in order to start the integration process. The initial value of ω can then be found from the Prandtl-Schlichting (1934) formula for fully-rough flow over a flat plate:

$$2\omega^2 = \left(2.87 + 1.58 \log_{10}\frac{x}{h_s}\right)^{-2.5} , \quad (4.16)$$

where h_s is the equivalent sand-roughness height (this was equal to approximately 80 microns for the surface R550). It was found that the integration process was not sensitive to the initial conditions chosen so the starting method could be used with confidence.

A PDP8 computer was programmed in BASIC to perform the calculations. For a fixed value of h_+ the calculation of friction curves is straightforward. Friction curves for constant values of x/h were found by an iterative procedure. The results of these calculations will be presented

in Section 4.8.

4.4 Evaluation of the Shear-Stress and Shear-Work Integrals

If the moment of momentum or the energy equations are to be used for the prediction of flows with a pressure gradient, then the shear-stress distribution must be modelled. Using Clauser's concept of eddy viscosity (see Section (2.3)), ν_t, the shear stress, τ, can be written as:-

$$\tau = \rho(\nu + \nu_t) \frac{\partial u}{\partial y} \quad , \tag{4.17}$$

where $\nu_t = \kappa y u_o$ in the inner region and $\nu_t = \alpha U_\infty \delta_*$ in the outer region. Incorporating the roughness function, $\Delta u/u_o$, into equation (2.21), the mean velocity distribution becomes:-

$$\frac{u}{u_o} = \frac{1}{\kappa} \log_e \frac{y u_o}{\nu} + B - \frac{\Delta u}{u_o} + \frac{\Pi}{\kappa} \left[6 \left(\frac{y}{\delta}\right)^2 - 4 \left(\frac{y}{\delta}\right)^3 \right] + \frac{1}{\kappa} \left(\frac{y}{\delta}\right)^2 \left(1 - \frac{y}{\delta}\right) . \tag{4.18}$$

The shear-stress integral can now be calculated from the above two equations. The result is:-

$$\frac{1}{\rho U_\infty^2} \int_o^\infty \tau \, dy = \delta \omega^2 \eta_o \left[1 + 2\Pi - \log_e \eta_o + \eta_o^2 \left(\frac{5-6\Pi}{3}\right) - \eta_o^3 \left(\frac{7+28\Pi}{4}\right) \right], \tag{4.19}$$

where $\eta_o = (\alpha G_1/\kappa)$. It will be recalled (Section 2.3) that for equilibrium layers $\alpha = 0.018$.

The shear-work integral can be evaluated by splitting the integral into three parts:-

$$\frac{1}{\rho U_\infty^3}\int_0^\infty \tau\frac{\partial u}{\partial y}\,dy = \frac{1}{\rho U_\infty^3}\left\{\int_0^{y''} \tau\frac{\partial u}{\partial y}\,dy + \int_{y''}^{y_o} \tau\frac{\partial u}{\partial y}\,dy + \int_{y_o}^{\infty} \tau\frac{\partial u}{\partial y}\,dy\right\} . \qquad (4.20)$$

The limits of the first integral correspond to an inner sub-range (see Lewkowicz, Horlock et al. (1970)) within which the shear stress is assumed to be constant and equal to the wall shear stress. The other parts correspond to the inner and outer regions where y_o denotes the joining point. Using equations (4.17) and (4.18) the result of the integration is:-

$$\frac{1}{\rho U_\infty^3}\int_0^\infty \tau\frac{\partial u}{\partial y}\,dy = \omega^2 + \frac{\omega^3}{\kappa}\left\{1 + \log_e \eta_o - \eta_o + \Pi^2\left[4.8\eta_o - 12\eta_o^4\right.\right.$$

$$\left. + 14.4\eta_o^5 - 4.8\eta_o^6\right] + \Pi\left[-2 + 12.4\eta_o - 12\eta_o^2 + 4\eta_o^3 - 4\eta_o^4 + 6\eta_o^5 - 2.4\eta_o^6\right]$$

$$\left. + \left[0.133\eta_o - 2\eta_o^2 + \eta_o^3 - 0.333\eta_o^4 + 0.6\eta_o^5 - 0.3\eta_o^6\right]\right\} , \qquad (4.21)$$

where, as before, $\eta_o = y_o/\delta = (\alpha G_1/\kappa)$. The terms involving powers greater than three can probably be neglected in most cases. Equations

(4.19) and (4.21), derived using the new wake function, can be compared with equations (2.53) and (2.54) which were derived by Lewkowicz, Horlock et al. (1970) using Hinze's approximation for the outer region. It should be noted that both of the integrals are independent of the roughness function.

Clauser's concept assumes that the eddy viscosity can be represented by two straight lines (equations (2.51) and (2.52)) describing the inner and outer regions. Although this gives satisfactory results, an improvement can be obtained by representing the distribution by the following quartic equation:-

$$\frac{\nu_t}{\delta\omega U_\infty} = a_1 + b_1\eta + c_1\eta^2 + d_1\eta^3 + e_1\eta^4 \quad , \qquad (4.22)$$

where $\eta = y/\delta$. The coefficients, a_1 to e_1, can be found by considering the known boundary-conditions which are:-

(1) $\eta = 0, \quad \nu_t = 0.$

(2) $\eta = 0, \quad \frac{d\nu_t}{d\eta} = \kappa\delta\omega U_\infty.$ (For the purpose of calculating the shear-stress and shear-work integrals, the cubic relationship for ν_t near the wall (see equation (2.12)) can safely be neglected. This boundary condition is certainly true at a small distance away from the wall).

(3) $\eta = \eta_*, \ \nu_t = \alpha U_\infty \delta_*.$ The value of η_* defines the point at which ν_t reaches its maximum

value in the outer region.

(4) $\eta = 1$, $\nu_t = 0$. This must be the case at the edge of the boundary layer.

(5) $\eta = 1$, $\frac{d\nu_t}{d\eta} = 0$, since for $\eta > 1, \nu_t = 0$.

The last two boundary conditions account for the intermittent nature of the turbulence in the outer region with which Clauser's model is inconsistent.

Applying the above boundary conditions to equation (4.22) results in the following matrix equation:-

$$\begin{pmatrix} \eta_*^2 & \eta_*^3 & \eta_*^4 \\ 2\eta_* & 3\eta_*^2 & 4\eta_*^3 \\ 1 & 1 & 1 \end{pmatrix} \begin{pmatrix} c_1 \\ d_1 \\ e_1 \end{pmatrix} = \begin{pmatrix} \alpha G_1 - \kappa\eta_* \\ -\kappa \\ -\kappa \end{pmatrix}, \qquad (4.23)$$

subject to:-

$$\kappa + 2c_1 + 3d_1 + 4e_1 = 0 \quad . \qquad (4.24)$$

The term αG_1 is evaluated using equation (4.10). The above two equations are easily solved for the coefficients c_1, d_1 and e_1 by finding η_*, using an iterative technique, such that both equations are satisfied. The coefficients a_1 and b_1 are found to be zero and κ respectively. Hence equation (4.22) becomes:-

$$\frac{\nu_t}{\delta\omega U_\infty} = \kappa\eta + c_1\eta^2 + d_1\eta^3 + e_1\eta^4 \quad . \tag{4.25}$$

This equation was compared with the eddy-viscosity distributions measured by Bradshaw and Ferriss (1965) in an equilibrium boundary-layer. An example is shown in Fig. 4.2 where the value of $\alpha = 0.02$ was used in accordance with the authors' findings. It can be seen that equation (4.25) leads to better agreement with the experimental data than the original eddy-viscosity model.

Very simple expressions can be found for the shear-stress and shear-work integrals by combining this eddy-viscosity distribution with the new wake function. From equations (4.17), (4.18) and (4.25) it can be shown, after some algebra, that:-

$$\frac{1}{\rho U_\infty^2}\int_0^\infty \tau\, dy = \delta\omega^2 G_{10} \tag{4.26}$$

and

$$\frac{1}{\rho U_\infty^3}\int_0^\infty \tau\frac{\partial u}{\partial y}\, dy = \omega^2 + \omega^3 G_{11} \ , \tag{4.27}$$

where G_{10} and G_{11} are functions of Π given by:-

$$G_{10} = \frac{1}{\kappa}\left\{\Pi\,(\kappa + 0.6c_1 + 0.4d_1 + 0.2857e_1)\right.$$

$$\left. + (0.9167\kappa + 0.4c_1 + 0.2333d_1 + 0.1548e_1)\right\} \tag{4.28}$$

and

$$G_{11} = \frac{1}{\kappa^2}\left\{\Pi^2\ (2.4\kappa + 1.3714c_1 + 0.8572d_1 + 0.5714e_1)\right.$$

$$+ \Pi(2\kappa + 1.8857c_1 + 1.0571d_1 + 0.6571e_1)$$

$$\left. + (0.1\kappa + 0.9191c_1 + 0.3774d_1 + 0.2048e_1)\right\} \quad . \qquad (4.29)$$

It is interesting to note that equation (4.27) has the same form as Rotta's expression for the shear-work integral (see equation (2.50)) although both formulae originate in quite different ways.

Equations (4.26) and (4.27) can be used for non-equilibrium flows where α is no longer constant but varies along the x direction. The functions G_{10} and G_{11} are related to α by equations (4.23) and (4.24). This is discussed further in the next section.

4.5 The Proposed Family of Prediction Methods

The prediction methods to be described in this section are variants of the methods proposed by Lewkowicz-Horlock et al. (1970). The new methods differ from the old methods in three ways. Firstly, the original methods were based on a mean velocity profile whose outer region was described by Hinze's (1959) approximation to Coles' (1956) wake function (see equations (2.16) and (2.17)); the proposed methods incorporate the new wake function into the mean velocity distribution. Secondly, the energy and moment of momentum methods originally applied only to equilibrium flows. It is proposed to extend these methods to cases of non-equilibrium flows for which α is

no longer constant. Thirdly, whereas the original methods applied to smooth walls, the proposed methods take into account the effects of surface roughness.

Although the governing equations have been discussed in Section 2.3 they will be re-stated for convenience in this section. The momentum, wall-friction, energy and moment of momentum equations are:-

$$\frac{d\theta}{dx} + (H+2)\frac{\theta}{U_\infty}\frac{dU_\infty}{dx} = \omega^2 + \frac{d}{dx}\int_0^\infty \frac{\overline{u'^2} - \overline{v'^2}}{U_\infty^2}\, dy \quad , \tag{4.30}$$

$$\frac{1}{\omega} = \frac{1}{\kappa}\log_e\left(\frac{\delta\omega U_\infty}{\nu}\right) + B - \frac{\Delta u}{u_0} + \frac{2\Pi}{\kappa} \quad , \tag{4.31}$$

$$\tfrac{1}{2}\frac{d}{dx}\left(U_\infty^3\,\delta_{**}\right) = \frac{1}{\rho}\int_0^\infty \tau\frac{\partial u}{\partial y}\, dy \tag{4.32}$$

and

$$\frac{1}{U_\infty^2}\frac{d}{dx}\left[U_\infty^2\int_0^\infty y\left(1-\frac{u}{U_\infty}\right)\frac{u}{U_\infty}\, dy\right] + \frac{1}{U_\infty}\int_0^\infty\left(1-\frac{u}{U_\infty}\right)\frac{d}{dx}\left[U_\infty\left(y + \int_0^y\frac{u}{U_\infty}\, dy\right)\right]dy$$

$$= \frac{1}{\rho U_\infty^2}\int_0^\infty \tau\, dy \tag{4.33}$$

respectively, where:-

$$H = \frac{\delta_*}{\theta} \quad , \tag{4.34}$$

$$\delta_* = \int_0^\infty \left(1 - \frac{u}{U_\infty}\right) dy \quad , \tag{4.35}$$

$$\theta = \int_0^\infty \frac{u}{U_\infty} \left(1 - \frac{u}{U_\infty}\right) dy \tag{4.36}$$

and

$$\delta_{**} = \int_0^\infty \frac{u}{U_\infty} \left[1 - \left(\frac{u}{U_\infty}\right)^2\right] dy \quad . \tag{4.37}$$

The normal-stress term in equation (4.30) can be accounted for in the following way. After analysing a total of 34 distributions of $\overline{u'^2}$ and $\overline{v'^2}$, corresponding to the present pipe-flow experiments and the data of El-Samanoudy (1974) for boundary-layer flows in different pressure gradients, it was found that the quantity

$$\int_0^1 \frac{\overline{u'^2} - \overline{v'^2}}{u_o^2} \, d\left(\frac{y}{\delta}\right)$$

was equal to approximately unity with a standard deviation of 0.21. The normal stress term in the momentum integral equation is very often neglected in prediction procedures since its magnitude becomes appreciable only near separation, as noted by Newman (1950). However, using the above quantity, the normal-stress term can be expressed as follows:-

$$\frac{d}{dx}\int_0^{\infty} \frac{\overline{u'^2} - \overline{v'^2}}{U_\infty^2}\, dy = \frac{d}{dx}\int_0^{1} \frac{\overline{u'^2} - \overline{v'^2}}{u_o'^2}\, d\left(\frac{y}{\delta}\right) \frac{\delta u_o^2}{U_\infty^2} = \frac{d}{dx}\,(\delta\omega^2)\ . \qquad (4.38)$$

By treating δ, Π and ω as dependent variables which describe the mean-velocity distribution at a particular streamwise co-ordinate, x, equations (4.30) to (4.33) can be transformed into differential equations of the first order using the definitions embodied in equations (4.34) to (4.37) and the mean velocity distribution described by equation (4.18). The algebra,which is extremely laborious, leads to the following relationships for the momentum, wall-friction, energy and moment of momentum equations respectively:

$$\frac{\omega d\delta}{dx}\left[G_1 - \omega(1+G_2)\right] + \frac{\omega\delta d\Pi}{dx}\left[\frac{1}{\kappa} - \omega G_3\right] + \frac{\delta d\omega}{dx}\left[G_1 - 2\omega(1+G_2)\right]$$

$$= \omega^2 - \frac{\omega\delta}{U_\infty}\frac{dU_\infty}{dx}\left[3G_1 - 2\omega(1+G_2)\right] \quad , \qquad (4.39)$$

$$\frac{1}{\kappa\delta}\frac{d\delta}{dx} + \frac{2}{\kappa}\frac{d\Pi}{dx} + \frac{d\omega}{dx}\left[\frac{1}{\omega^2} + \frac{1}{\omega\kappa} + \frac{0.005\,\frac{hU_\infty}{\nu}\exp\left(-0.005\,\frac{\omega hU_\infty}{\nu}\right) - \frac{C'}{B'}\,\frac{hU_\infty}{\nu}}{\frac{\kappa C'}{B'}\,\frac{\omega hU_\infty}{\nu} + \kappa\exp\left(-0.005\,\frac{\omega hU_\infty}{\nu}\right)}\right]$$

$$= -\frac{1}{\kappa U_\infty}\frac{dU_\infty}{dx}\left[1 + \frac{0.005\,\frac{\omega hU_\infty}{\nu}\exp\left(-0.005\,\frac{\omega hU_\infty}{\nu}\right) - \frac{C'}{B'}\,\frac{\omega hU_\infty}{\nu}}{\frac{C'}{B'}\,\frac{\omega hU_\infty}{\nu} + \exp\left(-0.005\,\frac{\omega hU_\infty}{\nu}\right)}\right], \qquad (4.40)$$

$$\frac{\omega d\delta}{dx}\left[G_1 - 1.5\omega G_2 + \omega^2 G_4\right] + \frac{\omega\delta d\Pi}{dx}\left[\frac{1}{\kappa} - 1.5\omega G_3 + \omega^2 G_5\right] + \frac{\delta d\omega}{dx}\left[G_1 - 3\omega G_2 + 3\omega^2 G_4\right]$$

$$= \omega^2 + \omega^3 G_{11} - \frac{\delta\omega}{U_\infty}\frac{dU_\infty}{dx}\left[3G_1 - 4.5\omega G_2 + 3\omega^2 G_4\right] \qquad (4.41)$$

and

$$\frac{\omega d\delta}{dx}\left[2G_6 - \omega G_7\right] + \frac{\omega\delta d\Pi}{dx}\left[\frac{0.3}{\kappa} - \omega G_8\right] + \frac{\delta d\omega}{dx}\left[G_6 - \omega G_9\right]$$

$$= \omega^2 G_{10} - \frac{\delta\omega}{U_\infty}\frac{dU_\infty}{dx}\left[4G_6 - \omega G_9\right] \quad , \qquad (4.42)$$

where B' and C' are given by equation (4.7), and G_1, G_2, G_{10} and G_{11} are given by equations (4.10), (4.11), (4.28) and (4.29) respectively. The remaining 'G functions' are:-

$$G_3 = \frac{1}{\kappa^2}(2.9714\Pi + 3.0428) \quad , \qquad (4.43)$$

$$G_4 = \frac{1}{\kappa^3}(1.2286\Pi^3 + 4.0474\Pi^2 + 5.4084\Pi + 2.9388) \quad , \qquad (4.44)$$

$$G_5 = \frac{1}{\kappa^3}(3.6857\Pi^2 + 8.0984\Pi + 5.4084) \quad , \qquad (4.45)$$

$$G_6 = \frac{1}{\kappa}(0.3\Pi + 0.2) \quad , \tag{4.46}$$

$$G_7 = \frac{1}{\kappa^2}(0.5\Pi^2 + 1.9895\Pi + 0.0211) \quad , \tag{4.47}$$

$$G_8 = \frac{1}{\kappa^2}(0.8429\Pi + 1.2876) \quad , \tag{4.48}$$

and

$$G_9 = \frac{1}{\kappa^2}(0.8429\Pi^2 + 2.8024\Pi + 0.4320) \quad . \tag{4.49}$$

It will be recalled that the functions G_{10} and G_{11} are related to α by equations (4.23) and (4.24). For equilibrium flows α is a constant, in which case a boundary-layer prediction involves the simultaneous solution of equations (4.39), (4.40) and either (4.41) or (4.42). For non-equilibrium flows, however, α may be regarded as a dependent variable in addition to δ, Π and ω. Hence, if the energy or moment of momentum auxiliary equations are to be used, a fourth equation is required which must relate α to the other dependent variables.

The following rate equation for the eddy kinematic viscosity is proposed:-

$$\frac{d\nu'_t}{dx} = C_r U_\infty (\alpha - \alpha_{eq}) \quad , \tag{4.50}$$

where ν'_t represents the local maximum value of ν_t in the outer region which is equal to $\alpha\delta_* U_\infty$, C_r is an empirical constant, and α_{eq} is the equilibrium value of α which is assumed to be 0.018. The stream-wise rate of change of eddy viscosity is related by this equation to the

degree of departure from equilibrium conditions. For the prediction of equilibrium flows $\alpha = \alpha_{eq}$ can be used as one of the initial conditions. Once the integration process is started it is found that α quickly settles on a value which is slightly different from 0.018 - being consistent with a non-zero value of dv'_t/dx.

The effect of equation (4.50) is to reduce the value of α for flows with adverse pressure gradients,which is in accord with experimental observations*. To some extent this overcomes an inherent difficulty with the older integral methods in that they fail to predict regions where the wall friction coefficient is approaching zero.

Equation (4.50) can be transformed, as before, into a differential equation of the first order. The result is:-

$$\omega G_1 \frac{d\delta}{dx} + \frac{\omega\delta}{\kappa}\frac{d\Pi}{dx} + \delta G_1 \frac{d\omega}{dx} + \frac{\omega\delta G_1}{\alpha}\frac{d\alpha}{dx} = C_r\left[1 - \frac{\alpha_{eq}}{\alpha}\right] - \frac{\omega\delta G_1}{U_\infty}\frac{dU_\infty}{dx}. \quad (4.51)$$

A value of $C_r = -0.06$ was used throughout the investigation since this was found to give good agreement with measured boundary-layers.

Instead of the energy or moment of momentum equations an entrainment relationship can be used for the auxiliary equation. Head (1960) postulated that the rate per unit length at which fluid is entrained by the boundary layer, given by the quantity

$$\frac{d}{dx}\left[U_\infty(\delta - \delta_*)\right],$$

is a function of the free-stream velocity, a measure of the boundary-layer thickness, and the shape of the velocity profile. Head chose the

*this, of course, applies only to non-equilibrium flows.

quantity $(\delta-\delta_*)$ as a representative thickness and $(\delta-\delta_*)/\theta$ as a shape parameter. Hence:-

$$\frac{d}{dx}\left[U_\infty(\delta-\delta_*)\right] = f_1\left[U_\infty,\ \delta-\delta_*,\ \frac{\delta-\delta_*}{\theta}\right] . \qquad (4.52)$$

For the two-layer concept of mean-velocity distribution used in this investigation the profile shape can be specified by ω and Π. However, it is easily shown, by integrating the velocity distribution in accordance with equation (4.35), that ω and Π are related by:

$$\omega G_1 = \omega\left(\frac{\Pi + 0.9167}{\kappa}\right) = \frac{\delta_*}{\delta} . \qquad (4.53)$$

Hence equation (4.52) can be expressed as:-

$$\frac{d}{dx}\left[U_\infty(\delta-\delta_*)\right] = f_2\,(U_\infty,\ \delta-\delta_*,\ \omega,\ \delta_*) . \qquad (4.54)$$

In non-dimensional terms this becomes:-

$$\frac{1}{U_\infty}\frac{d}{dx}\left[U_\infty(\delta-\delta_*)\right] = f_3\left[\omega,\ \frac{\delta_*}{\delta}\right]. \qquad (4.55)$$

After analysing a total of eleven boundary-layer flows published in the Proceedings of the Stanford University Conference (see Coles (1968)) the following empirical formula is proposed for the dimensionless entrainment equation:-

$$\frac{1}{U_\infty}\frac{d}{dx}\left[U_\infty(\delta-\delta_*)\right] = 97\omega\left(\frac{\delta_*}{\delta}\right)^3 \quad . \qquad (4.56)$$

In terms of Π this becomes:-

$$\log_{10}\left\{\frac{1}{\omega^4 U_\infty}\frac{d}{dx}\left[U_\infty(\delta-\delta_*)\right]\right\} = 3\log_{10}(\Pi+0.9167) + 3.15 \; . \qquad (4.57)$$

This equation is compared with experimental data in Fig. 4.3 where the code numbers refer to those used at the Stanford Conference. The data cover a wide range of pressure gradients and, although logarithmic axes are used, the data collapse satisfactorily when plotted in this way. Equation (4.57) can be transformed, as before, into the following differential equation:-

$$\frac{d\delta}{dx}\left[\frac{1}{\omega} - G_1\right] - \frac{\delta}{\kappa}\frac{d\Pi}{dx} - \frac{G_1\delta}{\omega}\frac{d\omega}{dx} = 1410(\kappa G_1\omega)^3 + \frac{\delta}{U_\infty}\frac{dU_\infty}{dx}\left[G_1 - \frac{1}{\omega}\right] \; . \qquad (4.58)$$

Summarising the calculation procedures, the energy method involves the simultaneous solution of equations (4.39), (4.40), (4.41) and (4.51); the moment of momentum method involves the simultaneous solution of equations (4.39), (4.40), (4.42) and (4.51); and the entrainment method involves the simultaneous solution of equations (4.39), (4.40) and (4.58). A FORTRAN program was written for processing by the 1906S machine at the Liverpool University Computer Laboratory. Details of the program can be found in Appendix 6.

4.6 Starting Conditions for the Test-Cases

Seven test-cases were studied, four of which were for smooth surfaces. A brief descriptive note of each flow follows:-

a) Schubauer and Klebanoff (Stanford code 2100).
Boundary-layer on large aerofoil-like body; pressure gradient firstly mildly negative, then strongly positive.

b) Bell (Stanford code 3000). Boundary layer on heated plate at constant pressure.

c) Moses (Stanford code 4100). Boundary layer on cylinder in axially-symmetric flow, with initial moderate pressure rise followed by relaxation at constant pressure.

d) Bauer (Stanford code 6300). Near-equilibrium boundary layer growing beneath potential flow on model spillway.

e) Betterman (1965). Uniformly-spaced square bars on a flat plate in a zero pressure-gradient.

f) Perry and Joubert (1963). Uniformly-spaced square bars on a flat plate in a positive pressure-gradient.

g) Arndt and Ippen (1967). Saw-tooth roughness on a flat plate in a negative pressure-gradient.

The Stanford code numbers refer to the Stanford University Conference on turbulent boundary layers (see Coles (1968)). It should be pointed out that none of the above flows was used to formulate the entrainment equation described in the previous section.

The above flows were chosen for two reasons. Firstly, they represented a broad spectrum of test-cases. Secondly, with the exception of Perry and Joubert's flow, the experimental data show reasonable agreement with the momentum integral equation (equation 4.30)) thus indicating that the flows were essentially two-dimensional. Three-dimensional effects are nearly always present to some extent, however, for flows with positive pressure gradients.

In order to start the process of numerical integration it is necessary to know the initial values of the dependent variables δ, Π and ω. The fourth dependent variable, α, will be dealt with at the end of this section. The results of experiments are usually given in terms of ω, H and θ. However, for the proposed prediction procedure it is important that these values are consistent with the constants in the logarithmic overlap region. This can be accomplished by selecting two of the initial dependent variables and calculating the third variable in terms of the relevant constants. The two initial variables selected for the present investigation were ω and θ. Certainly θ is known to a greater accuracy than H, since H involves the ratio of two integral quantities (equation (4.34)), but it is debatable as to which of the quantities, ω or H, has the lesser experimental error.

Using equations (4.9) and (4.53), equation (4.34) becomes:-

$$H = \frac{G_1}{G_1 - \omega G_2} \quad , \tag{4.59}$$

where G_1 and G_2 are given by equations (4.10) and (4.11). Remembering that $C_f = 2\omega^2$, equations (2.40) and (4.9) can be combined to give:-

$$\frac{1}{\omega} - \frac{1}{\kappa}\left[\log_e \frac{R_\theta}{G_1 - \omega G_2} + 2\Pi\right] = B - \frac{\Delta u}{u_o} \quad , \tag{4.60}$$

where $R_\theta = \theta U_\infty/\nu$. Hence, knowing ω and R_θ, the value of Π can be found. A Newton-Raphson iterative procedure was used for this purpose. For a smooth surface the roughness function, $\Delta u/u_o$, is zero. For a rough wall it can be calculated from:-

$$\frac{\Delta u}{u_o} = \frac{1}{\kappa} \log_e \left[\frac{C'}{B'} \frac{h\omega U_\infty}{\nu} + \exp\left[-0.005 \frac{h\omega U_\infty}{\nu}\right]\right] \quad . \tag{4.61}$$

The above equation results from combining equations (2.25) and (4.7). It was seen in Section 4.2 that B' has a universal value of 0.129; C' must be evaluated, for a given one-dimensional measure of roughness height, in terms of the measured roughness function. The third dependent variable, δ, can be calculated in terms of ω and Π from equation (2.40).

For the energy and moment of momentum methods α appears as an additional dependent variable. The initial value of α depends on the departure from equilibrium conditions of the cross-stream distribution of turbulent shear stress at the starting point. An estimate of the departure can be made on the basis of the value of Clauser's (1956) shape factor, G', as defined by equation (2.41). For the smooth surfaces, the initial values of G' were found to be very close to the equilibrium values given by equation (2.42); hence, an initial value of 0.018 was used. It was not possible, however, to repeat the exercise

for the rough walls because of a dearth of experimental data. Consequently, the same equilibrium value was used to start the integration.

4.7 The Effect of Surface Roughness on the Separation of a Two-Dimensional Turbulent Boundary-Layer

It is proposed to represent the free-stream velocity distribution of a ship in two-dimensions as shown in Fig. 4.13. The point of two-dimensional separation, at which the wall shear stress, τ_o, equals zero, is denoted by x_{sep}. Assuming the flow is fully turbulent at the leading edge,

$$x_{sep} = \xi_1 \left[\nu,\ \ell_1,\ \ell,\ h,\ U_{\infty_o},\ \left(\frac{du_\infty}{dx}\right)_1,\ \left(\frac{dU_\infty}{dx}\right)_2 \right] \quad . \tag{4.62}$$

Defining a non-dimensional separation distance to be

$$\left(\frac{x_{sep} - \ell}{\ell}\right)$$

and applying the Pi Theorem to equation (4.62) results in the following

$$\left(\frac{x_{sep} - \ell}{\ell}\right) = \xi_2 \left[\frac{\ell_1}{U_{\infty o}} \left(\frac{dU_\infty}{dx}\right)_1,\ \frac{\ell}{U_{\infty_o}} \left(\frac{dU_\infty}{dx}\right)_2,\ \frac{h}{\ell},\ \frac{\ell U_{\infty_o}}{\nu},\ \frac{\ell}{\ell_1} \right] . \tag{4.63}$$

A fixed body-shape implies constant values of $\ell_1/U_{\infty_o}\ (dU_\infty/dx)_1$, $\ell/U_{\infty_o}\ (dU_\infty/dx)_2$ and ℓ/ℓ_1. Keeping these three parameters constant, therefore, the effect of surface roughness on the value of the non-dimensional separation distance can be calculated for a given Reynolds

number, $\ell U_{\infty_0}/\nu$.

4.8 Presentation and Discussion of Results

The variation of the wall-friction coefficient for a smooth flat plate can be calculated using the method outlined in Section 4.3 but without the incorporation of the roughness function. The results are shown in Fig. 4.4 in terms of the total wall friction coefficient (obtained by integrating the local wall friction coefficient) and the plate Reynolds number based on the plate length and the free-stream velocity. The calculated values lie between the Schoenherr (1932) and I.T.T.C. (1957) curves (see Section 2.1) at low Reynolds numbers. There are no significant differences between the three curves, however, for Reynolds numbers typical of ocean-going vessels (greater than 10^7).

Fig. 4.5 shows the results of the integration of equation (4.15) for typical fixed values of either $h_{MAA}U_\infty/\nu$ or x/h_{MAA}, where h_{MAA} represents the mean apparent amplitude of the roughness as measured, for example, using the B.S.R.A. wall gauge (see Section 2.1). The calculations are based on the roughness function for the surface R550 and it is assumed that the roughness function has universal application regardless of the absolute value of the mean apparent amplitude. This would be true if the texture of the surface remains unchanged. However, the results of the measured roughness functions presented in Chapter 3 (Fig. 3.22) showed that the mean apparent amplitude is incapable of producing a universal curve for the different surfaces tested in the present investigation. Consequently, the results shown in Fig. 4.5 merely serve to demonstrate the method of calculation rather than to provide useful results. The predictions would be valid, however, for

the particular case of a ship (or, strictly, its equivalent flat plate) whose hull-roughness was identical to the surface R550.

The predictions for the smooth-wall test cases are shown in Figs. 4.6 to 4.9. The Bauer 6300 and Bell 3000 flows are predicted accurately despite an obvious mis-match, in the case of Bell's flow, of the experimental data (in relation to the law-of-the-wall constants) at the starting station (see Section 4.6). The difference in the predictions for the energy and moment of momentum methods are negligible in both cases. It should be pointed out that although Bell's flow corresponds to a zero pressure-gradient, the values of R_θ are too low for Π to be regarded as constant - as was the case in the analysis described in Section 4.3. Generally Π can be regarded as constant in a zero pressure-gradient for R_θ greater than about 6000, as reported by Coles (1956).

Fig. 4.8 shows the results for the Schubauer and Klebanoff 2100 flow. The predictions are accurate up to the point where the calculated development of R_θ departs from the experimental values. This point coincides with the onset of three-dimensional effects as is evident from the fact that, according to Coles (1968), the two-dimensional momentum integral equation, equation (4.30), is no longer satisfied at x greater than about 7 metres for this particular flow.

The results for the Moses 4100 flow are shown in Fig. 4.9. All the methods show reasonable agreement with the experimental data, although there appears to be some disparity in the absolute magnitudes of the flow variables. The entrainment method responds rather sluggishly to the initial positive pressure gradient but subsequently gives the best prediction in the relaxation region. The moment of

momentum method, on the other hand, over-responds to the pressure gradient and is slow to recover following its removal. The energy method seems to give the best all-round prediction.

The prediction for Betterman's rough-wall flow is shown in Fig. 4.10. The energy and moment of momentum methods show good agreement with experiment. The entrainment method, however, over-estimates both the local wall friction coefficient, C'_f, and the Reynolds number, R_θ. Equation (2.27) was used to describe the roughness function with $C_2 = -4.98$ (in accordance with Betterman's measurements).

The constant C_2 for Perry and Joubert's roughness was found to be -0.2; the corresponding predictions are shown in Fig. 4.11. Unfortunately there is considerable disagreement in the original experimental data between the values of C'_f deduced from the local velocity profiles (shown in Fig. 4.11) and the values deduced from the two-dimensional momentum integral equation indicating the presence of three-dimensional effects. Consequently, the development of R_θ is poorly predicted and this in turn affects the predictions for H and C'_f. Clearly, however, the predictions for the moment of momentum and the entrainment methods show considerable deviations from the experimental data, the former method tending to over-respond to the positive pressure gradient - as was the case for the Moses 4100 flow. By contrast, the energy method produces acceptable results.

Fig. 4.12 shows the results for Arndt and Ippen's saw-tooth roughness. The equivalent sand-roughness height was used to estimate C_2 which was found to be equal to -3.2. The entrainment method failed to predict this flow - probably because the entrainment function is poorly defined at the low values of Π associated with

such flows. The energy and moment of momentum methods, however, predict the flow with reasonable accuracy despite evidence of a mismatch in the experimental data at the starting station.

Summarising the performance of the three methods proposed, the energy method generally appears to predict the test flows most accurately. The proposed entrainment method, whilst producing acceptable results for the smooth surfaces and the rough surface in a zero pressure gradient, is unsatisfactory in its present form for rough surfaces in a pressure gradient. The moment of momentum method provides accurate predictions of the test flows except for a rough surface in a positive pressure gradient.

Fig. 4.14 shows the dimensionless separation distance in terms of the dimensionless roughness height. The calculations apply to the roughness function corresponding to the surface R550 and are subject to the same restrictions as those mentioned earlier in this section in relation to the validity of the roughness function for different values of the mean apparent amplitude. The value of x_{sep} was found, using the energy method, by a process of extrapolation. The numerical integration was stopped when C'_f became less than 0.0001 in order to avoid the inherent problems of ill-conditioning associated with very low values of ω (inspection of equations (4.39) and (4.41), which are two of the four equations used in the energy method, shows that they become identical as ω tends to zero). A parabola was then fitted to the last three values of u_o in order to find the value of x for a zero value of u_o.

The parameters associated with a fixed body-shape (see Section 4.7) were set to typical values (shown in Fig. 4.14) and held constant for

all the calculations. The calculations were performed for four typical Reynolds numbers. It is apparent that the effect of an increase in roughness height at a given Reynolds number is to bring forward (nearer to the leading edge) the point of separation. Similarly, for a given dimensionless roughness height the separation point is brought forward by a decrease in the Reynolds number. This latter phenomenon becomes less marked as the relative roughness increases. As the relative roughness decreases, the curves asymptotically approach the predictions for a smooth surface and the dimensionless separation distance then becomes independent of the roughness. The analysis thus confirms Sachdeva's (1973) predictions (that model tests tend to be pessimistic in so far as the effect of separation on total resistance is concerned) for the more general case of a surface with specified roughness. This is subject, however, to the underlying assumption that the dimensionless roughness height does not change appreciably between the model and full-scale cases.

Finally, a comparison for the Schubauer and Klebanoff 2100 flow between the new and the original (Lewkowicz-Horlock (1970)) families is presented in Figs. 4.15 to 4.20. An obvious improvement is obtained, using the new procedure, for both the energy and moment of momentum methods (the different methods predicted almost identical developments of R_θ and consequently the graphs are restricted to comparisons of H and C'_f). Referring to the entrainment method, the shape factor is predicted more accurately by the new procedure; the opposite is true, however, regarding the development of the local wall friction coefficient. It should be pointed out that the original entrainment procedure was based on Head's (1960) entrainment relationship so that a

comparison with the new entrainment procedure is tantamount to comparing the performance of the relationship described by equation (4.57) with that due to Head.

CHAPTER 5

THE TOPOGRAPHY OF THE SURFACES

5.1 Introduction

The investigation of the topography of the surfaces had two main objectives. Firstly, for a given section of pipe it was considered desirable to investigate the homogeneity of the surface roughness. Although each sample was originally selected for its homogeneous appearance, this property needed to be checked numerically. Secondly, quantitative information about the topography of the surfaces was required in order to search for roughness parameters which might characterise the behaviour of the roughness functions. The application of the surface measurements to the flow problem is dealt with in Chapter 6.

Initially, attempts were made to obtain profiles of the surfaces using a conventional stylus instrument ('Talysurf'); however, several problems were encountered. The rubber negatives could not be used because of their resilient nature. After one of the master copies had been traversed by the 'Talysurf' instrument it was found that the stylus had left a permanent track on the surface. This track was not visible to the naked eye but could be detected under a microscope. Rather than manufacture replicas of the master copies using a harder material it was decided to explore alternative methods of measuring the roughness.

After some experimentation a sectioning method was chosen. El-Samanoudy (1974) measured his sand-paper roughness by taking a plaster cast of the surface which was then cut at right-angles to the nominal

plane of the roughness.* The plane of the cut was smoothed with fine sand-paper and a roughness profile was examined using a shadow-graph machine at a magnification factor of 25. The profile, of length 64.5 mm, was divided into 126 equally-spaced ordinates which were then used to calculate an average roughness height for the whole surface.

Because of the brittle nature of the plaster it is doubtful whether the final profile obtained on the shadow-graph machine contained much of the original high-frequency components of the roughness. For the present investigation the rubber negativeswhich were used to manufacture the pipe-sections were also used to measure the surface roughness. The use of a surgical scalpel to section the rubber ensured the preservation of the high frequency components.

For a given pipe section two stages were involved in the measurement of its surface roughness. Firstly, a number of surface profiles were obtained. These profiles then had to be transformed into digital form suitable for input into the I.C.L. 1906S computer at the University of Liverpool. Secondly, the analysis of the profiles was performed by the computer, using a program specially designed for this purpose.

5.2 The Acquisition of Digital Profiles of the Surfaces

After all the sections of a test-pipe had been manufactured, the corresponding rubber negative was cut through the seam and laid out on a flat board with its rough side uppermost. The rubber was then cut, with an un-used surgical scalpel, along five lines which were coded according to the convention shown in Fig. 5.1. The profile B34, for example, corresponds to a profile along the line labelled B and

---

* This method was suggested to El-Samanoudy by A.K. Lewkowicz, University of Liverpool.

approximately mid-way between the lines labelled 3 and 4. A total of nine profiles was measured along the lines A, B and C which corresponded to the longitudinal direction of the pipe. No profiles were measured in the circumferential direction.

A special jig was used to ensure that the cuts were made at right-angles to a nominal plane of the roughness. The sharpness of the blade, combined with the resilience of the rubber, ensured that any deformation of the local surface profile caused by the cutting process was minimal.

The six rectangular strips of rubber containing the nine profiles to be measured were mounted individually on blockboard. The blockboard was firstly tested for flatness and then sealed to prevent absorption of moisture. A thin film of adhesive was applied to the under-side of the rubber which was then placed in position on the blockboard.

Tracings of the surface profiles were obtained using a shadowgraph machine with a magnification factor of 25. The length of each sample was 50 mm (this is the length currently being used to assess hull-roughness) corresponding to a trace of length 1.25m. A great deal of patience was exercised in making the traces and it is estimated that the maximum departure from the true profile was less than 15 microns (referring to the actual surface rather than the trace).

Digital records of the profiles were obtained using a Marconi digitising table. A rectangular 'window', measuring 40 mm by 1250 mm, was drawn around each tracing of a profile and the tracing paper was then fixed to the digitising table with adhesive tape. The table, which measured approximately 1.5 m^2, could be regarded as a Cartesian mapping space and the co-ordinates of a point were sent to a buffer

register by means of a cross-wire cursor. The location of the cursor was detected electronically by a mesh of fine wires embedded just beneath the surface of the table. The manufacturers claim a resolution of 25 microns and the maximum manual error associated with positioning the cursor is estimated to be approximately 500 microns (these figures, when referred to the actual surface, become 1 and 20 microns respectively).

Before the profile was digitised the corner points of the rectangular window were sent to the registers using a push-button on the cursor. These were used later to apply a transformation from table co-ordinates to window co-ordinates. Each point registered by the cursor was sent automatically to a tape-punching machine.

The profiles were digitised using a free-stream operating mode. The time interval between successive recordings of the position of the cursor could be varied on the control panel to suit the complexity of the profile. A total of at least one thousand points were recorded for each profile (corresponding to nine thousand points for each surface).

The paper tape records were used to create data files onto the disk storage system of the 1906S computer. A co-ordinate transformation was applied to each file to refer the profile to the Cartesian co-ordinates of the respective rectangular window. Copies were made on magnetic tape of all the transformed data files in case of damage to the original paper tapes.

5.3 Analysis of the Surface Profiles

The first part of the computer program used to analyse the profiles consisted of the determination of a mean line through the profile. It

will be appreciated that consecutive points along the profile correspond to equal time intervals. An interpolation procedure was used to convert the profile points so that they corresponded to 100$\mathring{A}$ equally-spaced intervals of length 50 microns in the X direction (the upper case will be used for Cartesian co-ordinates relating to surface profiles to distinguish them from the co-ordinate system used in the fluid dynamics aspect of the investigation). A least-squares straight line, corresponding to an un-filtered mean line, was then computed. A co-ordinate transformation was performed with respect to the window co-ordinates so that the X axis was in the direction of the mean line. The Y axis now referred to the surface height in microns.

Four different roughness heights were evaluated. The peak-to-valley height is simply the difference between the highest peak and the lowest valley. It is similar in magnitude to the Mean Apparent Amplitude (see Section 2.1). The ten-point height is the difference between the averages of the five highest peaks and the five lowest valleys. The ten-point height is a better parameter, from a statistical standpoint, than the peak-to-valley height, since the latter is very sensitive to atypical surface features such as a single sharp peak or valley. The centre-line average height is defined to be the quantity

$$\frac{1}{r} \sum_{i=1}^{i=r} |Y_i| \ .$$

where r is the number of sampled height ordinates per profile (= 1001). Finally, the root-mean-square height is simply the standard deviation of the profile about the mean line:-

$$\left[\frac{1}{r-1}\sum_{i=1}^{i=r} Y_i^2\right]^{\frac{1}{2}} .$$

In addition to the above height measurements the maximum peak and minimum valley ordinates were stored for subsequent printing.

The cumulative form of the height distribution was calculated using a class interval equal to one thirtieth of the peak-to-valley height. The skewness of the height distribution is the quantity

$$\frac{\frac{1}{r}\sum_{i=1}^{i=r} Y_i^3}{\left[\frac{1}{r-1}\sum_{i=1}^{i=r} Y_i^2\right]^{3/2}} ,$$

and the kurtosis is the quantity

$$\frac{\frac{1}{r}\sum_{i=1}^{i=r} Y_i^4}{\left[\frac{1}{r-1}\sum_{i=1}^{i=r} Y_i^2\right]^2} .$$

For a Gaussian height distribution these quantities are known to be 0 and 3 respectively. A positive skewness implies that the peaks are more prominent than the valleys (and vice versa for negative skewness). A kurtosis greater than 3 describes profiles with exaggerated peaks and valleys and the distribution is said to be leptokurtic. Platykurtic distributions, on the other hand, are associated with rather flat profiles and have a kurtosis less than 3.

A peak occurs at the i'th point along the profile if

$$Y_{i-1} < Y_i > Y_{i+1} \quad .$$

Similarly, a valley occurs if

$$Y_{i-1} > Y_i < Y_{i+1} \quad .$$

These definitions of a peak and a valley are dependent on the length of the sampling interval between successive points. Hence peaks of short wavelength will not be detected if a large sampling interval is used and vice versa. The sampling interval used in the present analysis was 50 microns. $50/\cos\theta$

The radius of curvature of the profile at a point is:

$$\frac{\left[1 + \left(\frac{dY}{dX}\right)^2\right]^{3/2}}{\frac{d^2Y}{dX^2}} \quad .$$

For a peak or valley, $dY/dX = 0$, hence the radius of curvature is simply the reciprocal of the second derivative. A numerical technique was devised, based on Stirling's formula (see Lennox and Chadwick (1970)), to estimate the second derivative knowing seven equally-spaced height ordinates. This results in the following expression for the second derivative at a peak, or valley, occurring at a point denoted by the subscript j:

$$\left(\frac{d^2Y}{dX^2}\right)_j = \frac{1}{180s^2}\left[2Y_{j+3} - 27Y_{j+2} + 270Y_{j+1} - 490Y_j + 270Y_{j-1} - 27Y_{j-2} + 2Y_{j-3}\right]. \qquad (5.1)$$

s is now $(50/\cos\theta)$

where s is the length of the sampling interval. An average value was calculated for each profile.

An auto-correlation coefficient was calculated by defining the lag, ΔX, to be an integral number of sampling intervals. Hence,

$$\Delta X = js \quad . \tag{5.2}$$

The auto-correlation coefficient is:-

$$C_j = \frac{\frac{1}{r-\lambda-j} \sum_{i=1}^{i=r-\lambda-j} (Y_i \; Y_{i+j})}{\frac{1}{r-\lambda} \sum_{i=1}^{i=r} Y_i^{\,2}} \quad . \tag{5.3}$$

When j is zero the coefficient is unity. If ΔX is large compared with the size of a typical feature then C_j is nearly zero. The auto-correlation coefficient was calculated for values of j from zero to 100, corresponding to a maximum lag of one tenth of the profile length. Lag-lengths greater than this can cause instability in the calculation procedure (see Bendat and Piersol (1966)).

The rate at which the coefficient decays from its initial value of unity is a measure of the spacing of the surface texture. This can be quantified by defining a correlation length by the lag-length corresponding to the auto-correlation coefficient having a value of 0.5. Since j is an integer, an interpolation procedure had to be used to find the exact value of the correlation length.

The slope of the profile is simply the first derivative. This can be derived from Stirling's formula in the form:-

$$\left(\frac{dY}{dX}\right)_j = \frac{1}{60s}\left[Y_{j+3} - 9Y_{j+2} + 45Y_{j+1} - 45Y_{j-1} + 9Y_{j-2} - Y_{j-3}\right] \quad . \tag{5.4}$$

Rather than use a fixed value of s equal to 50 microns, as was done earlier for the radius of curvature, the slope was evaluated for two different values of s. The values were:-

a) 50 microns

b) the correlation length

It should be noted that when s is not equal to 50 microns (which is the distance between adjacent points in the X direction) the serial representation of the height ordinates in equation (5.4) no longer corresponds to consecutive points along the profile. Since seven points are used, the distance between the first and last points in equation (5.4), measured along the X axis, is always 6s. The average slope is the average of the moduli of the first derivatives measured along the profile.

All the above roughness parameters were calculated for a bandwidth whose maximum wavelength was 50 mm. This upper limit was set by the length of the profile. Since the points were originally sampled at intervals of 50 microns, this establishes a Nyquist short-wavelength cut-off of 100 microns. Reference to the Appendix describing the computer program will be deferred until the next Chapter, when a method of filtering the profiles will be described.

5.4 Presentation and Discussion of Results

The 1906S computer was programmed to create grid-files of the surface profiles for subsequent plotting on a CALCOMP 936 digital graph plotter. The profiles are shown in Figs. 5.2 to 5.6.

The most striking feature of the profiles is that they exhibit

differences in texture between the surfaces besides differences in the degree of roughness. The surface R550, for example, which corresponds to an untreated hull-roughness (see Section 3.3), contains a good deal of high-frequency structure. The surfaces R420, R345 and R173 appear to have similar textures but the high-frequency structure, whilst present, is not as prominent as in the surface R550. The surface R253 shows evidence of a phenomenon known in the paints industry as 'pinholing'. This can be caused, for example, by contamination by rain or by the application of a further coat of paint before the previous coat has fully dried. The valley regions associated with this defect tend to be prominent features of the high-frequency structure.

Figs. 5.7 to 5.11 show the cumulative height distributions of the most Gaussian profile for each surface. The profiles were selected on the basis of the values of the skewness and kurtosis. The results are plotted on a scale so arranged that a Gaussian distribution appears as a straight line. The straight lines represent Gaussian distributions based on the measured values of standard deviation from the mean. The truncation of both the valleys and the peaks is a consistent feature for all the surfaces. This is undoubtedly caused by the application of protective paints, although it is surprising that the effect is observed for the R550 surface. The distributions for the most non-Gaussian profiles are shown in Figs. 5.12 to 5.16. Truncation of the valleys is again in evidence, although in the case of the R550 surface (Fig. 5.12) the extreme valley regions appear to revert to a near-Gaussian distribution. With the exception of the R550 surface all the distributions are skewed in the positive sense and show little evidence of truncation in the peak regions.

Whitehouse and Archard (1970) showed that surface profiles can be specified statistically in terms of the standard deviation of the height ordinates and a correlation length (which is defined differently from the one used in this investigation), providing the height distributions are Gaussian. Hence other parameters like the average slope and the average radius of curvature of the peaks can be related to these fundamental parameters. Since the present height distributions are obviously non-Gaussian, it would appear that specifications of the surface must involve more than two parameters.

The results of the analysis of the surfaces are shown in Tables 5.1 to 5.5. Bearing in mind the locations of the profiles with respect to the inside surfaces of the pipe-sections (see Fig. 5.1) there does not appear to be any systematic variation of the surface parameters with position, although the variance of some of the parameters is high.

The measurements of roughness height are shown on the first sheet of each table. The very small differences between the peak-to-valley and the ten-point heights indicate that a single peak-to-valley measurement is a much better representation of surface roughness than originally thought. This is substantiated by the near constancy of the ratio of the peak-to-valley height to the standard deviation. The value of this ratio is approximately 5 for all the surfaces. The minimum valley generally occurs at a greater distance from the mean line than the maximum peak for both the R550 and the R253 surfaces.

Unfortunately, the variance associated with the measurements of the peak and valley curvatures are too high to draw any conclusions. However, this does not affect the ability to detect differences in surface texture, since the significant parameters in this context are the slope and the

correlation length. The slope - based on a sampling interval equal to the correlation length - is highest for the R550 surface, which is consistent with the visual appearance of the profiles (see Fig. 5.2).

None of the measured parameters shows any evidence of the unusual valley regions reported earlier for the surface R253. This is not surprising, however, in view of the large bandwidth of wavelengths on which the analysis was based. The variation in the surface statistics with different bandwidths will be investigated in the next chapter.

CHAPTER 6

THE SEARCH FOR A UNIVERSAL ROUGHNESS FUNCTION IN TERMS OF THE SURFACE STATISTICS

6.1 Introduction

Three types of roughness can be identified on a ship's hull. Firstly, there is the macro-roughness comprising structural protuberances, welding seams and barnacles. The contribution to the total resistance made by the macro-roughness can be estimated knowing the form drag of one type of excrescence (for example a welding seam) and the associated roughness density. Secondly, there is the micro-roughness with which the present investigation is concerned. From the resistance point of view this manifests itself in the form of a roughness function and is present over the entire hull-surface - being responsible for the major part of the total wall-friction. Thirdly, lying between these two extremes of roughness is a bandwidth of surface wavelengths which does not contribute significantly to the total resistance. The wavelengths are too long to produce turbulence and hence affect the roughness function, and the associated roughness heights and surface slopes are too small to create any form drag. The latter may be regarded as 'long-wave curvature'.

This chapter is concerned with relating the measured roughness functions to the statistics of the surface micro-geometries. The problem is to define the boundary between the above-mentioned second and third categories of surface roughness. This is necessary because the statistics depend on the longest wavelength present in the surface profiles - hence-

forth to be referred to as the 'cut-off wavelength'. This wavelength must be of the same order of magnitude as the size of the energy-containing eddies near the surfaces if any correlation is to be observed between the roughness functions and the micro-geometries.

6.2 Investigation of the Surface Statistics for Different Cut-Off Wavelengths

The statistical analysis of the surface profiles has been described in Chapter 5. The analysis was repeated for two different cut-off wavelengths - 10 mm and 2 mm. These are in contrast with the unfiltered value of 50 mm for the raw profiles. The two cut-off wavelengths were chosen on the basis of the measured values of the macro-scales of turbulence as defined by equation (3.13). The average value of the macro-scales was found to be less than 10 mm at $y+\varepsilon/R = 0.02$. It is to be expected that nearer to the wall this figure would be lower in magnitude. There is no reason to suppose, however, that this length scale should be taken as an absolute measure of the cut-off wavelength required for the statistical analysis; the macro-scale merely represents the size of a typical energy-containing eddy. For this reason, although it was clear that a cut-off wavelength greater than 10 mm seemed rather high, it was by no means clear which was the best cut-off wavelength to choose. It was decided that 10 mm and 2 mm would represent the most likely extreme values.

A mid-point locus method was used to filter the surface profiles. For the case of a 10 mm cut-off wavelength the procedure was as follows. The raw profile was divided into five equal 10 mm lengths along the X axis forming what will be referred to as five 'sub-samples'. Regression

lines were then calculated for each sub-sample and the mid-points of each regression line were determined. Using a simple Lagrange interpolation procedure, parabolas were calculated to join the three consecutive mid-points of each group of three sub-samples (the three groups being sub-samples 1, 2 and 3; 2, 3 and 4; and 3, 4 and 5). The first halves of these parabolas, when joined together at their points of intersection, constituted the output of a low-pass filter since the high frequencies had been removed. The required high-pass output was obtained by finding the difference in height ordinates between the original profile and the low-pass output. The low-pass outputs corresponding to the first half of the first sub-sample and the last half of the last sub-sample were represented by the respective regression lines. A similar procedure was used for the 2 mm cut-off wavelength. The high-pass output for each profile was then subjected to the same analysis as was described in Chapter 5. Details of the computer program can be found in Appendix 7.

6.3 The Proposed Modification to the Roughness Reynolds Number

It was found in Chapter 3 that the roughness functions showed similar trends but differed in absolute magnitudes. Instead of a simple one-dimensional measure of roughness height, such as the mean apparent amplitude used thus far, it is proposed to modify the chosen roughness height in a way which depends on the texture of the surface and the degree of departure from a Gaussian height distribution. Although the investigation in the previous chapter showed that the peak-to-valley height and the standard deviation of a profile were in a nearly constant ratio for all the surfaces, the standard deviation

will be used for the one-dimensional measure of the roughness height since, from a statistical point of view, it is more efficient.

A good measure of the texture of the surfaces was found to be the average slope (see Chapter 5) based on a sampling interval equal to the correlation length. A Gaussian surface with a fine texture, associated with high values of the average slope, must have a higher effective roughness height than a Gaussian surface with a more open texture but with the same standard deviation. This is exemplified by considering isolated roughness elements with identical heights but different shapes. Referring to Fig. 6.1, consider the 'private' boundary layers associated with the two surface features shown in the diagram. Although both features have the same height, clearly the boundary layer is more likely to separate in the case of a steep slope downstream of the peak on account of the stronger adverse pressure gradient. Moreover, as this slope becomes steeper the point of separation of the private boundary layer moves nearer the peak. Thus the associated form-drag coefficients increase with the degree of bluffness of the roughness elements which can be crudely quantified by the values of the average slope of the elements. Within the small range of values of the average slope observed in the present investigation, it is proposed to augment the standard deviation by an amount equal to $(1 + as_p)$, where s_p is the average slope and a is an empirical constant, so that the effective roughness height for a Gaussian surface is assumed to be of the form:

$$h' = \sigma_r (1 + as_p) \quad , \tag{6.1}$$

where h' is the modified roughness height and σ_r is the standard deviation.

The degree of departure from a Gaussian height distribution can be represented by the skewness and the kurtosis. The effective roughness height, as defined in equation (6.1), must increase if the skewness is positive, since this corresponds to the peaks of the surface being more prominent than the valleys. Conversely h' must decrease if the skewness is negative. The magnitude of the increase in h' associated with a postive value of skewness must also depend on the kurtosis - which is a measure of departure of both the peaks and the valleys from a Gaussian height distribution. The increase must be greater for a leptokurtic distribution (kurtosis greater than 3) since this implies that the extreme height ordinates (and therefore the peaks) represent greater departures from the mean line than would be obtained if the surface was Gaussian with the same standard deviation. These exaggerated peaks create extra form drag which must be accounted for by an increase in h'. The opposite is true for a platykurtic distribution (kurtosis less than 3). Denoting the skewness by s_k and the kurtosis by k_u it is proposed, in view of the above comments, that the product $s_k\, k_u$ should be regarded as a significant parameter. This can be introduced into equation (6.1) to form the following modified roughness Reynolds number:

$$\frac{h'u_o}{\nu} = \frac{\sigma_r u_o}{\nu}(1 + as_p)(1 + bs_k k_u) \quad , \qquad (6.2)$$

where a and b are empirical constants.

This rather crude model is expected to fail for highly non-Gaussian surfaces with zero skewness since then the kurtosis ceases to feature as

a parameter. It was found, however, that none of the surfaces investigated came under this category.

6.4 Presentation and Discussion of Results

The effect of the filtering technique for a cut-off wavelength of 2 mm is shown in Figs. 6.2 to 6.6, which relate to the most non-Gaussian profile for each surface. The graphs were obtained using a CALCOMP 936 digital graph plotter and are distorted in such a way that the horizontal scale is magnified five times and the vertical scale is magnified fifty times. In general, the surface R420 was found to contain the largest amount of long-wave curvature.

The results of the analysis for the three different cut-off wavelengths considered are shown in Tables 6.1 to 6.5. The average values for the nine surface profiles are shown together with the errors corresponding to one standard deviation. Some trends can be found upon close inspection of the data. The errors associated with the measurement of both the centre-line average height and the standard deviation become less than those for the peak-to-valley and ten-point heights as the cut-off wavelength decreases - which lends support for the choice of one-dimensional roughness height used in equation (6.2). It appears that the kurtosis increases as the cut-off wavelength decreases; there is no reason to suppose, however, that this should always be the case. The effect of a shorter cut-off wavelength is to decrease the correlation length, so that it is not surprising to find a corresponding increase in the average slope based on a sampling interval equal to the correlation length.

Despite the relatively high errors associated with some of the

surface measurements, attempts were made to relate the measured roughness functions (see Figs. 3.21 and 3.22) to the modified roughness Reynolds number as defined in equation (6.2). This was done by programming the PDP8 computer to plot the roughness functions on a TETRONIX visual-display unit. The relevant surface measurements for a given cut-off wavelength were sent to the machine and the graphs were plotted for particular values of a and b. It soon became clear that a cut-off wavelength of 10 mm was too large to allow the roughness functions to collapse onto a single curve. This is not surprising in view of the fact that the statistics of the surfaces hardly changed as the cut-off wavelength decreased from 50 mm to 10 mm (see Tables 6.1 to 6.5). For a cut-off wavelength of 2 mm, however, the results showed encouraging support for the proposed form of the modified roughness Reynolds number. The roughness functions are shown in Figs. 6.7 and 6.8 where a = 0.5 (corresponding to units of degrees for s_p), b = 0.2 and the cut-off wavelength = 2 mm. The above values for a and b are by no means the optimum ones; it was felt that a more thorough numerical investigation could not be justified using the available statistical data.

The existence of universal curves for the roughness functions, when expressed in terms of the surface statistics, opens up new possibilities for predicting the wall friction on ships' hulls. The availability, in chip-form, of micro-processors and random-access-memory units should enable hull-roughness measurements to be processed on location using a purpose-built portable computer. The required resolution calls for a stylus tip-dimension of the order of 20 microns, although further studies are needed in order to define this figure more precisely.

Knowing the modified roughness height, h', it is a simple matter to incorporate the roughness function into the boundary-layer equations in the manner described in Chapter 4.

CHAPTER 7

CONCLUSIONS AND SUGGESTIONS FOR FUTURE WORK

7.1 Conclusions

This thesis has been concerned with turbulent shear flows near irregularly-rough surfaces with particular reference to ships' hulls. The investigation has been carried out in three phases: air-flows have been studied in a series of pipe-lines, five of which were lined with replicas of real ship-hull roughnesses; methods of predicting two-dimensional turbulent boundary-layers developing over irregularly-rough surfaces in an arbitrary pressure distribution have been proposed; finally, an attempt has been made to relate the statistics of the surface micro-geometries to the flow measurements.

In the past, methods of predicting the effects of hull-roughness on ship performance have relied on correlations between shaft horse-power and a one-dimensional measure of the peak-to-valley height of the surface roughness - such as the mean apparent amplitude (M.A.A.). The flow measurements have shown, however, that the M.A.A. is unsatisfactory in this respect. Specifically, for different degrees of surface roughness, the measured roughness functions diverge when expressed in terms of a roughness Reynolds number based on the M.A.A.. For a given hull-roughness, however, the roughness function is unique and its determination by experiment, using a process of surface replication, enables predictions of the effect of the surface on the development of turbulent boundary-layers to be made. This is possible because the roughness function is a parameter associated with the inner region of

the mean velocity distribution and its value is independent of the external pressure gradient. Moreover, once the roughness function is defined by experiment, boundary-layer predictions can be made up to arbitrarily-high Reynolds numbers based on the ship's length and speed.

The following important conclusions can be drawn in relation to the first phase of the investigation.

1) A method of replicating a sample area of a ship's hull whilst the ship is in dry dock has been established, using silicon rubber.
2) A pipe-line can be manufactured in such a way that the inside surface of the pipe is a positive copy of an actual hull-roughness.
3) Mean velocity measurements confirm that the outer region velocity distribution, when expressed in the velocity-defect form, is independent of the surface roughness.
4) The roughness functions show trends similar to those of Colebrook and White (1937) which apply to naturally-occurring surfaces.
5) The M.A.A. is incapable of producing a universal curve for the roughness functions. This highlights the importance of taking into account the statistical geometry of the surfaces.
6) For a given pipe Reynolds number, the effect of surface roughness on the non-dimensional longitudinal fluctuating velocity, $\sqrt{\overline{u'^2}}/u_o$, is to increase its value in relation to the value corresponding to a smooth surface - particularly in the region near the wall.
7) An increase in the pipe Reynolds number, for a rough-walled pipe, is associated with a decrease in the non-dimensional radial and peripheral fluctuating velocities, $\sqrt{\overline{v'^2}}/u_o$ and $\sqrt{\overline{w'^2}}/u_o$ respectively.

8) The existence of very weak secondary flows in the rough pipes could account for the unexpectedly low values of the shear stress, $-\rho\overline{u'v'}$, and the non-zero values of the cross-correlation, $\overline{u'w'}$.

9) All three sub-ranges of the frequency spectrum function, F(n), were clearly defined at $(y+\varepsilon)/R = 0.08$. At the pipe-centre-lines there was no evidence of a production sub-range. At $(y+\varepsilon)/R = 0.02$ the spectrum function shows a gradual change from the -1 (production) to the -7 (dissipation) sub-ranges with an ill-defined intermediate sub-range. The latter becomes more prominent as the pipe Reynolds number increases.

10) The value of the micro-scale of turbulence, for a given wall distance and pipe diameter, is independent of surface roughness except very near the wall, where roughness increases its value.

11) In the inner region, surface roughness acts so as to increase the value of the macro-scale of turbulence at a given pipe Reynolds number and pipe diameter. In the outer region, however, the macro-scale remains essentially constant.

For the surface with the code-name R550 (M.A.A. = 550 microns) it was possible to achieve fully-rough flow conditions and hence to define the roughness function at any roughness Reynolds number. A simple interpolation formula was used for this purpose. At moderately high Reynolds numbers it can be assumed that the wake-strength parameter, Π, remains constant for flow over a flat plate in a zero pressure gradient (corresponding to the major part of a ship's hull). Hence predictions of the resulting boundary-layer can be made by combining the momentum equation with a wall friction relationship derived from the mean velocity distribution - which incorporates the measured roughness function. The

resulting equation is easily solved numerically using Simpson's procedure, resulting in a prediction of the wall friction coefficient of a ship whose hull is covered with a roughness identical to the surface R550.

Calculations were performed firstly for a smooth ship. It was found that the friction line (total wall friction coefficient versus ship Reynolds number based on length and speed) lay very close to both the Schoenherr (1932) and I.T.T.C. (1957) lines - thus confirming the accuracy of the calculation procedure. Simple calculations, based on the predictions for a rough ship with a hull-roughness identical to the surface R550, suggest that for a ship length of 100m and speed 10 m/s the total resistance, due to wall friction alone, increases by approximately one-third by comparison with the value for a smooth hull. This emphasises the great economic importance of research into the effects of hull roughnesses on the performance of large ships.

For flows in an arbitrary pressure distribution, prediction procedures have been proposed based on the Lewkowicz-Horlock (1970) family of integral prediction methods. The original family has been improved in four ways. Firstly, a new mean velocity profile for the outer region has been used which ensures a zero value of the cross-stream mean velocity gradient at the edge of the boundary-layer. Secondly, a new cross-stream distribution of the turbulent shear stress has been proposed which not only satisfies known boundary conditions but also gives good agreement with reliable experimental data. This new shear-stress distribution has been used to derive simple expressions for the shear-stress and shear-work integrals which appear in the energy and moment of momentum equations. Thirdly, the inclusion of a rate equation for the

eddy viscosity enables better predictions of non-equilibrium flows to be made. Finally, the new family has been extended to include the effects of surface roughness by incorporating the measured roughness function into the wall friction equation. Additionally, a new entrainment relationship has been tentatively proposed which directly relates a dimensionless entrainment parameter to the wake strength parameter. The relationship was based on experimental data published at the Stanford Conference on turbulent boundary layers (1968).

The following conclusions can be drawn in relation to the predictions of seven test-cases with different pressure distributions and surfaces.

1) All three methods gave good predictions for a smooth surface in a zero or negative pressure gradient.

2) The energy and moment of momentum methods gave satisfactory predictions for rough surfaces in a zero or negative pressure gradient; however, the entrainment method failed to predict the rough-wall flow in a negative pressure gradient. It is thought likely that this was due to the poor definition of the entrainment relationship, at low values of the wake strength parameter, resulting from the lack of experimental data used in its formulation.

3) The entrainment method responded sluggishly to a positive pressure gradient although it predicted the correct trends. This resulted in the predicted wall friction coefficient being too large.

4) The moment of momentum method gave good predictions for a smooth surface in a positive pressure gradient. The method over-responded, however, for a rough surface, resulting in the wall friction coefficient being too low.

5) The energy method gave good predictions for both smooth and rough surfaces in a positive pressure gradient.

A numerical experiment has been performed to investigate the effect of surface roughness on the position of separation of a two-dimensional turbulent boundary-layer developing over a flat plate covered with ship-hull roughness. The plate was subjected to a pressure distribution typical of that existing on an ocean-going vessel and the calculations were performed for a fixed body-shape. It was found that, for a given plate Reynolds number, an increase in roughness brought the separation point forward towards the leading edge and that, for a fixed non-dimensional roughness height, the separation point was again brought forward by a decrease in the plate Reynolds number.

The micro-geometry of the surfaces was investigated using a sectioning technique to obtain surface profiles. Nearly fifty thousand height ordinates were processed to test the homogeneity of the surfaces and to search for a measure of the surface roughness which, by contrast with the M.A.A., relates more closely to the measured wall-friction. A method of filtering the surface profiles was devised which rejected wavelengths greater than a certain cut-off value. It was assumed that this cut-off wavelength should be of the same order of magnitude as the size of the energy-containing turbulent eddies in the fluid near the surface. The turbulence macro-scale was used for the purpose of estimating the size of these eddies. A new effective roughness height has been tentatively proposed whose magnitude depends not only on a measure of the roughness height (the standard deviation of the profile was used in the present investigation) but also on the values

of the average slope (based on a sampling interval equal to the correlation length) and the skewness and kurtosis of the height distribution. This has resulted in a modified roughness Reynolds number which gives rise to a near-universal curve for the roughness functions, as measured in the pipe-flow experiments, if a cut-off wavelength of 2 mm is chosen.

7.2 Suggestions for Future Work

The following suggestions are offered in relation to future work in the field of turbulent shear flows near irregularly-rough surfaces.

1) Flow experiments can be performed using a pipe whose internal surface can be made irregularly-rough in a controlled manner using, for example, beads of different sizes. Hence the effects of skewness, kurtosis and average slope can be investigated.
2) More raw data is required to search for a roughness function which is universally applicable to ship-hull roughness. The test surfaces should cover a wide range of roughness heights and textures.
3) To study the effects of welding seams and barnacles it is necessary to investigate the interaction between macro-roughness elements and the background (micro-) roughness.
4) A hot-wire technique is needed to detect weak secondary flows in rough pipes. This must be perfected before attempts can be made to explain the anomalous radial distributions of turbulent shear stress reported in Chapter 3.
5) In relation to the boundary-layer predictions it would be useful to know how sensitive the energy and moment of momentum methods are to the starting value of the equilibrium parameter, α.

6) The value of the constant, C_r = -0.06, appearing in the rate equation (equation (4.50)) should be checked by means of experiments in non-equilibrium flows over smooth and rough surfaces.

7) The conclusions reached in relation to the numerical exercise concerning two-dimensional separation on rough surfaces should be checked experimentally.

8) There is a dearth of reliable measurements of two-dimensional turbulent boundary-layers near rough surfaces. This situation needs to be rectified in order to improve proposed prediction methods.

9) Gadd's (1971) approximate method of calculating turbulent boundary-layers on ships' hulls should be extended, using the prediction procedures described in Chapter 4, to include the effects of surface roughness.

10) The theoretical and experimental aspects of the work should be complemented by boundary-layer measurements resulting from full-scale ship trials.

11) There is a need for an instrument which accurately records the high-frequency components of ship-hull roughness.

12) Future experimental investigations into the effect of surface roughness on the wall friction should include non-rigid roughness elements to simulate marine growth such as sea-weed. Such investigations would have to be performed using water as the fluid medium.

APPENDIX 1

(a) CHEMICALS USED FOR ROUGHNESS REPLICATION

1) Rubber negative from ship's hull:

100 parts SILASTIC ® 504
100 parts SILASTIC ® 3110
1 part CATALYST 4

} manufactured by Dow Corning International Limited

Cure time approximately 1½ hours at 20°C.

2) Epoxy-resin positive from rubber negative:

100 parts EPIKOTE 816
60 parts EPIKURE RTV

} manufactured by Shell Chemicals U.K. Limited

3) Rubber negative from epoxy-resin positive:

10 parts SILASTIC ® G
1 part SILASTIC ® G catalyst

} manufactured by Dow Corning International Limited

4) Plastic pipes from second rubber negative:

100 parts FILABOND 8748A
1 part CATALYST 'K'

} manufactured by Beck, Koller and Co. (England) Limited

® Registered trade mark of Dow Corning International Limited.

(b) MANUFACTURE OF THE PIPE-LINES

A frame was first built around the master copy which was placed face upwards and subsequently adjusted so that the surface lay in a nominally-horizontal plane. A liquid form of silicon rubber was then

poured onto the surface to a depth of approximately 5 mm. The slight meniscus formed at the edges of the frame could easily be removed with a razor once the rubber had cured. (Details of the chemicals are presented in the first part of this Appendix.)

This 'rubber negative' was then wrapped around a wooden mandrel, which had previously been accurately turned in a lathe, so that the exterior surface comprised the negative roughness. The seam was then joined, using a special adhesive (a slight under-cut in the seam of the negative was found necessary to allow for the slight compression on the underneath surface), and subsequently trimmed with a razor to ensure that no artificial features had been introduced into the roughness. The combined diameter of the mandrel and the rubber negative was such as to correspond to the type of pipe being made. A photograph of a rubber negative and the mandrell used for the small pipes is shown in Fig. 3.1.

The small pipes were manufactured in such a way that the flanges were an integral part of each section. The length of a section was 0.5m and the mandrel was first cut to this length so that the rubber negative was flush with each end. Wooden patterns of the flanges were then fixed at the ends of the mandrel and a coat of epoxy resin was applied over the rubber negative and on the inside surfaces of the patterns. This was followed by alternate layers of glass fibre matting and resin up to a thickness of approximately 4.0 mm. After the resin had catalysed (thus forming a section) the flanges were drilled and the patterns were then removed. The mandrel could now be pushed out of the rubber negative which was subsequently easily separated from the final pipe section (see Fig. 3.2).

Initially it was thought that the process of pushing the mandrel out of the completed section might have damaged the rubber negative - thus necessitating a new negative for each section. Accordingly, the silicon rubber used for making the negative was chosen for its good resilience and high tear-strength. In fact it transpired that the mandrel came out with no difficulty at all so that the same negative could be used for the whole pipe.

The large rough pipe was manufactured in a similar way with the exception that the flanges did not form an integral part of the sections. The sections in this case were used as liners and they were inserted into an outer pipe or 'jacket'. The safety officer at the university felt that the structural properties of glass-reinforced-plastics were rather unpredictable and in view of the fact that the larger diameter would give rise to large hoop stresses he recommended the use of such a jacket. For this purpose heavy-duty P.V.C. ('Polyork') piping which had an internal bore of 150 mm was used. This was cut into lengths of 0.6m and matching P.V.C. flanges were fixed to each end with a high-strength cement. A recess was machined on the inside rim of each flange to locate with steel clips which were glued onto the ends of the liners. The liners themselves were machined to overlap with adjoining liners thus providing accurate joints and avoiding step-wise jumps in surface roughness. The joints were greased to prevent minor air leakages and the liners were seated in their jackets using foam rubber. A completed liner is shown in Fig. 3.3.

APPENDIX 2

EFFECT OF COMPRESSIBILITY ON THE MEASUREMENT OF WALL FRICTION

It will be assumed that the pipe wall is sufficiently insulated for any heat transfer across the walls to be negligible. This seems a reasonable assumption in view of the fact that the measured temperature of the air-flow was typically within a few degrees of the ambient temperature. The flow can therefore be treated as adiabatic - but not as isentropic on account of the irreversible nature of the wall friction. The velocity profile will be considered to be sufficiently uniform for the flow to be treated in one-dimensional terms.

The continuity equation is:-

$$\rho U_{av} = \text{constant} = \frac{4\dot{m}}{\pi D^2} \quad , \qquad \text{(A2.1)}$$

where $\dot{m}$ is the mass flow-rate. The equation of state is:-

$$\frac{p}{\rho} = \bar{R}\,T \quad , \qquad \text{(A2.2)}$$

where $\bar{R}$ is the gas constant. For adiabatic flow the stagnation enthalpy, h_o, must remain constant:-

$$h_o = \frac{p}{\rho} + \frac{1}{2} U_{av}^2 + c_v T \quad . \qquad \text{(A2.3)}$$

The steady-flow momentum equation for a horizontal pipe is:-

$$\frac{dp}{\rho U_{av}^2} + \frac{dU_{av}}{U_{av}} + \frac{f}{2D}\,dx = 0 \quad , \qquad \text{(A2.4)}$$

where f is the pipe friction coefficient = $8\tau_o/\rho U_{av}^2$. Expressing c_v in equation (A2.3) in terms of the ratio of the specific heats, γ, and the gas constant: $c_v = \bar{R}/\gamma-1$, and introducing the Mach number, $M = U_{av}\sqrt{\rho/\gamma p}$, equations (A2.1) to (A2.4) can be combined to give:-

$$\left[\frac{M^2-1}{\frac{1}{2}(\gamma-1)M^2+1}\right]\frac{dM}{\gamma M^3} + \frac{f}{2D}\,dx = 0\,, \qquad \text{(A2.5)}$$

which is a standard result (see, for example, Massey (1970)). If the term $\frac{1}{2}(\gamma-1)M^2$ is small in relation to unity then the denominator in the first term of equation (A2.5) can be expanded using a binomial series:-

$$\left[1 + \left(\frac{\gamma-1}{2}\right) M^2\right]^{-1} = 1 - \left(\frac{\gamma-1}{2}\right) M^2\,. \qquad \text{(A2.6)}$$

Hence equation (A2.5) becomes:-

$$\int_{x_1}^{x_2} \frac{f\,dx}{2D} = \left(\frac{\gamma-1}{4\gamma}\right)\left(M_2^2-M_1^2\right) - \frac{1}{2\gamma}\left(\frac{1}{M_2^2} - \frac{1}{M_1^2}\right) - \left(\frac{\gamma+1}{4\gamma}\right)\log_e\frac{M_2^2}{M_1^2}\,, \qquad \text{(A2.7)}$$

where the subscripts 1 and 2 refer to the upstream and exit stations respectively.

It is experimentally more convenient to measure the static pressure than the Mach number. Combining equations (A2.1), (A2.2) and (A2.3) it is easily shown that:

$$M^2 = \frac{A}{\gamma p^2}\,, \qquad \text{(A2.8)}$$

where A is a constant to be determined from the exit conditions.

Hence equation (A2.7) becomes:-

$$\int_{x_1}^{x_2} \frac{f\,dx}{2D} = \frac{A(\gamma-1)}{4\gamma^2}\left[\frac{1}{p_2^2} - \frac{1}{p_1^2}\right] - \frac{1}{2A}(p_2^2 - p_1^2) - \left(\frac{\gamma+1}{4\gamma}\right)\log_e \frac{p_1^2}{p_2^2} \,. \quad \text{(A2.9)}$$

Now $p_1/p_2 = 1 + \Delta p/p_2$, where Δp is the pressure drop. If Δp is small in relation to p_2 then

$$\log_e \frac{p_1^2}{p_2^2} = \frac{2\Delta p}{p_2} \,. \quad \text{(A2.10)}$$

Combining the above three equations gives:

$$\int_{x_1}^{x_2} \frac{f\,dx}{2D} = \frac{\Delta p}{\rho_2 U_{av_2}^2}\left[1 - \frac{\rho_2 U_{av_2}^2}{\gamma p_2}\left(\frac{\gamma+1}{2} - \frac{\Delta p \gamma}{2\rho_2 U_{av_2}^2}\right)\right] \,. \quad \text{(A2.11)}$$

The pipe friction coefficient, f, is a function of Reynolds number, $R_e = \rho U_{av} D/\mu$. However, ρU_{av} is constant, according to equation (A2.1), so that for a given flow f is a function of x only in so far as the temperature affects the value of the molecular viscosity. At 20°C μ changes by only 0.23% per degree C. Since the static temperature was observed to change by a maximum of approximately 5°C over the length of the whole pipe-line, f may be considered constant between the measuring stations. After integrating the left-hand-side of equation (A2.11) and subsequently replacing f by $8u_o^2/U_{av}^2$, the final relationship for the wall friction-velocity becomes:

$$u_o^2 = \frac{\Delta p D}{4\rho_2 L_1}\left[1 - \frac{\rho_2 U_{av}^2}{\gamma p_2}\left[\frac{\gamma+1}{2} - \frac{\Delta p \gamma}{2\rho_2 U_{av}^2}\right]\right] , \qquad (A2.12)$$

where u_o and U_{av} are referred to the exit plane and L_1 corresponds to the distance between the measuring stations.

APPENDIX 3

CALCULATION OF THE ROUGHNESS FUNCTION

For a given value of ε, u_o and χ, the sum of the squares of the residuals, σ_1 in equation (3.6), becomes a minimum when

$$\frac{\partial}{\partial \chi} \sum_{i=1}^{5} \left[\frac{u_i^2}{u_o^2} + \frac{1}{\kappa^2} \log_e^2 \frac{y_i+\varepsilon}{h} + \chi^2 + \frac{2\chi}{\kappa} \log_e \frac{y_i+\varepsilon}{h} - \frac{2u_i}{u_o} \left(\frac{1}{\kappa} \log_e \frac{y_i+\varepsilon}{h} + \chi \right) \right] = 0 \quad . \tag{A3.1}$$

This leads to equation (3.5).

The five equations in the five unknowns (χ, u_o, ε, Π and U_{av}) are:-

$$\frac{U_{av}}{U_c} = 1 - \frac{u_o}{\kappa U_c} \left(\frac{43+42\Pi}{30} \right) \quad , \tag{A3.2}$$

$$u_o^2 = \frac{\Delta p D}{4 \rho_a L_1} \left[1 - \frac{\rho_a U_{av}^2}{\gamma p_a} \cdot \left(\frac{\gamma+1}{2} - \frac{\Delta p \gamma}{2 \rho_a U_{av}^2} \right) \right] \quad , \tag{A3.3}$$

$$\chi = \frac{1}{5} \sum_{i=1}^{5} \left[\frac{u_i}{u_o} - \frac{1}{\kappa} \log_e \frac{y_i+\varepsilon}{h} \right] \quad , \tag{A3.4}$$

$$\frac{U_c}{u_o} = \frac{1}{\kappa} \log_e \frac{R}{h} + \chi + \frac{2\Pi}{\kappa} \tag{A3.5}$$

and

$$\sigma_1 = \sum_{i=1}^{5} \left[\frac{u_i}{u_o} - \left(\frac{1}{\kappa} \log_e \frac{y_i+\varepsilon}{h} + \chi \right) \right]^2 , \qquad (A3.6)$$

where y_i, u_i, U_c, Δp and p_a are experimentally-determined parameters and κ, γ, h, R, L_1 and ρ_a are known. The five equations must be solved subject to σ_1 being a minimum. The procedure used in the investigation was to set ε and then solve the above equations to find σ_1. This procedure was repeated, using different values of ε, until the minimum value of σ_1 was located. The following intermediate parameters can be defined in terms of ε and the experimental measurements:-

$$A_e = \frac{1}{\kappa} \log_e \frac{R}{h} - \frac{1}{5} \sum_{i=1}^{5} \frac{1}{\kappa} \log_e \frac{y_i+\varepsilon}{h} , \qquad (A3.7)$$

$$B_e = \frac{2\gamma p_a}{(\gamma+1)\rho_a} , \qquad (A3.8)$$

$$C_e = 1 + \frac{\Delta p}{2p_a} , \qquad (A3.9)$$

$$D_e = \frac{4\rho_a L_1}{\Delta p D} \qquad (A3.10)$$

$$E_e = U_c - \frac{21}{30} \left[U_c - \frac{1}{5} \sum_{i=1}^{5} u_i \right] , \qquad (A3.11)$$

$$F_e = \frac{43-21\kappa A_e}{30\kappa} \qquad (A3.12)$$

and

$$G_e = U_c - \frac{1}{5} \sum_{i=1}^{5} u_i . \qquad (A3.13)$$

It is easily shown that the required quantities can be expressed in terms of these intermediate parameters as follows:-

$$u_o = \frac{2E_eF_e + \sqrt{4E_e^2F_e^2 - 4(F_e^2 + B_eD_e)(E_e^2 - B_eC_e)}}{2(F_e^2 + B_eD_e)} \qquad \text{(A3.14)}$$

$$U_{av} = \sqrt{B_e(C_e - D_eu_o^2)} \quad , \qquad \text{(A3.15)}$$

$$\Pi = \frac{\kappa}{2}\left(\frac{G_e}{u_o} - A_e\right) \qquad \text{(A3.16)}$$

and $$\chi = \frac{U_c - G_e}{u_o} + A_e - \frac{1}{\kappa}\log_e\frac{R}{h} \quad . \qquad \text{(A3.17)}$$

APPENDIX 4

THE RESPONSE EQUATIONS FOR AN INCLINED HOT-WIRE

The diagram at the end of this appendix (Fig. A4.1) refers to an inclined hot-wire for two orientations in the x-y plane. The two configurations will be denoted by the subscripts 1 and 2.

For the first configuration the component of the instantaneous velocity along a normal to the wire is given by:-

$$q_{n_1}^2 = \left[(u+u')\sin\Phi - v'\cos\Phi\right]^2 + w'^2 \quad .$$

For the component parallel to the wire:-

$$q_{p_1}^2 = \left[(u+u')\cos\Phi + v'\sin\Phi\right]^2 \quad .$$

According to equation (3.8) the instantaneous effective cooling velocity is therefore:-

$$q_{eff_1}^2 = \left[(u+u')\sin\Phi - v'\cos\Phi\right]^2 + w'^2 + k^2\left[(u+u')\cos\Phi + v'\sin\Phi\right]^2 \quad . \qquad (A4.1)$$

The time-averaged value is (with $\Phi = 45^o$):-

$$\overline{q_{eff_1}^2} = \overline{w'^2} + \left(\frac{k^2+1}{2}\right)\left(u^2+\overline{u'^2}+\overline{v'^2}\right) + (k^2-1)\overline{u'v'} \quad . \qquad (A4.1a)$$

Similarly, for the second configuration:-

$$q_{eff_2}^2 = \left[(u+u')\sin\Phi + v'\cos\Phi\right]^2 + w'^2 + k^2\left[(u+u')\cos\Phi - v'\sin\Phi\right]^2 \quad (A4.2)$$

and

$$\overline{q_{eff_2}^2} = \overline{w'^2} + \left[\frac{k^2+1}{2}\right](u^2 + \overline{u'^2} + \overline{v'^2}) - (k^2-1)\overline{u'v'} \quad . \quad (A4.2a)$$

The electronic lineariser generates a transfer function such that equation (3.9) transforms to:-

$$e_b = A_L\, q_{eff} \quad , \quad (A4.3)$$

where e_b is the instantaneous linearised bridge voltage which can be expressed as the sum of the mean and fluctuating parts as follows:-

$$e_b = E_b + e'_b \quad . \quad (A4.4)$$

The quantity A_L in equation (A4.3) is a constant which depends on the setting of the linearisers gain controls.

Subtracting equation (A4.1a) from (A4.2a) gives:-

$$\overline{q_{eff_2}^2} - \overline{q_{eff_1}^2} = 2(1-k^2)\overline{u'v'} \quad . \quad (A4.5)$$

Combining equations (A4.3), (A4.4) and (A4.5):-

$$\frac{\overline{(E_{b_2} + e'_{b_2})^2}}{A_{L_2}^2} - \frac{\overline{(E_{b_1} + e'_{b_1})^2}}{A_{L_1}^2} = 2(1-k^2)\overline{u'v'} \quad . \quad (A4.6)$$

The mean components of the bridge voltages are arrived at in the following way. The effective cooling velocity can be expressed as the sum of the mean and fluctuating parts:-

$$q_{eff} = q_m + q' \quad ;$$

hence

$$\overline{q_{eff}^2} = q_m^2 + \overline{q'^2} \quad .$$

It is clear from equations (A4.1) and (A4.2) that:-

$$q_{m_1}^2 = q_{m_2}^2 = \left(\frac{1+k^2}{2}\right) u^2 \quad .$$

Combining this result with equations (A4.3) and (A4.4) it is seen that:-

$$\frac{E_{b_1}^2}{A_{L_1}^2} = \frac{E_{b_2}^2}{A_{L_2}^2} = \left(\frac{1+k^2}{2}\right) u^2 \quad . \qquad \text{(A4.7)}$$

Clearly, if it is arranged that $A_{L_1} = A_{L_2}$, then the mean bridge voltages are equal. Hence equation (A4.6) becomes:-

$$\overline{u'v'} = \frac{\overline{e'_{b_2}^2} - \overline{e'_{b_1}^2}}{2A_L^2(1-k^2)} \quad . \qquad \text{(A4.8)}$$

Defining a new lineariser constant (for experimental convenience), $G_L = u/E_b$, it follows from equation (A4.7) that:-

$$G_L^2 = \frac{2}{A_L^2(1+k^2)} \quad .$$

Substituting for A_L in equation (A4.8), the final expression for the cross-correlation of the longitudinal and transverse fluctuating velocities becomes:-

$$\overline{u'v'} = \frac{G_L^2}{4} \frac{1+k^2}{1-k^2} \left(\overline{e'_{b_2}{}^2} - \overline{e'_{b_1}{}^2} \right) . \qquad \text{(A4.9)}$$

Expressions for the longitudinal and transverse fluctuating velocities can be derived by expanding equations (A4.1) and (A4.2) using a binomial series (with $\Phi = 45^o$). For the first configuration:-

$$q_{eff_1} \doteq \frac{u}{\sqrt{2}} \left[1 + \tfrac{1}{2}k^2 + \frac{w'^2}{u^2} + \left(\frac{1+k^2}{2}\right) \left(\frac{u'^2}{u^2} + \frac{v'^2}{u^2} + \frac{2u'}{u} \right) \right.$$

$$\left. - (1-k^2) \left(\frac{v'}{u} + \frac{u'v'}{u^2} \right) \right] . \qquad \text{(A4.10)}$$

Considering only the fluctuating parts, it follows from equation (A4.3) that:-

$$\frac{e'_{b_1}}{A_L} = \frac{u}{\sqrt{2}} \left[\frac{w'^2}{u^2} + \left(\frac{1+k^2}{2}\right) \left(\frac{u'^2}{u^2} + \frac{v'^2}{u^2} + \frac{2u'}{u} \right) - (1-k^2) \left(\frac{v'}{u} + \frac{u'v'}{u^2} \right) \right] .$$

(A4.11)

Similarly, for the second configuration:-

$$\frac{e'_{b_2}}{A_L} = \frac{u}{\sqrt{2}} \left[\frac{w'^2}{u^2} + \left(\frac{1+k^2}{2} \right) + \left(\frac{u'^2}{u^2} + \frac{v'^2}{u^2} + \frac{2u'}{u} \right) + (1-k^2) \left(\frac{v'}{u} + \frac{u'v'}{u^2} \right) \right].$$

(A4.12)

Expressing A_L in terms of G_L and introducing the instantaneous sum and difference voltages so that:-

$$e'_s = e'_{b_2} + e'_{b_1}$$

and

$$e'_d = e'_{b_2} - e'_{b_1} \quad ,$$

it follows from equations (A4.11) and (A4.12) that:-

$$\overline{u'^2} = \frac{G_L^2 \, \overline{e'^2_s}}{4(1+k^2)} \qquad \text{(A4.13)}$$

and

$$\overline{v'^2} = \frac{G_L^2 \, \overline{e'^2_d} \, (1+k^2)}{4(1-k^2)^2} \qquad \text{(A4.14)}$$

to first order approximations.

FIG.A4.1 ORIENTATIONS OF HOT-WIRES IN x-y PLANE

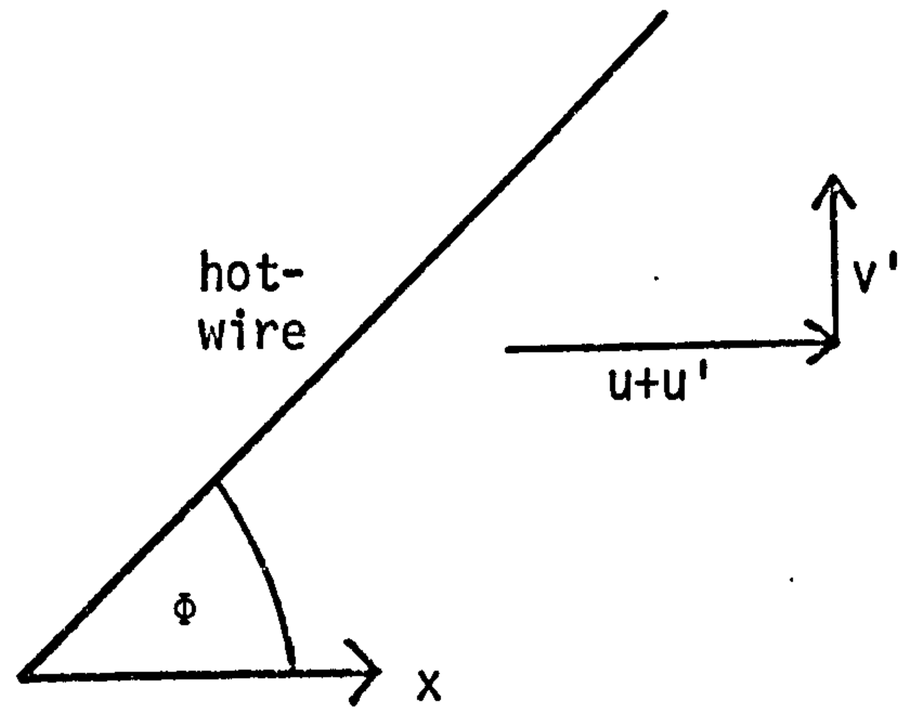

Configuration 1

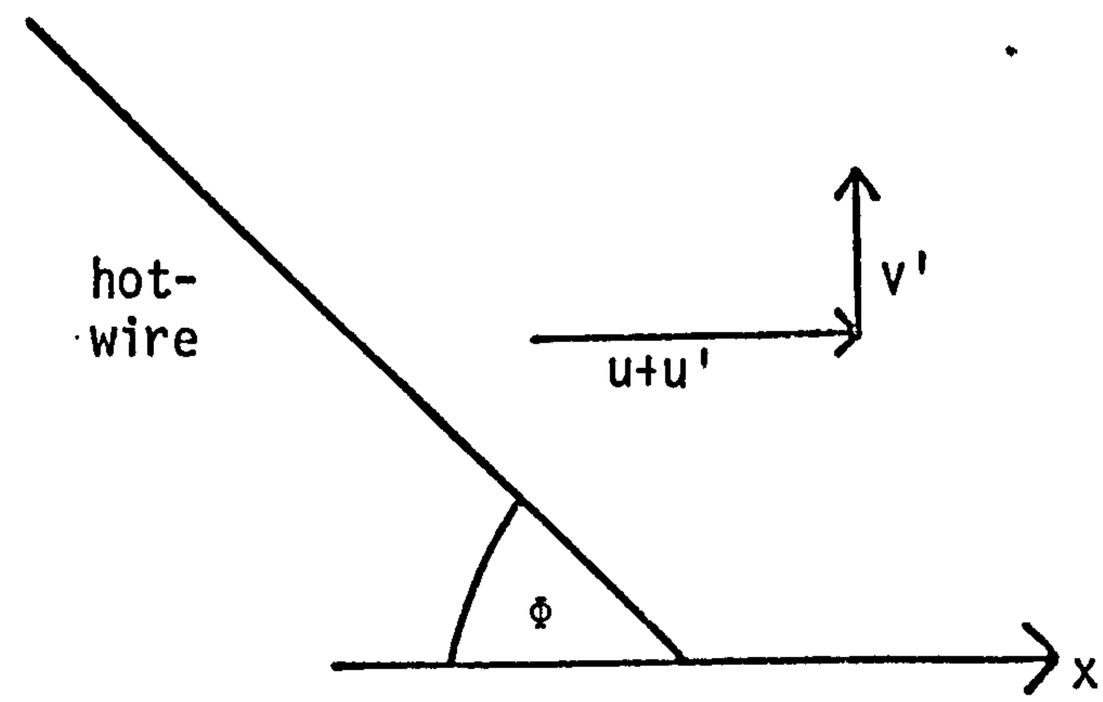

Configuration 2

APPENDIX 5

CALCULATION OF THE LENGTH SCALES OF THE TURBULENCE FROM THE MEASURED FREQUENCY SPECTRA

The computer program* used to calculate the length scales of the turbulence begins by calculating the frequency spectrum function. The only input data required for the whole program are the local velocity (m/s) and the readings from the level recorder (dB). The associated frequency is printed prior to each request for a decibel reading. The data is divided into six regions, each having a fixed interval in frequency:-

1) $20 \leqslant n \leqslant 100$ in steps of 10
2) $100 \leqslant n \leqslant 300$ in steps of 50
3) $300 \leqslant n \leqslant 1000$ in steps of 100
4) $1000 \leqslant n \leqslant 3000$ in steps of 500
5) $3000 \leqslant n \leqslant 10000$ in steps of 1000
6) $10000 \leqslant n \leqslant 18000$ in steps of 2000

where n is measured in Hz.

A least squares parabola is fitted to each of the six regions so that for the i'th region the spectrum function is represented by:-

$$F(n) = a_i + b_i n + c_i n^2 \quad , \tag{A5.1}$$

where a_i, b_i and c_i are the coefficients of the parabola. The quantity

$$\sum_{i=1}^{6} \int_{n_1}^{n_2} (a_i + b_i n + c_i n^2) dn$$

$\int_0^\infty F(n)\,dn = 1$

is then calculated and compared with unity (see equation (3.10)). The

---

* The program is written in TSS/8 BASIC.

limits of the integral, n_1 and n_2, represent the lowest and highest frequencies for the i'th region. Small adjustments are then made to the reference level (of the unfiltered signal) so that the above quantity is within approximately 1% of unity. The program then prints out the quantities $2\pi n/u$, $uF(n)/2\pi$, $F(n)$ and $n^2F(n)$ for each value of n.

The spatial correlation coefficient is:-

$$R_T = \int_0^\infty F(n) \cos \frac{2\pi n \Delta x}{u} \, dn \quad ,$$

which is approximately equal to

$$\sum_{i=1}^{6} \int_{n_1}^{n_2} (a_i + b_i n + c_i n^2) \cos \frac{2\pi n \Delta x}{u} \, dn$$

$$= \frac{u}{2\pi \Delta x} \sum_{i=1}^{6} \left\{ \left[a_i + b_i n + c_i n^2 - \frac{c_i u^2}{2\pi^2 \Delta x^2} \right] \sin \frac{2\pi n \Delta x}{u} \right.$$

$$\left. + \frac{u}{2\pi \Delta x} (b_i + 2c_i n) \cos \frac{2\pi n \Delta x}{u} \right\}_{n_1}^{n_2} \qquad \text{(A5.2)}$$

for a given value of Δx. This is printed for increasing values of Δx.

The value of Δx at which R_T is zero is calculated by parabolic interpolation and it is this value which is used to define the upper limit of the integration for the determination of the macro-scale (see equation (3.13)). A Simpson integration is used for the final calculations of the two length scales. A listing of the program is given at the end of this appendix.

PROGRAM LISTING

```
10 DIM F(37),N(37),S(37),A(6),B(6),C(6),R(70),D(5),T(5),E(70)
15 X=0.05\N(1)=20
16 S1=-0.05
17 P2=3.14159265
18 REM INPUT EXPERIMENTAL DATA
20 D5=10\PRINT "VEL(M/S)=";\INPUT U\U=U*100
25 FOR I=1 TO 9
30 PRINT "N(HZ)=";\PRINT N(I);\PRINT "S(DB)=";\INPUT S(I)
40 N(I+1)=N(I)+D5
45 B1=(S(I)-46)/20\B2=10↑B1
50 F(I)=(B2↑2)/(0.06*N(I))\NEXT I
55 M=9\D1=0\F1=0\G1=0\H1=0\J1=0\L1=0\P1=0
60 M1=1\M2=9\J=1
65 GOSUB 400
70 D5=50\N(10)=150
75 FOR I=10 TO 13
80 PRINT "N(HZ)=";\PRINT N(I);\PRINT "S(DB)=";\INPUT S(I)
85 N(I+1)=N(I)+D5\B1=(S(I)-46)/20\B2=10↑B1
90 F(I)=(B2↑2)/(0.06*N(I))\NEXT I
95 M=5\D1=0\F1=0\G1=0\H1=0\J1=0\L1=0\P1=0
100 M1=9\M2=13\J=2\GOSUB 400
110 D5=100\N(14)=400
115 FOR I=14 TO 20
120 PRINT "N(HZ)=";\PRINT N(I);\PRINT "S(DB)=";\INPUT S(I)
125 N(I+1)=N(I)+D5\B1=(S(I)-46)/20\B2=10↑B1
130 F(I)=(B2↑2)/(0.06*N(I))\NEXT I
135 M=8\D1=0\F1=0\G1=0\H1=0\J1=0\L1=0\P1=0
140 M1=13\M2=20\J=3\GOSUB 400
145 D5=500\N(21)=1500
150 FOR I=21 TO 24
155 PRINT "N(HZ)=";\PRINT N(I);\PRINT "S(DB)=";\INPUT S(I)
160 N(I+1)=N(I)+D5\B1=(S(I)-46)/20\B2=10↑B1
165 F(I)=(B2↑2)/(0.06*N(I))\NEXT I
170 M=5\D1=0\F1=0\G1=0\H1=0\J1=0\L1=0\P1=0
175 M1=20\M2=24\J=4\GOSUB 400
177 D5=1000\N(25)=4000
178 FOR I=25 TO 31
179 PRINT "N(HZ)=";\PRINT N(I);\PRINT "S(DB)=";\INPUT S(I)
180 N(I+1)=N(I)+D5\B1=(S(I)-46)/20\B2=10↑B1
181 F(I)=(B2↑2)/(0.06*N(I))\NEXT I
182 M=8\D1=0\F1=0\G1=0\H1=0\J1=0\L1=0\P1=0
183 M1=24\M2=31\J=5\GOSUB 400
184  D5=2000\N(32)=12000
186 FOR I=32 TO 36
188 PRINT "N(HZ)=";\PRINT N(I);\PRINT "S(DB)=";\INPUT S(I)
190 N(I+1)=N(I)+D5\B1=(S(I)-46)/20\B2=10↑B1
192 F(I)=(B2↑2)/(0.06*N(I))\NEXT I
194 M=6\D1=0\F1=0\G1=0\H1=0\J1=0\L1=0\P1=0
196 M1=31\M2=36\J=6\GOSUB 400
211 S6=0\GOSUB 600
212 REM S1 IS DECREMENT IN S(DB)TO SECURE INT.F(N)DN=1
215 PRINT
220 PRINT "  N","F(N)","N↑2 F(N)","2PIN/U","UF(N)/2PI"
221 PRINT "  HZ","SECS","SEC↑-1","CM↑-1","  CM"\PRINT
```

Continued.....

```
225 FOR I=1 TO 36
226 REM OUTPUT SPECTRAL DATA
230 PRINT N(I),F(I),((N(I)↑2)*F(I)),2*P2*N(I)/U,U*F(I)/(2*P2)\NEXT I
233 PRINT "   X(CM)","     R(X)"
235 PRINT\S3=0\FOR K=1 TO 58\S2=0
236 REM CALCULATE R(K)=CORRELATION FUNCTION
240 J=1\L=20\U1=100\GOSUB 500\S2=S2+S3
245 J=2\L=100\U1=300\GOSUB 500\S2=S2+S3
250 J=3\L=300\U1=1000\GOSUB 500\S2=S2+S3
255 J=4\L=1000\U1=3000\GOSUB 500\S2=S2+S3
260 J=5\L=3000\U1=10000\GOSUB 500\S2=S2+S3
261 REM START MACROSCALE CALCULATION ON LINE 269
262 J=6\L=10000\U1=20000\GOSUB 500\R(K)=S2+S3
265 PRINT X,R(K)\IF K>19 GOTO 266\X=X+0.05\X=X-1\GOTO 267
266 IF K>29 GOTO 267\X=X+0.2\X=X-1
267 X=X+1\NEXT K\GOTO 285
268 PRINT\PRINT "DATA POSN.","MACROSCALE(MM)"
269 E1=0.0166667*(S6+4*R(1)+R(2))
270 FOR K=1 TO 9\E1=E1+0.016667*(R(2*K)+4*R(2*K+1)+R(2*K+2))
271 PRINT (2*K+2),10*E1\NEXT K\G2=0
272 FOR K=10 TO 14\E1=E1+0.066667*(R(2*K)+4*R(2*K+1)+R(2*K+2))\E(K)=E1
273 PRINT (2*K+2),10*E1\IF R(2*K+2)<0 GOTO 275
274 GOTO 276
275 M1=K-3\M2=K\M=4\GOSUB 800
276 NEXT K
277 FOR K=15 TO 28\E1=E1+0.3333*(R(2*K)+4*R(2*K+1)+R(2*K+2))\E(K)=E1
278 PRINT (2*K+2),10*E1\IF R(2*K+2)<0 GOTO 280
279 GOTO 281
280 M1=K-3\M2=K\M=4\GOSUB 800
281 NEXT K\GOTO 900
282 REM CALCULATE MICROSCALE
285 E2=166.67*(4*N(15)↑2*F(15)+N(20)↑2*F(20))
290 E2=E2+166.67*(N(20)↑2*F(20)+4*N(21)↑2*F(21)+N(22)↑2*F(22))
295 E2=E2+333.33*(N(22)↑2*F(22)+4*N(24)↑2*F(24)+N(25)↑2*F(25))
300 FOR I=25 TO 29 STEP 2
305 E2=E2+333.33*(N(I)↑2*F(I)+4*N(I+1)↑2*F(I+1)+N(I+2)↑2*F(I+2))
306 NEXT I\FOR I=31 TO 33 STEP 2
307 E2=E2+667*(N(I)↑2*F(I)+4*N(I+1)↑2*F(I+1)+N(I+2)↑2*F(I+2))
310 NEXT I\PRINT 'MICROSCALE(MM)=";10*U/(2*P2*SQR(E2))
315 GOTO 268
320 GOTO 900
399 REM CALCULATE LEAST SQUARES PARABOLA TO FIT F(N) DATA
400 FOR I=M1 TO M2
405 D1=D1+N(I)\F1=F1+N(I)↑2\G1=G1+N(I)↑4
410 H1=H1+N(I)↑3\J1=J1+F(I)\L1=L1+N(I)*F(I)
415 P1=P1+F(I)*N(I)↑2\NEXT I
420 D3=(F1*G1-H1*H1)*M-(D1*G1-F1*H1)*D1+(D1*H1-F1*F1)*F1
425 N1=(F1*G1-H1*H1)*J1-(D1*G1-F1*H1)*L1+(D1*H1-F1*F1)*P1
430 N2=(F1*H1-D1*G1)*J1-(F1*F1-M*G1)*L1+(D1*F1-M*H1)*P1
435 N3=(D1*H1-F1*F1)*J1-(M*H1-D1*F1)*L1+(M*F1-D1*D1)*P1
440 A(J)=N1/D3\B(J)=N2/D3\C(J)=N3/D3
445 RETURN
```

Continued.....

```
499 REM CALCULATE FOURIER TRANSFORM INTEGRAL
500 I=1\D(I)=U1
505 A1=U/(2*P2*X)
510 A2=(A(J)+B(J)*D(I)+C(J)*D(I)↑2)*SIN(D(I)/A1)
515 A3=A1*(B(J)+2*C(J)*D(I))*COS(D(I)/A1)
520 T(I)=A2+A3-((U↑2)*C(J)/(2*(P2↑2)*(X↑2)))*SIN(D(I)/A1)
525 I=I+1\D(I)=L\IF I=2 GOTO 505
530 S3=(T(1)-T(2))*A1
535 RETURN
539 REM CALCULATE INTEGRAL UNDER F(N) CURVE
540 S5=A(J)*U1+B(J)*(U1↑2)/2+C(J)*(U1↑3)/3
545 S5=S5-(A(J)*L+B(J)*(L↑2)/2+C(J)*(L↑3)/3)
550 RETURN
599 REM ADJUST S(DB) TO ENSURE THAT INTEGRAL F(N)DN<1
600 J=1\L=20\U1=100\GOSUB 540\S6=S6+S5
605 J=2\L=100\U1=300\GOSUB 540\S6=S6+S5
610 J=3\L=300\U1=1000\GOSUB 540\S6=S6+S5
615 J=4\L=1000\U1=3000\GOSUB 540\S6=S6+S5
620 J=5\L=3000\U1=10000\GOSUB 540\S6=S6+S5
621 J=6\L=10000\U1=20000\GOSUB 540\S6=S6+S5\Q=Q+1
622 PRINT "INTEGRAL F(N)DN=";S6
625 GOTO 700
630 FOR I=1 TO 31\S(I)=S(I)+S1
635 B1=(S(I)-46)/20\B2=10↑B1
640 F(I)=(B2↑2)/(0.06*N(I))\NEXT I\S6=0
645 M=9\D1=0\F1=0\G1=0\H1=0\J1=0\L1=0\P1=0
650 M1=1\M2=9\J=1\GOSUB 400
655 M=5\D1=0\F1=0\G1=0\H1=0\J1=0\L1=0\P1=0
660 M1=9\M2=13\J=2\GOSUB 400
665 M=8\D1=0\F1=0\G1=0\H1=0\J1=0\L1=0\P1=0
670 M1=13\M2=20\J=3\GOSUB 400
675 M=5\D1=0\F1=0\G1=0\H1=0\J1=0\L1=0\P1=0
680 M1=20\M2=24\J=4\GOSUB 400
685 M=8\D1=0\F1=0\G1=0\H1=0\J1=0\L1=0\P1=0
690 M1=24\M2=31\J=5\GOSUB 400
695 GOTO 600
700 IF Q=1 GOTO 710
705 IF S1<0 GOTO 720\GOTO 725
710 IF S6>1 GOTO 630
715 S1=-S1\GOTO 630
720 IF S6<1 GOTO 750\GOTO 630
725 IF S6>1 GOTO 750\GOTO 630
750 RETURN
799 REM SUBROUTINE TO FIND MACROSCALE FOR ZERO R(X)
800 J=6\D1=0\F1=0\G1=0\H1=0\J1=0\L1=0\P1=0\G2=G2+1
801 IF G2>1 GOTO 820
805 FOR I=M1 TO M2\N(I)=R(2*I+2)\F(I)=E(I)\NEXT I
810 GOSUB 400\PRINT 'MACROSCALE(MM)=";(10*A(J))\PRINT
820 RETURN
900 END
```

APPENDIX 6

COMPUTER PROGRAM FOR PREDICTION OF TWO-DIMENSIONAL TURBULENT BOUNDARY-LAYERS

The program prints the values of the flow variables at the end of each step in the integration, given the starting values of C'_f and R_θ and the longitudinal distributions of U_∞ and dU_∞/dx.

The program firstly calculates the starting values of δ, Π and ω which must be compatible with the constants in the law of the wall (see Section 4.6). Starting with the energy method, the subroutine D02AHF, which integrates the system of equations (see Section 4.5) over one step interval in x, is called. This subroutine calls the auxiliary subroutine DERIVS to calculate the derivatives, which in turn calls the following subroutines:

INTVAL - this finds, from the input data, the intermediate values of U_∞ and dU_∞/dx at any value of x;

COMPARE, INTERP } auxiliary subroutines called by INTVAL;

F04ATF - this is called by DERIVS to solve algebraically the system of simultaneous equations; the solution set for the derivatives is returned to DERIVS.F04ATF is also called by INTERP to calculate the intermediate values of U_∞ and dU_∞/dx;

SHEARCOEF - this calculates the coefficients in G_{10} and G_{11} which are needed to find the shear stress and shear work integrals (see Section 4.4).

The integration proceeds until the maximum value of x is reached - when the process is restarted for the next method. The accuracy of the integration can be assessed by the value of the FORTRAN variable B2, which is the constant B in equation (4.60). This should be equal to 5 but in practice the step size is controlled to keep B2 to within a maximum of $\pm$ 0.1 of this value.

The following input data is required:-

FORTRAN SYMBOL	DESCRIPTION
RTHETO	starting value for R_θ
CFO	starting value for C'_f
XB(I)	array containing x values
UINF(I)	array containing U_∞ values
DUINDX(I)	array containing dU_∞/dx values
DX	step interval in x
NU, RHI	ν,h
RC2	C'/B' (equation (4.7))
N	maximum value of I
ORDER	order of matrix for Lagrange interpolation (a value of 3 is recommended).

At the end of each step in the integration the following is printed:

FORTRAN SYMBOL	DESCRIPTION
X	x
CF	C'_f

H1	H
RTHETA	R_θ
B2	B
DELTA	δ
OMEGA	ω
PI	π
UOO	u_o
CRATE	C_r (= constant)
ALPHA	α
Y1	αG_1 (equation (4.23))
DXEST	estimate of step size used for next interval.

The subroutine D02AHF employs an Adams method of integration and has been developed by The National Algorithms Group (U.K.), as has subroutine F04ATF. These subroutines are not listed in the FORTRAN 4 program which follows.

PROGRAM LISTING

```
      MASTER MAINPROG
      REAL K1,NU
      INTEGER ORDER,T,DD,JMAX(3)
      DIMENSION Y(4),G(4),Y0(4),EE(4),AA(4,15),BB(4,15)
      COMMON K1,DELTA,OMEGA,PI,UINF1,DUIND1,XB(50),UINF(50),DUINDX(50),N
     1,ORDER,METHOD,NU,ALPHA,CRATE,RH1,RC1,RC2
      EXTERNAL DERIVS
C READ INPUT DATA
      READ(5,1000) N,ORDER
      READ(5,1010) RH1
      READ(5,1010) RTHET0
      READ(5,1010) CF0
      READ(5,1010) RC2
      READ(5,1010) NU
      READ(5,1010) DX
      METHOD=1
      DO 5 I=1,N
      READ(5,1020) XB(I)
    5 CONTINUE
      DO 6 I=1,N
      READ(5,1020) UINF(I)
    6 CONTINUE
      DO 7 I=1,N
      READ(5,1020) DUINDX(I)
    7 CONTINUE
      X=XB(1)
      CRATE=-0.06
C CALCULATE INITIAL VALUES FOR DELTA,PI,OMEGA
      B1=5.0
      RC1=0.005
      ALPHA=0.018
      K1=0.41
   20 OMEGA=SQRT(CF0/2.0)
      UINF1=UINF(1)
      DUU0=(1.0/K1)*ALOG(RC2*RH1*OMEGA*UINF1/NU+EXP(-1.0*RC1*RH1*OMEGA*U
     1INF1/NU))
      PI=0.0
   22 PI1=(1.0/OMEGA)-(1.0/K1)*(ALOG(RTHET0/(G1(K1,PI)-OMEGA*G2(K1,PI)))
     1+2.0*PI)-B1+DUU0
      PI2=(1.0/K1)*((((1.0/K1)-OMEGA*(1.0/(K1**2.0))*(2.9/14*PI+3.0428))
     1/(G1(K1,PI)-OMEGA*G2(K1,PI)))-2.0)
      PI3=PI-(PI1/PI2)
      IF(ABS(PI3-PI).LT.0.0001) GOTO 23
      PI=PI3
      GOTO 22
   23 DELTA=EXP(K1*(1.0/OMEGA+DUU0-5.0-2.0*PI/K1)-ALOG(OMEGA*UINF1/NU))
C METHOD=1 ....ENERGY
C METHOD=2 ....ENTRAINMENT
C METHOD=3 ....MOMENT OF MOMENTUM
      I=METHOD
      IF(METHOD.EQ.1) GOTO 25
      IF(METHOD.EQ.2) GOTO 30
      WRITE(6,1050)
      GOTO 40
   25 WRITE(6,1060)
      GOTO 40
```

Continued.....

```
C STARTING VALUES
   30 WRITE(6,1070)
   40 WRITE(6,1030) DELTA,OMEGA,PI
      X=XB(1)
      UINF1=UINF(1)
      DUIND1=DUINDX(1)
      Y(1)=DELTA
      Y(2)=PI
      Y(3)=OMEGA
      Y(4)=ALPHA
      G(1)=0.01
      G(2)=0.01
      G(3)=0.01
      G(4)=0.01
      IFAIL=1
      DXEST=0.05*DX
      T=1
C INTEGRATE FOR STEP-LENGTH DX
   50 CALL D02AMF(X,Y,G,T,4,DX,DXEST,DERIVS,YW,EE,AA,BB,4,DD,IFAIL)
      IF(IFAIL.EQ.1) GOTO 56
      DELTA=Y(1)
      PI=Y(2)
      OMEGA=Y(3)
      IF(OMEGA.LT.0.0) GOTO 56
      ALPHA=Y(4)
      H1=(G1(K1,PI))/(G1(K1,PI)-OMEGA*(G2(K1,PI)))
      RTHETA=(UINF1/NU)*(DELTA*OMEGA*(G1(K1,PI)-OMEGA*(G2(K1,PI))))
      B2=(1.0/OMEGA)-(1.0/K1)*(ALOG(H1*RTHETA/G1(K1,PI))+2.0*PI)+(1.0/K1
     1)*ALOG(RC2*RH1*OMEGA*(UINF1/NU)+EXP(-1.0*RC1*RH1*UINF1*OMEGA/NU))
      CF=2.0*(OMEGA**2)
      BDIFF=ABS(B2-5.0)
      IF(BDIFF.GT.0.1) GOTO 56
      UW0=OMEGA*UINF1
      WRITE(6,1030) X,CF,H1,RTHETA,B2,DELTA,OMEGA,PI,UW0
      Y1=ALPHA*G1(K1,PI)
      WRITE(6,1080) CRATE,ALPHA,Y1,DXEST
55 IF(Y1.LT.0.0) GOTO 56
   IF(CF.LT.0.000001) GOTO 56
   IF(X.LT.XB(N)) GOTO 50
56 METHOD=METHOD+1
   IF(METHOD.GT.3) GOTO 2000
   ALPHA=0.018
   GOTO 20
1000 FORMAT(2(I2))
1010 FORMAT(F0.0)
1020 FORMAT(F0.0)
1030 FORMAT(F12.2,F12.6,F12.4,F12.1,F12.4,F12.3,F12.5,F12.5,F12.5)
1050 FORMAT(14H MOMENT METHOD)
1060 FORMAT(14H ENERGY METHOD)
1070 FORMAT(19H ENTRAINMENT METHOD)
1080 FORMAT(3F12.3,F15.9)
2000 STOP
     END
```

Continued.....

```
      SUBROUTINE DERIVS(C,Y,X)
C CALCULATES DERIVATIVES FOR ADAMS INTEGRATION SUBROUTINE DW2AHF
      REAL K1,NU
      INTEGER ORDER
      DIMENSION Y(4),A(4,4),C(4),B(4),AA(4,4),WKS1(4),WKS2(4)
      COMMON K1,DELTA,OMEGA,PI,UINF1,DUIND1,XB(50),UINF(50),DUINDX(50),N
     1,ORDER,METHOD,NU,ALPHA,CRATE,RM1,RC1,RC2
      DELTA=Y(1)
      PI=Y(2)
      OMEGA=Y(3)
      ALPHA=Y(4)
      CALL INTVAL(UINF1,DUIND1,X,XB,UINF,DUINDX,N,ORDER)
      A(1,1)=(G1(K1,PI)*OMEGA)-(G2(K1,PI)*(OMEGA**2.0))-OMEGA**2.0
      A(1,2)=OMEGA*DELTA/K1-(OMEGA**2.0)*DELTA*G3(K1,PI)
      A(1,3)=(G1(K1,PI)*DELTA)-2.0*G2(K1,PI)*DELTA*OMEGA-2.0*DELTA*OMEGA
      A(1,4)=0.0
      B(1)=OMEGA**2.0-(1.0/UINF1)*DUIND1*(3.0*G1(K1,PI)*OMEGA*DELTA-2.0*
     1G2(K1,PI)*(OMEGA**2.0)*DELTA-2.0*DELTA*OMEGA**2.0)
      A(2,1)=1.0/(K1*DELTA)
      A(2,2)=2.0/K1
      RUF1=EXP(-1.0*RC1*OMEGA*RM1*UINF1/NU)
      RUFCOR=(RC1*RUF1-RC2)/(K1*RC2*OMEGA+K1*RUF1/(RM1*UINF1/NU))
      A(2,3)=1.0/(OMEGA**2.0)+1.0/(OMEGA*K1)+RUFCOR
      A(2,4)=0.0
      B(2)=(-1.0/(K1*UINF1))*DUIND1*(1.0+RUFCOR*K1*OMEGA)
      IF(METHOD.EQ.1) GOTO 10
      IF(METHOD.EQ.2) GOTO 20
      GOTO 30
C ENERGY METHOD
   10 A(3,1)=OMEGA*(G1(K1,PI)-1.5*OMEGA*G2(K1,PI)+(OMEGA**2.0)*G4(K1,PI)
     1)
      A(3,2)=OMEGA*DELTA*((1.0/K1)-1.5*OMEGA*G3(K1,PI)+(OMEGA**2.0)*G5(K
     11,PI))
      A(3,3)=DELTA*(G1(K1,PI)-3.0*OMEGA*G2(K1,PI)+3.0*(OMEGA**2.0)*G4(K1
     1,PI))
      A(3,4)=0.0
      CALL SHEARCOEF(K1,PI,C1,C2,C3,C4,C5,ALPHA)
      B(3)=OMEGA**2.0+(OMEGA**3.0)*(G11(K1,PI,C3,C4,C5))-(DELTA*OMEGA/UI
     1NF1)*DUIND1*(3.0*G1(K1,PI)-4.5*OMEGA*G2(K1,PI)+3.0*(OMEGA**2.0)*G4
     11(K1,PI))
      GOTO 40
C ENTRAINMENT METHOD
   20 A(3,1)=(1.0-G1(K1,PI)*OMEGA)
      A(3,2)=-1.0*OMEGA*DELTA/K1
      A(3,3)=-1.0*G1(K1,PI)*DELTA
      A(3,4)=0.0
      B(3)=(1.0/UINF1)*(G1(K1,PI)*OMEGA*DELTA-DELTA)*DUIND1+1410.0*((K1*
     1G1(K1,PI)*OMEGA)**3)*OMEGA
      IFAIL=0
      GOTO 40
C MOMENT OF MOMENTUM METHOD
```

Continued.....

```
30  A(3,1)=OMEGA*(2,0*G6(K1,PI)-OMEGA*G7(K1,PI))
    A(3,2)=OMEGA*DELTA*(0,3/K1-OMEGA*G8(K1,PI))
    A(3,3)=DELTA*(G6(K1,PI)-OMEGA*G9(K1,PI))
    A(3,4)=0,0
    CALL SHEARCOEF(K1,PI,C1,C2,C3,C4,C5,ALPHA)
    B(3)=(-1,0/UINF1)*DUIND1*(4,0*G6(K1,PI)-OMEGA*G9(K1,PI))*OMEGA*DEL
   1TA+(OMEGA**2,0)*(G10(K1,PI,C1,C2))
40  IFAIL=0
    A(4,1)=UINF1*OMEGA*G1(K1,PI)
    A(4,2)=UINF1*OMEGA*DELTA/K1
    A(4,3)=UINF1*DELTA*G1(K1,PI)
    A(4,4)=OMEGA*DELTA*UINF1*G1(K1,PI)/ALPHA
    B(4)=CRATE*UINF1*(1,0-(0,018/ALPHA))-OMEGA*DELTA*G1(K1,PI)*DUIND1
   50 CALL F04ATF(A,4,B,4,C,AA,4,WKS1,WKS2,IFAIL)
    RETURN
    END

    SUBROUTINE SHEARCOEF(K1,PI,C1,C2,C3,C4,C5,ALPHA)
C   THIS SUBROUTINE FINDS THE COEFFICIENTS C1,C2,C3,C4 AND C5
C WHICH ARE NEEDED IN ORDER TO CALCULATE THE G10 AND G11
C FUNCTIONS APPEARING IN THE SHEAR STRESS AND DISSIPATION INTEGRALS
    REAL K1
    A=K1
    Y1=ALPHA*G1(K1,PI)
    X=0,001
    XJ=0,1
    K=1
    I=3
30  I1=I
    E1=A*(1,0-2,0*X)*(X**2,0-X**3,0)-(A*(X-X**2,0)-Y1)*(2,0*X-3,0*X**2
   1,0)
    E2=(2,0*X-4,0*X**3,0)*(X**2,0-X**3,0)-(X**2,0-X**4,0)*(2,0*X-3,0*X
   1**2,0)
    E=E1/E2
    D1=A*(1,0-2,0*X)*(X**2,0-X**3,0)-E*(2,0*X-4,0*X**3,0)*(X**2,0-X**3
   1,0)
    D=D1/((2,0*X-3,0*X**2,0)*(X**2,0-X**3,0))
    C=-A-E-D
    R=A+2,0*C+3,0*D+4,0*E
    R1=ABS(R)
    IF(R1,LT,0,00001) GOTO 300
    K=K+1
    IF(K,GT,2) GOTO 110
    I1=IFIX(SIGN(1,0,R))
110 I=IFIX(SIGN(1,0,R))
    IF(I,EQ,I1) GOTO 120
    GOTO 130
120 X=X+XJ
    GOTO 30
130 XJ=-XJ/10,0
    X=X+XJ
    GOTO 30
300 C1=0,9167*K1+(0,4*C+0,23333*D+0,1548*E)
    C2=K1+(0,6*C+0,4*D+0,2857*E)
    C3=0,91905*C+0,3738*D+0,20476*E+0,1*K1
    C4=1,88571*C+1,05714*D+0,65714*E+2,0*K1
    C5=1,37143*C+0,8515*D+0,57142*E+2,4*K1
    RETURN
    END
```

Continued.....

```
      SUBROUTINE INTVAL(UINF1,DUIND1,X,XB,UINF,DUINDX,N,ORDER)

C INTVAL IS A LAGRANGE INTERPOLATION SUBROUTINE TO FIND INTERMEDIATE
C VALUES OF UINF1 AND DUIND1 FOR A GIVEN VALUE OF X AS REQUIRED BY THE
C AUXILIARY SUBROUTINE DERIVS WHICH FINDS THE DERIVATIVES,A TWO-
C DIMENSIONAL ARRAY OF ORDER EQUAL TO 'ORDER' IS FIRST SET UP AND SUB-
C SEQUENTLY SOLVED IN SUBROUTINE INTERP.
      INTEGER ORDER
      DIMENSION XB(N),UINF(N),DUINDX(N),C(15)
      CALL COMPARE(X,XB,N1,N,ORDER)
      CALL INTERP(XB,UINF,N,C,ORDER,N1)
      UINF1=0.0
      DO 10 I=1,ORDER
      UINF1=UINF1+C(I)*X**(FLOAT(I-1))
   10 CONTINUE
      CALL INTERP(XB,DUINDX,N,C,ORDER,N1)
      DUIND1=0.0
      DO 20 I=1,ORDER
      DUIND1=DUIND1+C(I)*X**(FLOAT(I-1))
   20 CONTINUE
      RETURN
      END
```

Continued.....

```
      SUBROUTINE COMPARE(X,XB,N1,N,ORDER)

C COMPARE WILL FIND THE DIFFERENCES BETWEEN X AND THE TABULATED DATA VAL-
C UES OF X(=XB).THE MINIMUM VALUE OF THE RESULTANT ONE-DIMENSIONAL ARRAY
C DIFF(I) IS THEN FOUND AND THE CORRESPONDING ARRAY SUBSCRIPT IS PUT
C EQUAL TO N1.N1 IS ADJUSTED IF NECESSARY TO ENSURE IT IS CENTRAL.THIS
C OCCURS WHEN N1 IS LESS THAN (ORDER+1)/2 OR GREATER THAN N-(ORDER+1)/2

      INTEGER ORDER
      DIMENSION XB(N),DIFF(50)
C N1 IS SUBSCRIPT FOR XB SUCH THAT X IS NEAREST TO XB
      DO 5 I= 1,N
      DIFF(I)=ABS(X-XB(I))
    5 CONTINUE
      J=1
   10 I=J
      J=J+1
   15 IF(J.GT.N) GOTO 100
      IF(DIFF(I).GT.DIFF(J)) GOTO 10
      J=J+1
      GOTO 15
  100 N1=I
      IF(N1.LT.((ORDER+1)/2)) GOTO 120
  110 GOTO 130
  120 N1=(ORDER+1)/2
  130 IF(N1.GT.(N-(ORDER+1)/2)) GOTO 150
  140 GOTO 160
  150 N1=N-(ORDER+1)/2+1
  160 RETURN
      END
```

Continued.....

```
      SUBROUTINE INTERP(XB,B,N,C,ORDER,N1)

C INTERP CALCULATES THE ELEMENTS OF THE TWO-DIMENSIONAL MATRIX AS RE-
C QUIRED BY THE LAGRANGE INTERPOLATION METHOD.THE MATRIX EQUATION IS
C THEN SOLVED BY CROUT'S FACTORISATION METHOD(NAG SUBROUTINE F04ATF)AND
C THE SOLUTION MATRIX RETURNED TO INTVAL TO CALCULATE THE INTERMEDIATE
C VALUES OF UINF1 AND DUIND1.

      INTEGER ORDER
C B EQUALS EITHER UINF(N) OR DUINDX(N)
C (ORDER IS ORDER OF MATRIX FOR LAGRANGE INTERPOLATION)
C ORDER MUST BE ODD
      DIMENSION XB(N),B(N),C(ORDER),XA(15,15),WKS1(15)
      DIMENSION WKS2(15),WKS3(15,15),BA(15)
      DO 10 I=1,ORDER
      DO 10 J=1,ORDER
      XA(I,J)=XB(N1-(ORDER-1)/2-1+I)**(FLOAT(J-1))
   10 CONTINUE
      IFAIL=0
      DO 20 I=1,ORDER
      BA(I)=B(N1-(ORDER-1)/2-1+I)
   20 CONTINUE
      CALL F04ATF(XA,15,BA,ORDER,C,WKS3,15,WKS1,WKS2,IFAIL)
      IF(IFAIL.EQ.0) GOTO 30
      WRITE(6,100) IFAIL
  100 FORMAT(I2)
      STOP
   30 RETURN
      END
```

Continued.....

```
FUNCTION G1(K1,PI)
REAL K1
G1=(PI+0,91667)/K1
RETURN
END

FUNCTION G2(K1,PI)
REAL K1
G2=(1,0/(K1**2,0))*(1,4857*PI**2,0+3,0428*PI+1,9123)
RETURN
END

FUNCTION G3(K1,PI)
REAL K1
G3=(1,0/(K1**2,0))*(2,9714*PI+3,0428)
RETURN
END

FUNCTION G4(K1,PI)
REAL K1
G4=(1,22857*PI**3,0+4,04742*PI**2,0+5,40835*PI+2,93879)/(K1**3,0)
RETURN
END

FUNCTION G5(K1,PI)
REAL K1
G5=(3,68571*PI**2,0+8,09483*PI+5,40835)/(K1**3,0)
RETURN
END

FUNCTION G6(K1,PI)
REAL K1
G6=(0,2+0,3*PI)/K1
RETURN
END

FUNCTION G7(K1,PI)
REAL K1
G7=(0,021M914+1,589524*PI+0,5*PI**2,0)/(K1**2,0)
RETURN
END

FUNCTION G8(K1,PI)
REAL K1
G8=(1,287619+0,842857*PI)/(K1**2,0)
RETURN
END

FUNCTION G9(K1,PI)
REAL K1
G9=(0,432044+2,8M2381*PI+0,842857*PI**2,0)/(K1**2,0)
RETURN
END
```

Continued.....

```
FUNCTION G10(K1,PI,C1,C2)
REAL K1
G10=(C1+C2*PI)/K1
RETURN
END

FUNCTION G11(K1,PI,C3,C4,C5)
REAL K1
G11=(C3+C4*PI+C5*PI**2.0)/(K1**2.0)
RETURN
END
FINISH
```

APPENDIX 7

COMPUTER PROGRAM FOR ANALYSIS OF SURFACE PROFILES

The input data correspond to an array of X,Y co-ordinates measured with respect to a rectangular 'window' (see Section 5.2). The co-ordinates correspond to the actual surface profiles and distances are measured in microns. A maximum of 1050 data points can be entered into the program (although this can be increased by suitable modification to the DIMENSION statement) although after interpolating the data to correspond to equal X intervals the final number of points used in the analysis is 1001.

The analysis is performed for three different cut-off wavelengths: 50000, 10000 and 2000 microns. The following is a list of the FORTRAN names used in the output:-

FORTRAN NAME	DESCRIPTION
HN(K)	ordinate corresponding to the top of the K'th class interval divided by the class interval.
P(K)	probability density
PCUML(K)	cumulative probability
HNM(K)	normalised height from mean
SLOPE1	average slope based on sampling interval = CORLEN

SLOPE	average slope based on sampling interval = 50 microns
PTV	peak-to-valley height
TENPTH	ten-point height
CLA	centre-line average height
S	standard deviation
PL	maximum peak from mean
SV	minimum valley from mean
CORLEN	correlation length
PRCAV	average radius of curvature of peaks
VRCAV	average radius of curvature of valleys
PPERMT	number of peaks per metre (sampling interval = 50 microns)
FLAT	kurtosis
SKEW	skewness
LAMDAC	cut-off wavelength

A listing of the FORTRAN 4 program follows.

PROGRAM LISTING

```
      MASTER TOPOG
      REAL MAX,MIN,LAG(120),MX(10),MN(10),MPX(50),MPY(50)
      DIMENSION X(1050),Y(1050),XM(1050),YM(1050),C(120),P(50),PCUML(50)
     1,F(50),HN(50),HNM(50),D(50),E(50),AP(50),BP(50),CP(50),XLP(1450),Y
     1LP(1050)
         LAMDAC=50000
         DX=50.0
         XA=0.0
         I=1
         X(I)=XA
       2 READ (5,1000) X1,Y1
       5 READ (5,1000) X2,Y2
         IF (X2.EQ.X1) GOTO 5
         IF (X2.GT.XA) GOTO 20
      10 X1=X2
         Y1=Y2
         GOTO 5
      20 Y(I)=Y1+(X(I)-X1)*(Y1-Y2)/(X1-X2)

C Y(I) CORRESPONDS TO EQUAL X VALUES(LINEAR INTERPOLATION)

         XA=XA+DX
         IF(XA.GT.50000.0) GOTO 30
         I=I+1
         X(I)=XA
         IF (XA.GT.X2) GOTO 10
         GOTO 20
      25 GOTO 30
      30 DO 35 I=1,1001
      35 CONTINUE
         A1=0.0
         A2=0.0
         A3=0.0
         A4=0.0
         DO 40 I=1,1001

C CALCULATE LEAST SQUARES STRAIGHT LINE THROUGH DICON COORDINATES
C AFTER PROCESSING FOR EQUAL X INTERVALS

         A1=A1+X(I)
         A2=A2+X(I)**2
         A3=A3+X(I)*Y(I)
         A4=A4+Y(I)
      40 CONTINUE
         A=(A1*A4-1001.0*A3)/(A1**2-1001.0*A2)
         B=(A1*A3-A4*A2)/(A1**2-1001.0*A2)
```

Continued.....

```
C FACTOR ADJUSTS COORDINATES FOR TILT OF MEAN LINE

      FACTOR=COS(ATAN(A))
      V=0.0
      SKEW=0.0
      FLAT=0.0
      CLA=0.0
      MAX=0.0
      MIN=0.0
      DO 50 I=1,1001
      XM(I)=X(I)/FACTOR
      YM(I)=FACTOR*(Y(I)-B-(A*X(I)))
      V=V+YM(I)**2
      SKEW=SKEW+YM(I)**3
      FLAT=FLAT+YM(I)**4
      CLA=CLA+ABS(YM(I))
      IF(YM(I).LT.MAX) GOTO 45

C CALCULATE HIGHEST PEAK AND LOWEST VALLEY

      MAX=YM(I)
   45 IF(YM(I).GT.MIN) GOTO 50
      MIN=YM(I)
   50 CONTINUE
      PL=MAX
      SV=MIN
      V=V/1001.0
      S=SQRT(V)
      SKEW=SKEW/(1001.0*(S**3))
      FLAT=FLAT/(1001.0*(S**4))
      CLA=CLA/1001.0
      PTV=ABS(MAX-MIN)
      CLASIN=PTV/30.0
C NEXT SEGMENT CALCULATES AUTOCOVARIANCE FUNCTION

   90 J=1
      I=1
      J1=I+J
      C(J)=0.0
   95 C(J)=C(J)+YM(I)*YM(J1)
      I=I+1
      J1=I+J
      IF(I.GT.(1001-J)) GOTO 100
      GOTO 95
  100 C(J)=C(J)/(FLOAT(I))
      J=J+1
      IF(J.GT.100) GOTO 110
      I=1
      J1=I+J
      C(J)=0.0
      GOTO 95
  110 CONTINUE
      DO 120 J=1,100
```

Continued.....

```
C AUTOCORRELATION FUNCTION IS NOW NORMALISED

      C(J)=C(J)/V
      LAG(J)=FLOAT(J)*DX/FACTOR
      IF (J.EQ.1) GOTO 120
      IF(C(J).LT.0.5.AND.C(J-1).GT.0.5) GOTO 115
      GOTO 120
  115 CORLEN=((0.5-C(J-1))*(LAG(J-1)-LAG(J))/(C(J-1)-C(J)))+LAG(J-1)
  120 CONTINUE

C HN(K) IS THE ORDINATE CORRESPONDING TO THE TOP
C OF THE CLASS INTERVAL DIVIDED BY STD.DEVIATION

      DO 130 K=1,30
      HN(K)=CLASIN*FLOAT(K)/S
      HNM(K)=(MIN/S)+HN(K)
      WRITE(6,1170) HN(K),P(K),PCUML(K),HNM(K)
  130 CONTINUE

C NEXT SEGMENT CALCULATES SLOPE OF PROFILE AND PEAK
C AND VALLEY CURVATURES AND DENSITIES

      NP=0
      NV=0
      SLOPE=0.0
      PEAKRC=0.0
      VALLRC=0.0
      DO 180 I=1,995
      SLOPE=SLOPE+ABS(-YM(I)+9.0*YM(I+1)-45.0*YM(I+2)+45.0*YM(I+4)-9.0*Y
     1M(I+5)+YM(I+6))/3000.0
      IF(YM(I+3).GT.YM(I+2).AND.YM(I+3).GT.YM(I+4)) GOTO 150
      IF(YM(I+3).LT.YM(I+2).AND.YM(I+3).LT.YM(I+4)) GOTO 160
      GOTO 180
  150 PEAKRC=PEAKRC+ABS(450000.0/(2.0*YM(I)-27.0*YM(I+1)+270.0*YM(I+2)-4
     190.0*YM(I+3)+270.0*YM(I+4)-27.0*YM(I+5)+2.0*YM(I+6)))
      NP=NP+1
      GOTO 180
  160 VALLRC=VALLRC+ABS(450000.0/(2.0*YM(I)-27.0*YM(I+1)+270.0*YM(I+2)-4
     190.0*YM(I+3)+270.0*YM(I+4)-27.0*YM(I+5)+2.0*YM(I+6)))
      NV=NV+1
  180 CONTINUE
      PPERMT=FLOAT(NP)/0.05
      VPERMT=FLOAT(NV)/0.05
      SLOPE=(ATAN(SLOPE/995.0))*57.3
      PRCAV=PEAKRC/FLOAT(NP)
      VRCAV=VALLRC/FLOAT(NV)
```

Continued.....

```
C THIS SECTION FINDS 5 HIGHEST AND LOWEST POINTS

      J=1
  200 J=J+1
      MX(J-1)=MAX
      MN(J-1)=MIN
      IF(J.EQ.6) GOTO 300
      MAX=0.0
      MIN=0.0
      DO 250 I=1,1001
  205 IF(YM(I).GE.MX(J-1)) GOTO 250
      IF(YM(I).LE.MN(J-1)) GOTO 250
      IF(YM(I).LT.MAX) GOTO 210
      MAX=YM(I)
  210 IF(YM(I).GT.MIN) GOTO 250
      MIN=YM(I)
  250 CONTINUE
      GOTO 200
  300 TENPTH=0.0
      DO 310 J=1,5
      TENPTH=TENPTH+MX(J)-MN(J)
  310 CONTINUE
      TENPTH=TENPTH/5.0
      J=1
  320 I=1

C M=NO.OF POINTS PER CORRELATION LENGTH

      M=IFIX(CORLEN/53.0)

C THIS SECTION CALCULATES SLOPES FOR DIFFERENT SAMPLE LENGTHS

  325 SLOPE1=0.0
  330 I1=I
      I2=I+M
      I3=I+2*M
      I4=I+4*M
      I5=I+5*M
      I6=I+6*M
      SLOPE1=SLOPE1+ABS(-YM(I1)+9.0*YM(I2)-45.0*YM(I3)+45.0*YM(I4)-9.0*Y
     1M(I5)+YM(I6))/(3400.0*FLOAT(M))
      I=I+M
      IF((I+6*M).GE.1001) GOTO 350
      GOTO 330
  350 I=I-M
      NO=(M+I-1)/M
      SLOPE1=(ATAN(SLOPE1/FLOAT(NO)))*57.3
      WRITE(6,2000) SLOPE1,SLOPE,PTV,TENPTH,CLA,S,PL
      WRITE(6,2010) SV,CORLEN,PRCAV,VRCAV,PPERMT,FLAT,SKEW,LAMDAC
      DO 410 I=1,1001
      X(I)=XM(I)
      Y(I)=YM(I)
  410 CONTINUE
```

Continued.....

```
C LAMDAC IS THE CUT-OFF LENGTH

      LAMDAC=LAMDAC/5
      IF (LAMDAC.LT.1000) GOTO 5000
  415 N=LAMDAC/50
      KD=1000/N
      DO 450 K=1,KD

C CALCULATE REGRESSION LINE FOR SUB-SAMPLES

      A1=0.0
      A2=0.0
      A3=0.0
      A4=0.0
      KE=1+(K-1)*N
      KF=1+K*N
      DO 420 I=KE,KF
      A1=A1+DX*FLOAT(I-KE)
      A2=A2+(DX*FLOAT(KE-I))**2
      A3=A3+Y(I)*(DX*FLOAT(I-KE))
      A4=A4+Y(I)
  420 CONTINUE
      FN=FLOAT(N)
      D(K)=(A1*A4-FN*A3)/(A1**2-FN*A2)
      E(K)=(A1*A3-A4*A2)/(A1**2-FN*A2)

C CALCULATE MID-POINTS OF SUB-SAMPLE REGRESSION LINES

      MPX(K)=FLOAT(LAMDAC/2+LAMDAC*(K-1))
      MPY(K)=E(K)+(D(K))*FLOAT(LAMDAC/2)
  450 CONTINUE
      KG=(1000/N)-2

C CALCULATE JOINING PARABOLAS
      DO 500 J=1,KG
      XP1=MPX(J)
      YP1=MPY(J)
      XP2=MPX(J+1)
      YP2=MPY(J+1)
      XP3=MPX(J+2)
      YP3=MPY(J+2)
      CP(J+1)=((YP1-YP2)*(XP2-XP3)-(YP2-YP3)*(XP1-XP2))/((XP1**2-XP2**2)
     1*(XP2-XP3)-(XP2**2-XP3**2)*(XP1-XP2))
      BP(J+1)=(YP2-YP3-(XP2**2-XP3**2)*CP(J+1))/(XP2-XP3)
      AP(J+1)=YP1-XP1*BP(J+1)-(CP(J+1))*XP1**2
  500 CONTINUE
```

Continued.....

```
C CALCULATE LOW-PASS OUTPUT

      J=2

C XLP AND YLP ARE ARRAYS HOLDING LOW PASS OUTPUT
C ORIGIN (0,0) IS L,H,S, OF REGRESSION LINE FOR 50000 CUT-OFF
      XLP(1)=0.0
      YLP(1)=E(1)
      DO 505 I=2,((N/2)+1)
      XLP(I)=XLP(I-1)+DX
      YLP(I)=E(1)+D(1)*XLP(I)
  505 CONTINUE
      DO 600 I=((N/2)+2),(1000-N/2)
      XLP(I)=XLP(I-1)+DX
      IF (J.GT.KG) GOTO 510
      IF(XLP(I).GT.MPX(J)) GOTO 520
  510 YLP(I)=AP(J)+BP(J)*X(I)+CP(J)*X(I)**2
      GOTO 600
  520 J=J+1
      GOTO 510
  600 CONTINUE
      I=(1000-N/2)
      XLP(I)=-50.0
      DO 610 I=(1001-(N/2)),1001
      XLP(I)=XLP(I-1)+DX
      YLP(I)=E(KO)+D(KO)*(XLP(I)+FLOAT(LAMDAC/2))
  610 CONTINUE
      DO 620 I=1,1001

C XM AND YM ARE ARRAYS HOLDING THE HIGH-PASS OUTPUT
C ORIGIN FOR HIGH PASS IS SAME FOR LOW PASS

      XM(I)=X(I)
      YM(I)=Y(I)-YLP(I)
  620 CONTINUE
      DO 630 I=1,1001
      Y(I)=YM(I)
  630 CONTINUE
      GOTO 35
 1000 FORMAT(1P2E19.10)
 1160 FORMAT(1H1,17HNORMALISED HEIGHT,5X,19HPROBABILITY DENSITY,5X,22HCU
     1MULATIVE PROBABILITY,5X,17HNORMALISED HEIGHT)
 1165 FORMAT(16H0FROM MIN VALLEY,61X,9HFROM MEAN)
 1170 FORMAT(4X,F6.3,16X,F6.4,22X,F6.4,19X,F6.3)
 2000 FORMAT(1X,7F8.2)
 2010 FORMAT(1X,7F8.2,I7)
 5000 STOP
      END
      FINISH
```

REFERENCES

1. Abbot, E.J. and Firestone, F.A. (1933). Specifying surface quality. Mechanical Engineering, Vol. 55, 1933, p.569.

2. Abell, C.J. (1974). Ph.D. Thesis, University of Melbourne, 1974, See also Perry, A.E. and Abell, C.J. (1977). Asymptotic similarity of turbulence structures in pipes. Jnl. Fluid Mechs., Vol. 79, Part 4, p.785.

3. Aertson, G. (1960). Sea trials on the sand-blasted 'Lubumbashi'. Trans. Roy. Instn. Nav. Arch., London. Vol. 102, p.174.

4. Allan, J.F. and Cutland, R.S. (1955). The effect of roughness on ship resistance. Trans. N-E Cst. Inst. Engrs., Shipb., Vol. 72, p.257.

5. Ambrose, H.H. (1954). The effect of character of surface roughness on velocity distribution and boundary resistance. University of Tennessee, Dept. of Civil Eng., Report to Office of Naval Research, Contract 811(03), 1954.

6. Arndt, R.E. and Ippen, A.T. (1967). Cavitation near surfaces of distributed roughnesses. Rep. 104, Hydro. Lab., Massachusetts Inst. Tech., Cambridge, Mess., 1967.

7. Bendat, J.S. and Piersol, A.G. (1966). Measurement and analysis of random data. John Wiley, London, 1966.

8. Bertelrud, A. (1976). Wind tunnel measurements in the boundary layer on a 3-D swept wing. The Aeronautical Research Institute of Sweden, Tech. Note AU-1191, Stockholm, 1976.

9. Betterman, D. Contribution a l'etude de la couche limite turbulente le long de plaques rugueuses. Centre National de la Recherche Scientifique, Paris, Rapport 65-6, 1965. Also: Int. of Heat and Mass Transfer, Vol. 9, 1966, p.153.

10. Bradley, J.N. and Thompson, I.R. (1951). Friction factors for large conduits flowing full. U.S. Bureau of Reclamation, Eng. Monographs, No. 7, 1951.

11. Bradshaw, P. and Ferriss, D.H. (1965). The response of a retarded equilibrium turbulent boundary layer to the sudden removal of pressure gradient. National Physical Lab., Aero. Div., Report 1145 - A.R.C. 26 758, 1965.

12. Bradshaw, P., Ferris, D.H. and Atwell, N.P. (1967). Calculation of boundary layer development using the turbulent energy equation. J. Fluid Mech., Vol. 28, 1967, p.593.

13. Brooke-Benjamin, T. (1960). Effects of a flexible boundary on hydrodynamic stability. J. Fl. Mech., Vol. 9, pt. 4, p.513.

14. Bull, M.K. (1969). Velocity profiles of turbulent boundary layers. The Aero. J. of The Roy. Aero. Soc., Vol. 73, 1969, p.143.

15. Canham, H.J.S. and Lynn, W.M. (1961). The propulsive performance of a group of intermediate tankers. Trans. Instn. Nav. Arch., London, March 1961.

16. Cebeci, T., Smith, A.M.O. and Mosinskis, G. (1970). Solution of the incompressible turbulent boundary layer with heat transfer. J. Heat Transfer, Vol. 92, No. 1, 1970, p.133.

17. Champagne, F.H. (1965). Boeing Scientific Research Lab., Rep. No. 103, 1965.

18. Clauser, F.H. (1954). Turbulent boundary layers in adverse pressure gradients. J. Aero. Sc., Vol. 21, 1954, p.91.

19. Clauser, F.H. (1956). The turbulent boundary layer. Advances in Applied Mechanics, Vol. 4, Academic Press Inc., N.Y. 1956, p.1.

20. Colebrook, C.F. (1939). Turbulent flow in pipes with particular reference to the transition region between smooth and rough pipe-laws. J. Ins. Civ. Engrs., Vol. 11, p.133.

21. Colebrook, C.F. and White, C.M. (1937). Experiments with fluid friction in roughened pipes. Proc. Roy. Soc., London, A161, p.367.

22. Coles, D.E. (1956). The law of the wake in the turbulent boundary layer. J. Fluid Mech., Vol. 1, Pt. 2, p.191.

23. Coles, D.E. (1968). Computation of turbulent boundary layers - 1968 AFOSR-IFP - Stanford Conference Proceedings, Vol. 2, Thermo-sciences Division, Stanford University, 1968.

24. Collis, D.C. and Williams, M.J. (1959). Two dimensional convection from heated wires at low.Reynolds numbers. J. Fluid Mech., Vol. 6, 1959, p.357.

25. Conn, J.F.C., Lackenby, H. and Walker, W.P. (1953). B.S.R.A. resistance experiments on the 'Lucy Ashton'. Part II. The ship model correlation for the naked hull condition. Trans. Inst. Nav. Arch., London, Vol. 95, p.350.

26. Cornish, J.J. III (1960). A universal description of turbulent boundary layer profiles with or without transpiration. Mississippi State University, Aerosphysics Department, Research Report 29, 1960.

27. Dean, R.B. (1976). A single formula for the complete velocity profile in a turbulent boundary layer. J. of Fluids Engineering, Dec. 1976, p.723.

28. Dirling, R. (1973). A method of computing rough-wall heat transfer rates on re-entry nose tips. A.I.A.A., Paper 73-763, July 1973.

29. Dvorak, F.A. (1969). Calculation of turbulent boundary layers on rough surfaces in pressure gradient. A.I.A.A. Journal, Vol. 7, 1969, p.1752.

✓30. El-Samanoudy, M.A. (1974). Turbulent boundary layers on an irregularly rough surface. Ph.D. Thesis, University of Liverpool, 1974.

31. Favre, A.J., Gaviglio, J.J. and Dumas, R.J. (1958). Further space-time correlations of velocity in a turbulent boundary layer. J. Fluid Mech., Vol. 3, 1958, p.344.

32. Fediaevsky, K. (1937). Turbulent boundary layer of an aerofoil. J. Aero. Sc., Vol. 4, 1937, p.491.

33. Finley, P.J., Khoo Chong Phoe and Chin Jeck Poh (1966). Velocity measurements in a thin turbulent water layer, La Houille Blanche, Vol. 21, 1966, p.713.

34. Froude, W. (1872). Report to the British Association for the Advancement of Science.

35. Froude, W. (1874). Experiments with H.M.S. Greyhound. Trans. Inst. Nav. Arch., London, Vol. 15, p.36.

36. Furuya, Y., Miyata, M. and Fujita, H. (1976). Turbulent boundary layer and flow resistance on plates roughened by wires. J. Fluids Eng., 1976, p.635.

37. Gadd, G.E. (1971). The approximate calculation of turbulent boundary layer development on ship hulls. Trans. Roy. Inst. Nav. Archs., Vol. 113, 1971, p.59.

38. Gawn, R.W.L. (1950). Fish propulsion in relation to ship design, Trans. Instn. Nav. Arch., London, Vol. 92, p.323.

39. Goddard, F.E. (1957). Effect of uniformly-distributed roughness on turbulent skin friction drag at supersonic speeds. Rept. 20-113, 1957, Jet Propulsion Laboratory, California Inst. of Technology.

40. Goldberg, P. (1966). Upstream history and apparent stress in turbulent boundary layers. M.I.T., Gas Turbine Lab., Rep. No. 85, May 1966.

41. Goldstein, S. (1958). Modern developments in fluid mechanics: an account of theory and experiment relating to boundary layers, turbulent motion and wakes. Vol. 1, p.254, Oxford, Clarendon Press, 1958.

42. Granville, P.S. (1958). The frictional resistance and turbulent boundary layer of rough surfaces. Report No. 1024, David Taylor Model Basin, Washington D.C., 1958.

43. Granville, P.S. (1972). The torque and boundary layer of rotating discs with smooth and rough surfaces and in drag reducing polymer solutions. N.S.R.D.C. Report 3711, 1972.

44. Granville, P.S. (1975). A modified law of the wake for turbulent shear flows. Naval Ship Research and Development Centre, Report 4639, 1975.

45. Grothues-Spork, H. (1968). The 1967 experimental voyages of the 'Meteor'. Part B. Resistance and propulsion. Jahrbuch der schiffbautechrischen Gesellschaft, Vol. 62, p.159.

46. Guerrero, J.L. and Black, J.T. (1972). Stylus tracer resolution and surface damage as determined by scanning electron microscopy. Trans. A.S.M.E., J. Eng. Ind., Vol. 94B, 1972, p.1087.

47. Hama, F.R. (1954). Boundary layer characteristics for smooth and rough surfaces. Trans. Soc. Nav. Arch. Mar. Engrs., Vol. 62, 1954, p.333.

48. Harrison, A.J.M. (1967). Boundary layer displacement thickness on flat plates. J. Hyd. Div., Proc. A.S.C.E., July 1967, HY4, p.79.

49. Head, M.R. (1960). Entrainment in the turbulent boundary layer. Aero. Res. Council, R. and M., No. 3152, H.M.S.O., 1960.

50. Head, M.R. and Patel, V.C. (1970). Improved entrainment method for calculating turbulent boundary layer development. Aero. Res. Council, R&M 3643, H.M.S.O., London, 1970.

51. Heisenberg, W. (1948). Zur statistischen theorie der turbulenz. Zs.f.Phys., Bd.124, Heft 7/12, 1948, p.628.

52. Hinze, J.O. (1959). Turbulence. McGraw-Hill, New York, 1959.

53. Hoyt, J.W. (1972). The effect of additives on fluid friction. J. Bas. Eng., June 1972, p.258.

54. Hughes, G. (1954). Frictional and form resistance in turbulent flow and proposed formulation for use in model and ship correlation. Trans. Istn. Nav. Arch., London, Vol. 96, p.314.

55. Kempf, von G. (1929). New results obtained in measuring frictional resistance. Trans. Instn. Nav. Arch., London, Vol. 71, p.104.

56. Kempf, von G. (1937). Über den einfluss der rauhigkeit auf den widerstand von schiffen. Jb. schiffbautech. Ges., Vol.38, p.159.

57. King, L.V. (1915). Precision measurements of air velocity by means of the linear hot wire anemometer. Phil. Mag., Vol. 29, 1915, p.556.

58. Kjellström, B. and Hedberg, S. (1970). Calibration of a DISA hot-wire anemometer and measurements in a circular channel for confirmation of calibration. DISA Information, No. 9, 1970, p.8.

59. Kolmogoroff, A. (1941). The local structure of turbulence in incompressible viscous fluids for very large Reynolds numbers. Comp. Rend. Acad. Sci., URSS, Vol. 30, No. 4, Feb. 1941, p.301.

60. Kramer, M.O. (1960). Boundary layer stabilisation by distributed damping. J. Amer. Soc. Nav. Engrs., Vol. 72, No. 1, p.25.

61. Kramer, M.O. (1961). The dolphin's secret. J. Amer. Soc. Nav. Engrs., Vol. 73, No. 1, p.103.

62. Krogh, F.T. (1973). Algorithms for changing the step size used by a multi-step method. S.I.A.M. J. Numer. Anal., Vol. 10, 1973, p.949.

63. Kubo, M. (1964). Measurement and analysis of surface roughness based on the information theory. Acta Imeko, 1964, p.115.

64. Lackenby, H. (1937). Re-analysis of William Froude's experiments on surface friction and their extension in the light of recent experiments. Trans. Instn. Nav. Arch., London, Vol. 79, p.120.

65. Lackenby, H. (1962). The resistance of ships, with special reference to skin friction and hull surface condition. The thirty-fourth Thomas Lowe Gray Lecture, The Institution of Mechanical Engineers, L4/62, London.

66. Laufer, J. (1954). The structure of turbulence in fully-developed pipe flow. N.A.C.A. Report 1174, 1954 (formerly TN 2954).

67. Lennox, S.C. and Chadwick, M. (1970). Mathematics for engineers and applied scientists. Heinemann Educational Books, London, 1970, p.333.

68. Lewkowicz, A.K., Horlock, J.H., Hoadley, D. and Perkins, H.J. (1970). A family of integral methods for predicting turbulent boundary layers. A.I.A.A. Jnl., Vol. 8, No. 1, 1970, p.44.

69. Ludwieg, H. and Tillman, W. (1949). Investigation of the wall shearing stress in the turbulent boundary layer. N.A.C.A. TM 1285, 1950. Translated from Ing. Archiv., Vol. 17, p.288, 1949.

70. McDonald, H. (1966). On incompressible two-dimensional turbulent boundary layers. United Aircraft Research Laboratories, Rep. E110339-2, November, 1966.

71. McDonald, H. and Stoddart, J.A.P. (1965). On the development of the incompressible turbulent boundary layer. British Aircraft Corp., (Warton) Ltd., Ae 225, March 1965.

72. Millikan, C.B. (1938). A critical discussion of turbulent flows in channels and circular tubes. Proc. 5th Int. Congress of Applied Mechanics, 1938, p.386.

73. Millionshchikov, M.D., Subbotin, V.I., Ibragimov, M.Kh., Taranov, G.S. and Gomonov, I.P. (1974). Hydraulic drag in tubes having granular roughness. Soviet Atomic Energy, Vol. 36, No. 3, 1974, p.234.

74. Monzavi, M.T. (1972). Widerstandsgesetz auf statistischer basis für extreme natürliche rauhigkeiten in druckrohren. Aus dem Inst. für Hydraulik und Hydrologie der Technischen Hochschule Darmstadt, Technischer Bericht Nr. 8, 1972.

75. Moody, L.F. (1944). Friction factors for pipe flow. Trans. A.S.M.E., Vol. 66, 1944, p.671.

76. Moore, W.F. (1951). An experimental investigation of the boundary layer development along a rough surface. Ph.D. Thesis, State University of Iowa, 1951.

77. Moses, H.L. (1964). The behaviour of turbulent boundary layers in adverse pressure gradients. Gas Turbine Laboratory, Massachusetts Inst. of Technology, Report 73, 1964.

78. Musker, A.J., Lewkowicz, A.K. and Preston, J.H. (1976). Investigation of the effect of surface roughness of a ship on the wall friction, using a pipe flow technique. Liverpool University, Dept. of Mech. Eng., Rep. No. FM/24/76.

79. Musker, A.J. (1977). Tabulated experimental data for flow in pipes with irregularly-rough surfaces. Liverpool University, Dept. of Mech. Eng., Report No. FM/41/77.

80. Myers, N.O. (1962). Characterisation of surface roughness. Wear, Vol. 5, 1962, p.182.

81. Nash, J.F. and MacDonald, A.G.J. (1966). A calculation method for the incompressible turbulent boundary layer, including the effect of upstream history on the turbulent shear stress. N.P.L., Aero. Report 1234, ARC 29088, December 1966.

82. Nash, J.F. and MacDonald, A.G.J. (1967). The calculation of momentum thickness in a turbulent boundary layer at Mach numbers up to unity. CP 963, Aero. Res. Council, 1967.

83. Nash, J.R. (1965). Turbulent-boundary-layer behaviour and the auxiliary equation. Aero. Div., National Physical Laboratory, Report 1137, 1965.

84. Newman, B.G. (1950). Skin friction in a retarded turbulent boundary layer near separation. Commonwealth of Australia, Dept. of Supply, Aero. Res. Labs., Rep. A.73, Melbourne, Nov. 1950.

85. Nikuradse, J. (1933). Strömungsgesetze in rauhen rohren. Forsch Arb.Ing.Wes., No. 361.

86. O'Brien, M.P., Folsom, R.G. and Jonassen, F. (1939). Fluid resistance in pipes. Ind. and Eng. Chem.,Vol. 31, 1939, p.477.

87. Oka, S. and Kostić, Ž., (1971). Influence of wall proximity on hot-wire velocity measurements. Euromech 24 Colloquium, Liblice Castle, Czechoslovakia, April 1971. See also DISA Information, No. 13, 1972, p.29.

88. Oonishi, Y. (1966). Measurement of bearing curves of surface profiles. Bull. Japan Soc. Proc. Eng., Vol. 1, 1966, p.249.

89. Pai, S.I. (1953). On turbulent flow in circular pipes. Jnl. of the Franklin Inst., Vol. 20, 1953, p.337.

90. Patankar, S.V. and Spalding, D.B. (1970). Heat and mass transfer in boundary layers. 2nd Edition, Intertext Books, London, 1970.

91. Patel, V.C. (1965). Calibration of the Preston tube and limitations on its use in pressure gradients. J. Fluid Mech., Vol. 23, Part 1, p.185.

92. Payne, M.P. (1936). Historical note on the derivation of Froude's skin friction constants. Trans. Instn. Nav. Arch., London, Vol. 78, p.93.

93. Perry, A.E. and Joubert, P.N. (1963). Rough-wall boundary layers in adverse pressure gradients. J. Fluid Mech., Vol. 17, 1963, p.193.

94. Perry, A.E., Schofield, W.H. and Joubert, P.N. (1969). Rough wall turbulent boundary layers. J. Fluid Mech., Vol. 37, 1969, p.383.

95. Pletcher, R.H. (1970). On a solution for turbulent boundary layer flows with heat transfer, pressure gradients and wall suction or blowing. 4th Int. Heat Transfer Conf., Paris, Vol. 2, 1970.

96. Prandtl, L. (1933). See H. Schlichting, Boundary-layer theory, p.572. McGraw-Hill, 1968, 6th edition.

97. Prandtl, L. and Schlichting, H. (1934). Das widerstandsgesetz rauher platten. Werft, Reederei, Hafen 1-4, 1934.

98. Preston, J.H. and Norbury, J.F. (1960). The three-quarter radius flowmeter - a reassessment. Flow Measurement in Closed Conduits, Vol. 1, H.M.S.O., 1962.

99. Reason, R.E. (1944). Surface finish and its measurement. J. Inst. Prod. Engrs., Vol. 23, 1944, p.347.

100. Reason, R.E. (1956). Significance and measurement of surface finish. Part 2. How transducers affect instrument performance; how to select proper cutoff values. Grinding and Finishing, Vol. 2, No. 41, October 1956, p.32.

101. Reichardt, H. (1951). Z. angew. Math. Mech., Vol. 31, 1951, p.208.

102. Robertson, J.M., Burkhart, T.H. and Martin, J.D. (1965). A study of turbulent flow in rough pipes. Dept. Theoretical and Applied Mechanics, University of Illinois, Report No. 279, May 1965.

103. Ross, D. and Robertson, J.M. (1950). Shear stress in a turbulent boundary layer. J. Appl. Phys., Vol. 21, 1950, p.557.

104. Rotta, J.C. (1962). Turbulent boundary layers in incompressible flow, Progress in Aeronautical Sciences. Vol. II, Pergamon Press, 1962.

105. Rouse, H. (1942). Evaluation of boundary roughness. Proc. 2nd Hydraulics Conf., Bul. 27, State University of Iowa, Studies in Engineering, 1942, p.105.

106. Roy, J.F. (1975). Flow around rotating cylinders and frictional resistance of ships. Internal report, Institut de Recherches de la Construction Navale, Paris. Paper delivered at Euromech 61 conference on viscous flows over rough surfaces, Liverpool University, April 1975.

107. Sachdeva, R.C. (1973). The development of three-dimensional incompressible turbulent boundary layers. Ph.D. Thesis, Liverpool University, 1973.

108. Schlichting, H. (1936). Experimentelle untersuchungen zum rauhigkeitsproblem. Ing. Arch., 7, 1936, p.1.

109. Schoenherr, K.E. (1932). Resistance of flat surfaces. Trans. Soc. Nav. Arch., N.Y., Vol. 40, p.279.

110. Schubauer, G.B. and Klebanoff, P.S. (1951). Investigation of separation of the turbulent boundary layer, N.A.C.A. Report No. 1030.

111. Schultz-Grunow, F. (1940). Neues reibungswiderstandsgesetz für glatte platten. Luftfahrtforschung, Vol. 17, No. 8, p.239.

112. Shaw, M.C. and Peklenik, J. (1963). A light projection technique for studying surface topology. Ann. C.I.R.P., Vol. 12, 1963, p.93.

113. Shaw, R. (1960). The influence of hole dimensions on static pressure measurements. J. Fluid Mechs., Vol. 7, 1960, p.550.

114. Simpson, R.L. (1973). A general correlation of roughness density effects on the turbulent boundary layer. A.I.A.A. Jnl, Vol. 11, No. 2, p.242.

115. Singhal, A.K. and Spalding, D.B. (1975). Predictions of flows over rough surfaces. 'Euromech' Conference held at Liverpool University, 1975. Unpublished.

116. Spalding, D.B. (1961). A single formula for the law of the wall. J. App. Mech., Trans. A.S.M.E., Series E., Vol. 83, 1961, p.455.

117. Stewart, R.W. and Townsend, A.A. (1951). Similarity and self-preservation in isotropic turbulence. Phil. Trans. Roy. Soc., Vol. A243, 1951, p.359.

118. Stratford, B.S. (1959). An experimental flow with zero skin-friction throughout its region of pressure rise. J. Fluid Mech., Vol. 5, p. 17.

119. Straub, L.G., Bowers, C.E. and Pilch, M. (1960). Resistance to flow in two types of concrete pipe. St. Anthony Falls Hydraulic Laboratory, Univ. of Minnesota, Tech. Paper No. 22, Series B, 1960.

120. Szablewski, W. (1955). Wandnahe geschwindig Keitsverteilung turbulenter grenzschichtströmungen mit druckanstieg. Ing. Archiv., Vol. 23, p.295.

121. Tarasov, L.P. (1945). Relation of surface roughness readings to actual surface profile. Trans. A.S.M.E., Vol. 67, 1945, p.189.

122. Taylor, G.I. (1938). The spectrum of turbulence. Proc. Roy. Soc., London, A164, 1938, p.476.

123. Tchen, C.M. (1953). On the spectrum of energy in turbulent shear flow. Research paper RP 2388, Jnl. Research, National Bureau of Standards, Vol. 50, No. 1, Jan. 1953, p.51.

124. Telfer, E.V. (1960). The reconciliation of model data, measured mile results and service performance of ships. Trans. N.-E. Cst. Instn. Engrs. Shipb., Vol. 76, p.S105.

125. Tetervin, N. and Lin, C.C. (1951). A general integral form of the boundary layer equation for incompressible flow with an application to the calculation of the separation point of turbulent boundary layers. N.A.C.A. Report 1046, 1951.

126. Thompson, B.G.J. (1967). A new two-parameter family of mean velocity profiles for incompressible turbulent boundary layers on smooth walls. U.K. Aero. Res. Council, R&M No. 3463, 1967.

+113
= 301

127. Todd, F.H. (1951). Skin friction resistance and the effects of surface roughness. Trans. Soc. Nav. Arch., N.Y., Vol. 59, p.315.

128. Townes, H.W., Gow, J.L., Powe, R.E. and Weber, N. (1972). Turbulent flow in smooth and rough pipes. J. Basic Eng., June 1972, p.353.

129. Townes, H.W. and Sabersky, R.H. (1966). Experiments on the flow over a rough surface. Int. J. Heat and Mass Transfer, Vol. 9, 1966, p.729.

130. Townsend, A.A. (1960). The development of turbulent boundary layers with negligible wall stress. J. Fluid Mech., Vol. 8, p.143.

131. Truckenbrodt, E. (1952). Ein quadraturverfahren zur berechnung der laminaren und turbulenten reiburgsschicht bei ebener und rotationssymmetrischer strömung. Ing. -Arch., Vol. 20, 1952, p.211.

132. Van Driest, E.R. (1956). On turbulent flow near a wall. J. Aero. Sc., Vol. 23, 1956, p.1007.

133. Walklate, P., Heikal, M.R.F. and Hatton, A.P. (1977). Measurements and prediction of turbulence and heat transfer in the entrance region of a pipe. Proc. Instn. Mech. Engrs., Vol. 190, 1977, p.37.

134. Walz, A. (1961). Compressible turbulent boundary layers. Proceedings of the International Symposium of the National Scientific Research Centre. The Mechanics of Turbulence. Marseille, 1961. Published by Gordon and Breach, N.Y. and London, 1964.

135. Whitehouse, D.J. and Archard, J.F. (1970). The properties of random surfaces of significance in their contact. Proc. Roy. Soc., A316, 1970, p.97.

136. Williamson, J.B.P., Pullen, J. and Hunt, R.T. (1969). The shape of solid surfaces. Surface Mechanics, A.S.M.E., New York, 1969.

137. Willinkson, J.H. and Reinsch, C. (1971). Handbook for automatic computation. Vol. 2, Linear Algebra, Springer-Verlag, 1971, p.93.

138. Young, A.D. and Maas, J.N. (1936). The behaviour of a pitot tube in a transverse total pressure gradient. Aero. Res. Council. R&M 1770, 1936.

FIG. 2.1 MEAN VELOCITY DISTRIBUTION NEAR A SMOOTH WALL

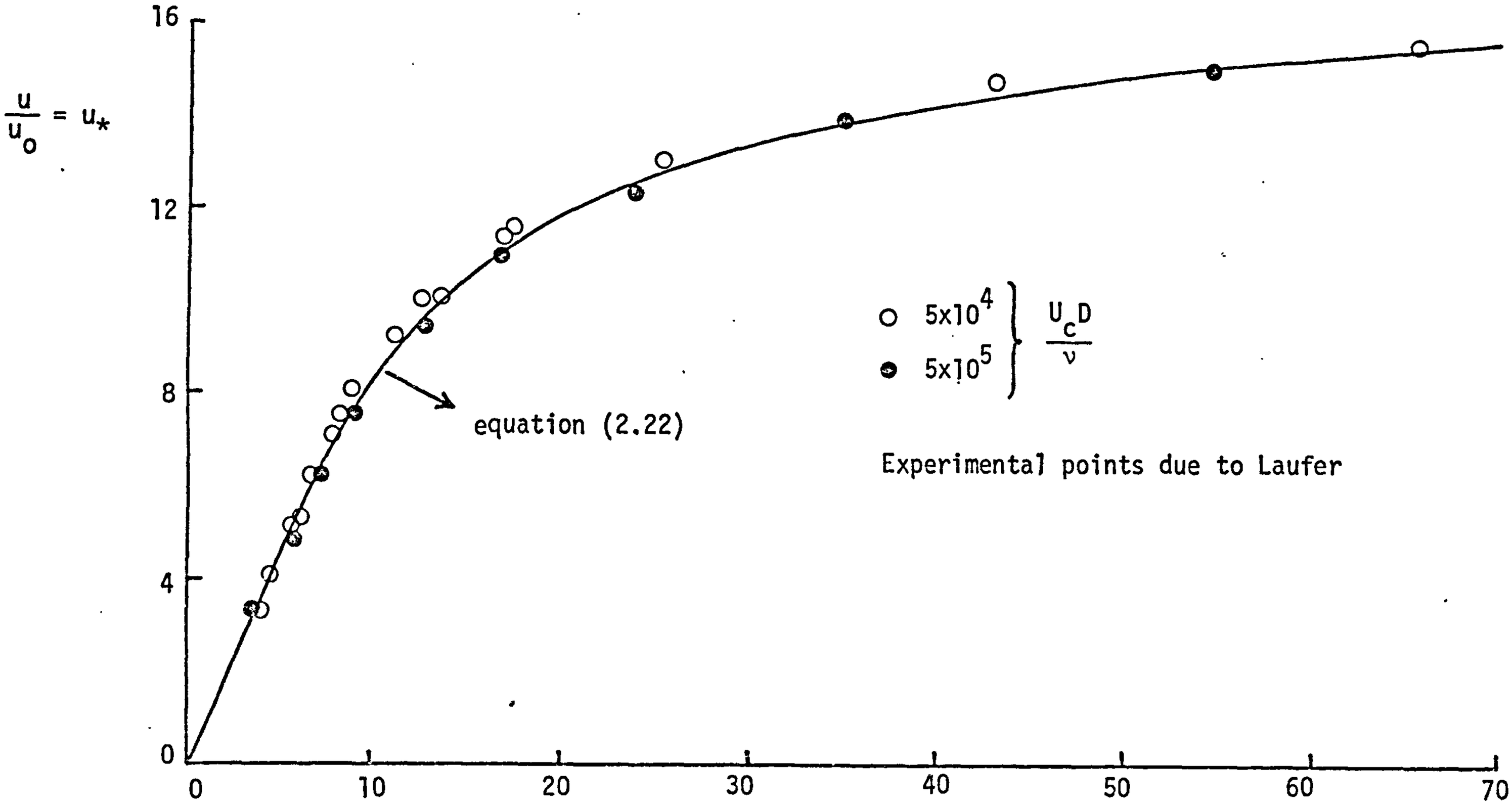

FIG. 2.2 COMPARISON OF ROUGHNESS FUNCTIONS FOR DIFFERENT SURFACES

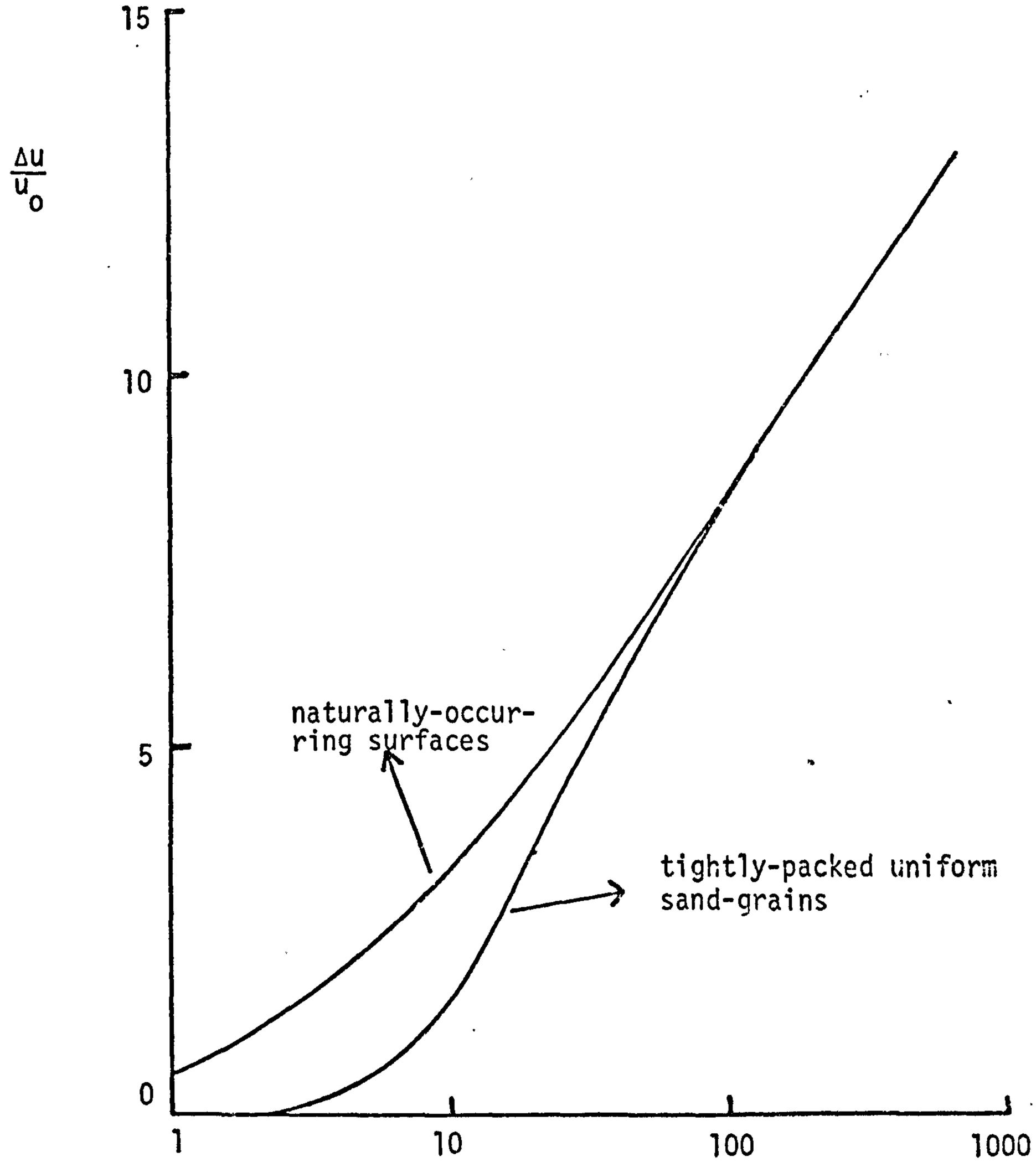

h_s = equivalent sand-grain roughness

FIG. 3.1 MANDREL WITH ONE OF RUBBER NEGATIVES USED IN MANUFACTURE OF SMALL PIPES

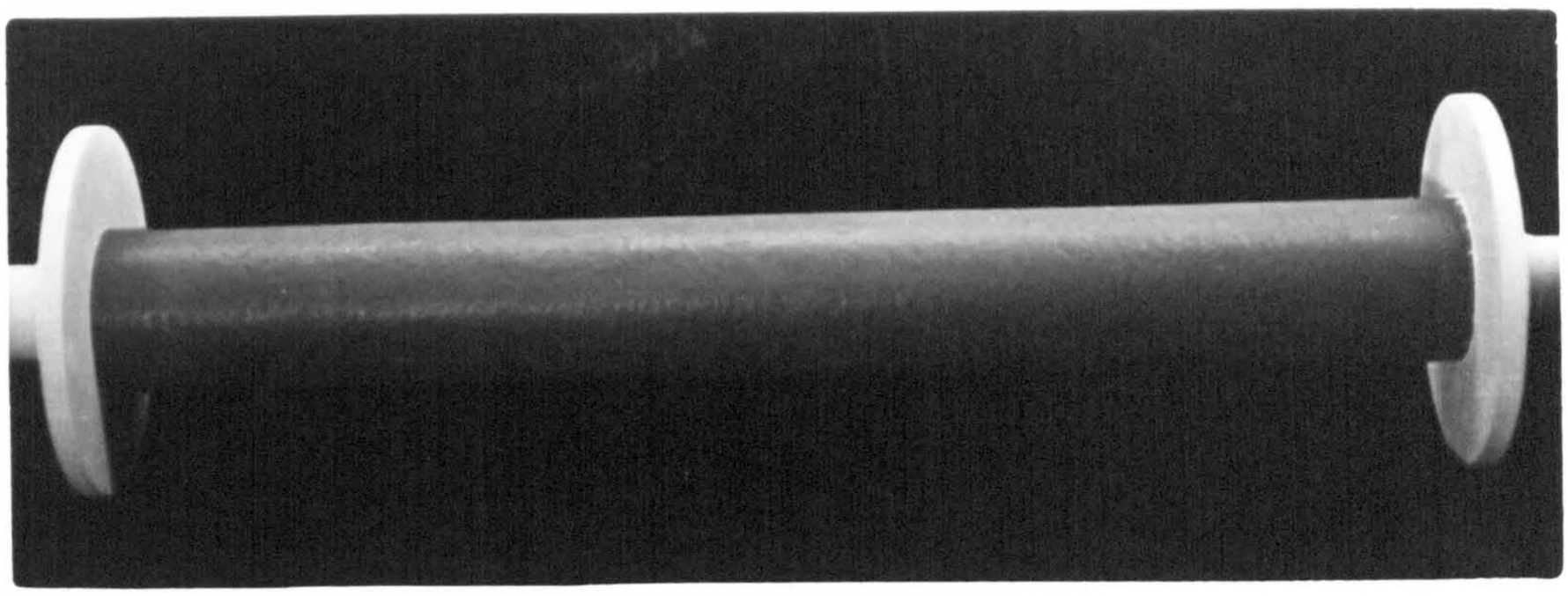

FIG. 3.2 COMPLETED SECTION FROM ONE OF SMALL PIPES

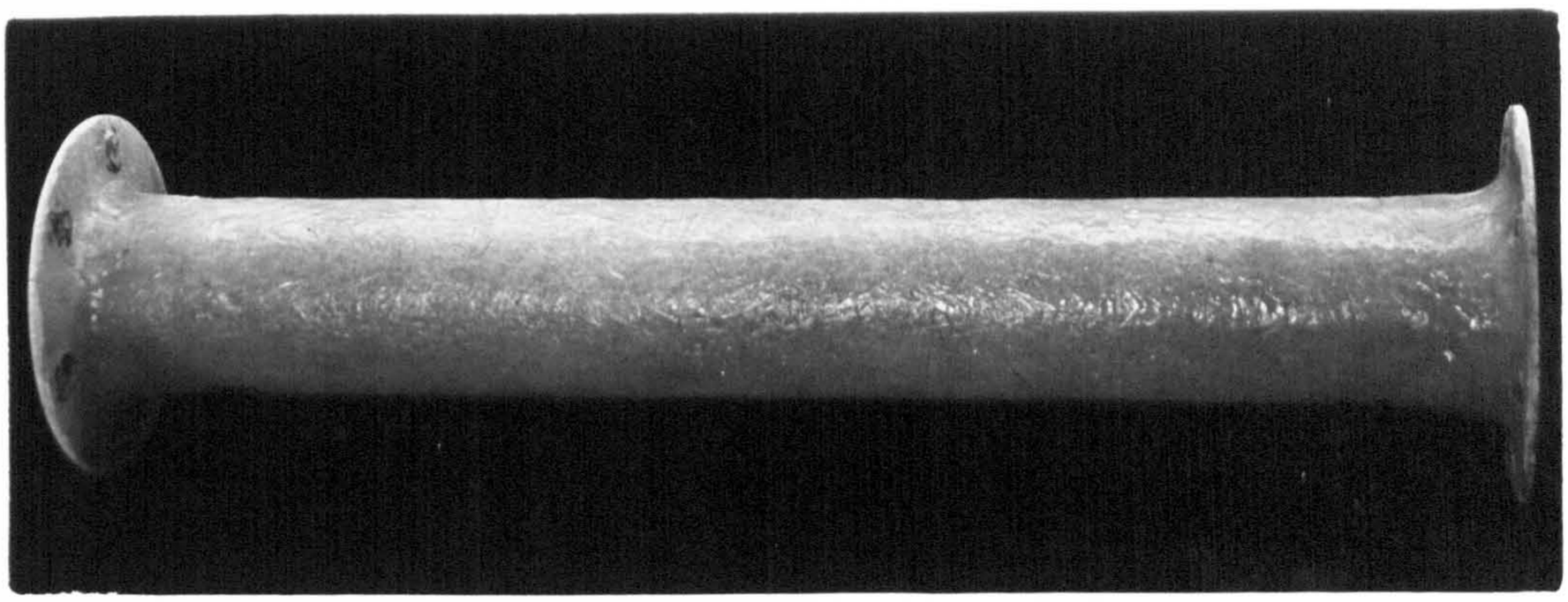

FIG. 3.3 COMPLETED LINER FROM ONE OF LARGE PIPE-LINES

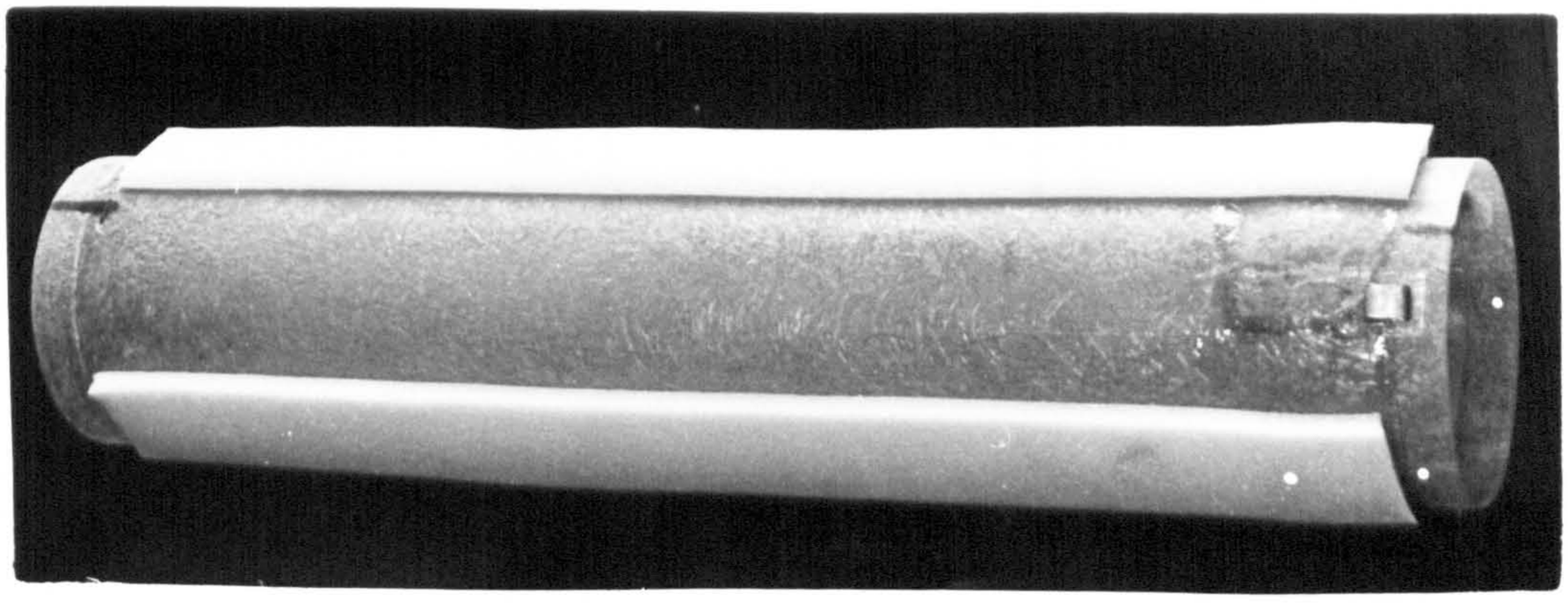

FIG. 3.4 GENERAL LAYOUT OF APPARATUS FOR LARGE PIPE-LINES

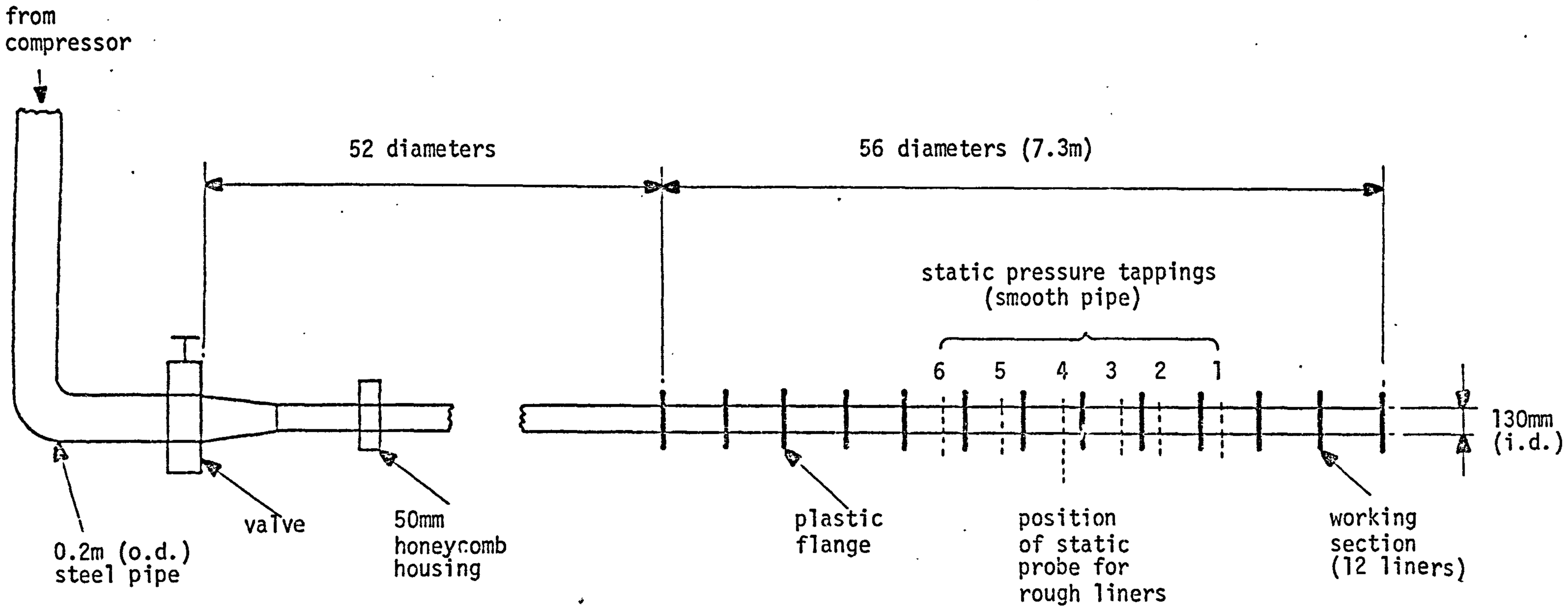

FIG. 3.5 GENERAL LAYOUT FOR SMALL PIPE-LINES

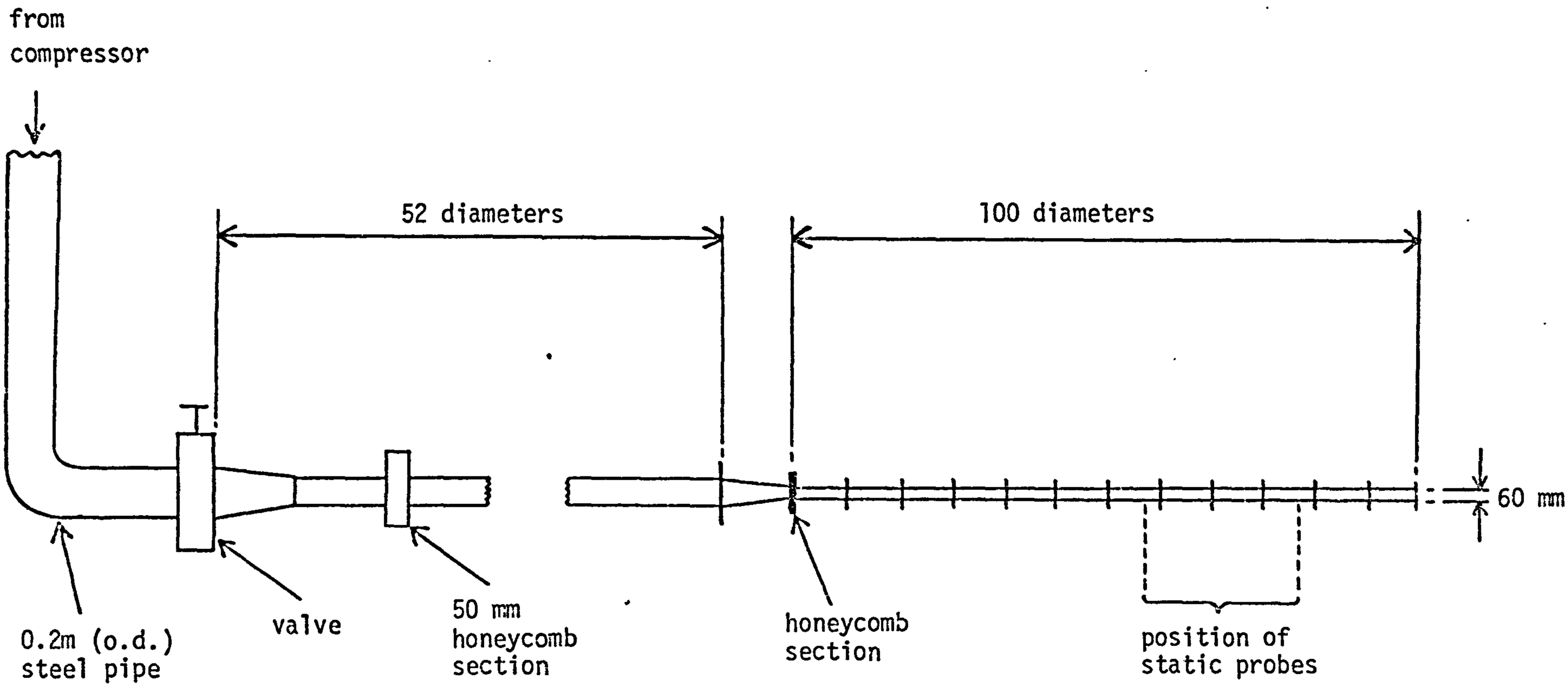

FIG. 3.6 DETAILS OF STATIC PROBE

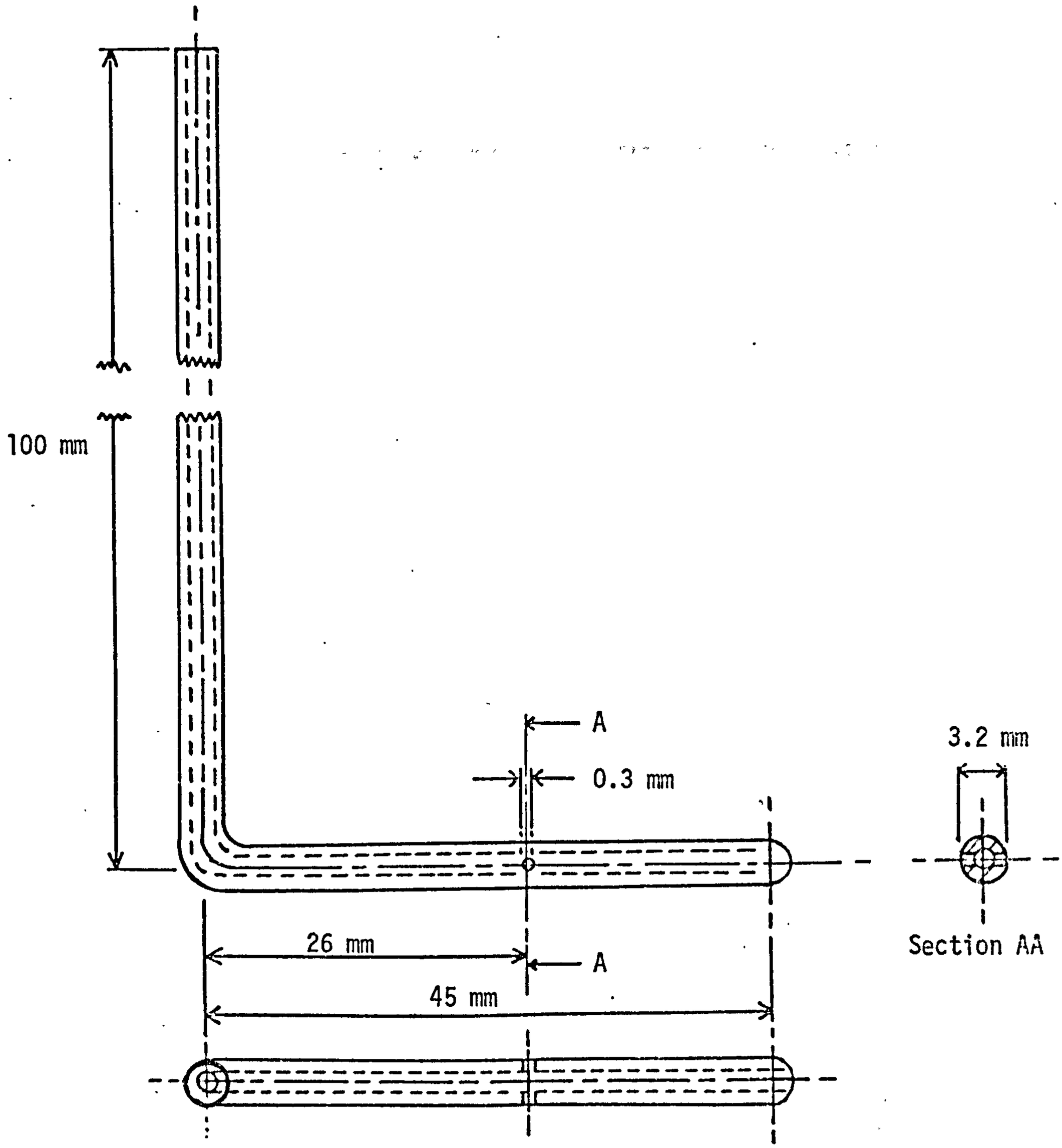

FIG. 3.7 TRAVERSE GEAR USED FOR SMALL PIPE-LINES

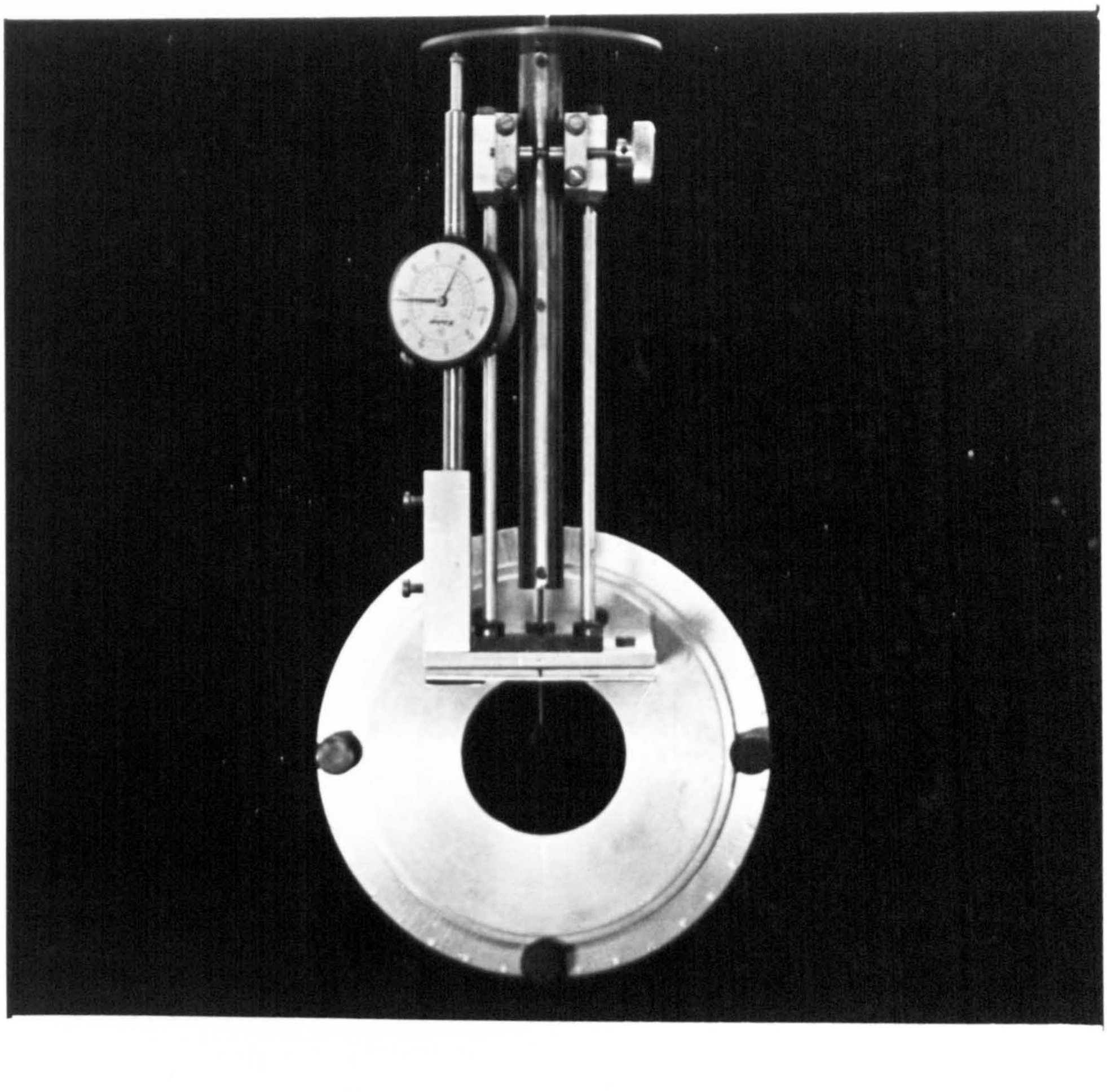

FIG. 3.8 INTER-CONNECTIONS FOR TURBULENCE-MEASURING EQUIPMENT

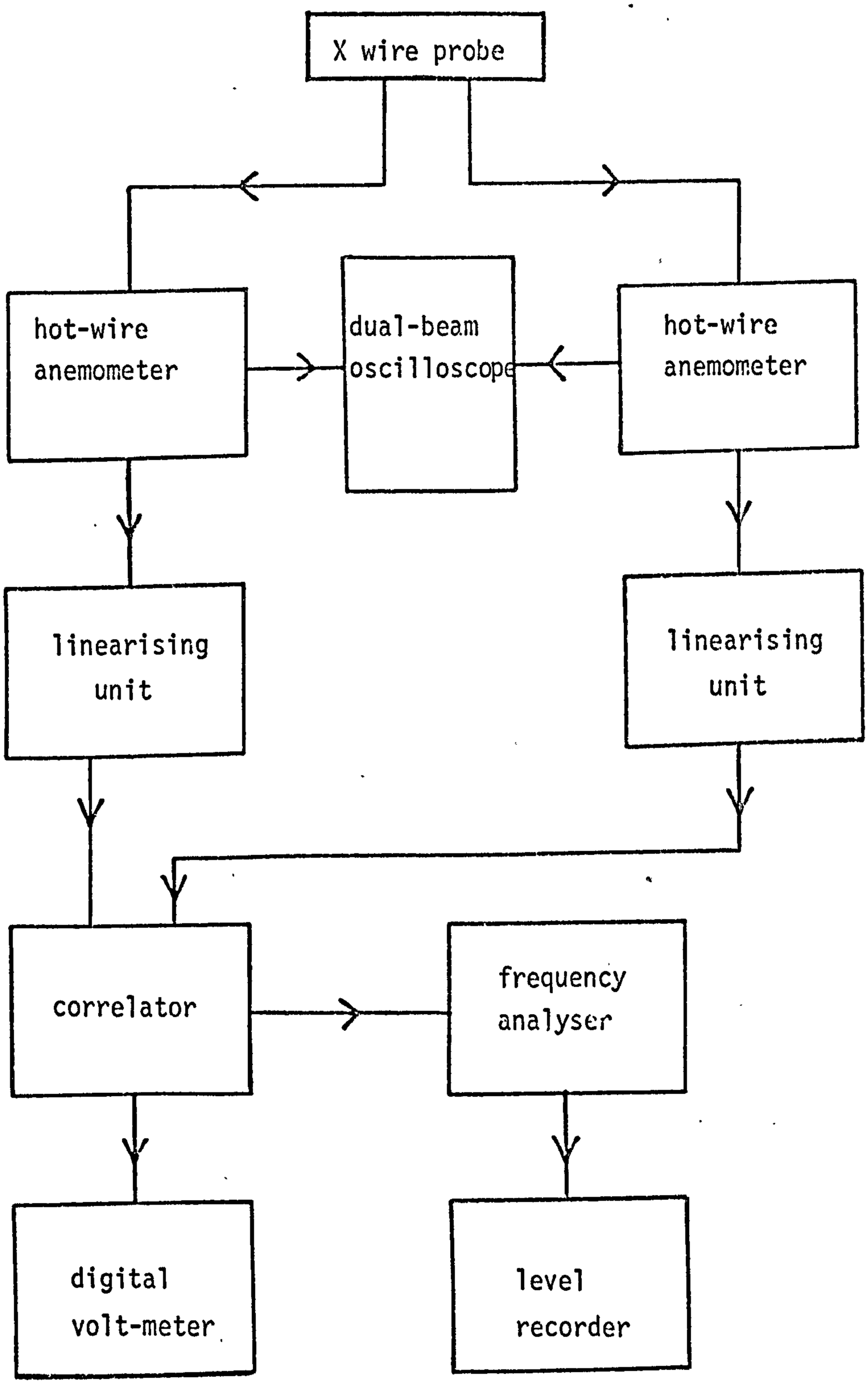

FIG. 3.9 VELOCITY DISTRIBUTIONS FOR THE SMOOTH PIPE IN 'LAW-OF-THE-WALL' CO-ORDINATES

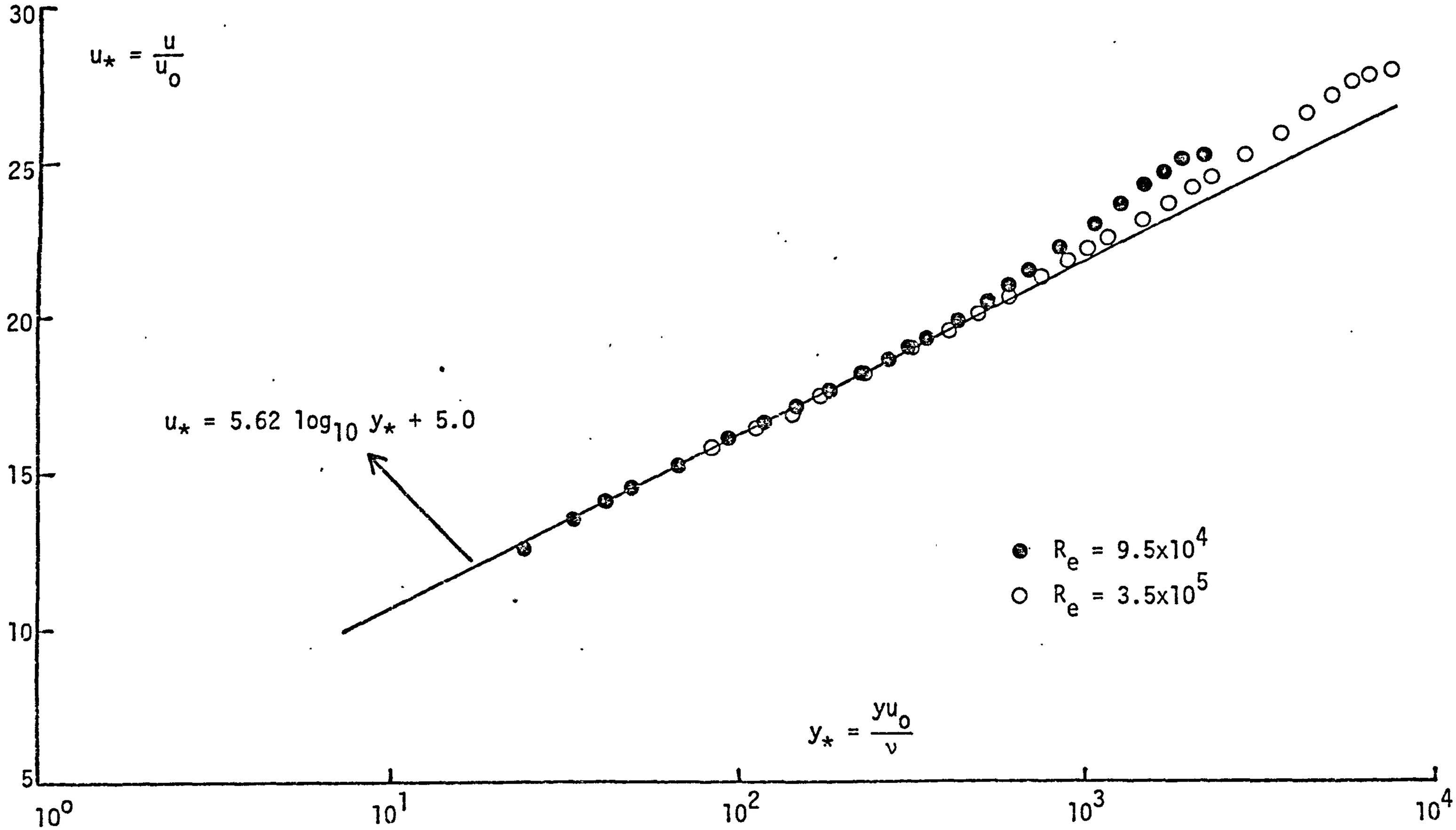

FIG. 3.10 PIPE FRICTION COEFFICIENT FOR THE SMOOTH SURFACE

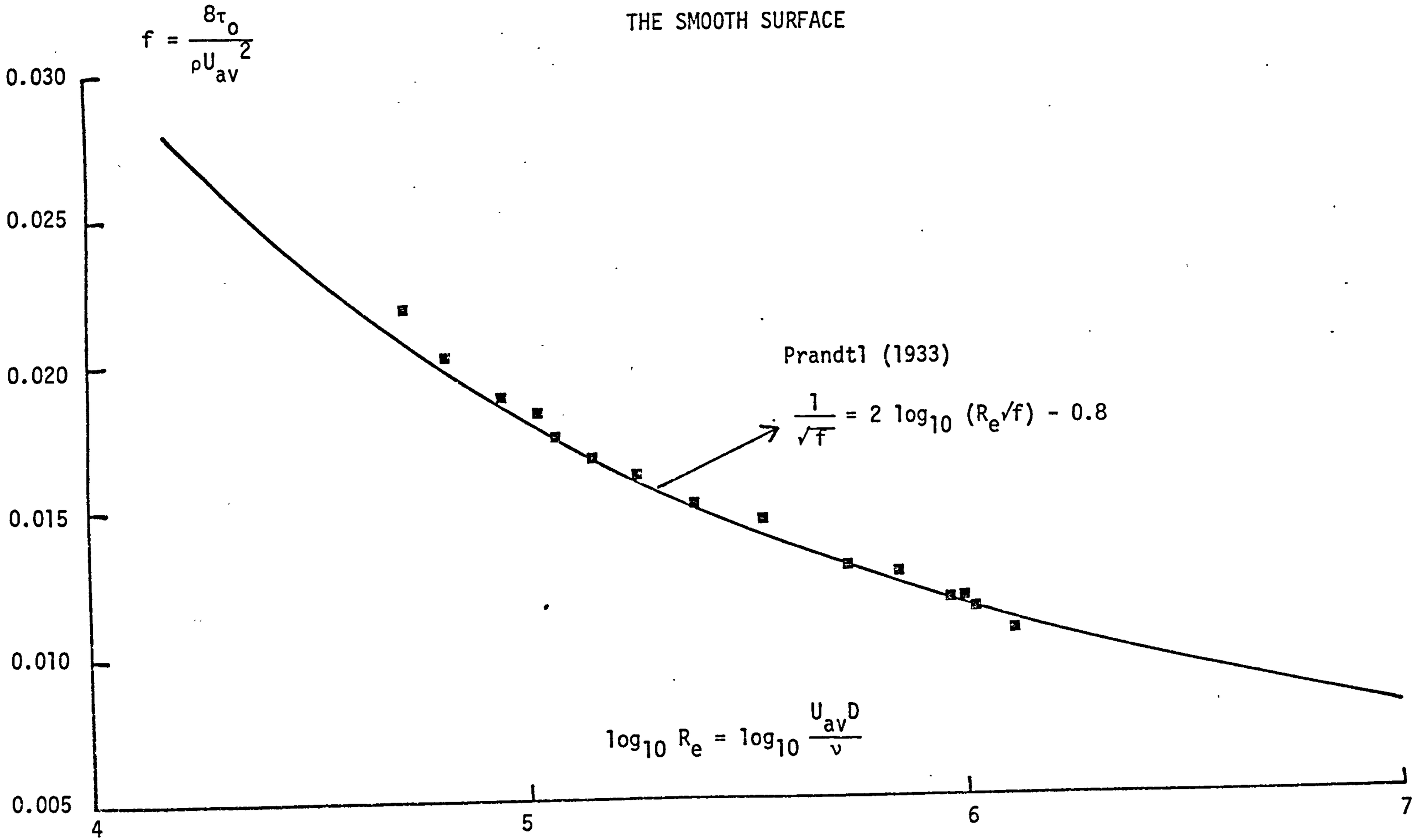

FIG. 3.11 MEAN VELOCITY DISTRIBUTIONS FOR THE SMOOTH AND R550 SURFACES

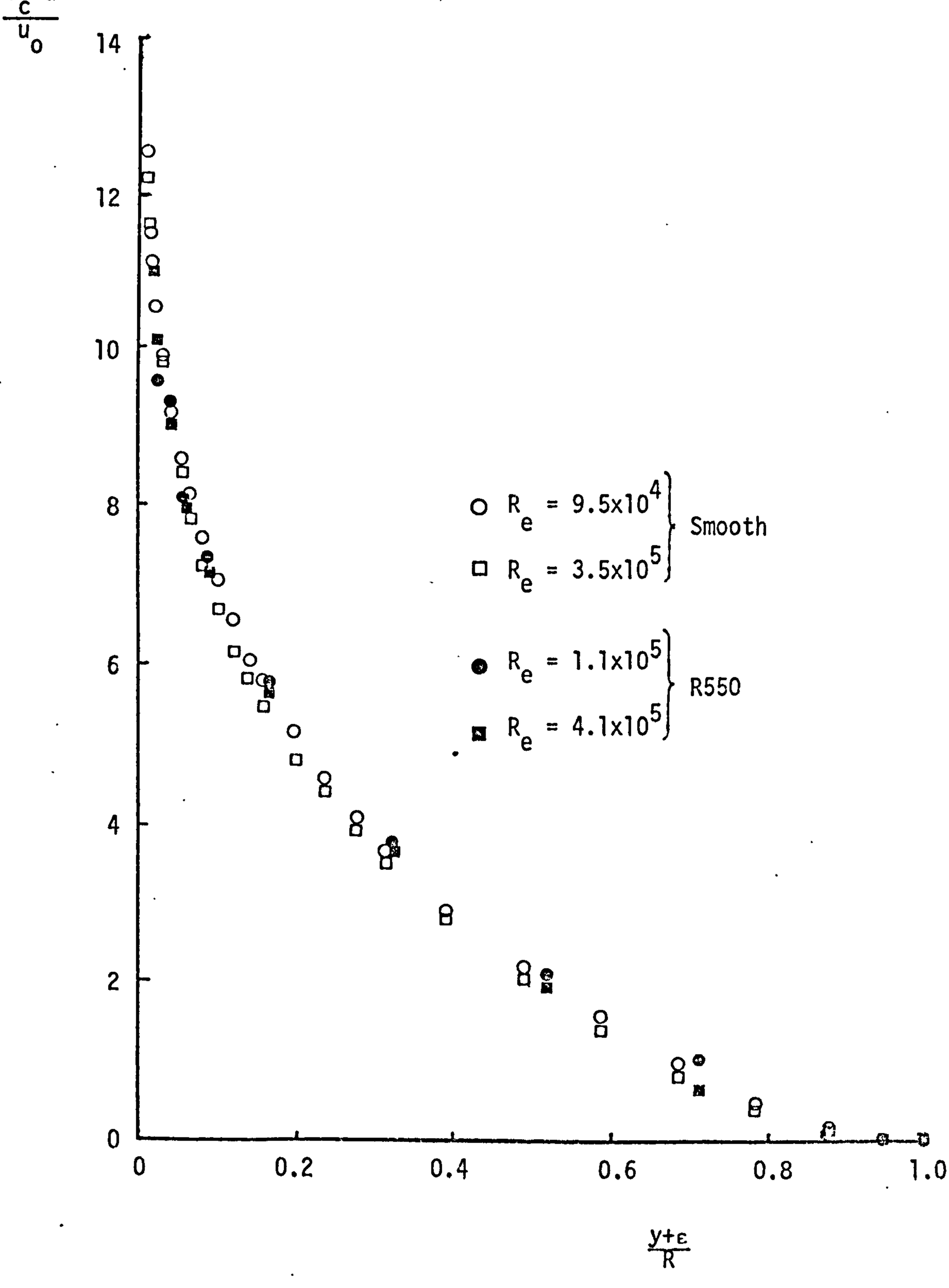

FIG. 3.12 MEAN VELOCITY DISTRIBUTIONS FOR THE SMOOTH AND R420 SURFACES

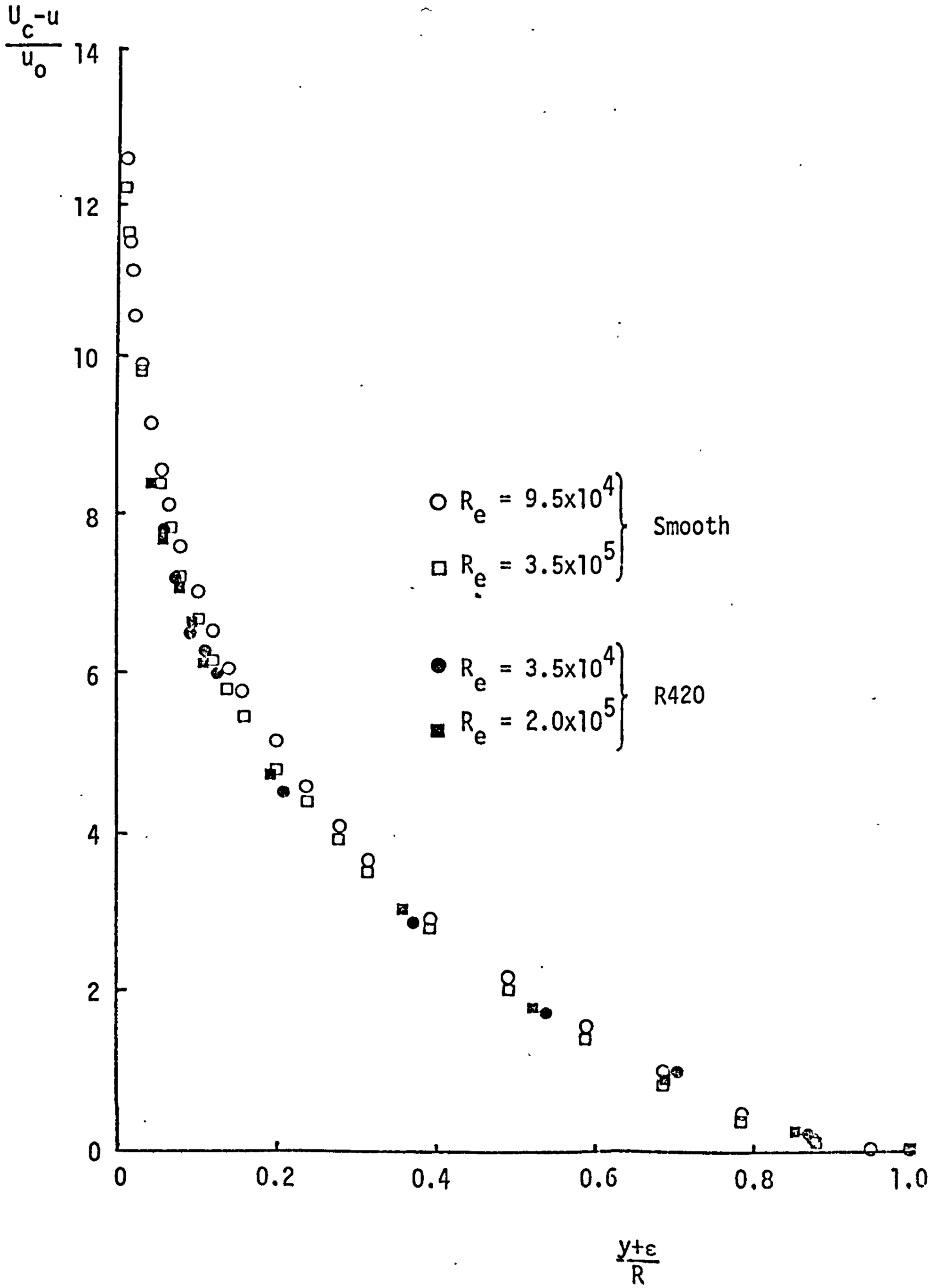

FIG. 3.13 MEAN VELOCITY DISTRIBUTIONS FOR THE SMOOTH AND R345 SURFACES

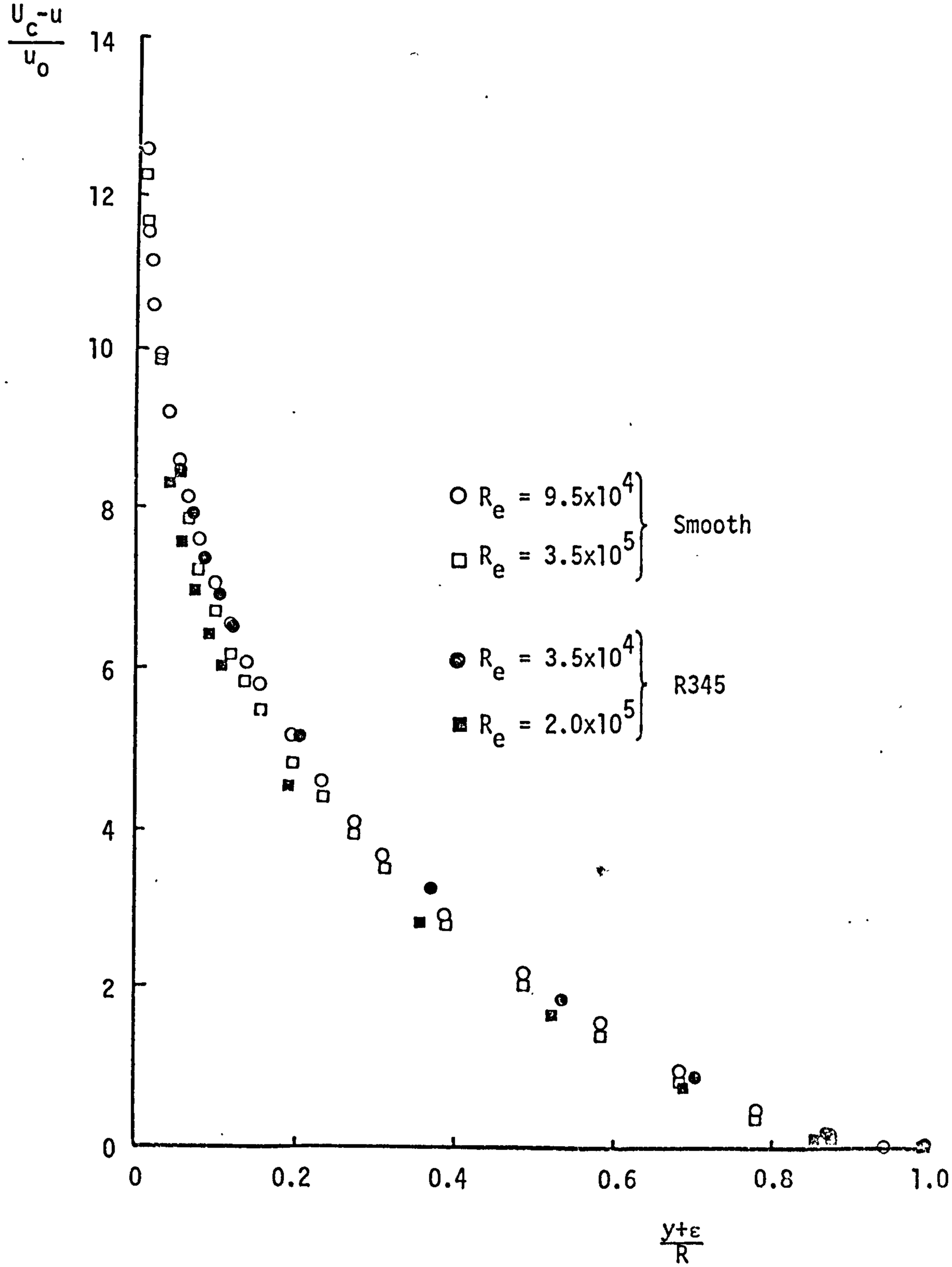

FIG. 3.14 MEAN VELOCITY DISTRIBUTIONS FOR THE SMOOTH AND R253 SURFACES

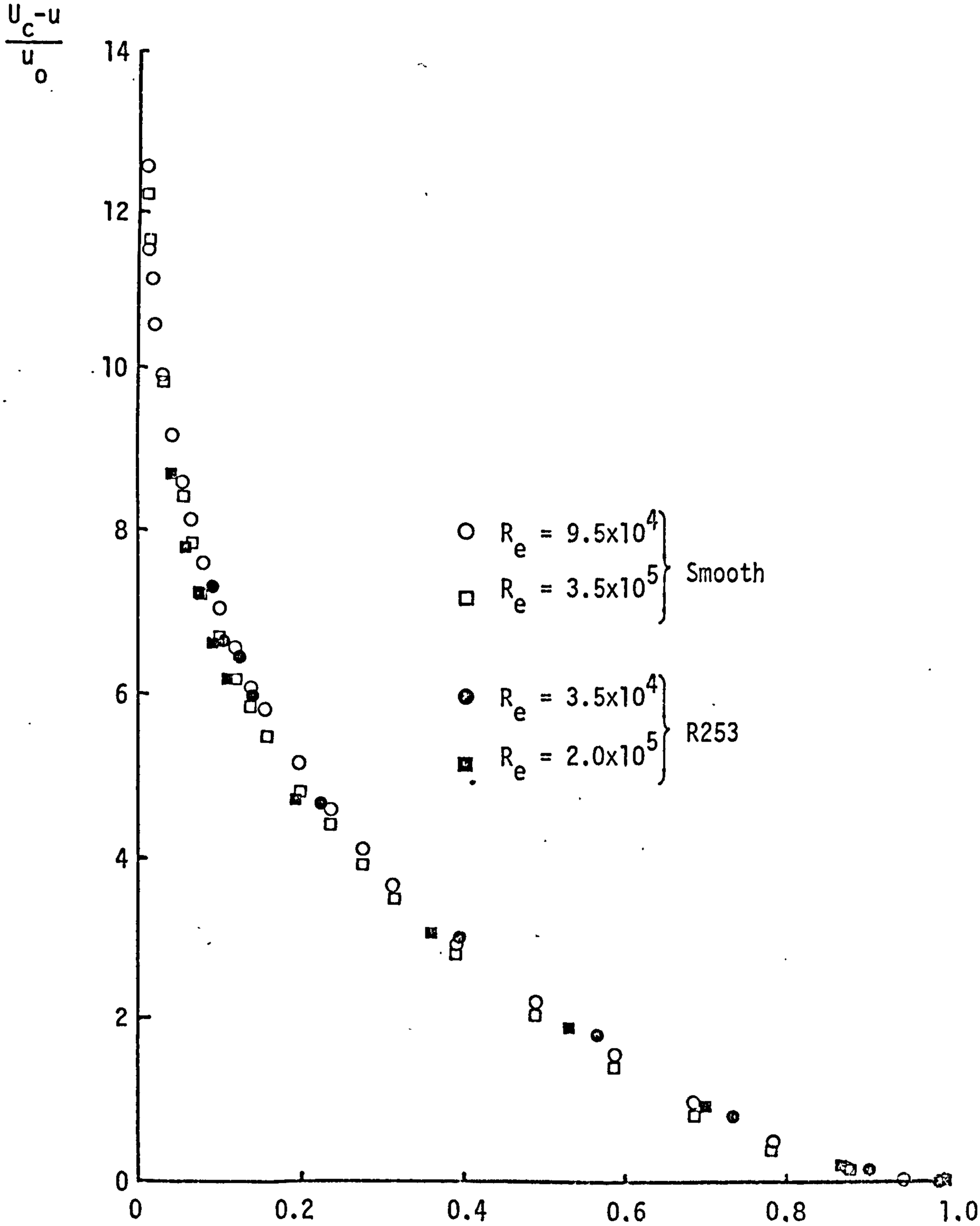

FIG. 3.15 MEAN VELOCITY DISTRIBUTIONS FOR THE SMOOTH AND R173 SURFACES

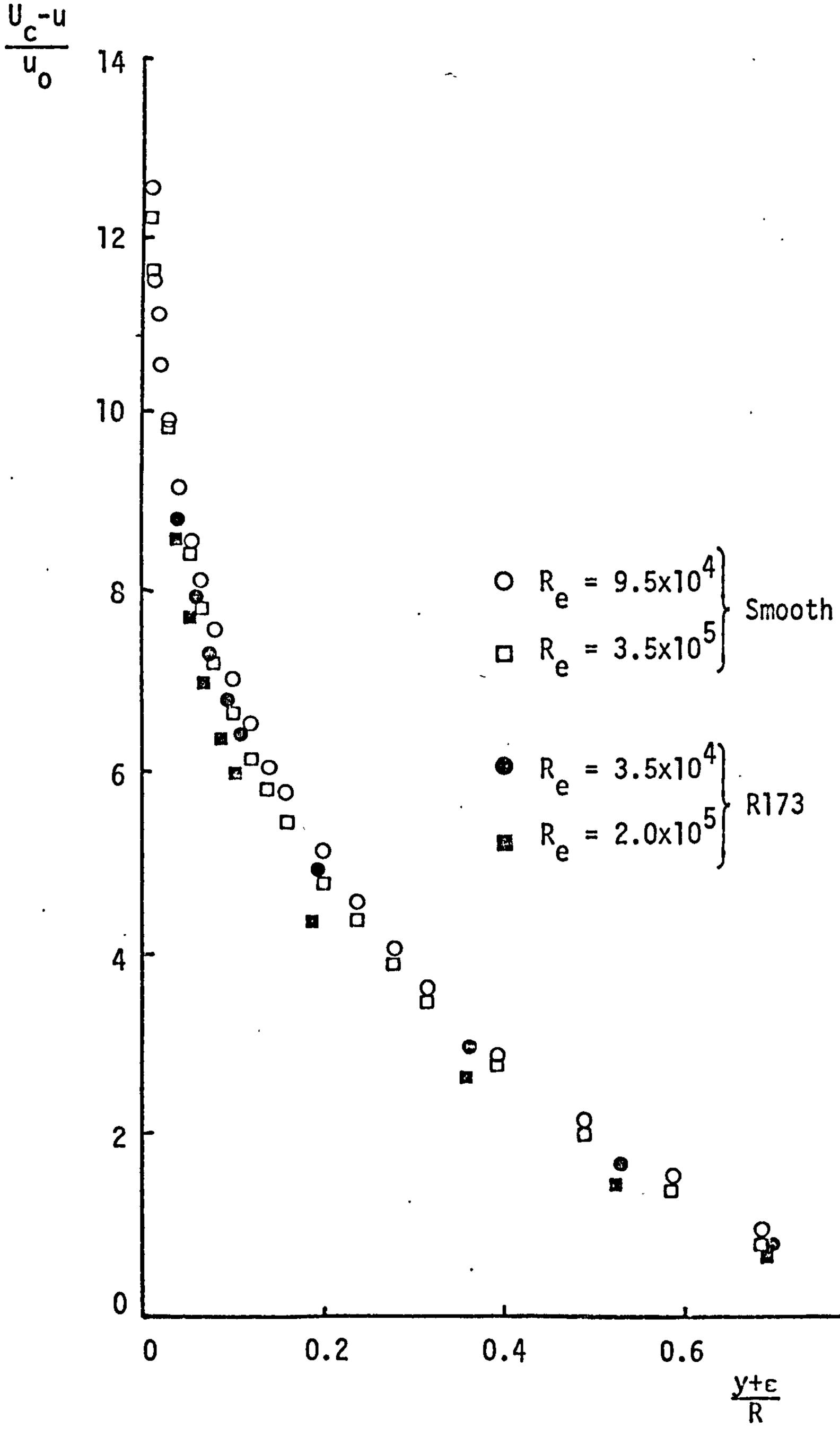

FIG. 3.16 INNER-REGION VELOCITY DISTRIBUTIONS
FOR THE SMOOTH AND R550 SURFACES

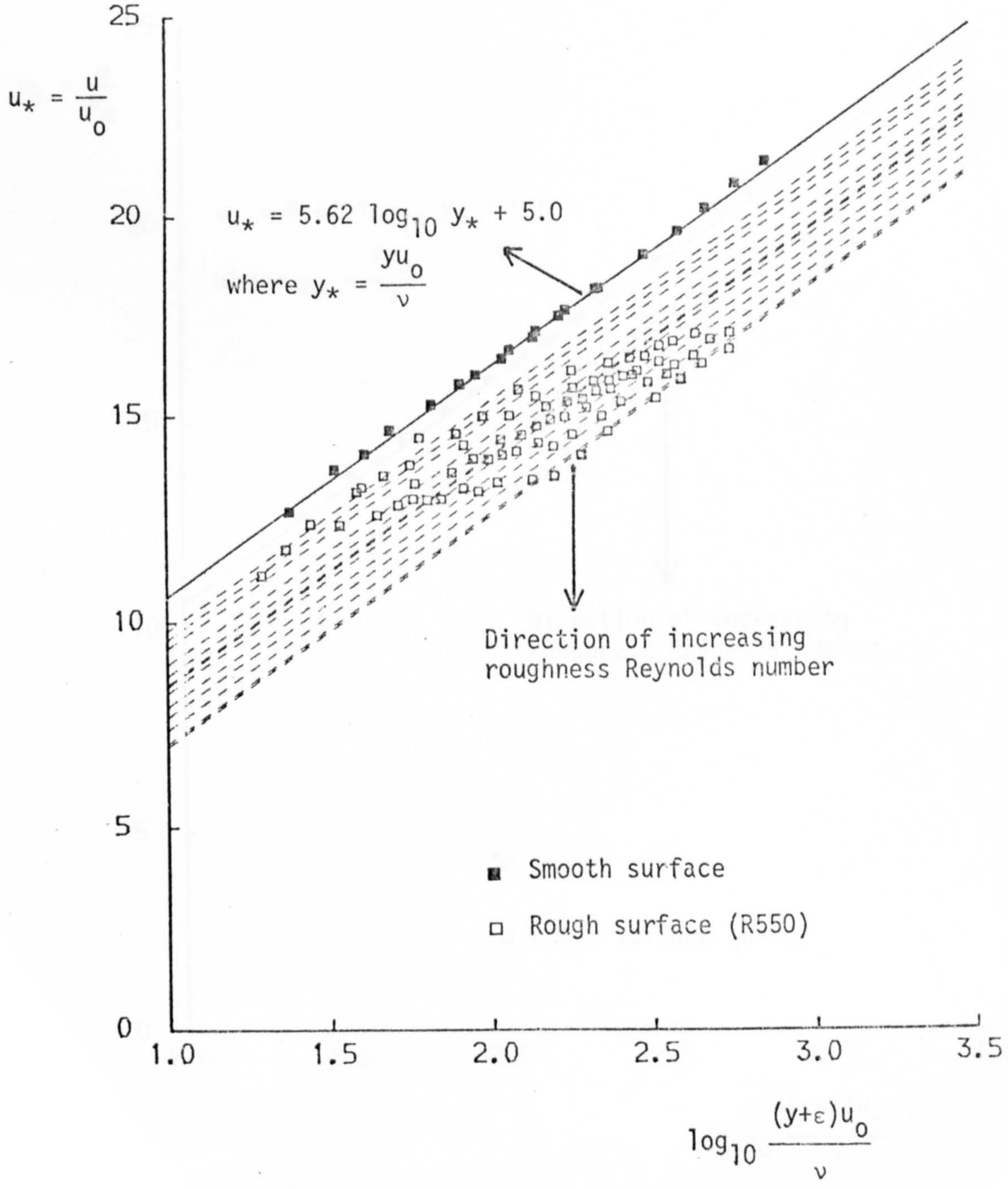

FIG. 3.17 INNER-REGION VELOCITY DISTRIBUTIONS

FOR THE SMOOTH AND R420 SURFACES

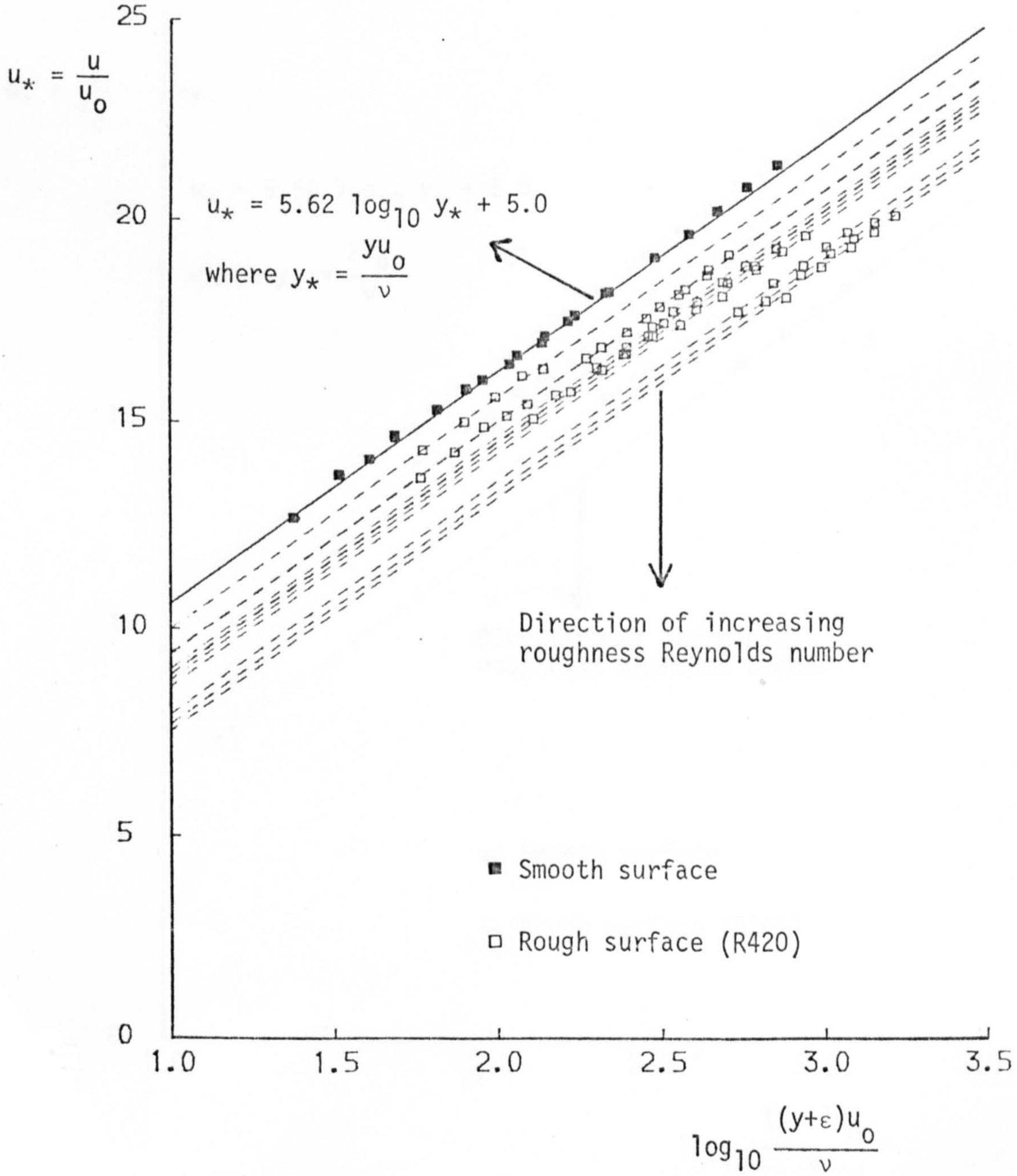

FIG. 3.18 INNER-REGION VELOCITY DISTRIBUTIONS FOR THE SMOOTH AND R345 SURFACES

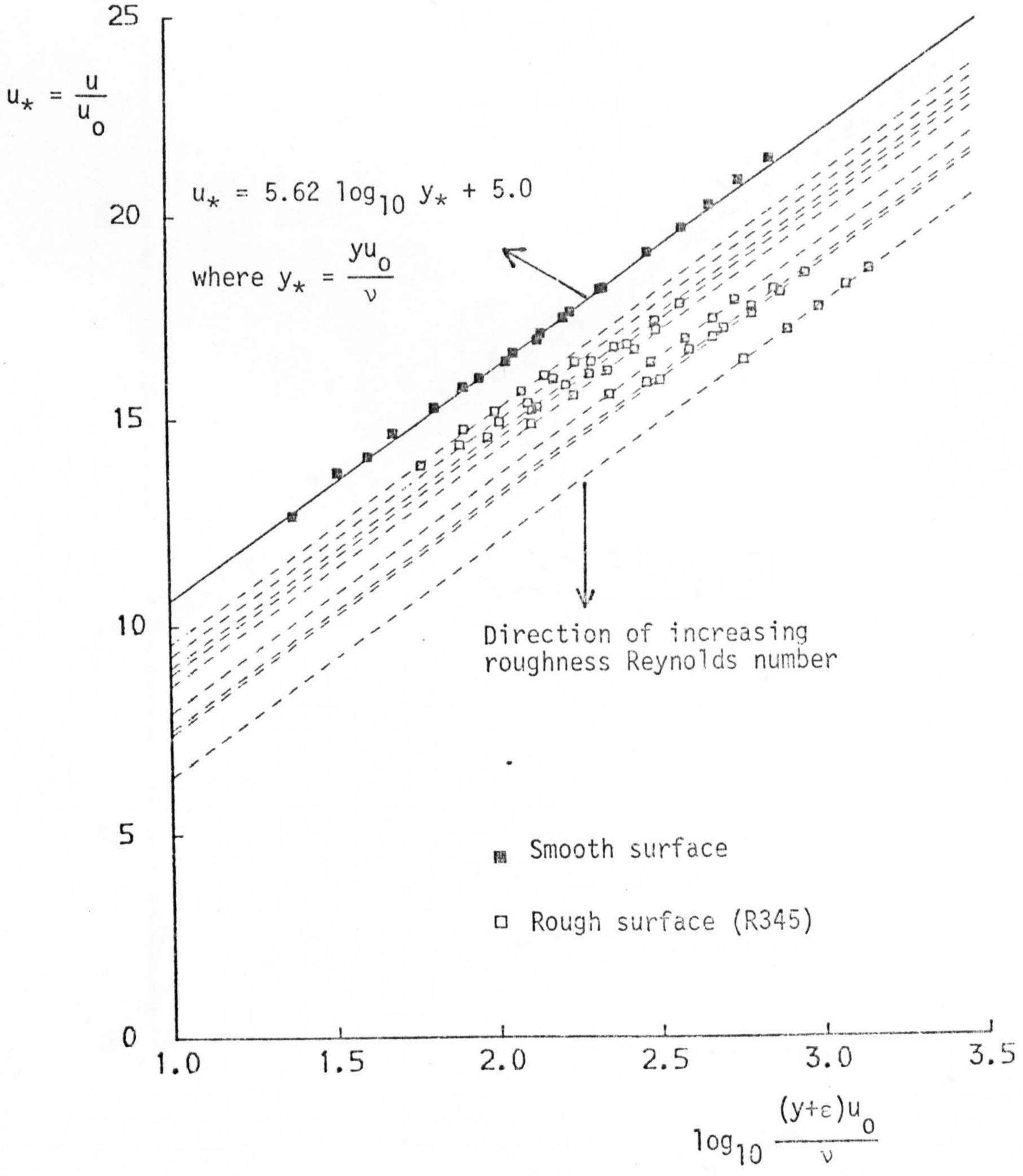

FIG. 3.19 INNER-REGION VELOCITY DISTRIBUTIONS

FOR THE SMOOTH AND R253 SURFACES

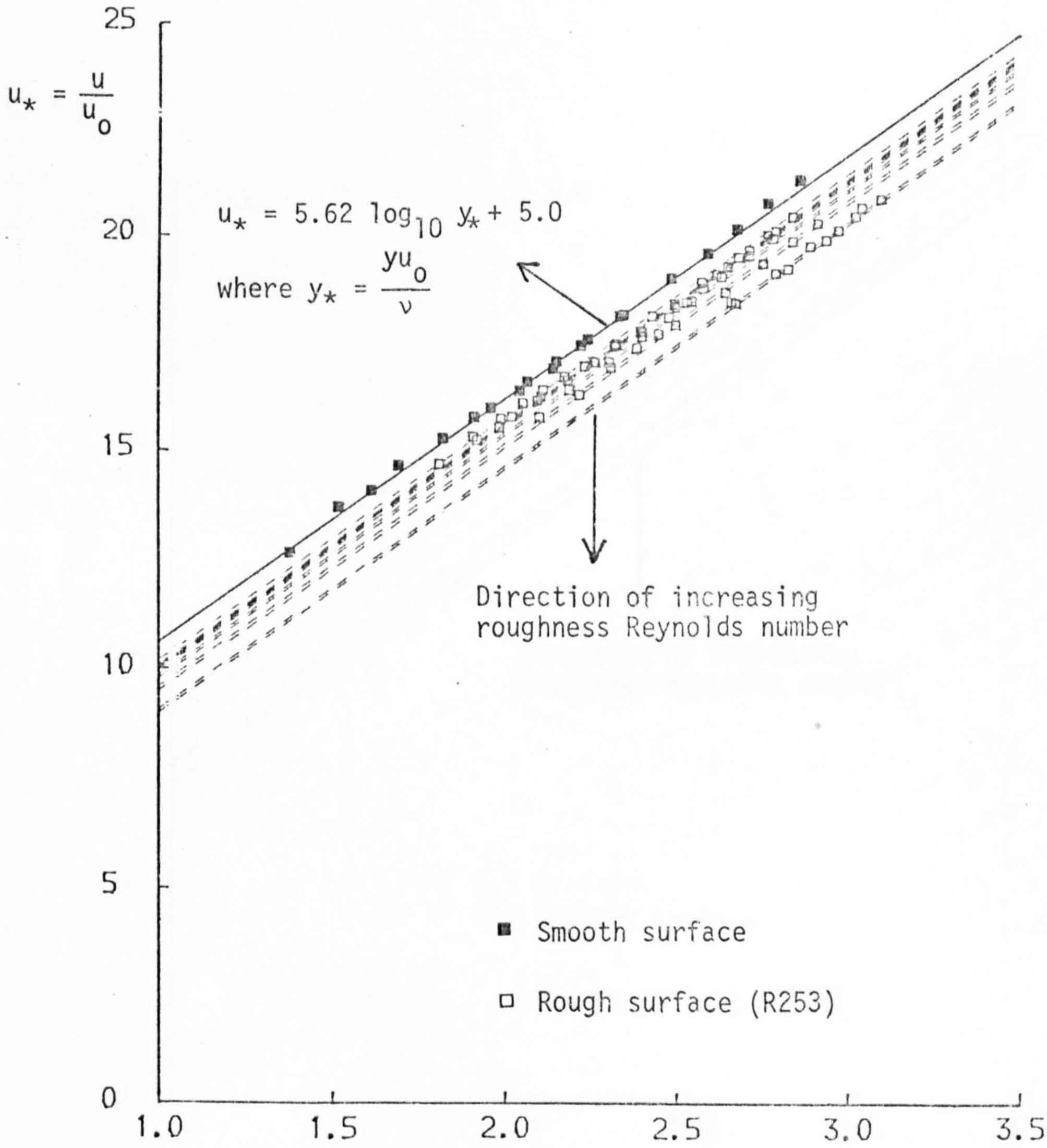

FIG. 3.20 INNER-REGION VELOCITY DISTRIBUTIONS FOR THE SMOOTH AND R173 SURFACES

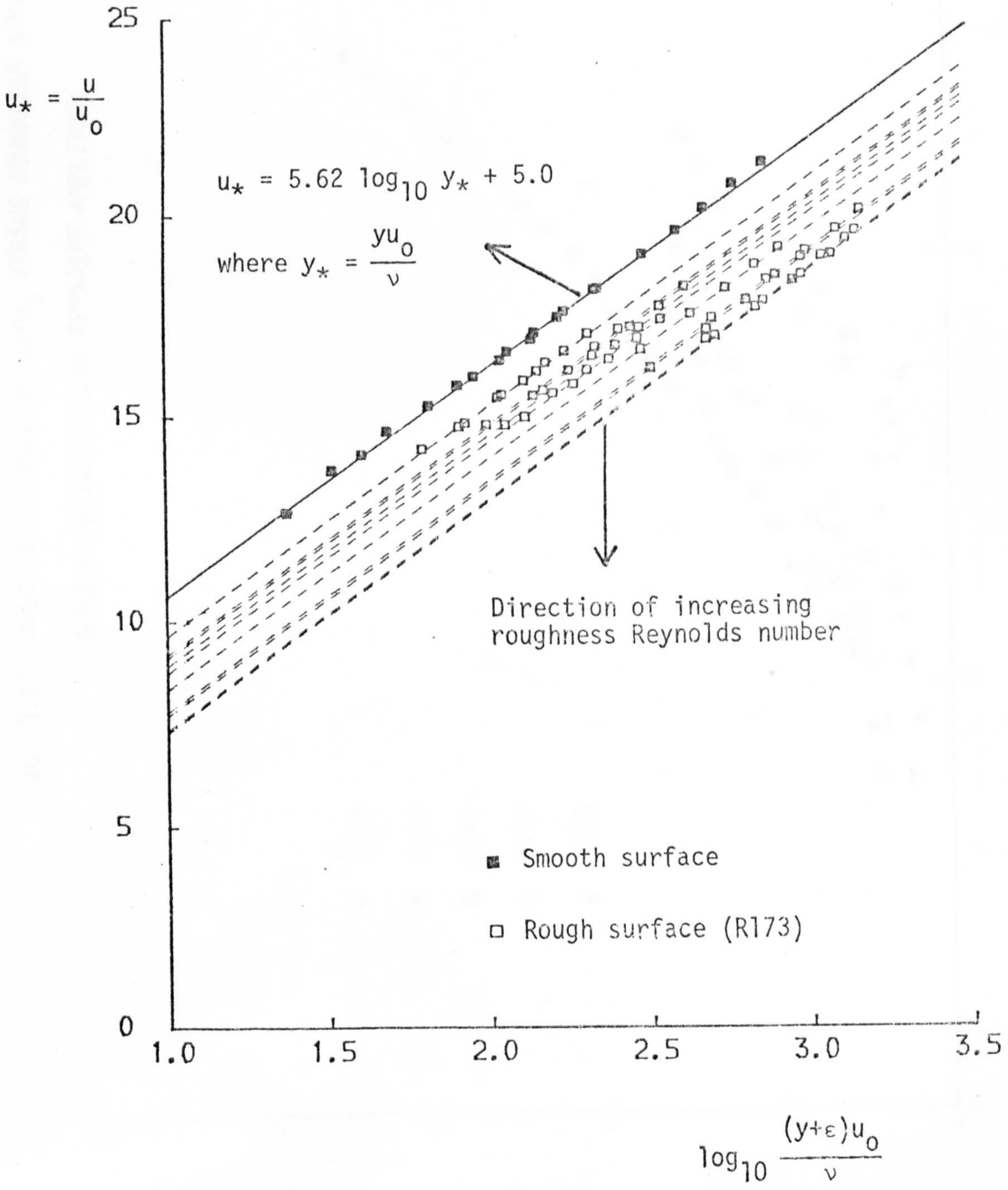

FIG. 3.21 ROUGHNESS FUNCTION $\Delta u/u_o$ VERSUS ROUGHNESS REYNOLDS NUMBER BASED ON MEAN APPARENT AMPLITUDE

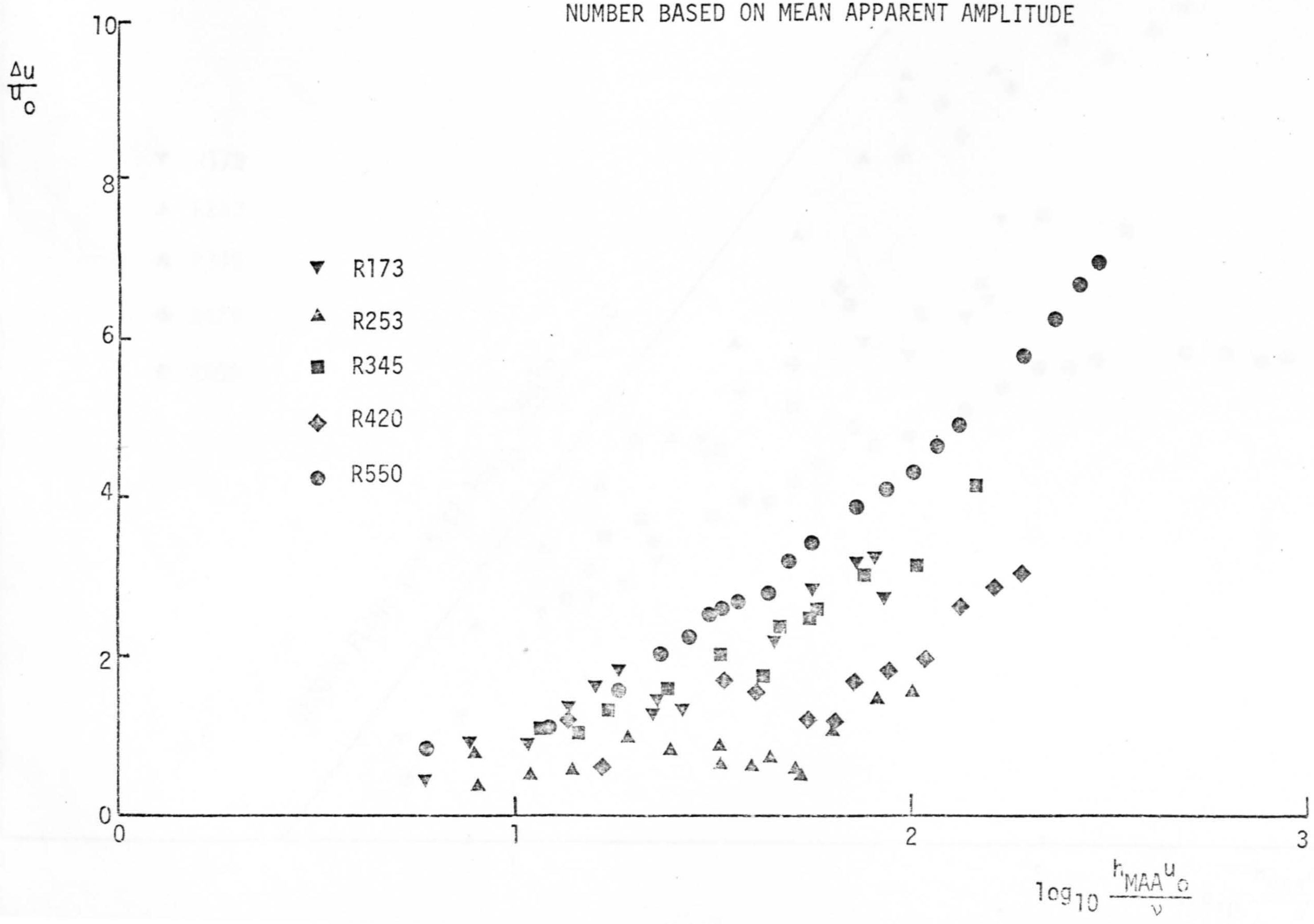

FIG. 3.22 ROUGHNESS FUNCTION χ VERSUS ROUGHNESS REYNOLDS NUMBER BASED ON MEAN APPARENT AMPLITUDE

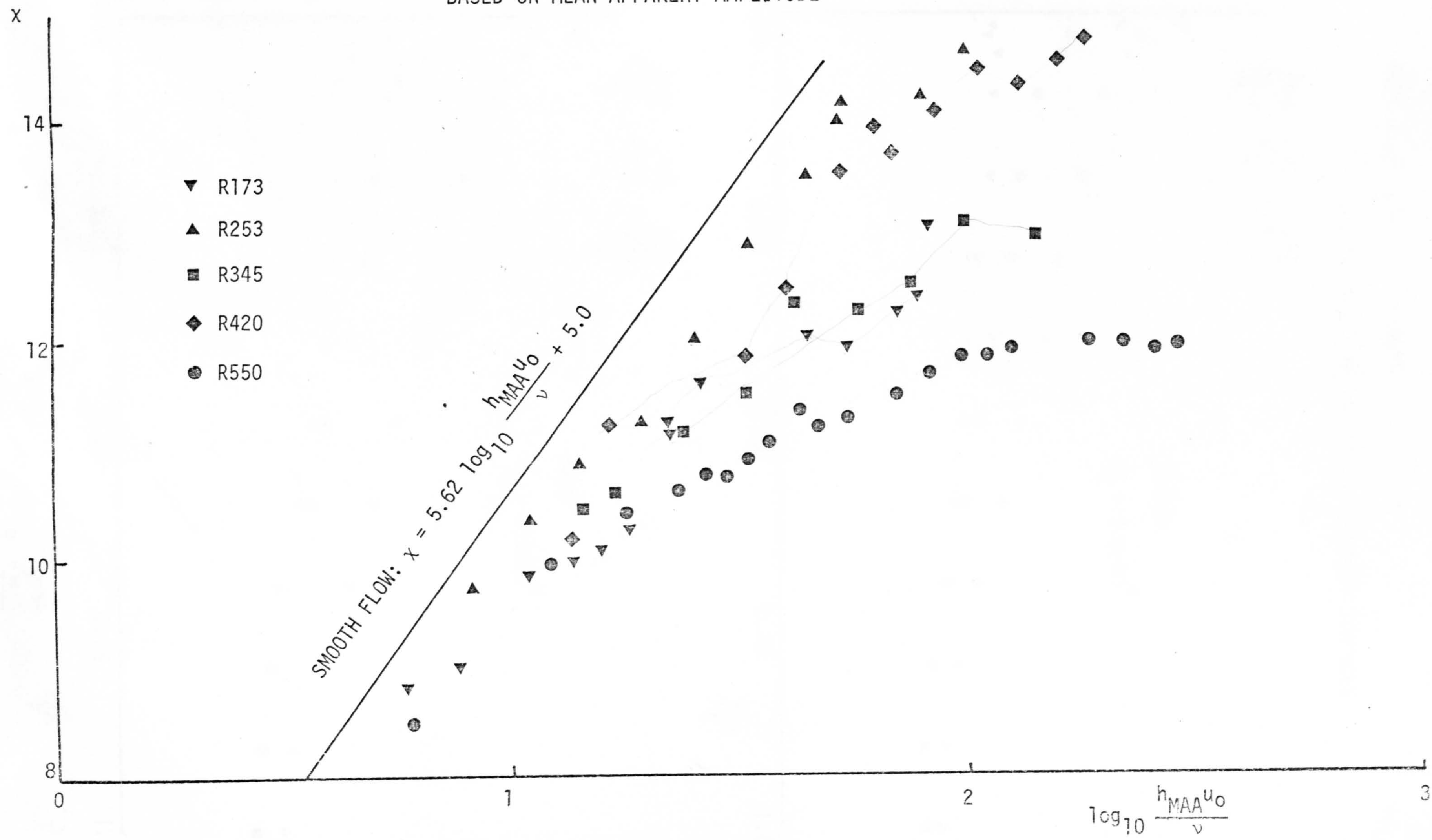

FIG. 3.23 R.M.S. COMPONENTS OF VELOCITY FLUCTUATIONS FOR THE SMOOTH AND R550 SURFACES

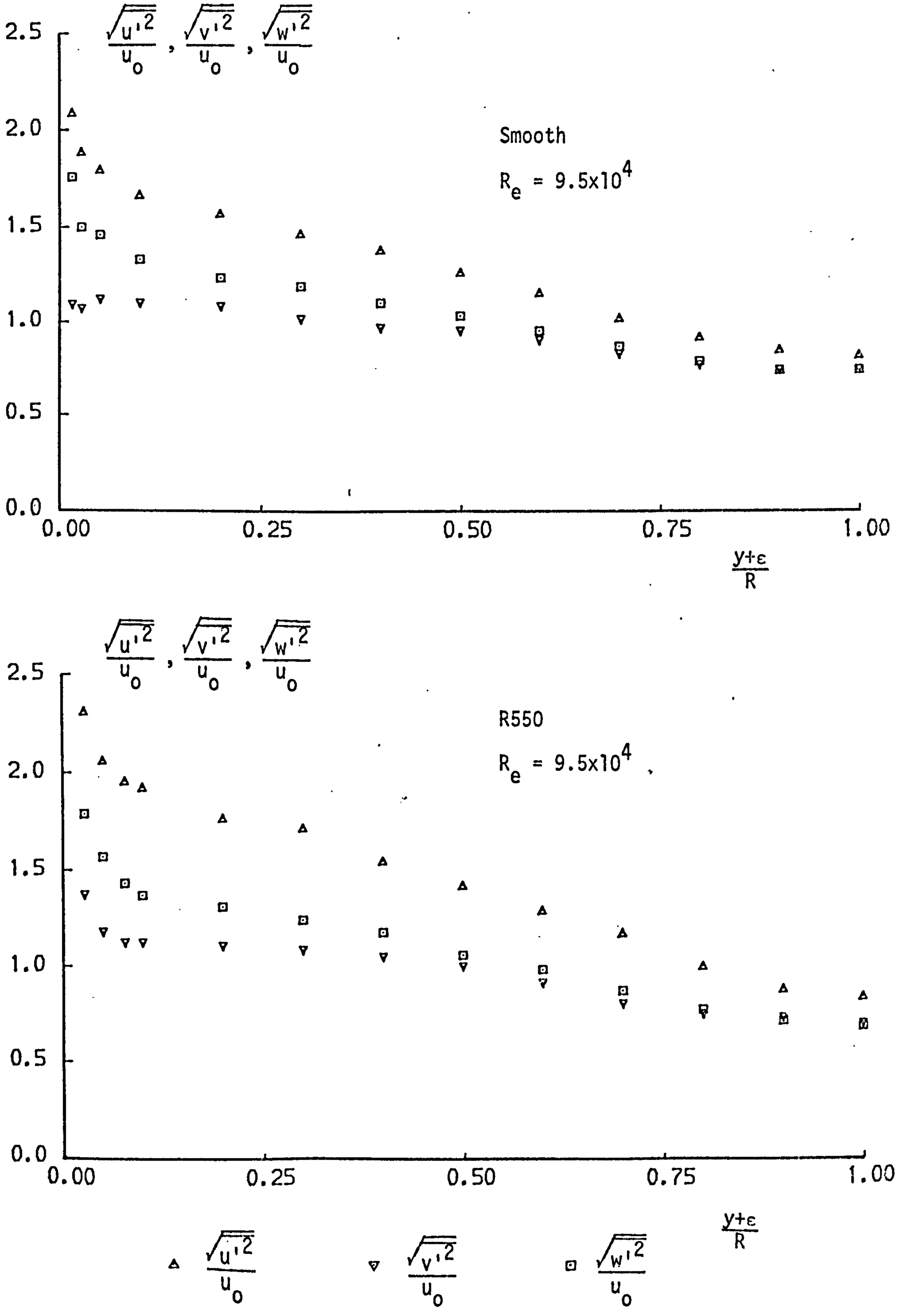

FIG. 3.24 R.M.S. COMPONENTS OF VELOCITY FLUCTUATIONS FOR THE R420 SURFACE

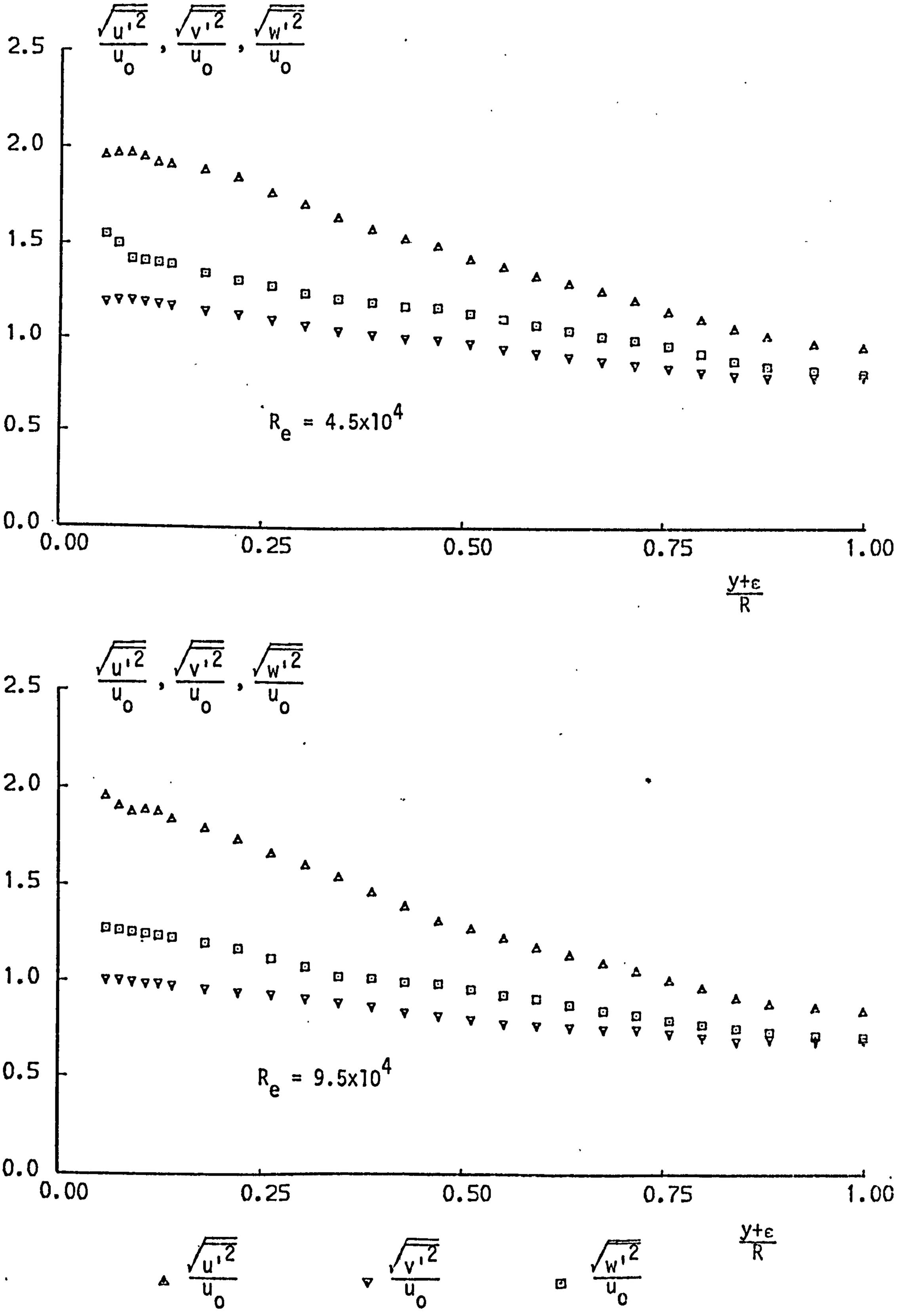

FIG. 3.25 R.M.S. COMPONENTS OF VELOCITY FLUCTUATIONS FOR THE R345 SURFACE

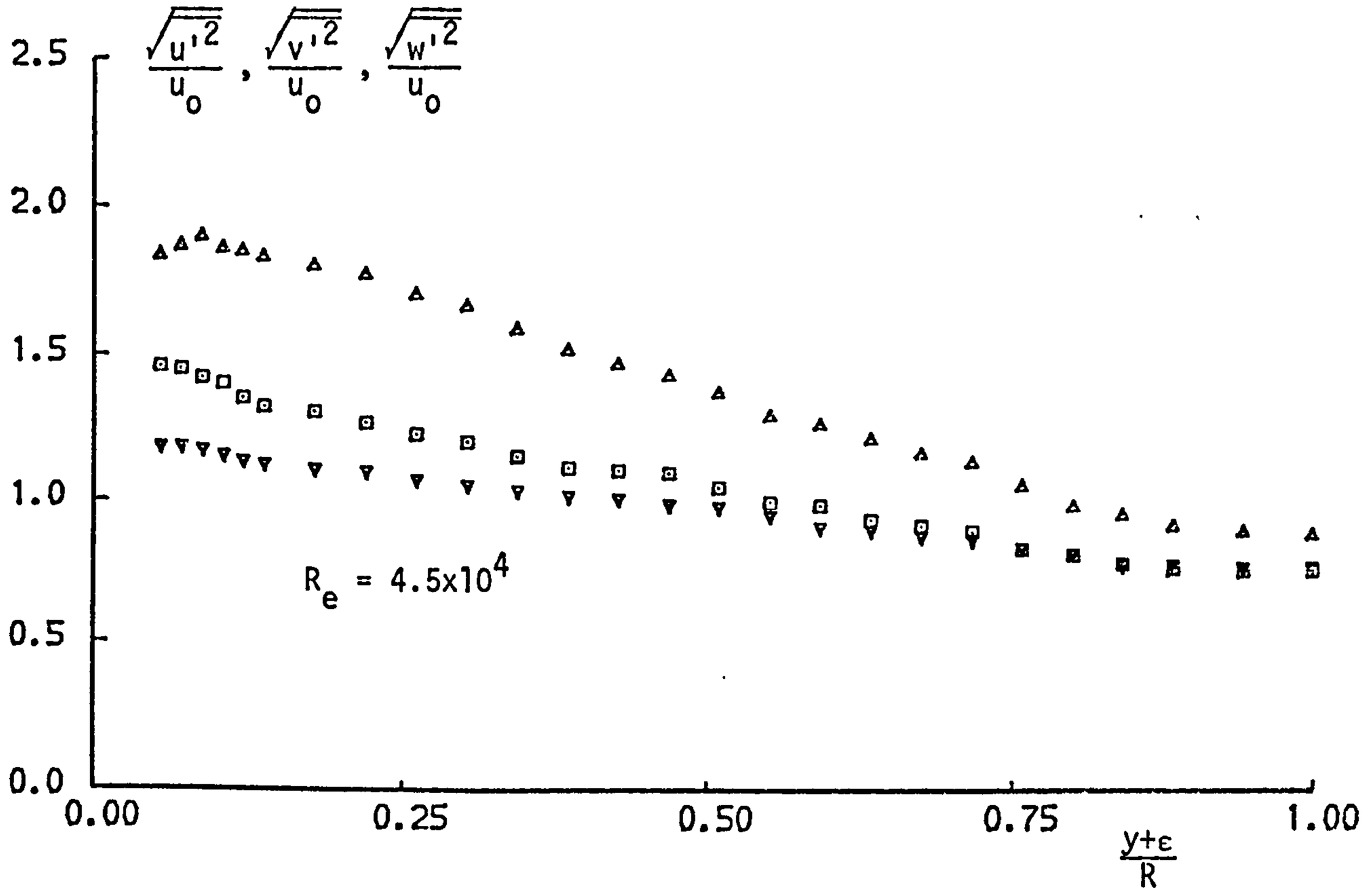

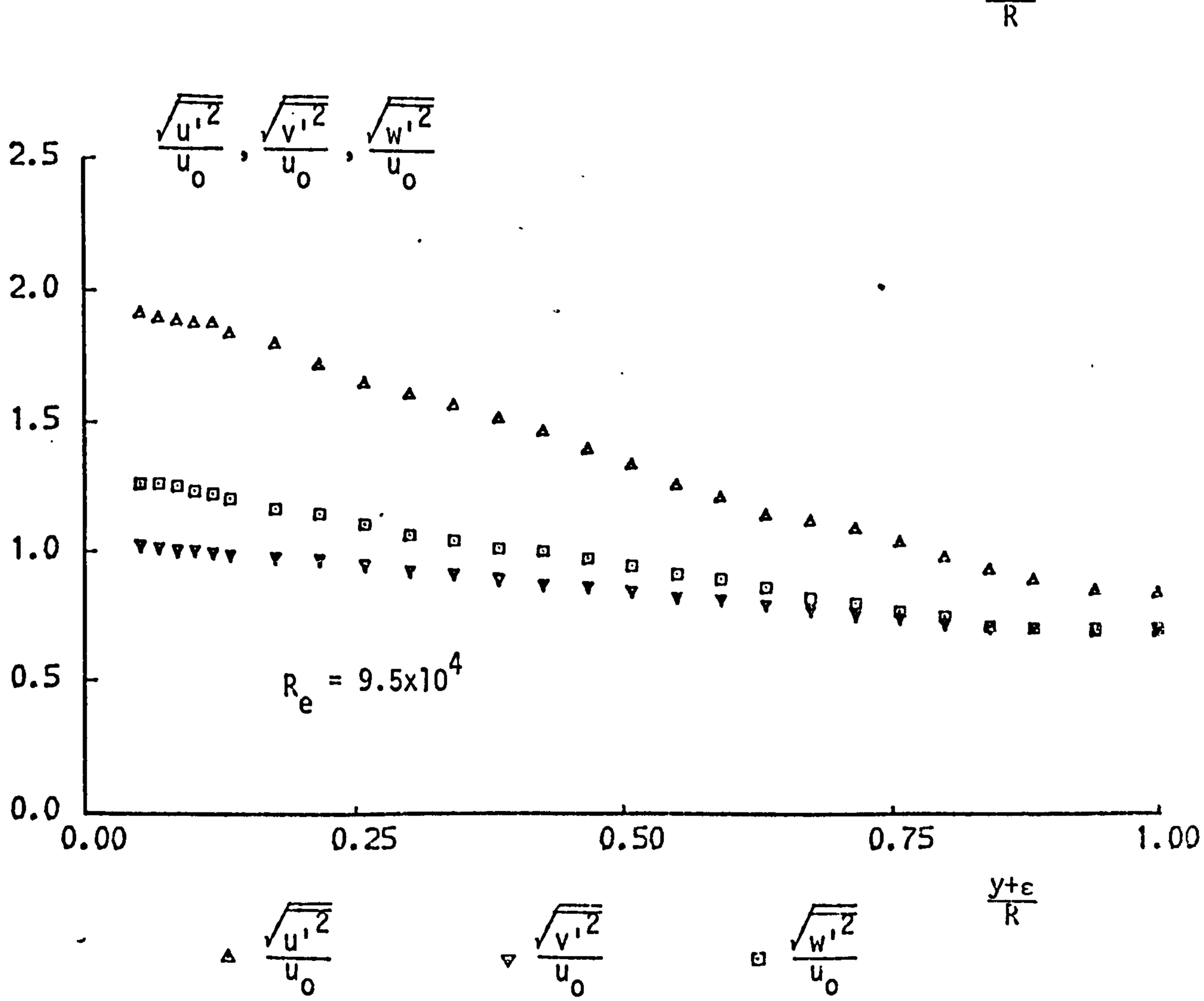

RIG. 3.26 R.M.S. COMPONENTS OF VELOCITY FLUCTUATIONS FOR THE R253 SURFACE

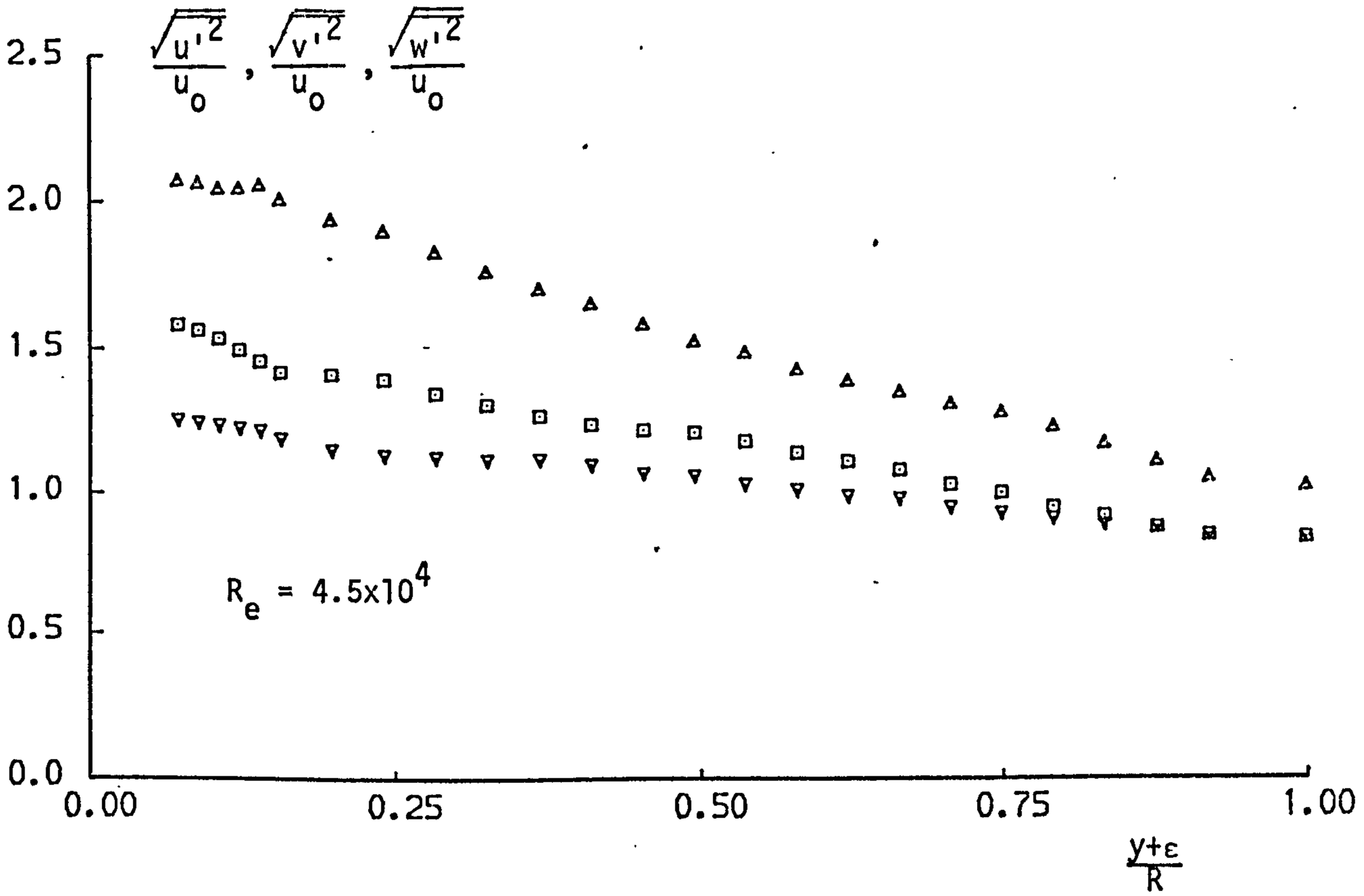

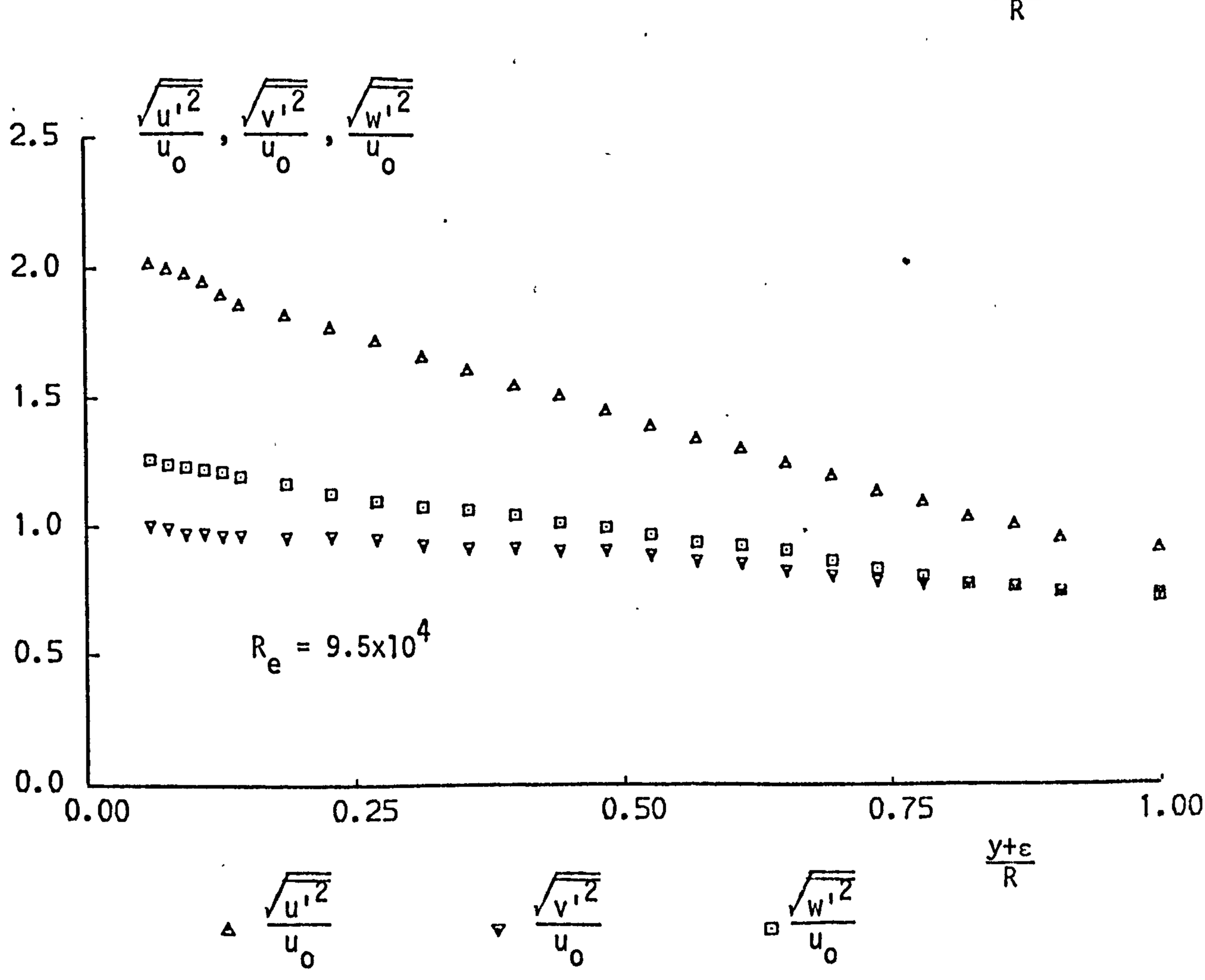

FIG. 3.27 R.M.S. COMPONENTS OF VELOCITY FLUCTUATIONS FOR THE R173 SURFACE

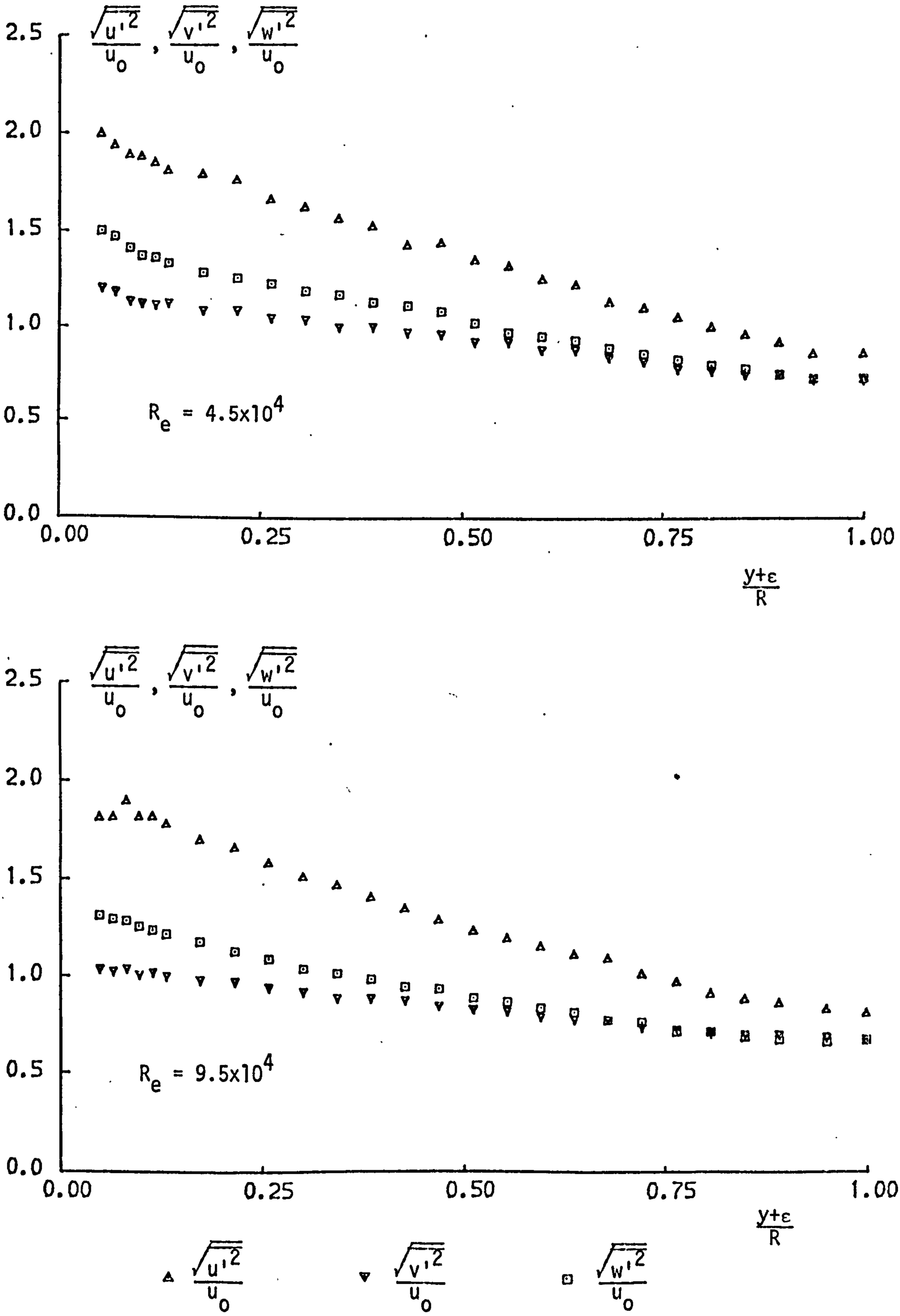

FIG. 3.28 TURBULENT SHEAR STRESSES FOR THE SMOOTH AND R550 SURFACES

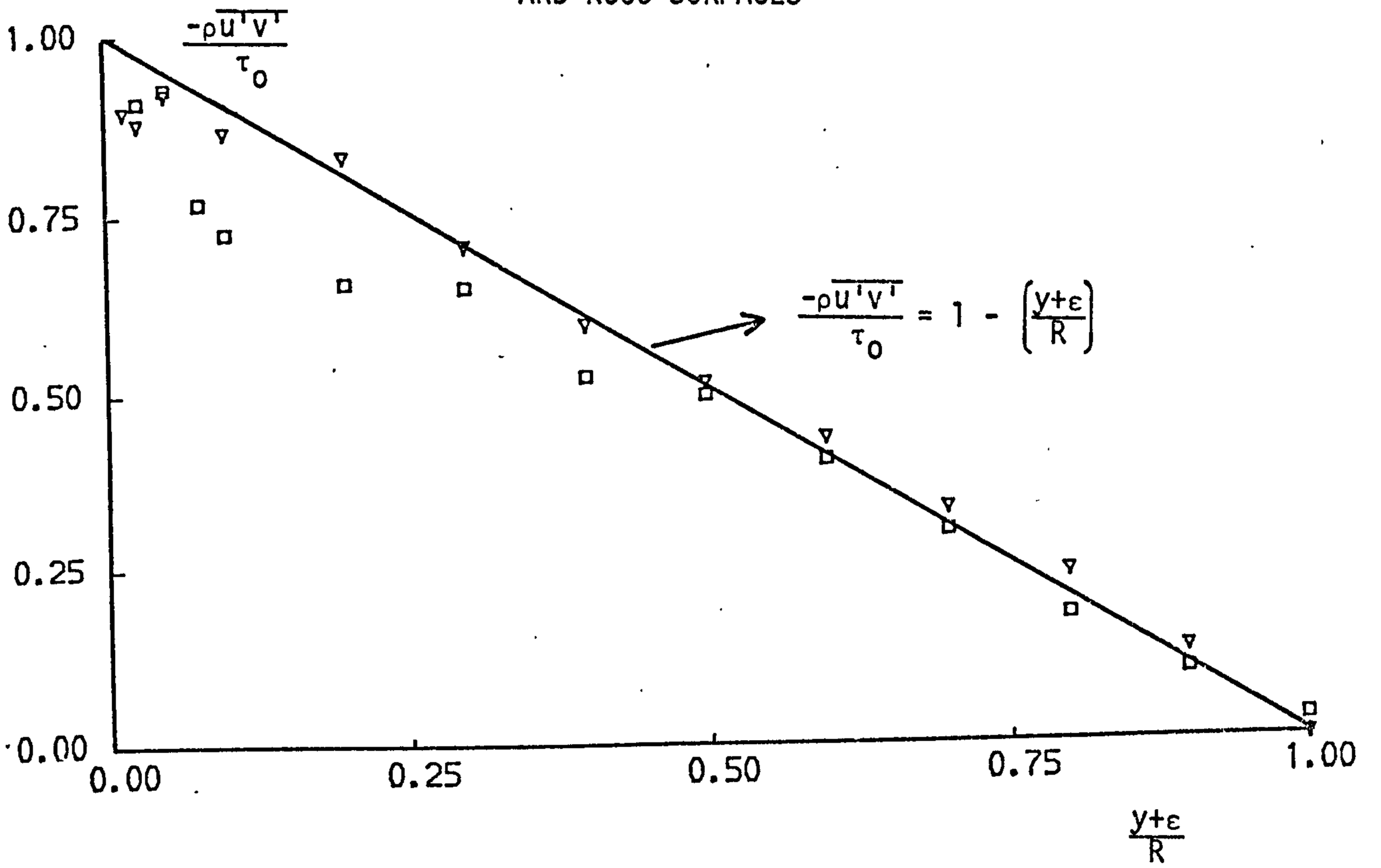

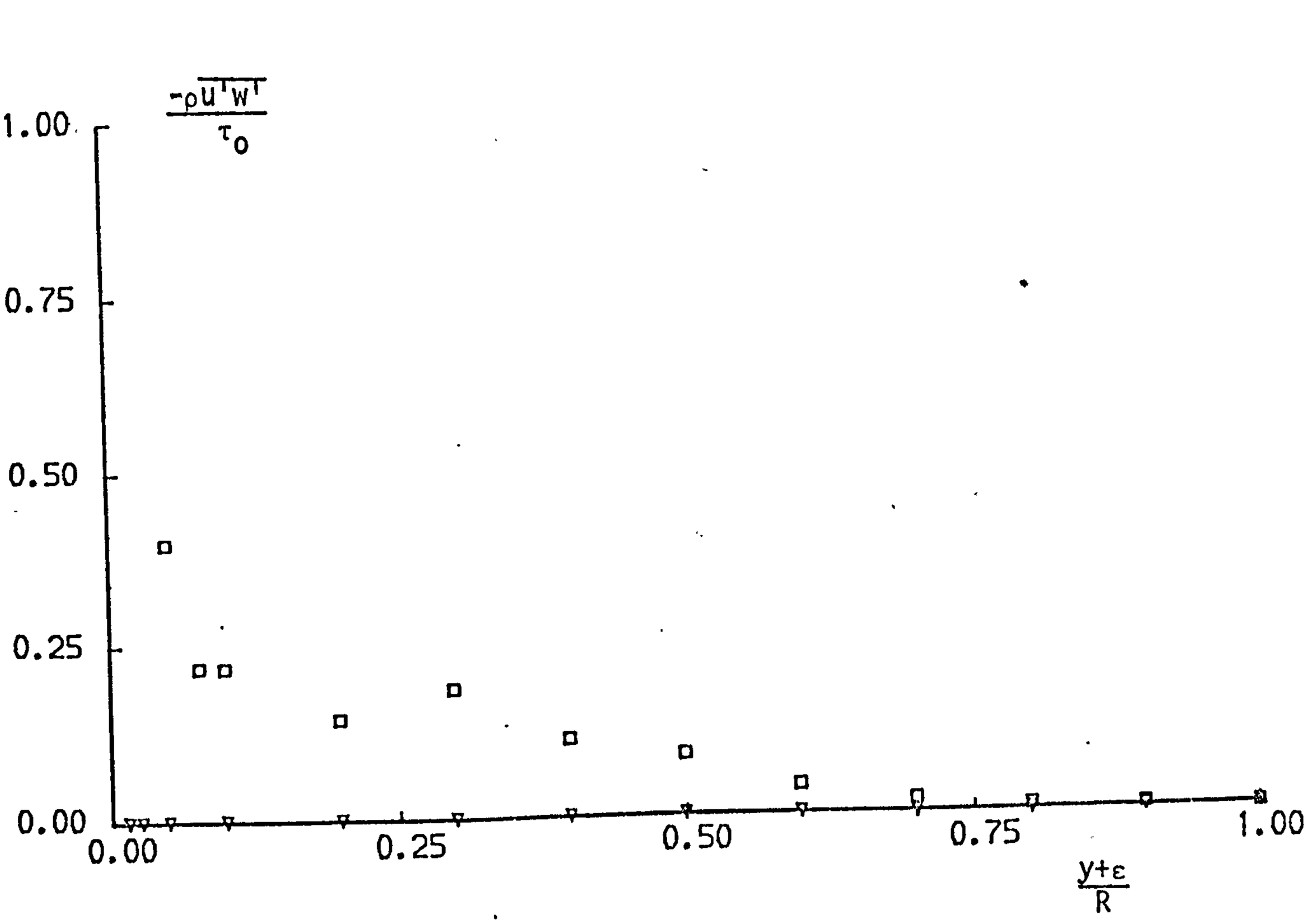

▽ Smooth
□ R550
} $R_e = 9.5 \times 10^4$

FIG. 3.29 TURBULENT SHEAR STRESS FOR THE SURFACE R420

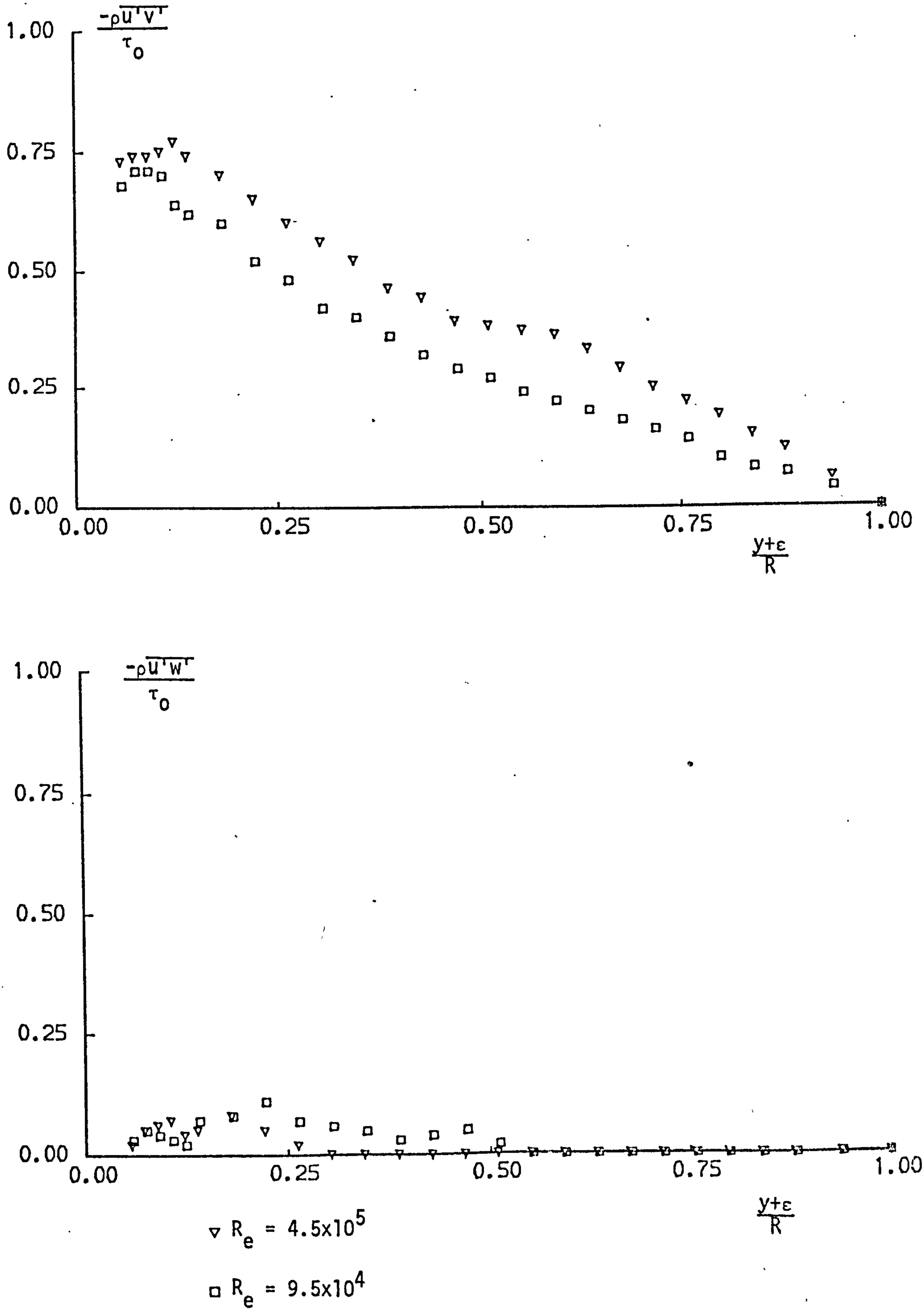

FIG. 3.30 TURBULENT SHEAR STRESSES FOR THE SURFACE R345

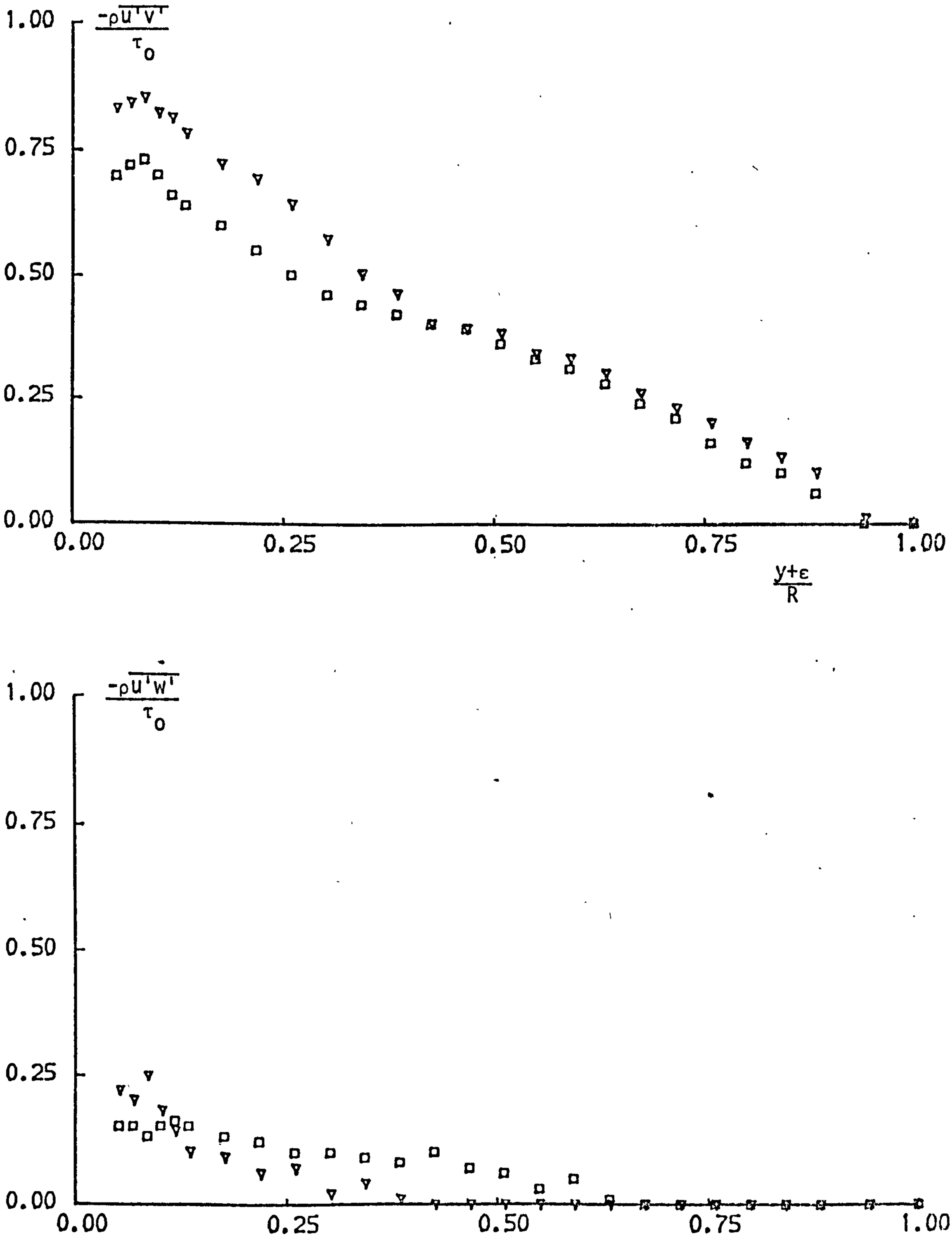

FIG. 3.31 TURBULENT SHEAR STRESSES FOR THE SURFACE R253

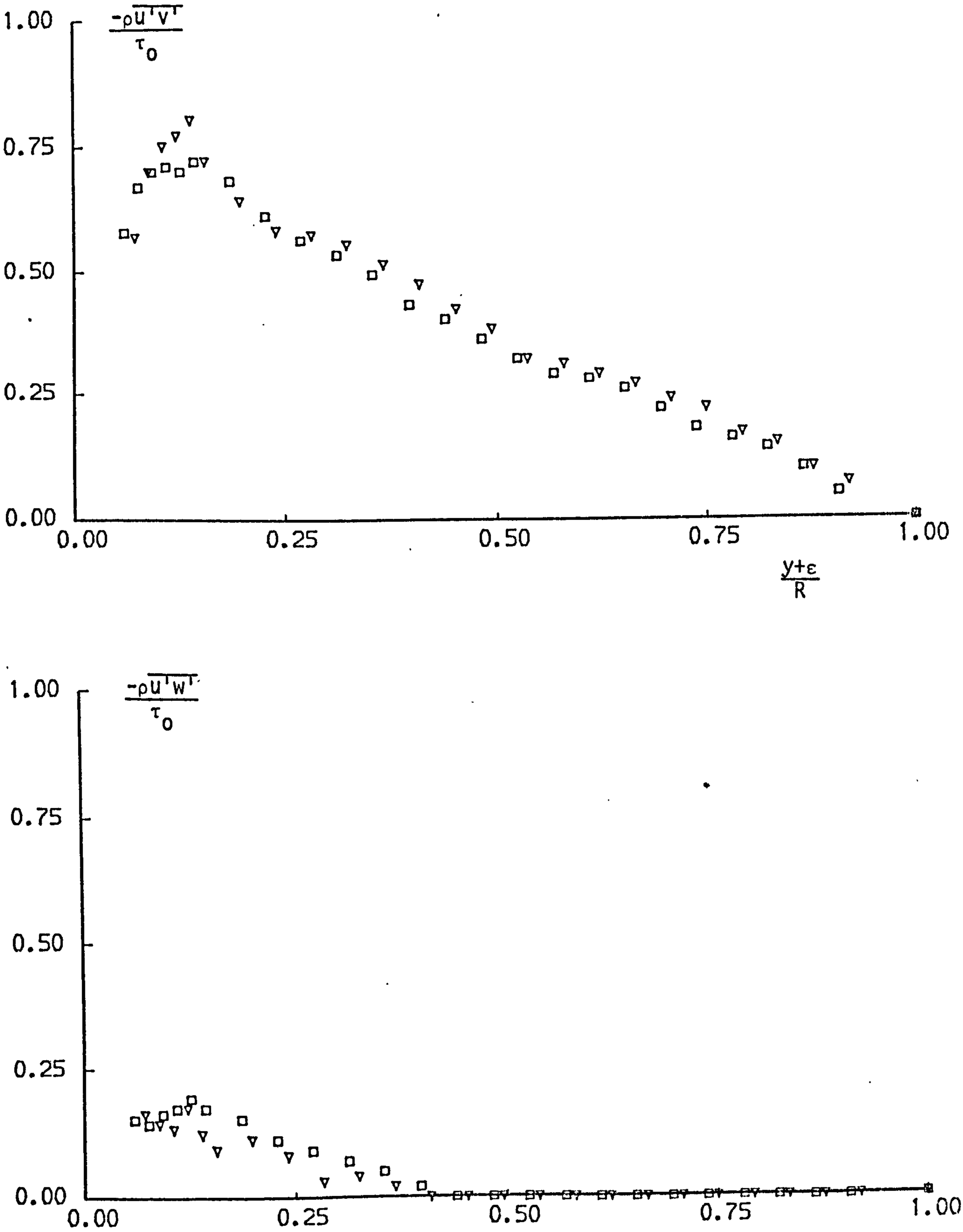

FIG. 3.32 TURBULENT SHEAR STRESSES FOR THE SURFACE R173

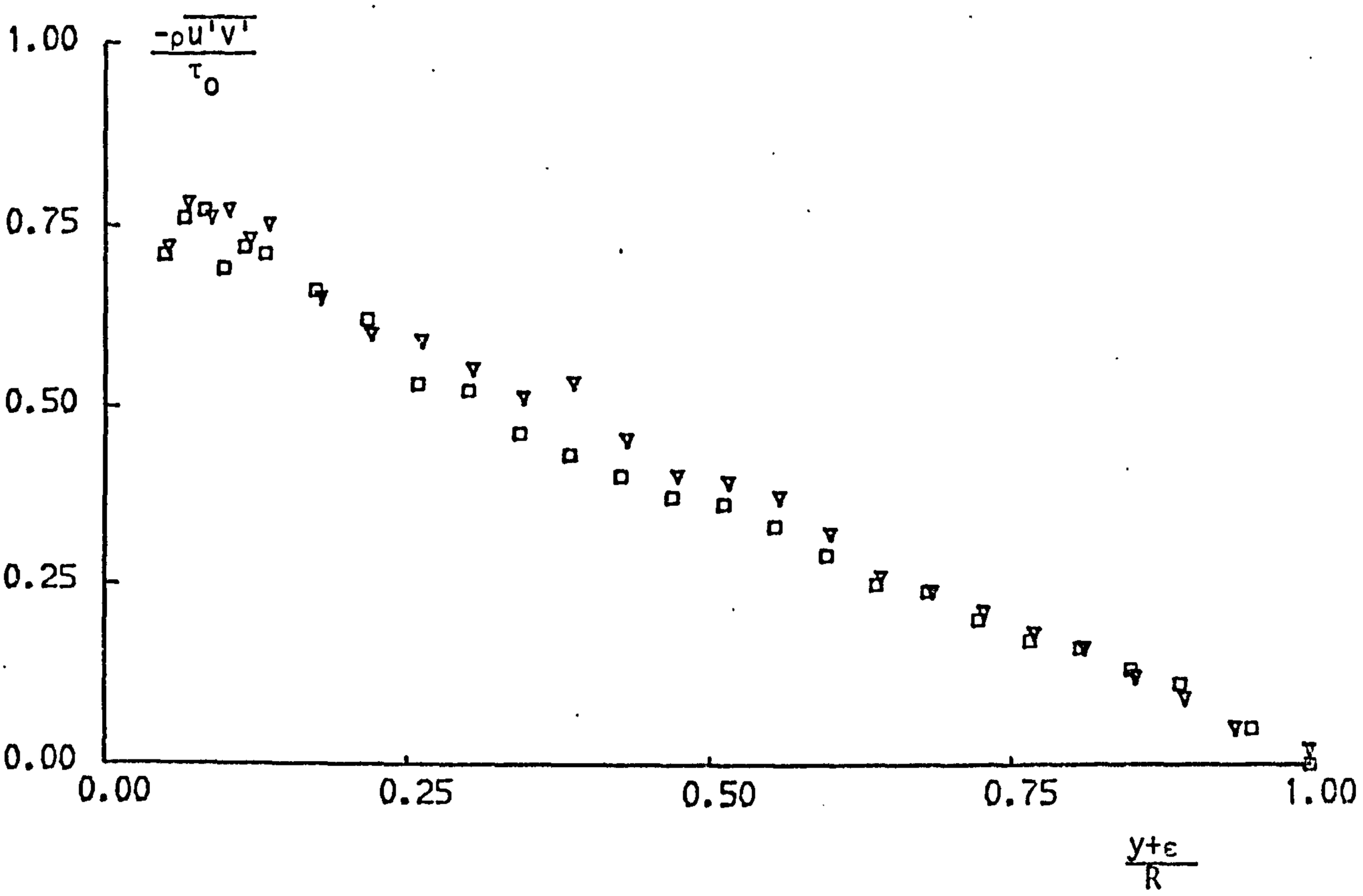

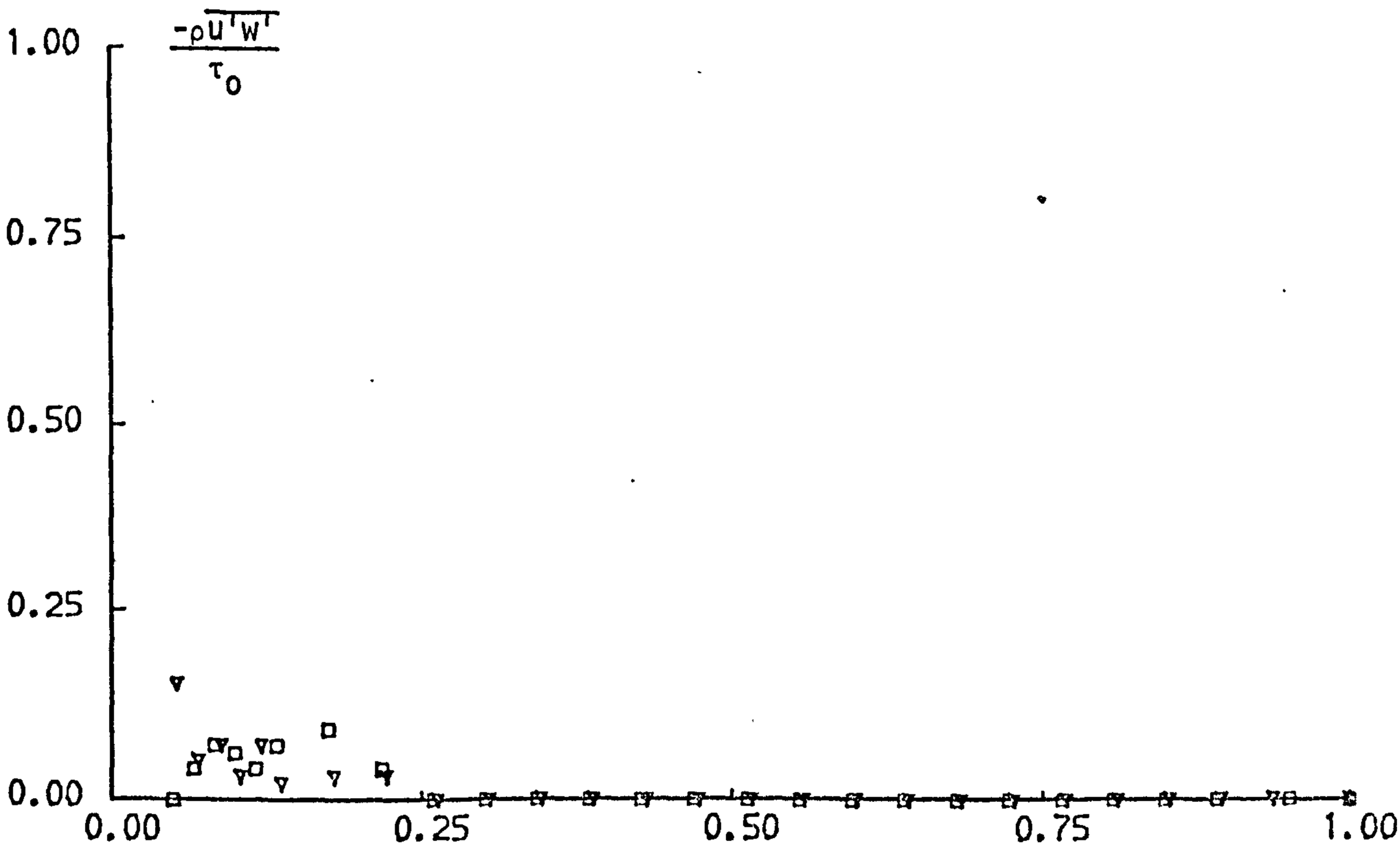

▽ $R_e = 4.5 \times 10^4$

□ $R_e = 9.5 \times 10^4$

FIG. 3.33 FREQUENCY SPECTRA OF THE LONGITUDINAL FLUCTUATING VELOCITY AT $R_e = 4.5 \times 10^4$ AND $\frac{y+\varepsilon}{R} = 0.02$

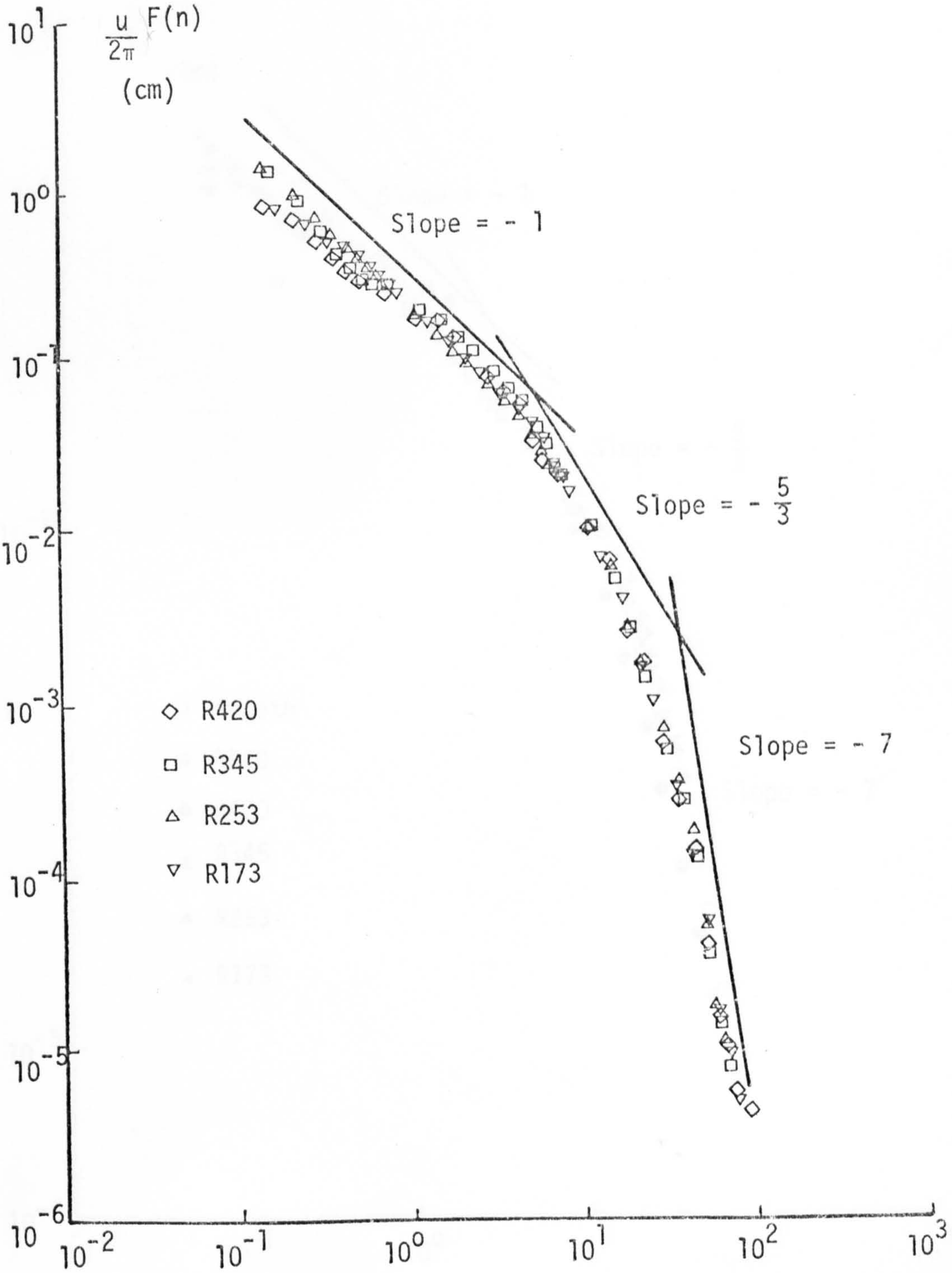

FIG. 3.34 FREQUENCY SPECTRA OF THE LONGITUDINAL FLUCTUATING VELOCITY AT $R_e = 9.5 \times 10^4$ AND $\frac{y+\varepsilon}{R} = 0.02$

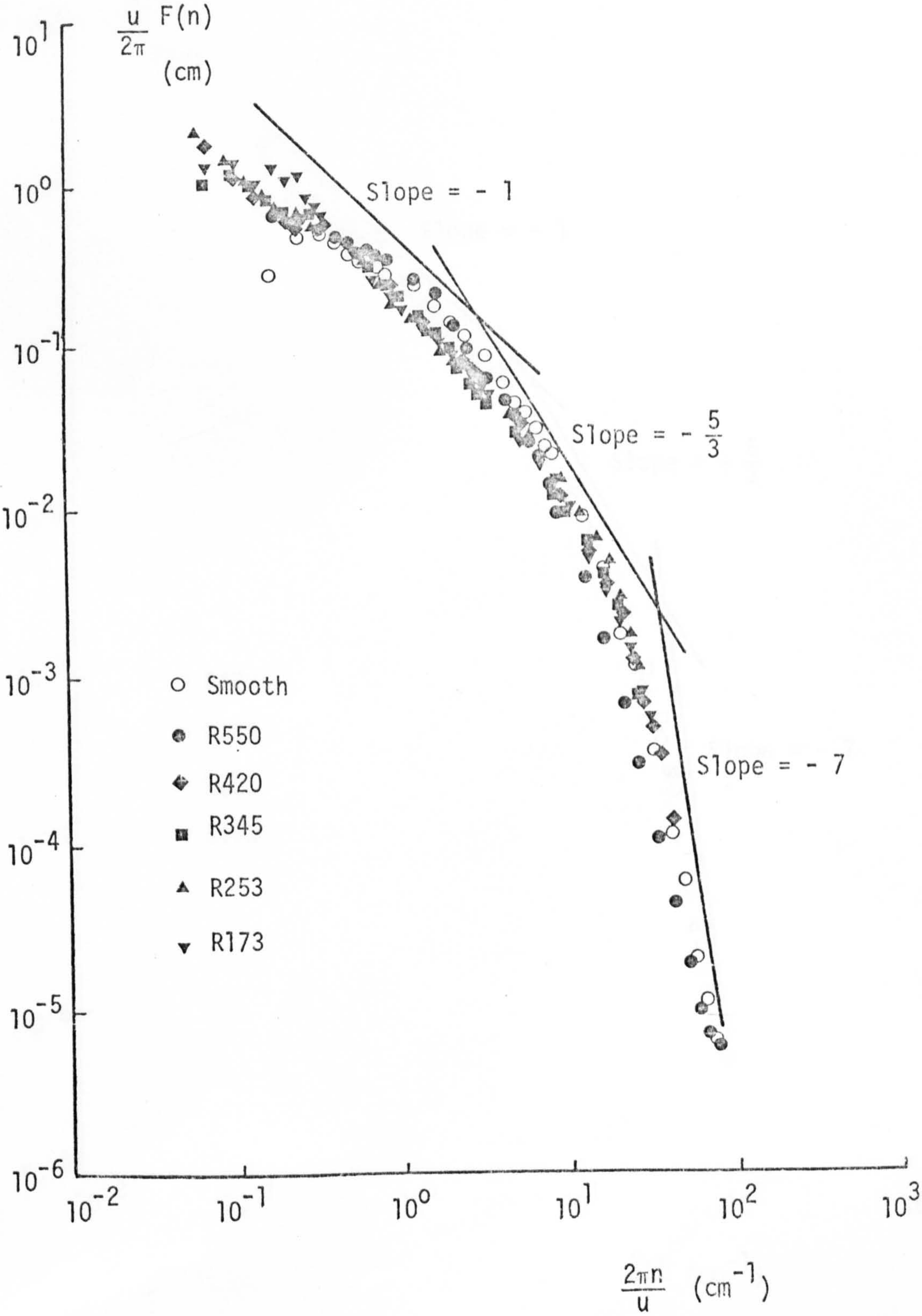

FIG. 3.35 FREQUENCY SPECTRA OF THE LONGITUDINAL FLUCTUATING VELOCITY AT $R_e = 4.5 \times 10^4$ AND $\frac{y+\varepsilon}{R} = 0.08$

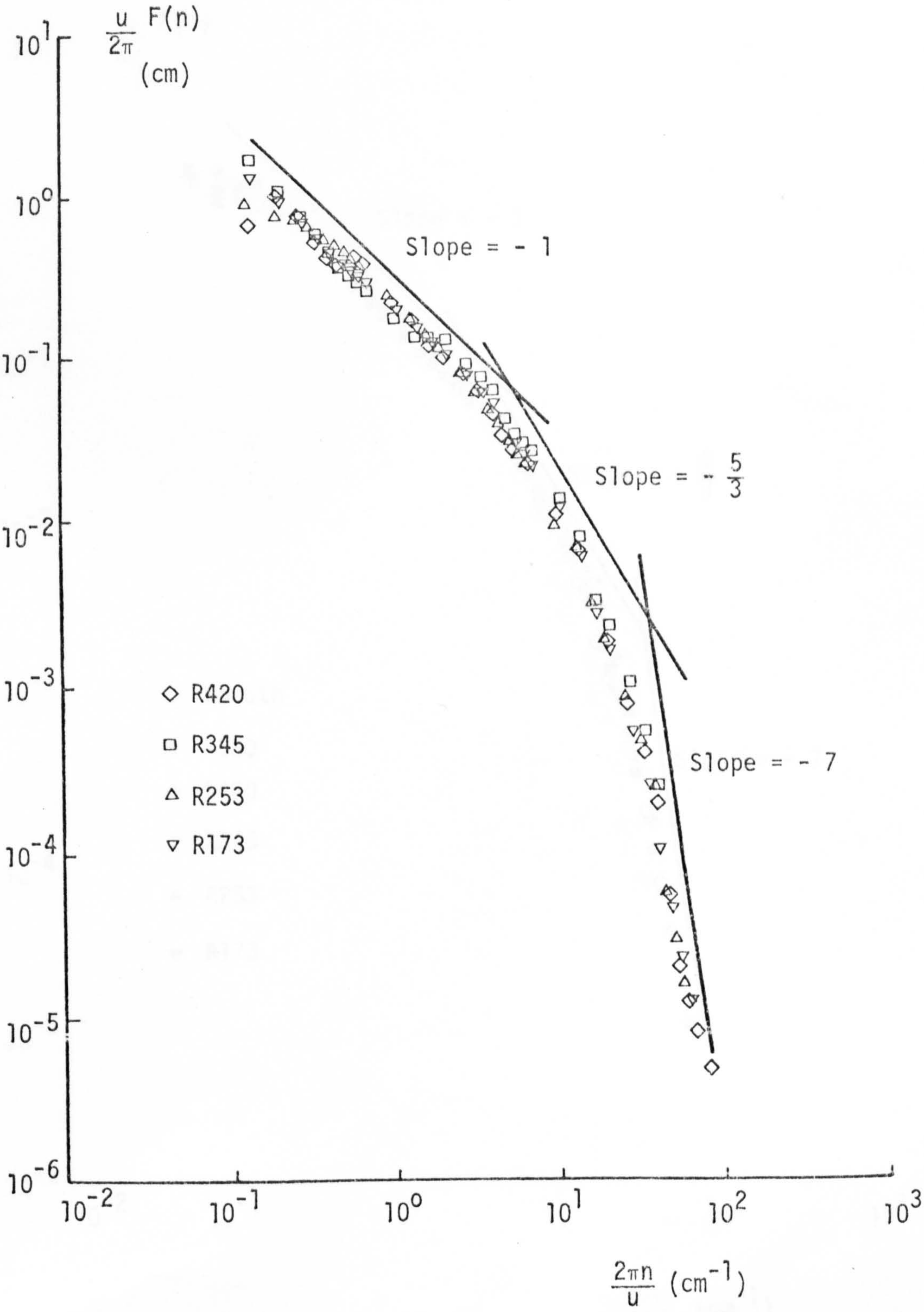

FIG. 3.36 FREQUENCY SPECTRA OF THE LONGITUDINAL FLUCTUATING VELOCITY AT $R_e = 9.5 \times 10^4$ AND $\frac{y+\varepsilon}{R} = 0.08$

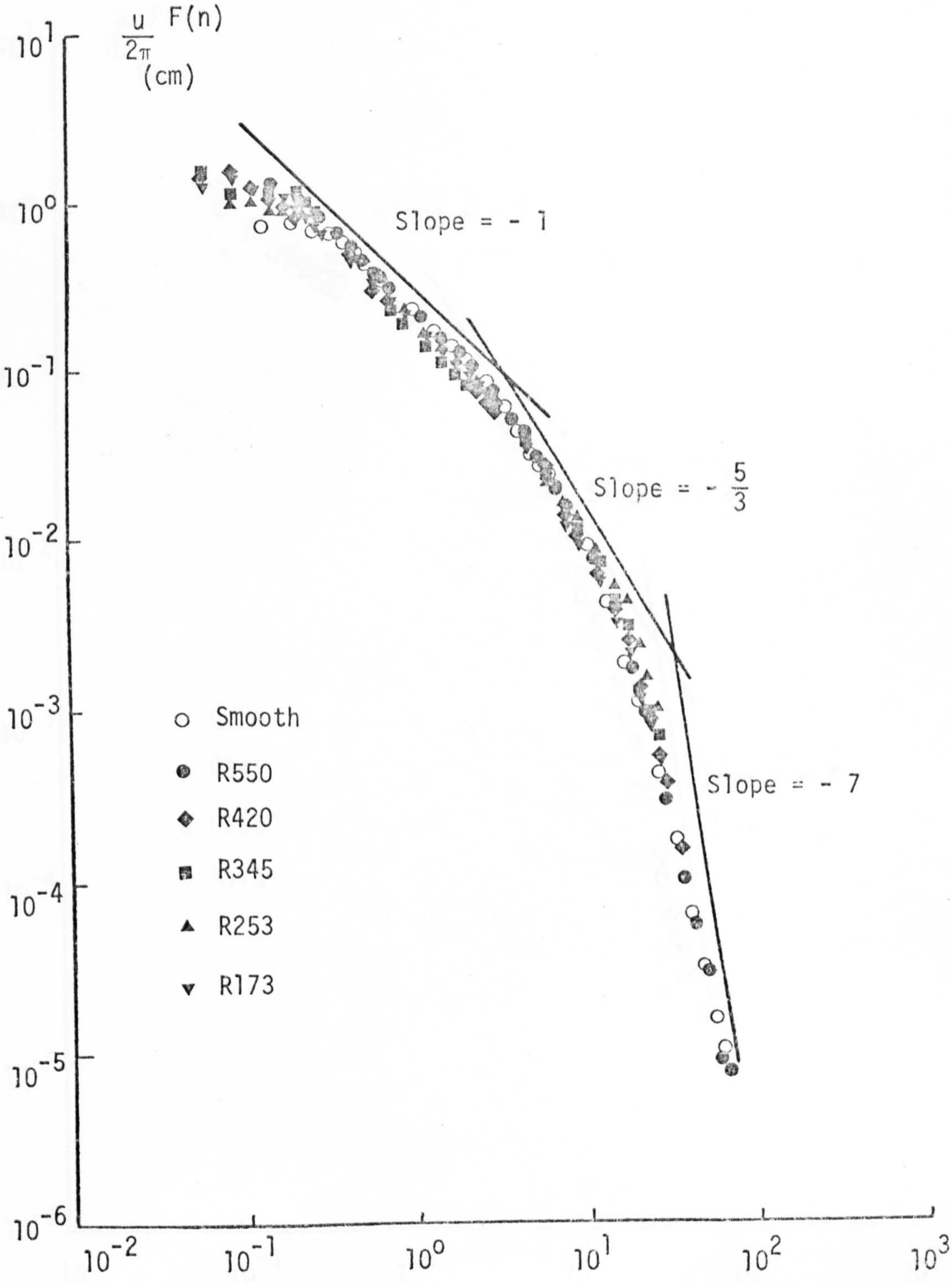

FIG. 3.37 FREQUENCY SPECTRA OF THE LONGITUDINAL FLUCTUATING VELOCITY AT $R_e = 4.5 \times 10^4$ AND $\frac{y+\varepsilon}{R} = 1$

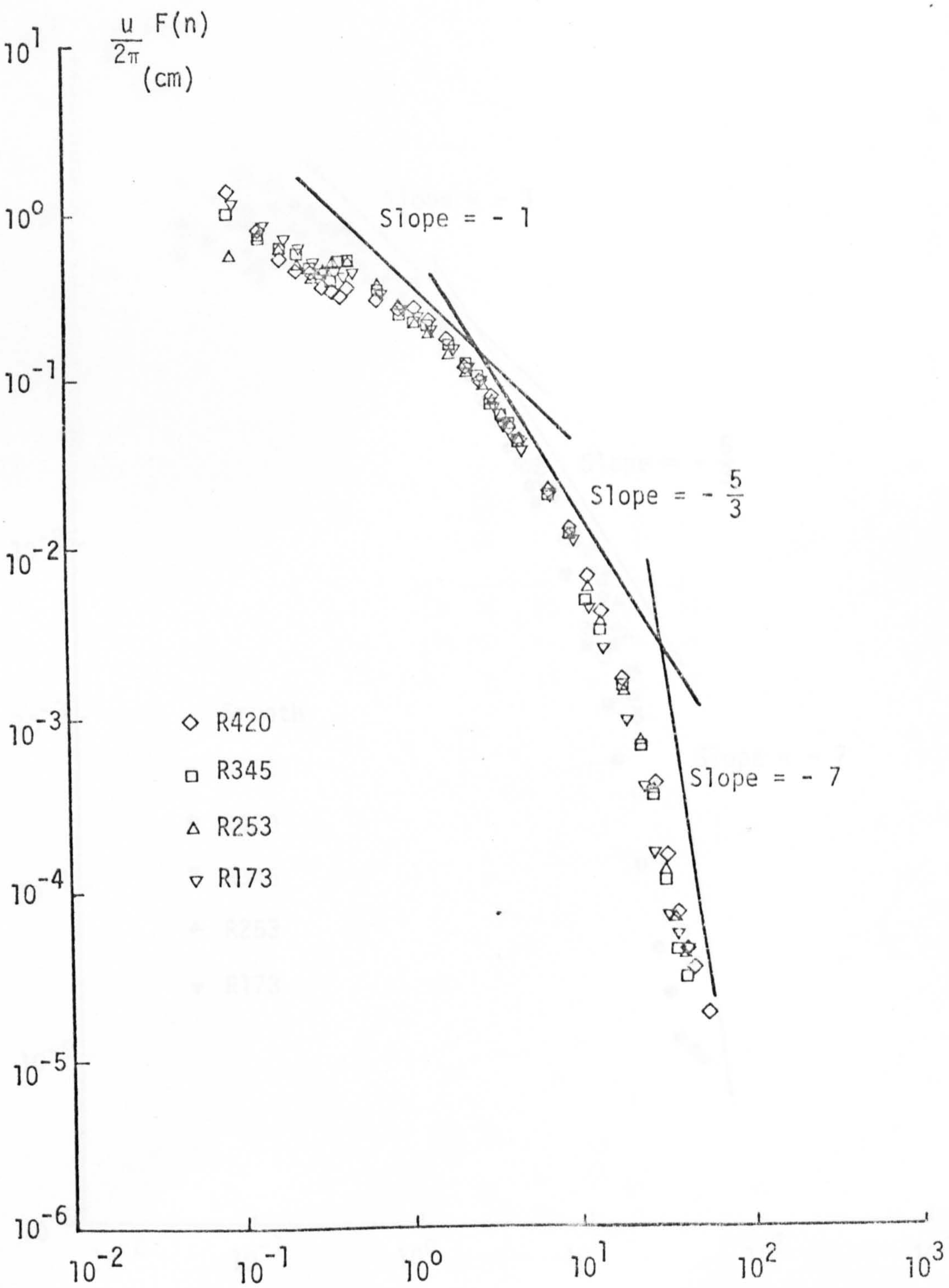

FIG. 3.38 FREQUENCY SPECTRA OF THE LONGITUDINAL FLUCTUATING VELOCITY AT $R_e = 9.5 \times 10^4$ AND $\frac{y+\varepsilon}{R} = 1$

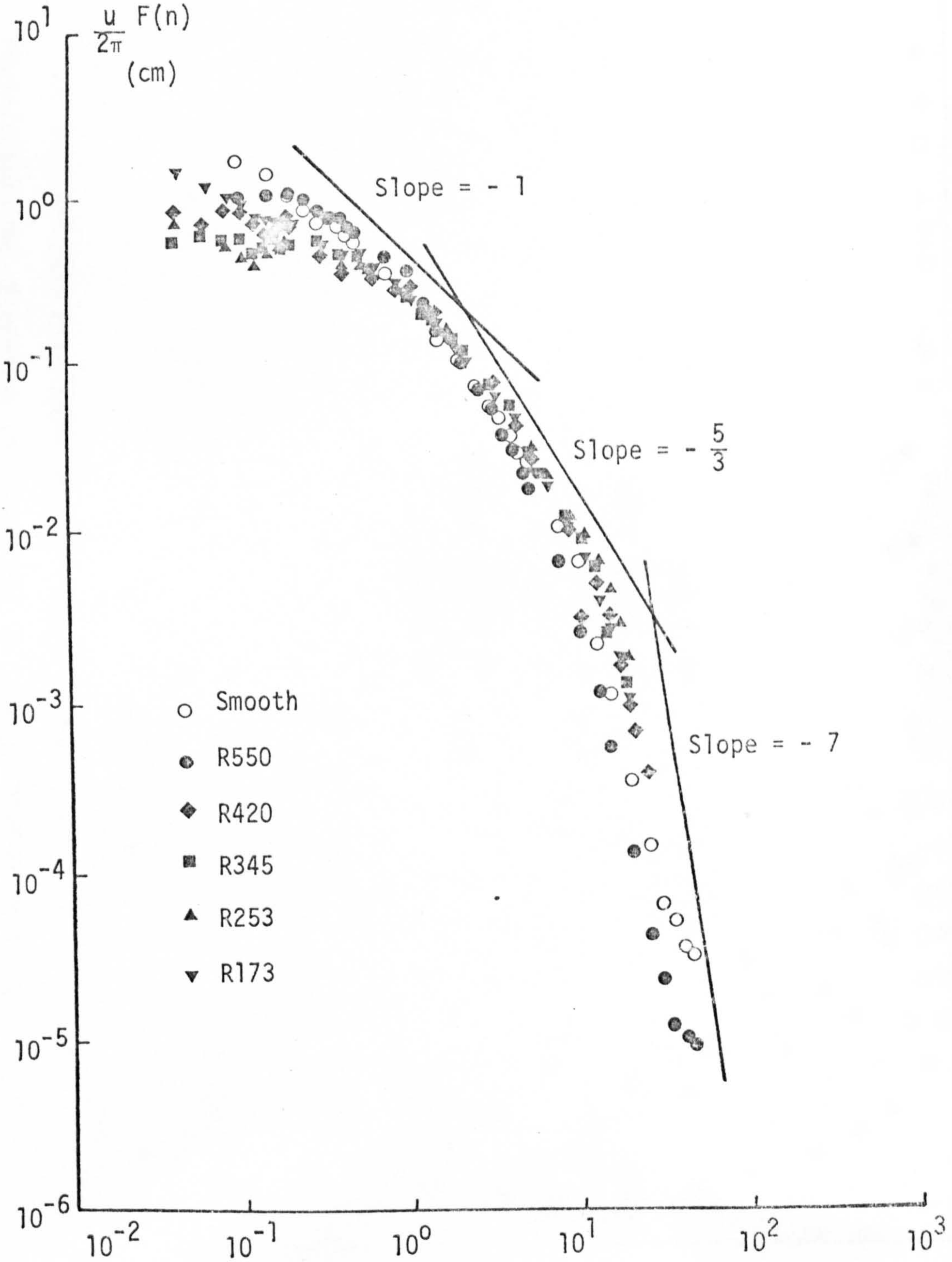

FIG. 3.39 SECOND MOMENTS OF THE FREQUENCY SPECTRA OF THE LONGITUDINAL FLUCTUATING VELOCITY FOR THE SMOOTH AND R550 SURFACES AT $R_e = 9.5 \times 10^4$

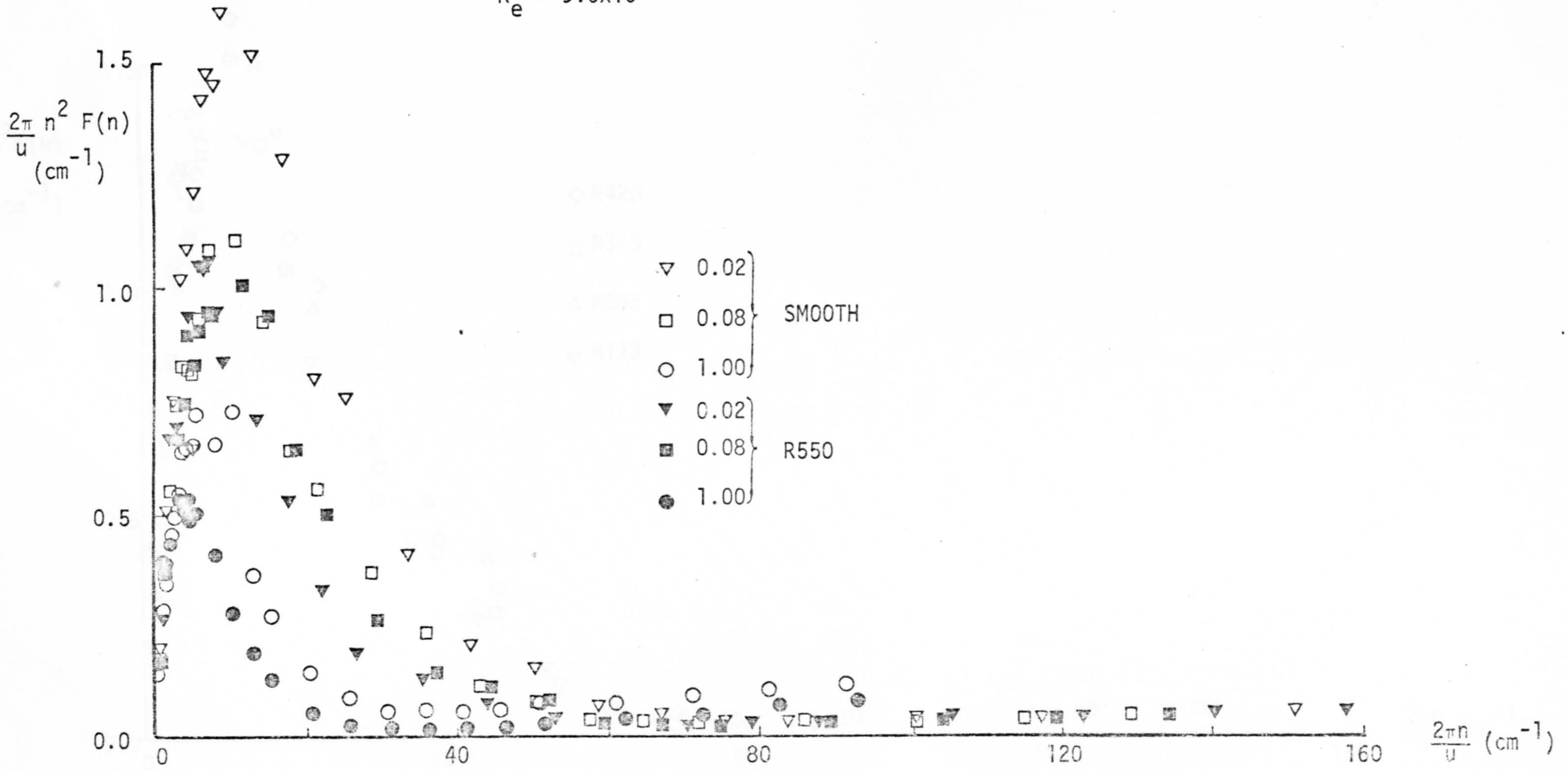

FIG. 3.40 SECOND MOMENTS OF THE FREQUENCY SPECTRA OF THE LONGITUDINAL FLUCTUATING VELOCITY AT $R_e = 4.5 \times 10^4$ AND $\frac{y+\epsilon}{R} = 0.02$

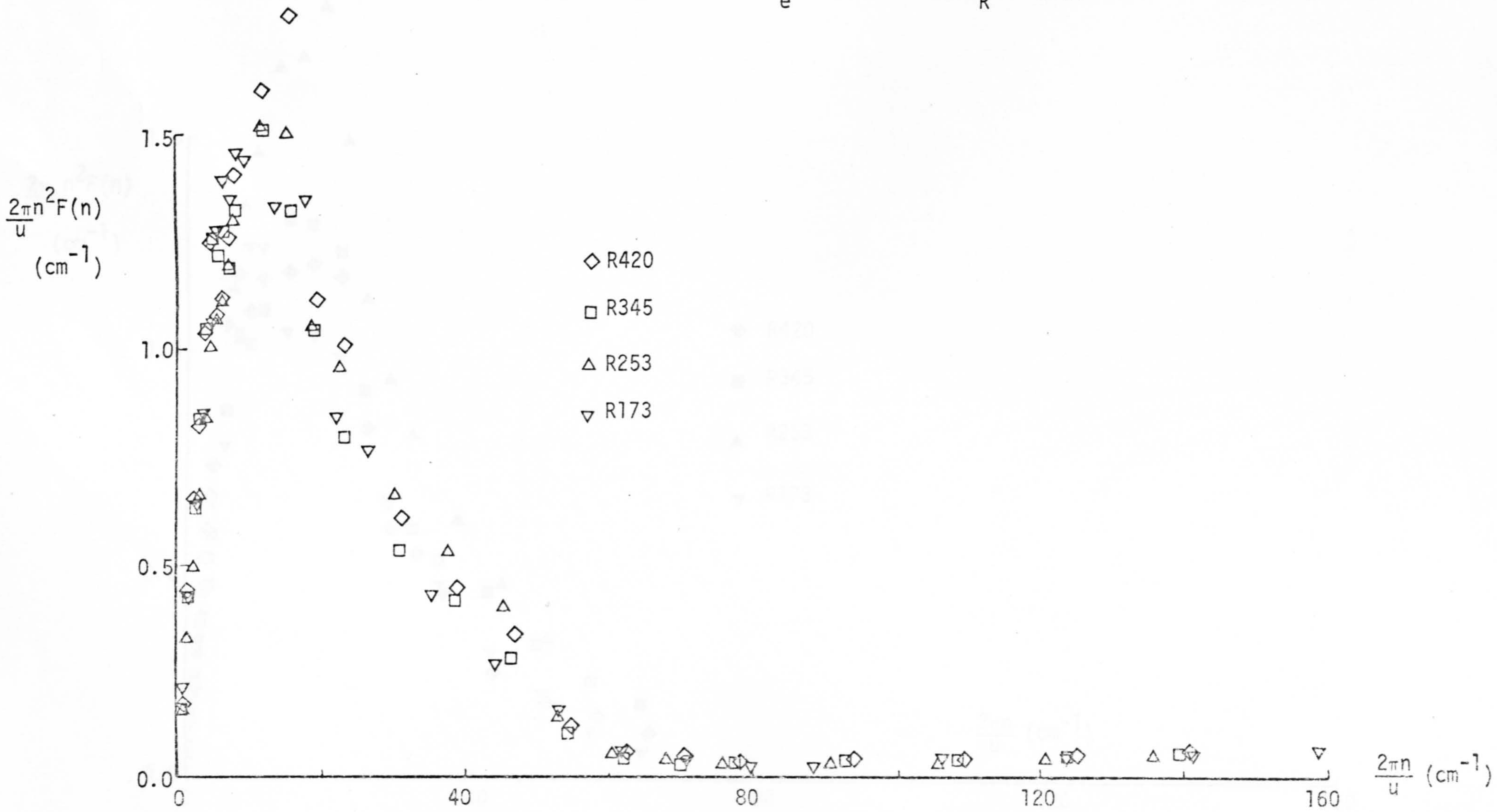

FIG. 3.41 SECOND MOMENTS OF THE FREQUENCY SPECTRA OF THE LONGITUDINAL FLUCTUATING VELOCITY AT $R_e = 9.5 \times 10^4$ AND $\frac{y+\varepsilon}{R} = 0.02$

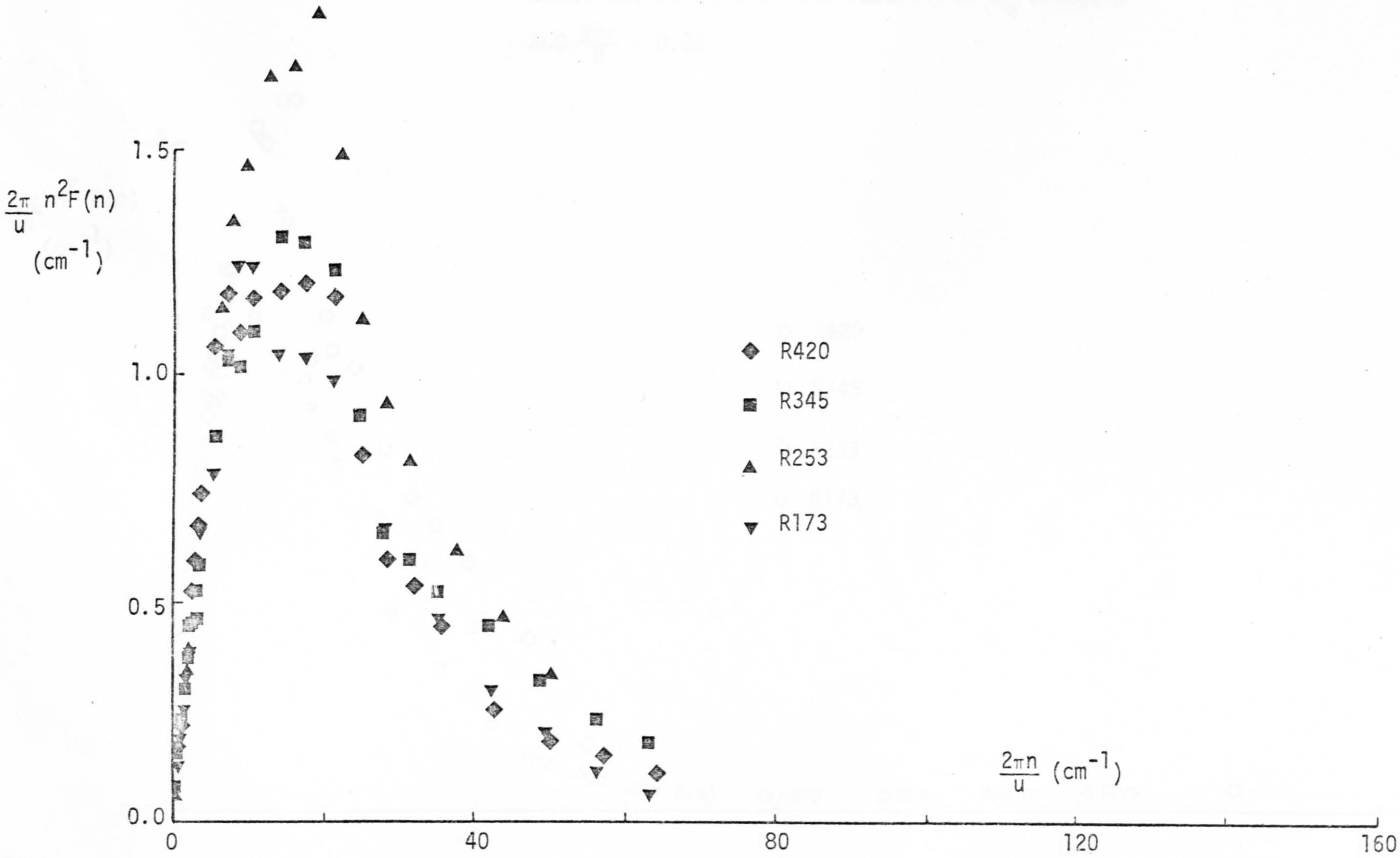

FIG. 3.42 SECOND MOMENTS OF THE FREQUENCY SPECTRA OF THE LONGITUDINAL FLUCTUATING VELOCITY AT $R_e = 4.5 \times 10^4$ AND $\frac{y+\varepsilon}{R} = 0.08$

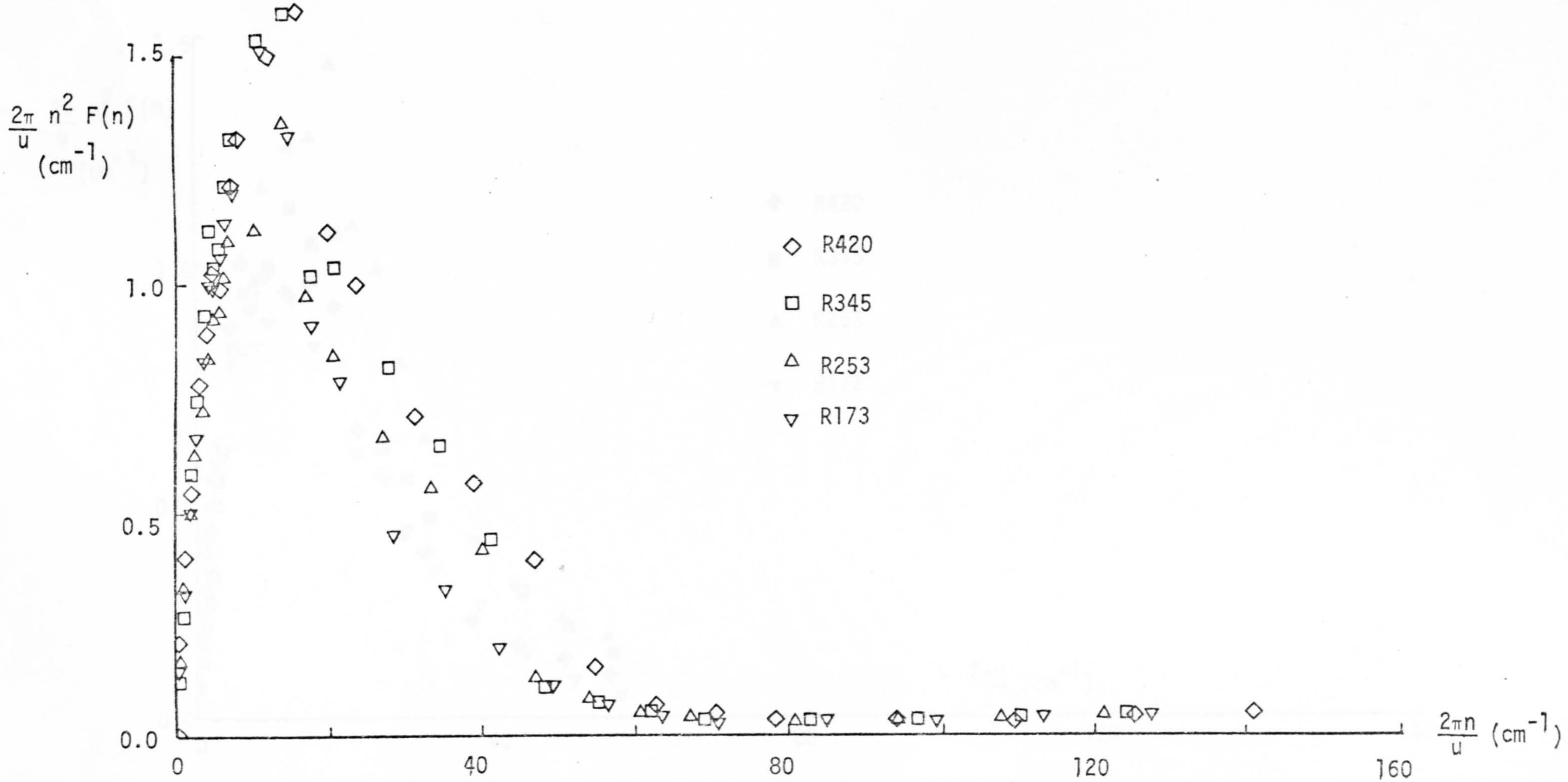

FIG. 3.43 SECOND MOMENTS OF THE FREQUENCY SPECTRA OF THE LONGITUDINAL FLUCTUATING VELOCITY AT $R_e = 9.5 \times 10^4$ AND $\frac{y+\varepsilon}{R} = 0.08$

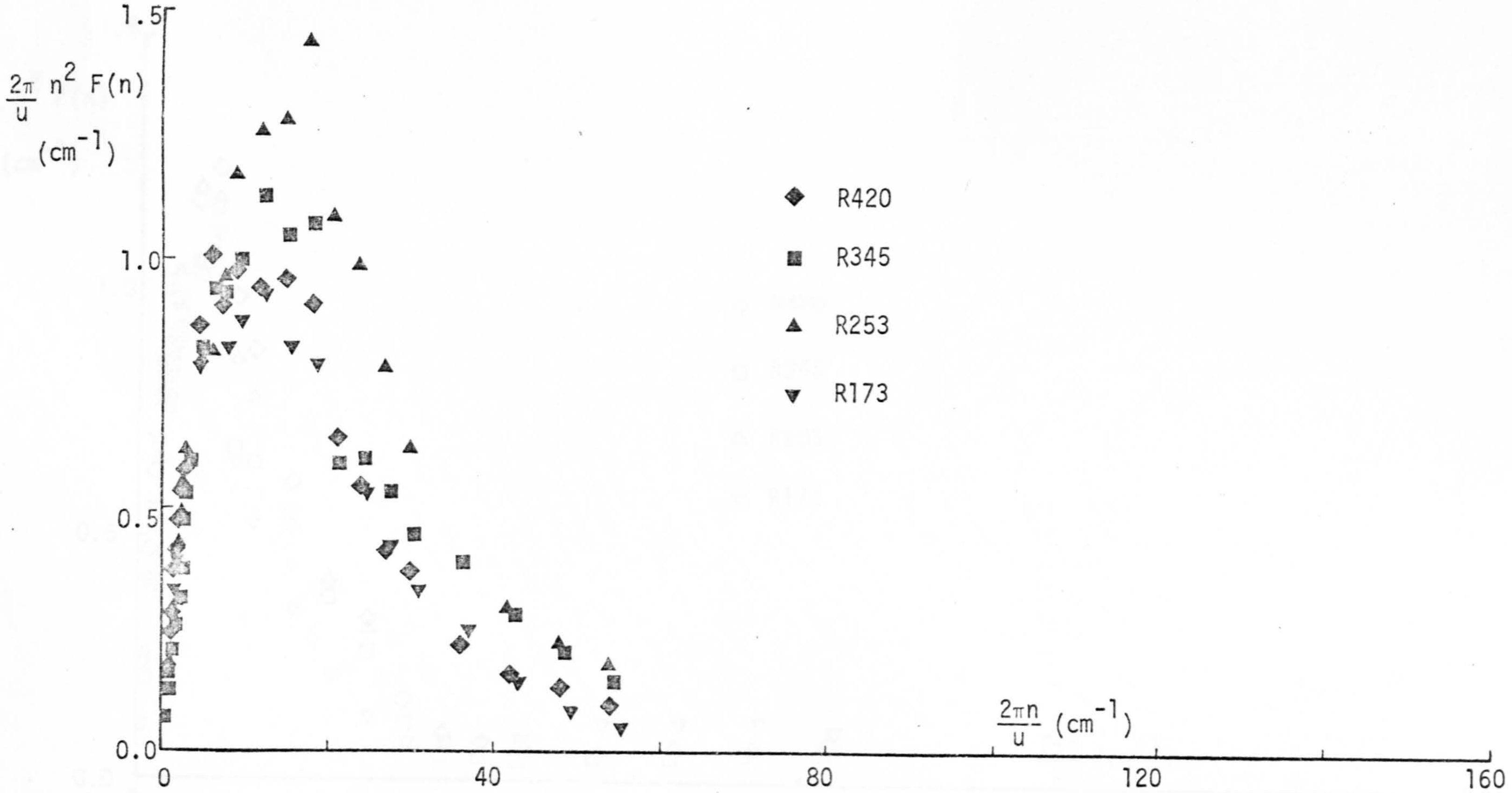

FIG. 3.44 SECOND MOMENTS OF THE FREQUENCY SPECTRA OF THE LONGITUDINAL FLUCTUATING VELOCITY AT $R_e = 4.5 \times 10^4$ AND $\frac{y+\varepsilon}{R} = 1$

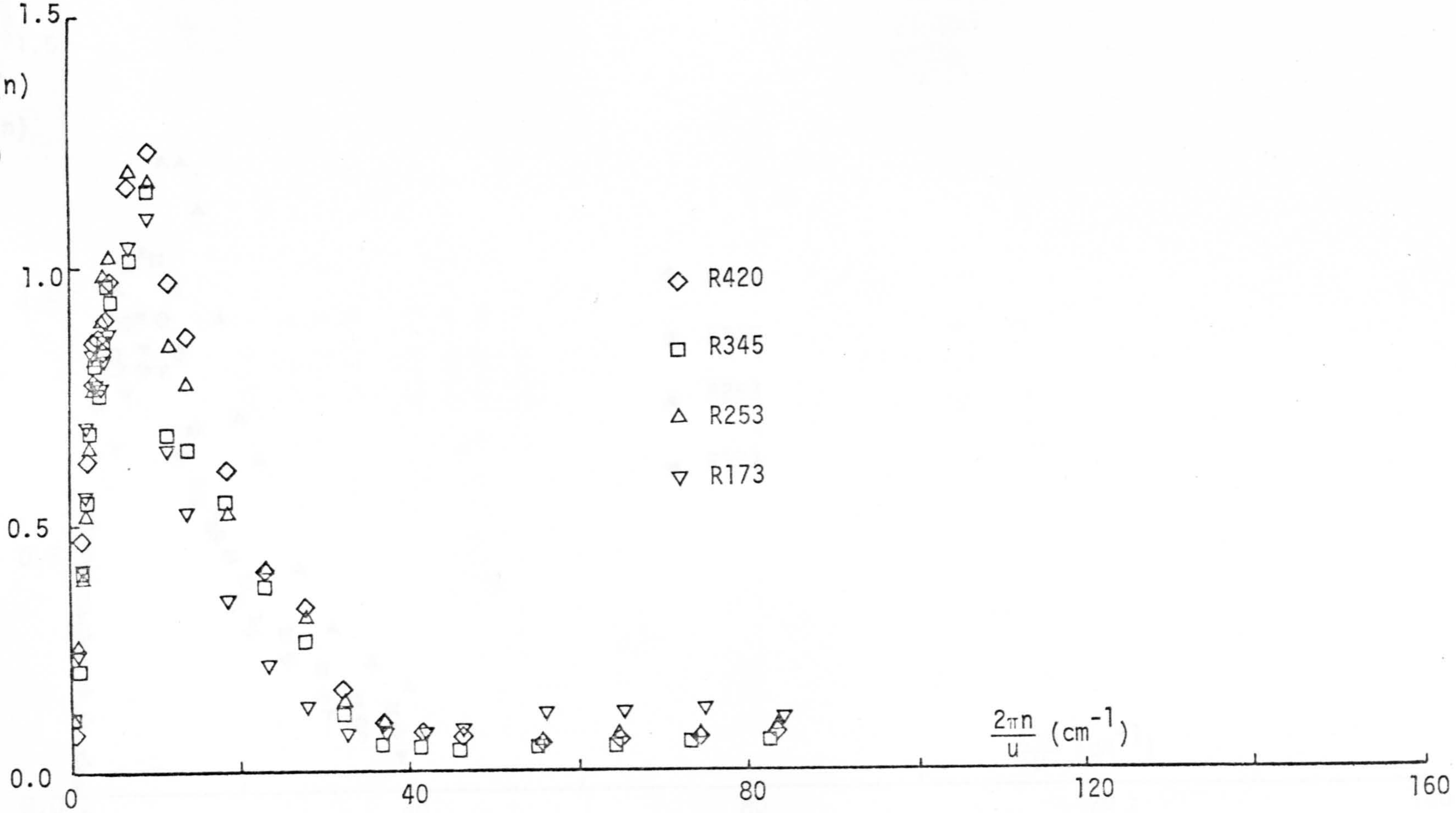

FIG. 3.45 SECOND MOMENTS OF THE FREQUENCY SPECTRA OF THE LONGITUDINAL FLUCTUATING VELOCITY AT $R_e = 9.5 \times 10^4$ AND $\frac{y+\varepsilon}{R} = 1$

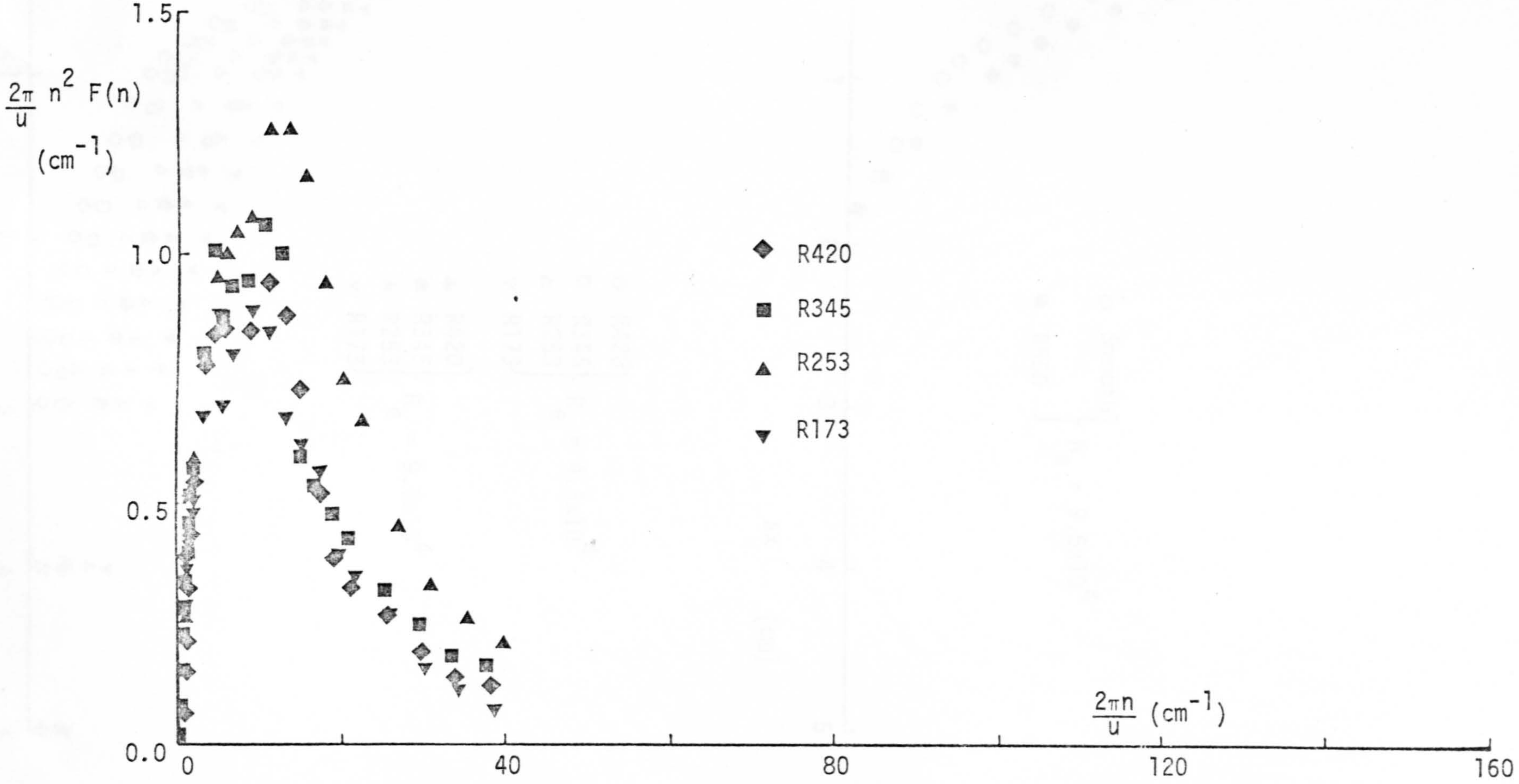

FIG. 3.46 LONGITUDINAL SPATIAL CORRELATION COEFFICIENT AT $\frac{y+\varepsilon}{R} = 0.02$

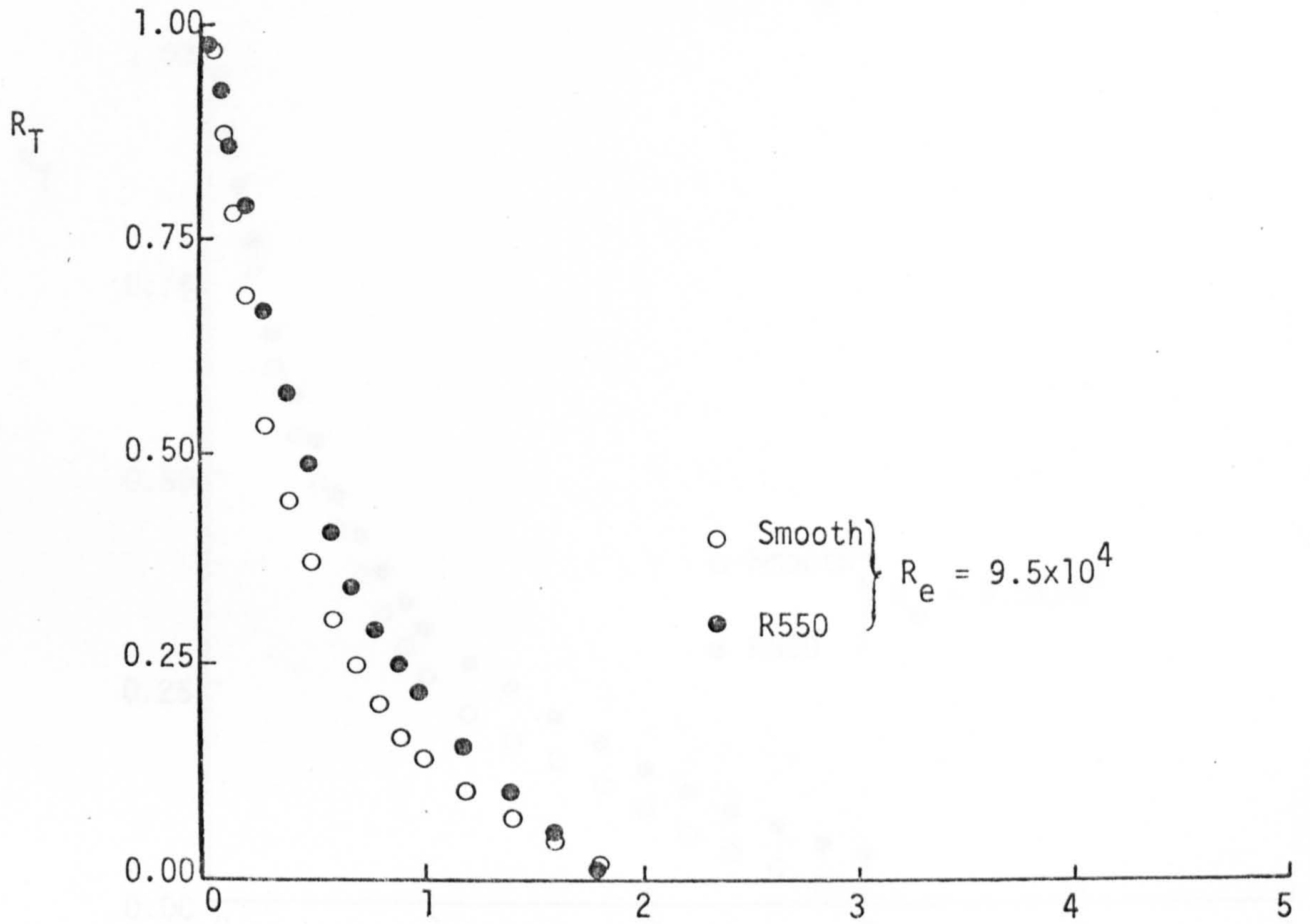

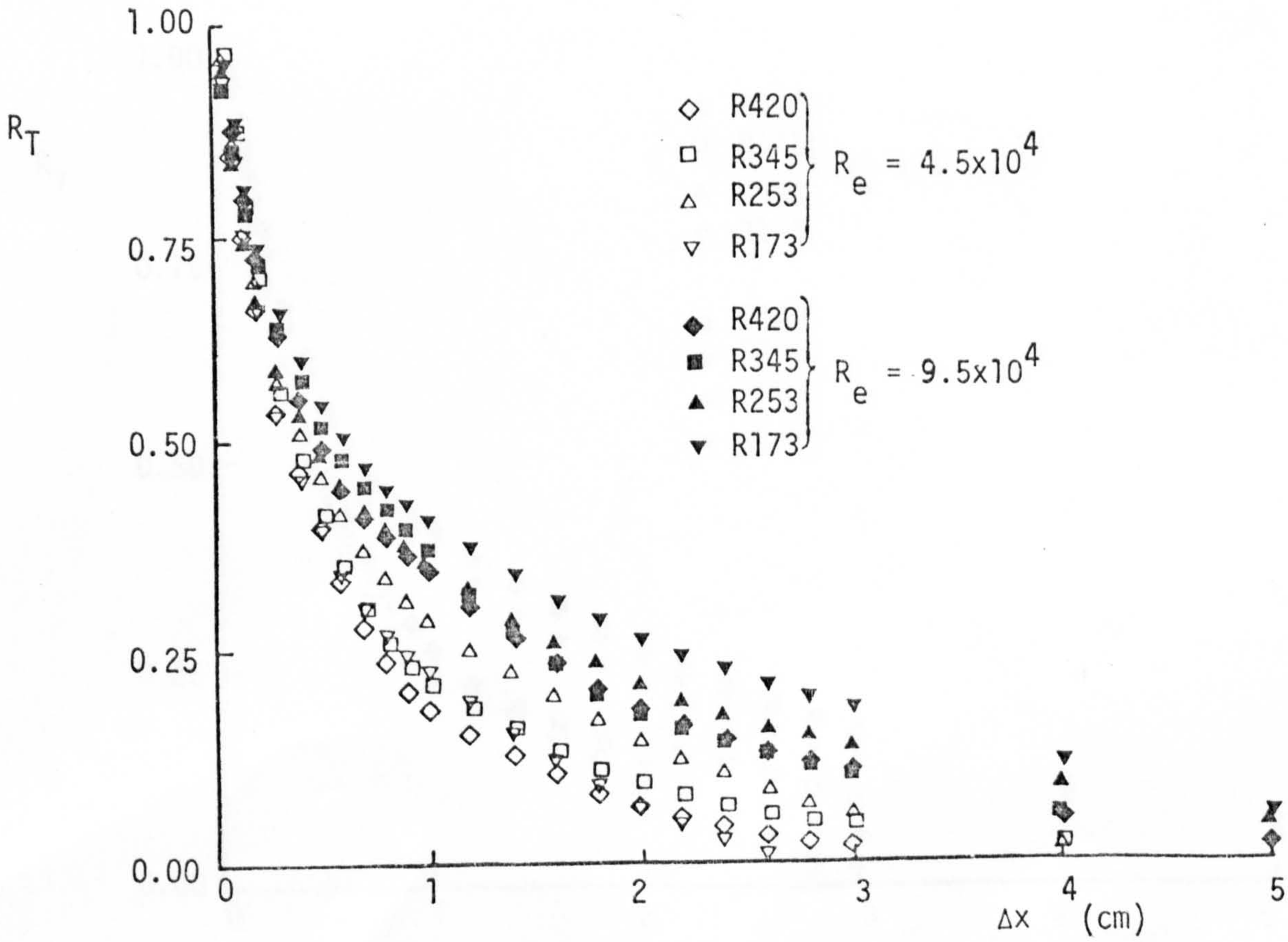

FIG. 3.47 LONGITUDINAL SPATIAL CORRELATION COEFFICIENT AT $\frac{y+\varepsilon}{R}$ = 0.08

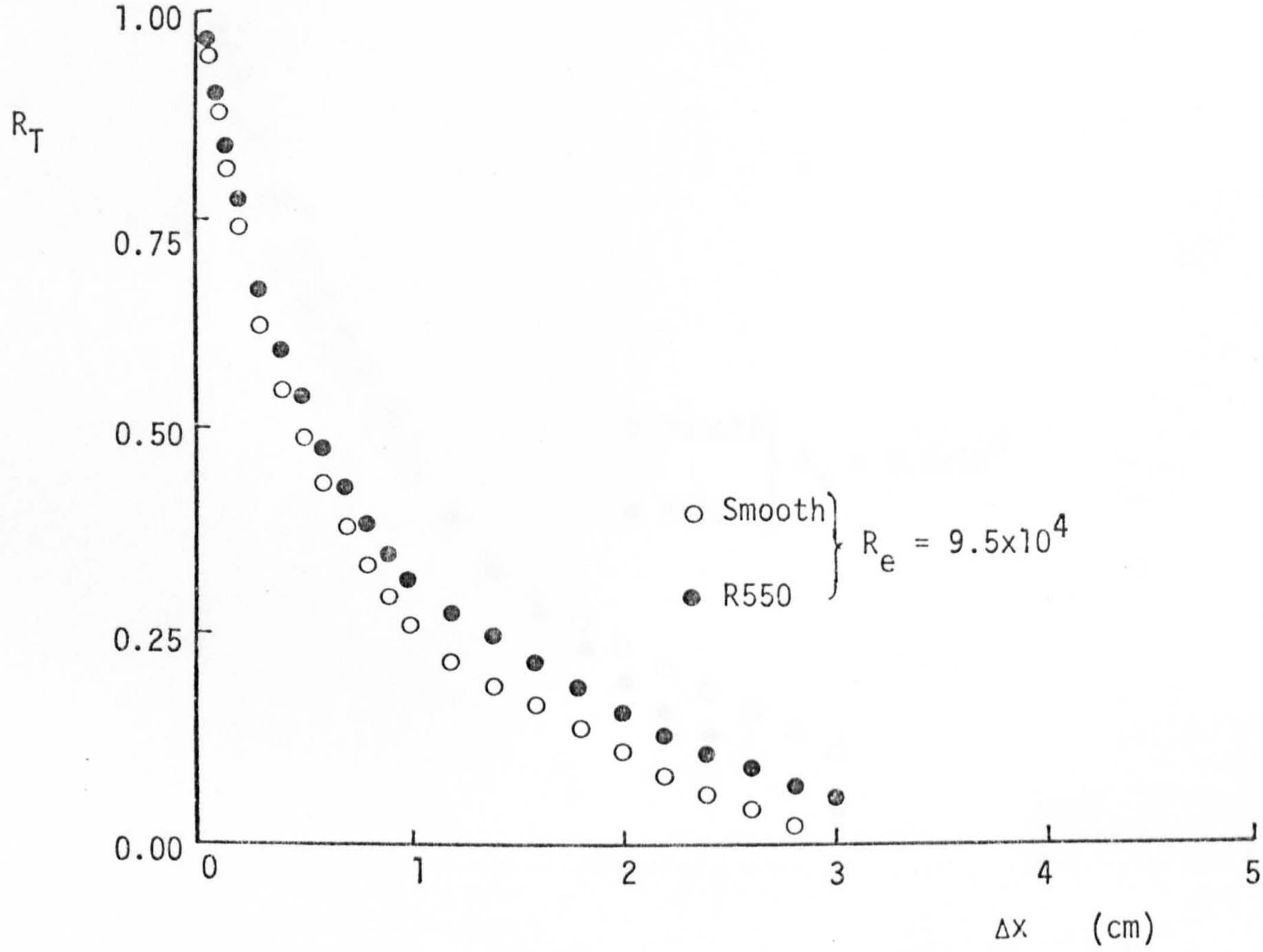

FIG. 3.48 LONGITUDINAL SPATIAL CORRELATION COEFFICIENT AT $\frac{y+\varepsilon}{R} = 1$

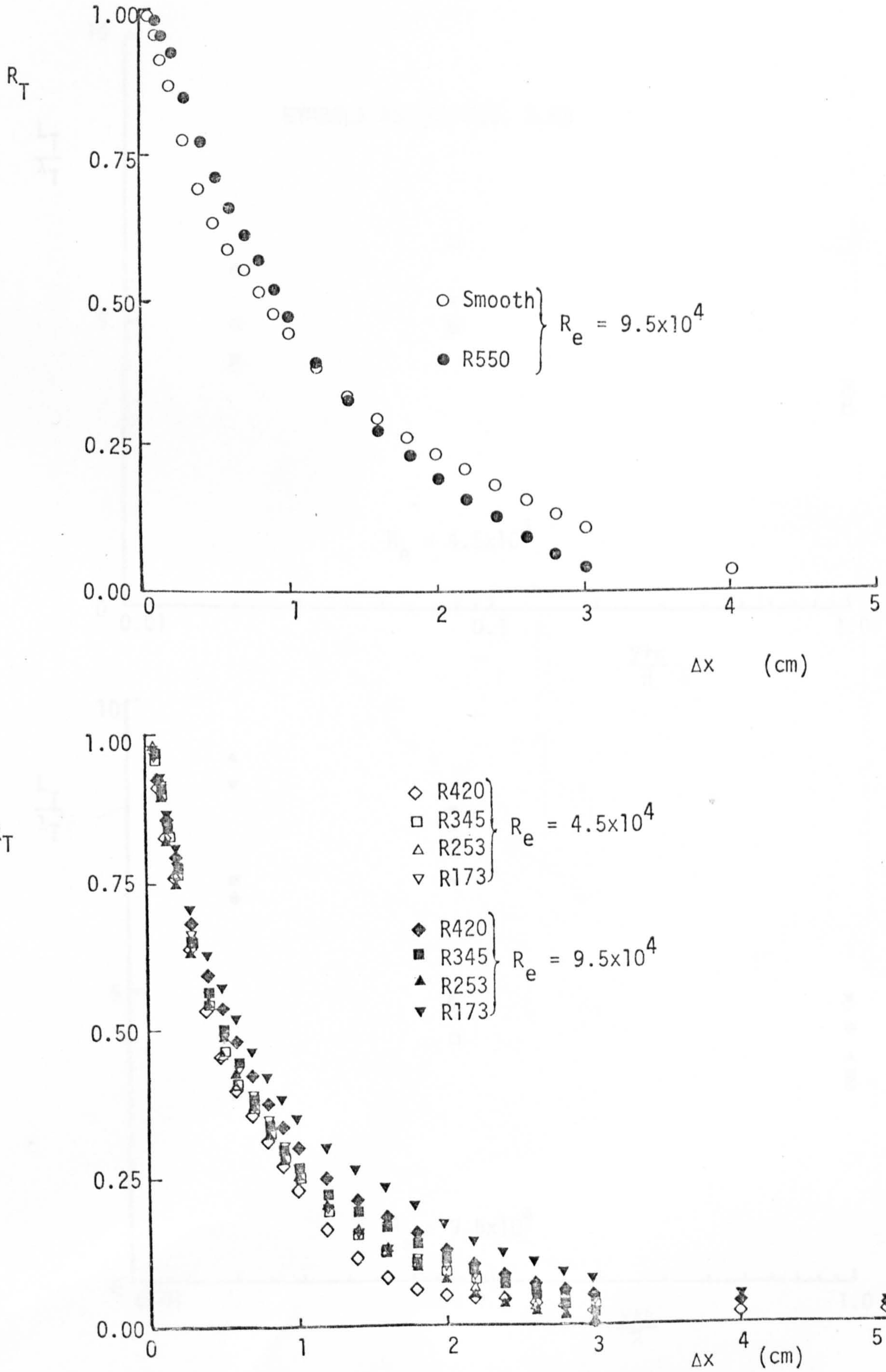

FIG. 3.49 DISTRIBUTIONS OF THE RATIO OF THE MACRO-SCALE TO THE MICRO-SCALE

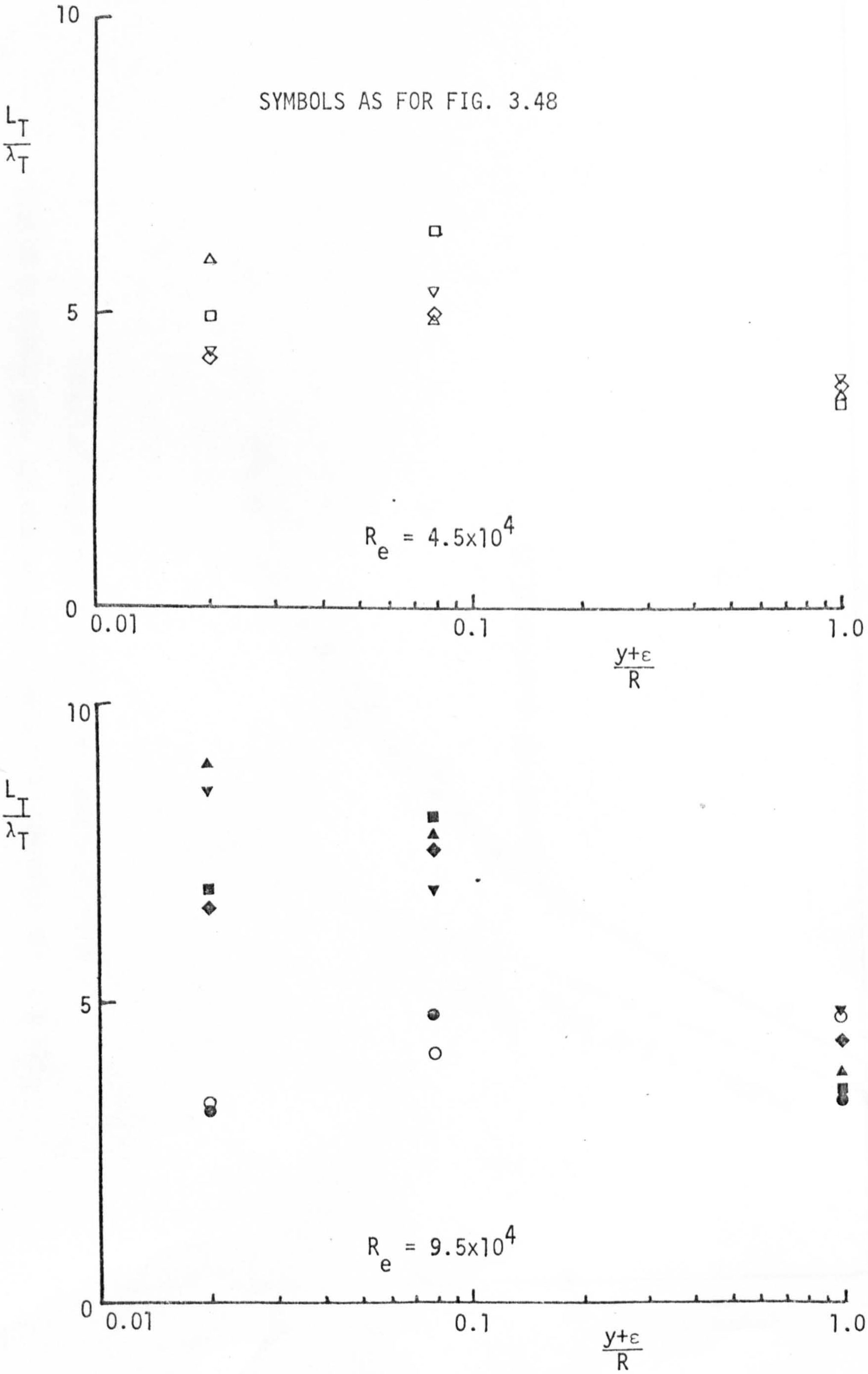

FIG. 4.1 THE ROUGHNESS FUNCTION χ FOR THE SURFACE R550 VERSUS ROUGHNESS REYNOLDS NUMBER BASED ON MEAN APPARENT AMPLITUDE

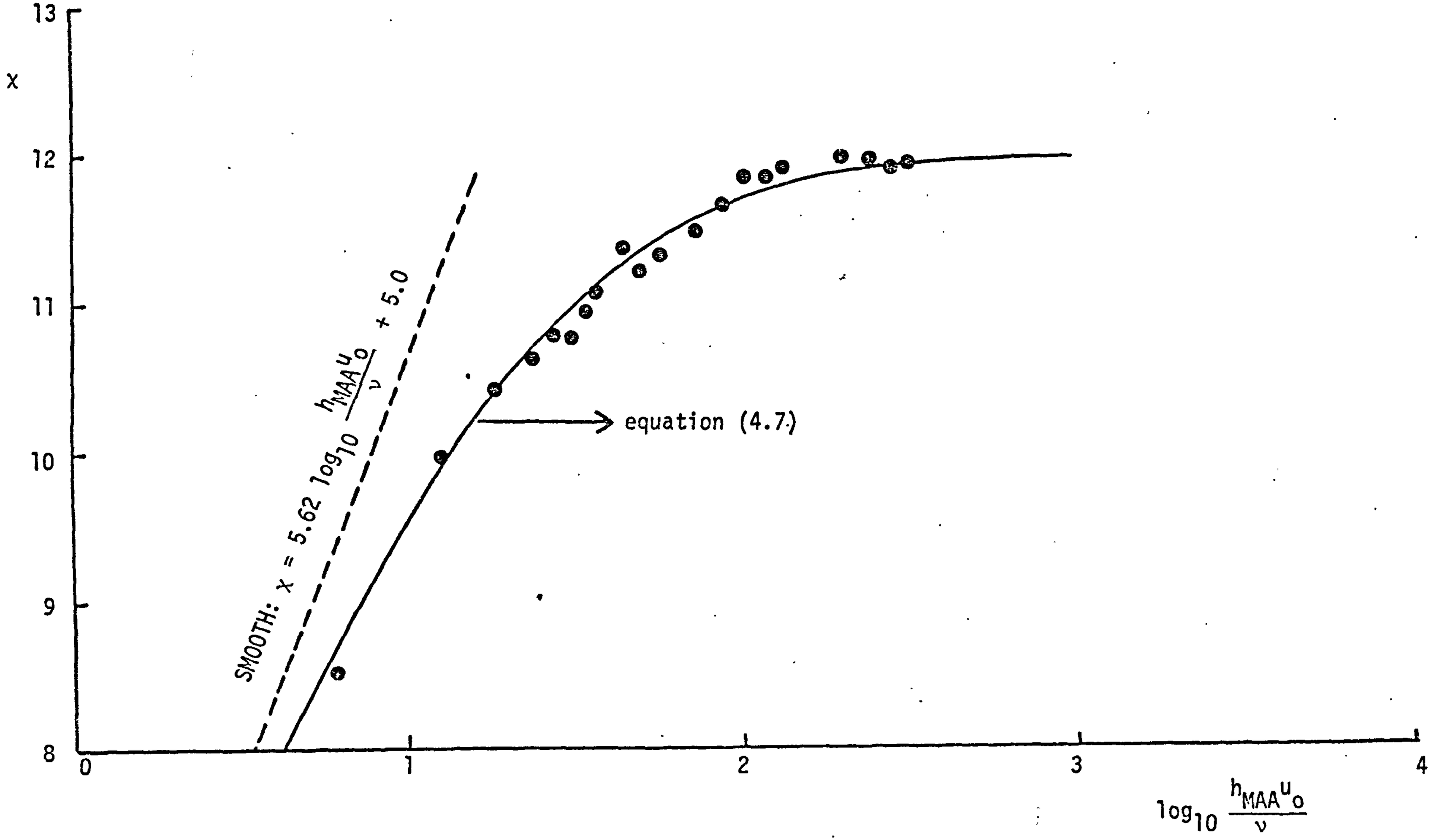

FIG. 4.2 THE PROPOSED EDDY-VISCOSITY MODEL COMPARED WITH THE DATA OF BRADSHAW AND FERRISS (1965)

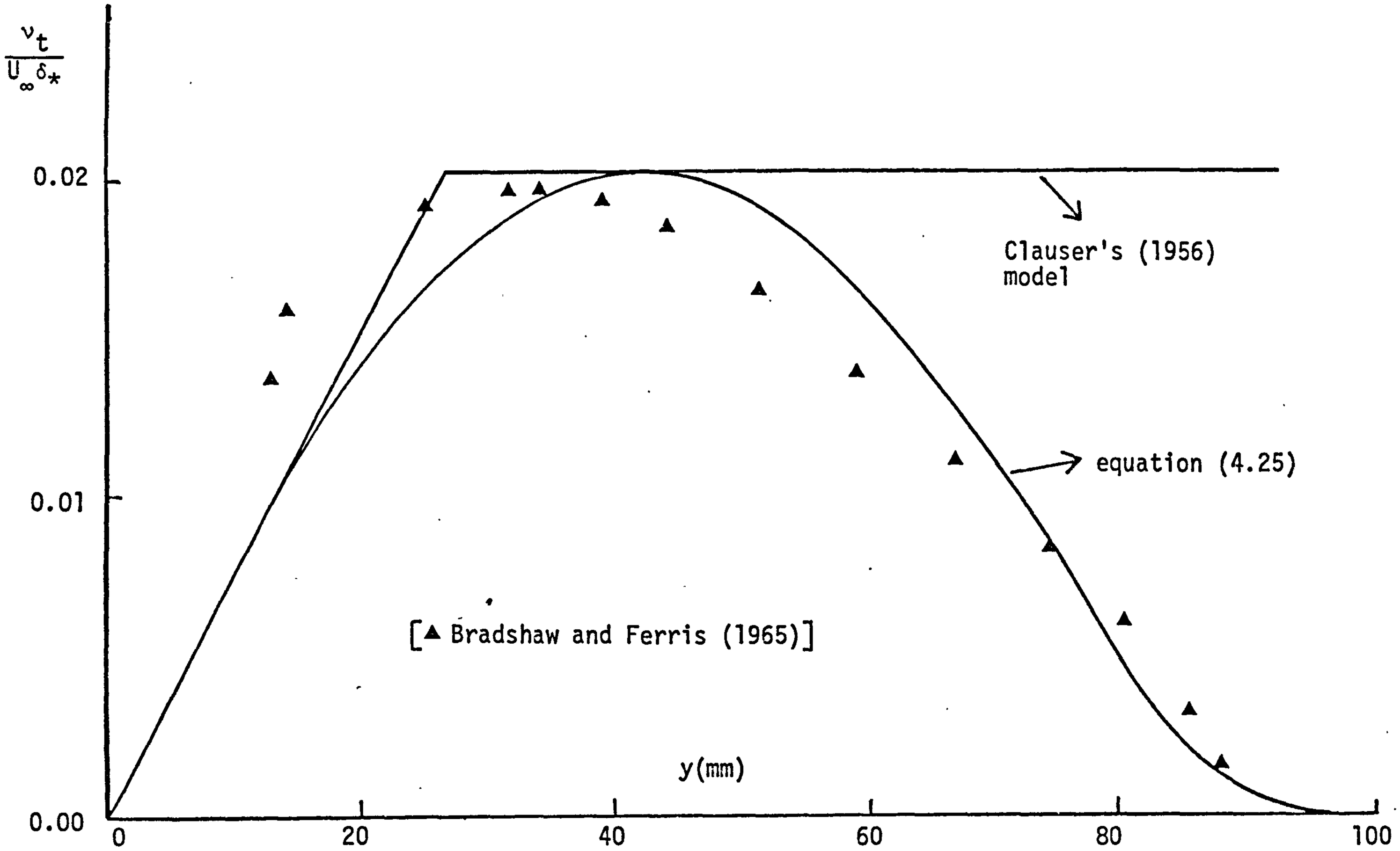

FIG. 4.3 THE PROPOSED ENTRAINMENT FUNCTION IN TERMS OF THE WAKE-STRENGTH PARAMETER Π

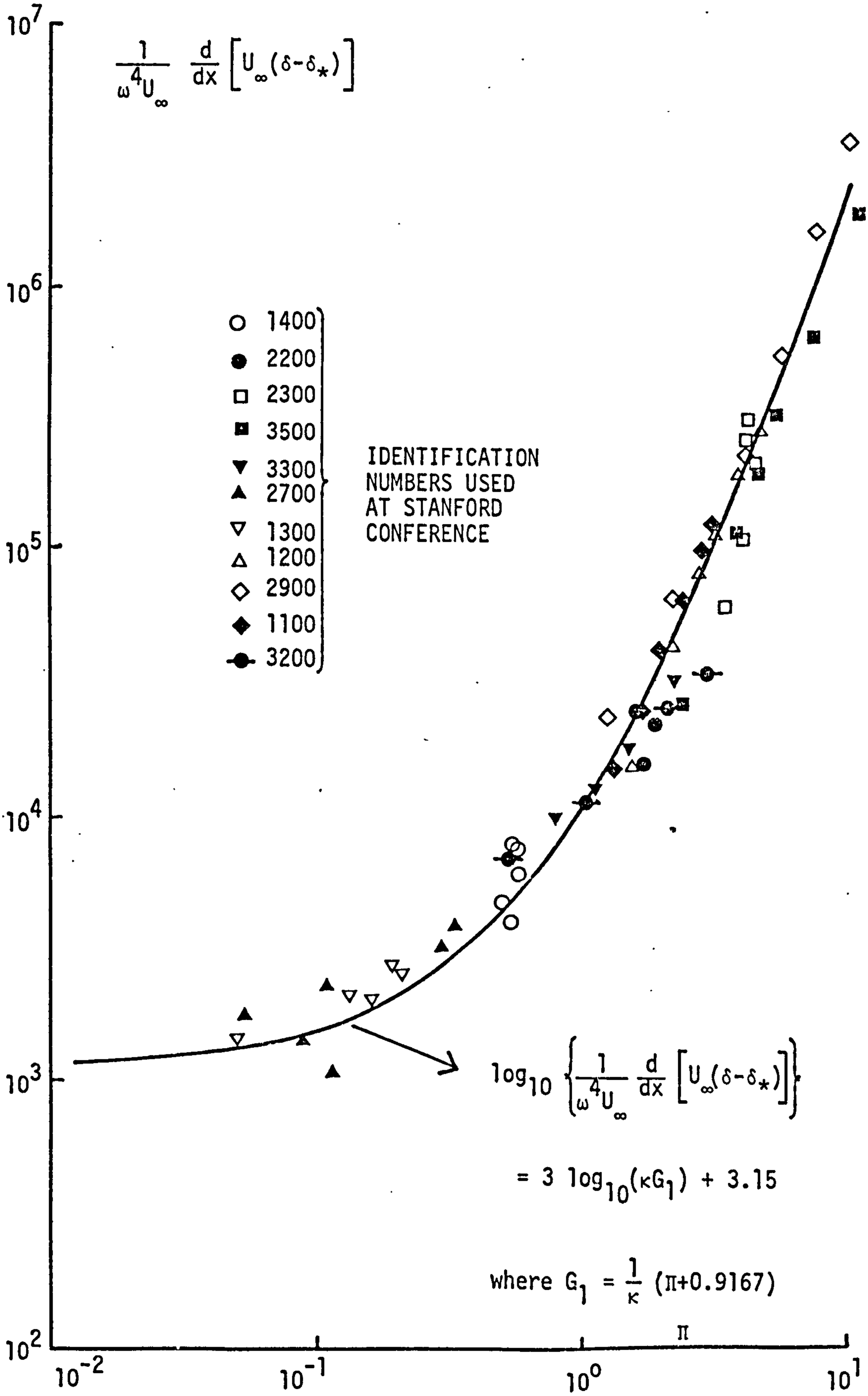

FIG. 4.4 TOTAL WALL-FRICTION COEFFICIENT FOR SMOOTH FLAT PLATE IN A ZERO PRESSURE-GRADIENT

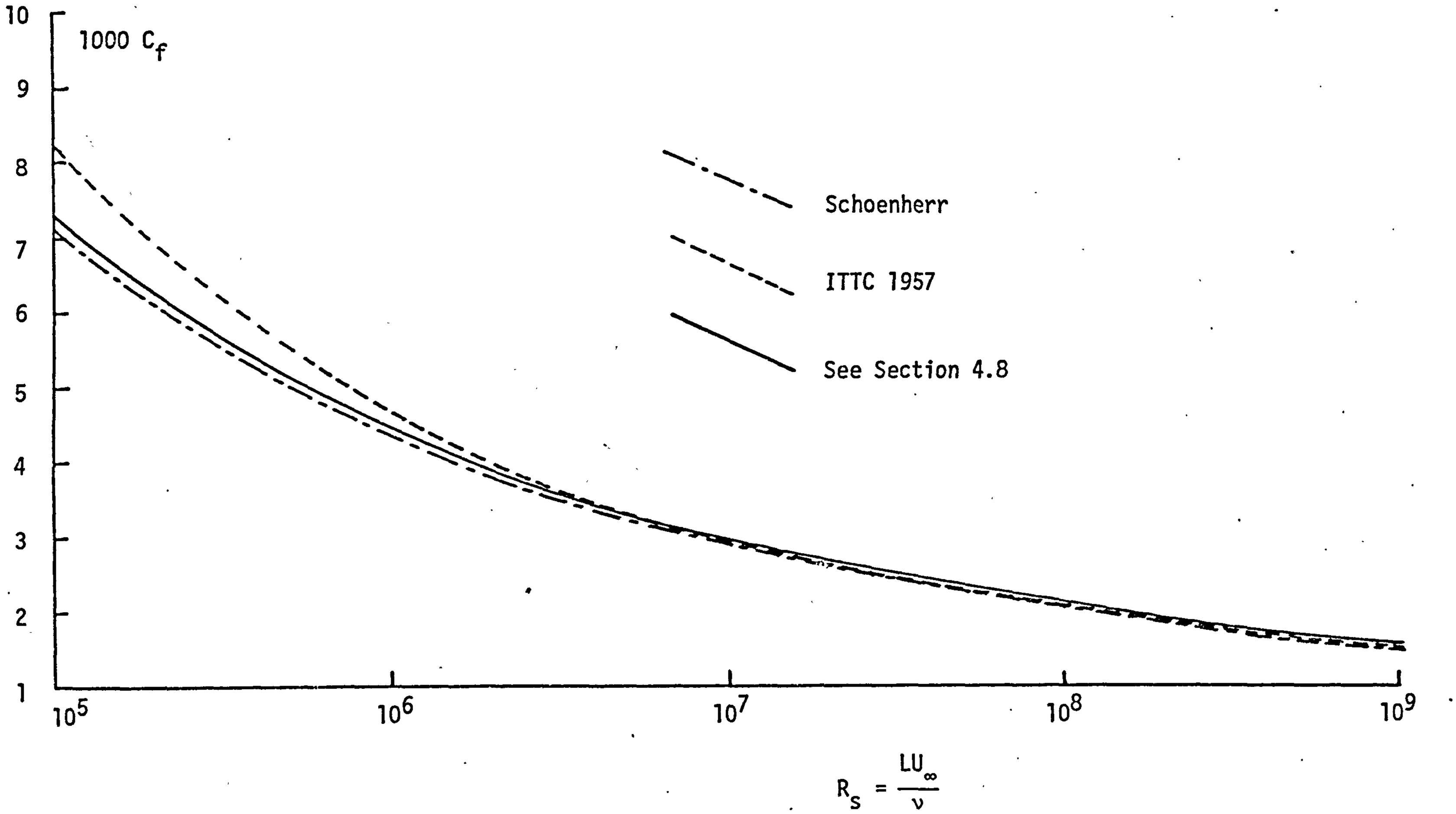

FIG. 4.5 THE LOCAL WALL FRICTION COEFFICIENT FOR A ROUGH FLAT PLATE IN A ZERO PRESSURE-GRADIENT. PREDICTIONS BASED ON MEASURED ROUGHNESS FUNCTION FOR THE SURFACE R550

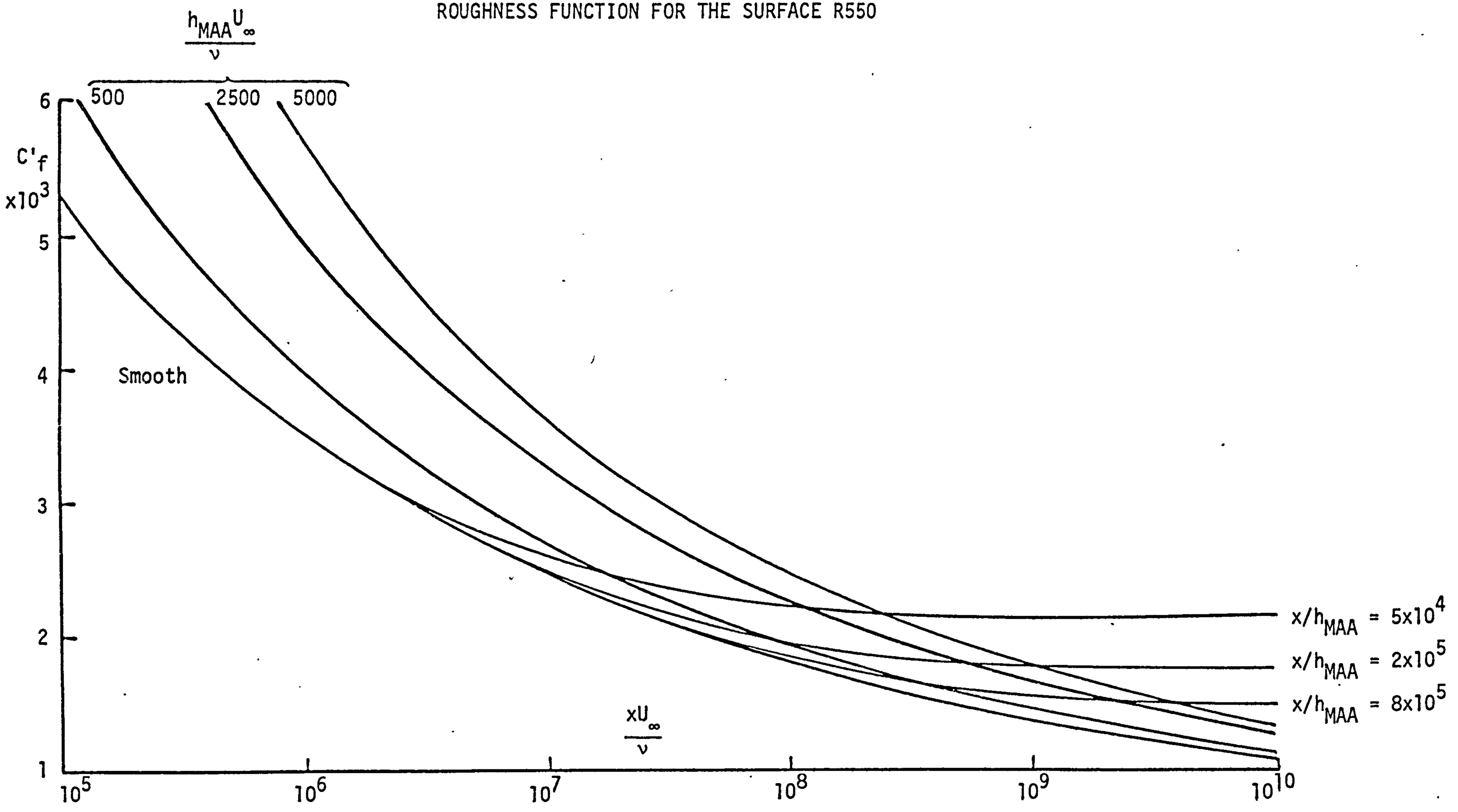

FIG. 4.6 PREDICTION OF SMOOTH-WALL FLOW IN A NEGATIVE PRESSURE-GRADIENT (BAUER 6300)

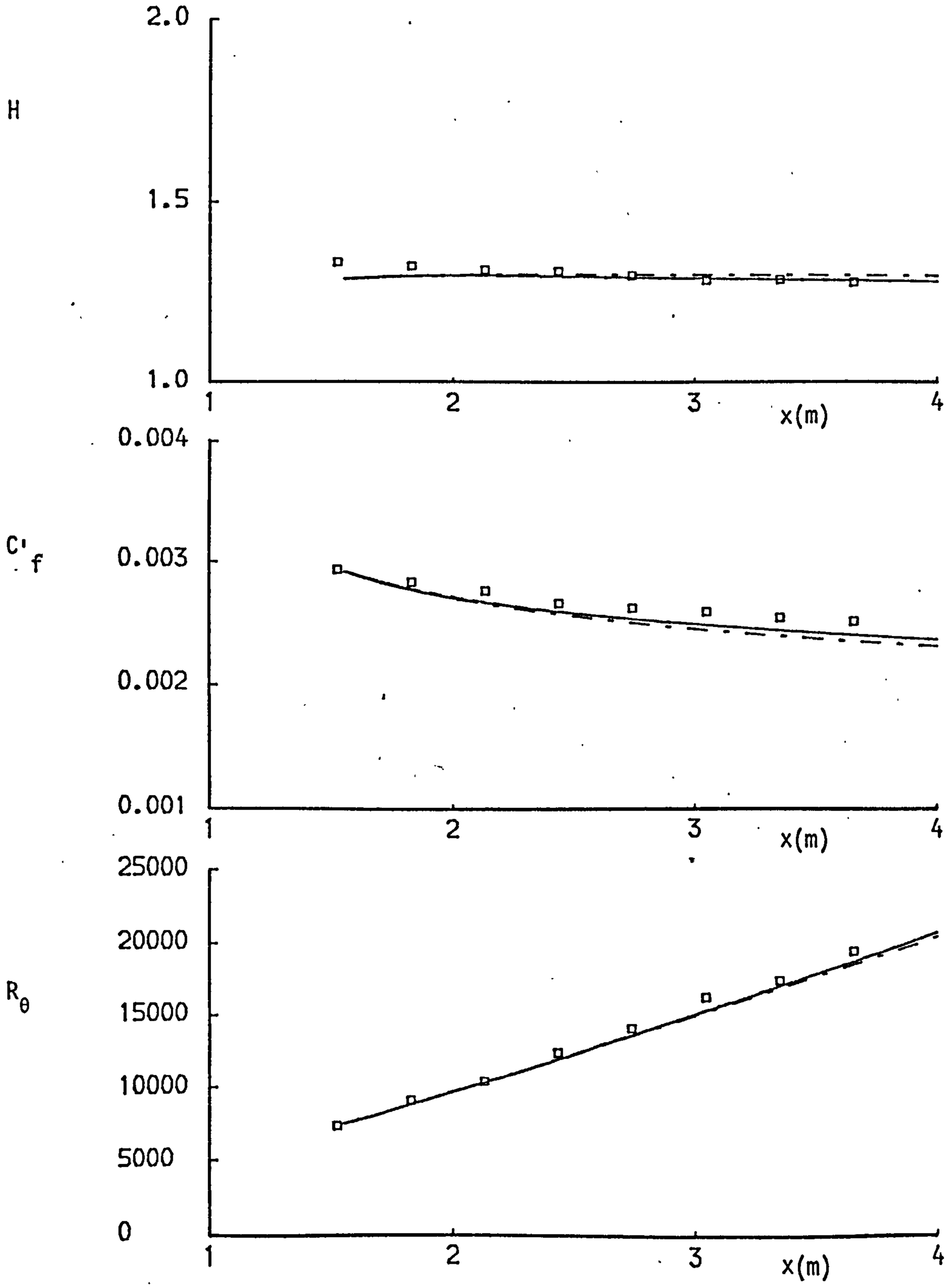

FIG. 4.7 PREDICTION OF SMOOTH-WALL FLOW IN A ZERO PRESSURE-GRADIENT (BELL 3000)

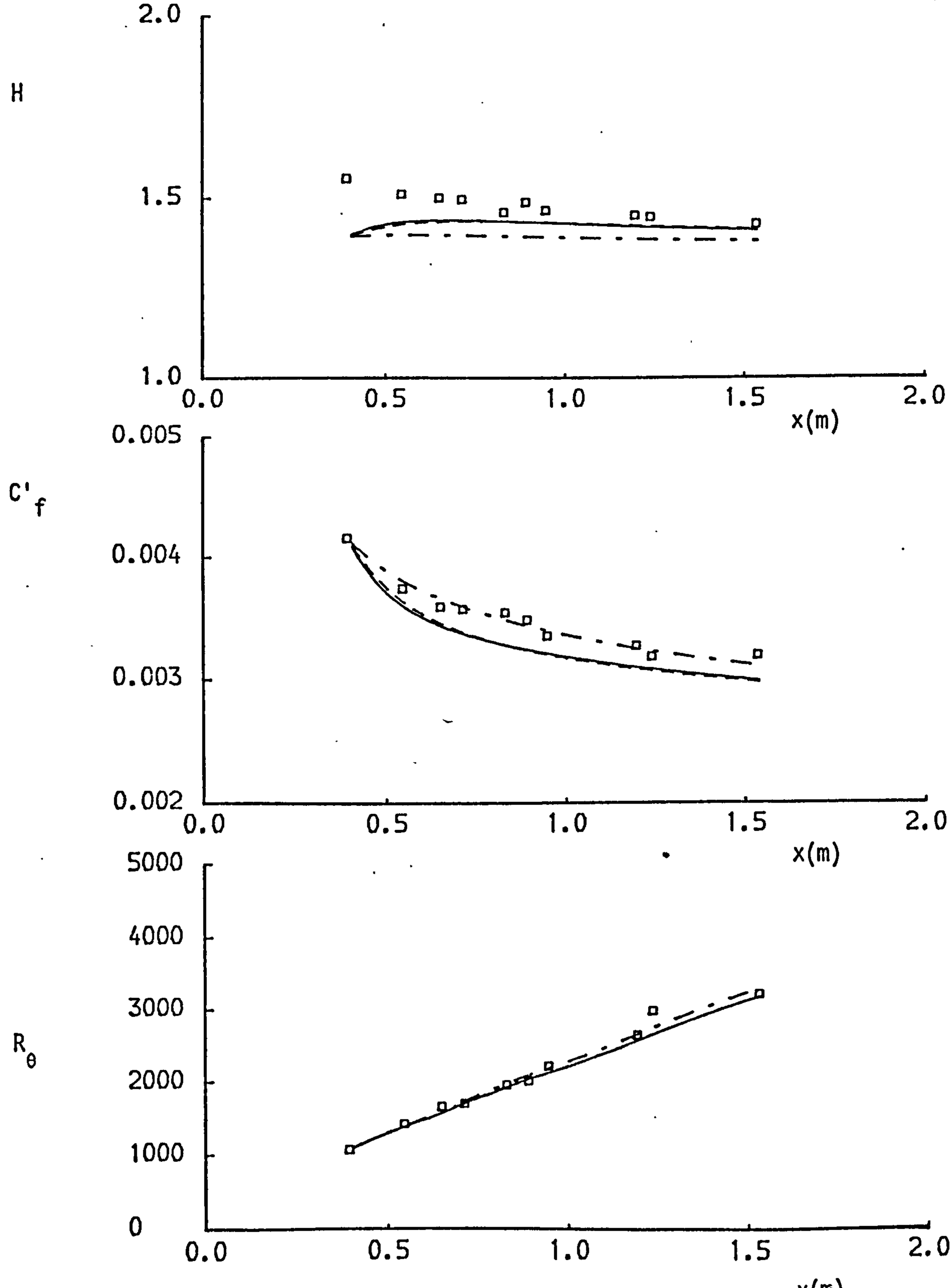

FIG. 4.8 PREDICTION OF SMOOTH-WALL FLOW IN A POSITIVE PRESSURE-GRADIENT (SCHUBAUER AND KLEBANOFF 2100)

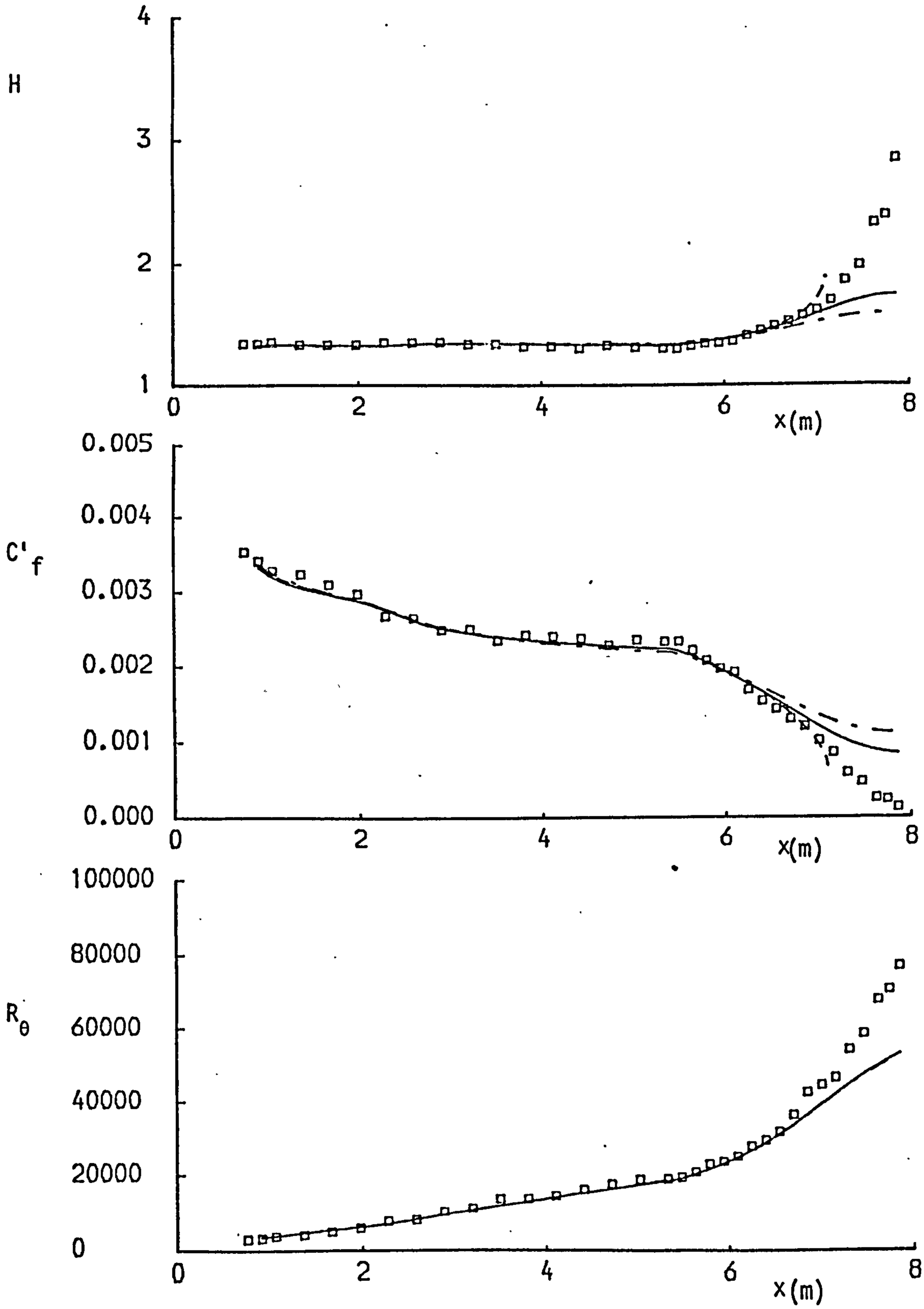

FIG. 4.9 PREDICTION OF SMOOTH-WALL FLOW IN A POSITIVE PRESSURE-GRADIENT FOLLOWED BY RELAXATION AT CONSTANT PRESSURE (MOSES 4100)

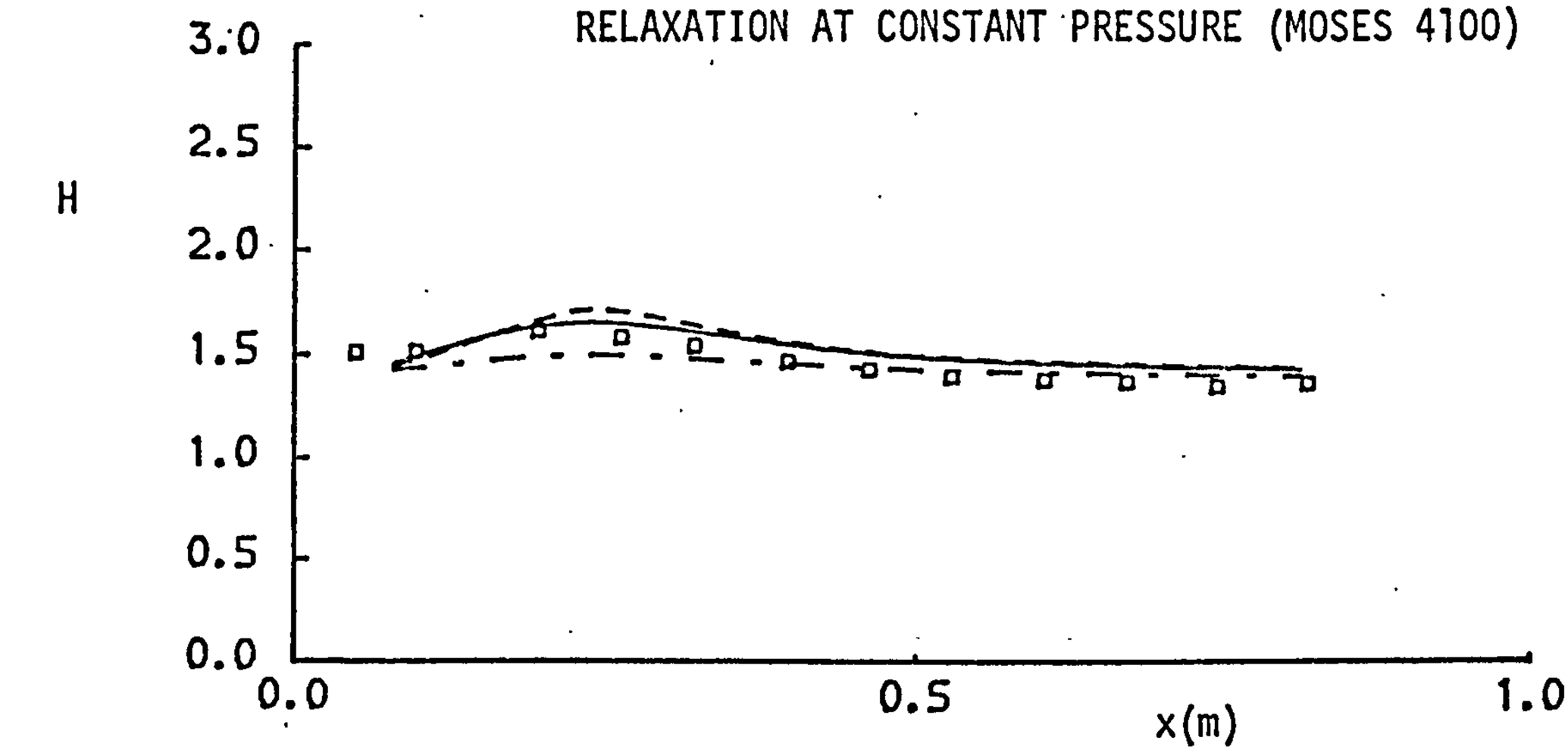

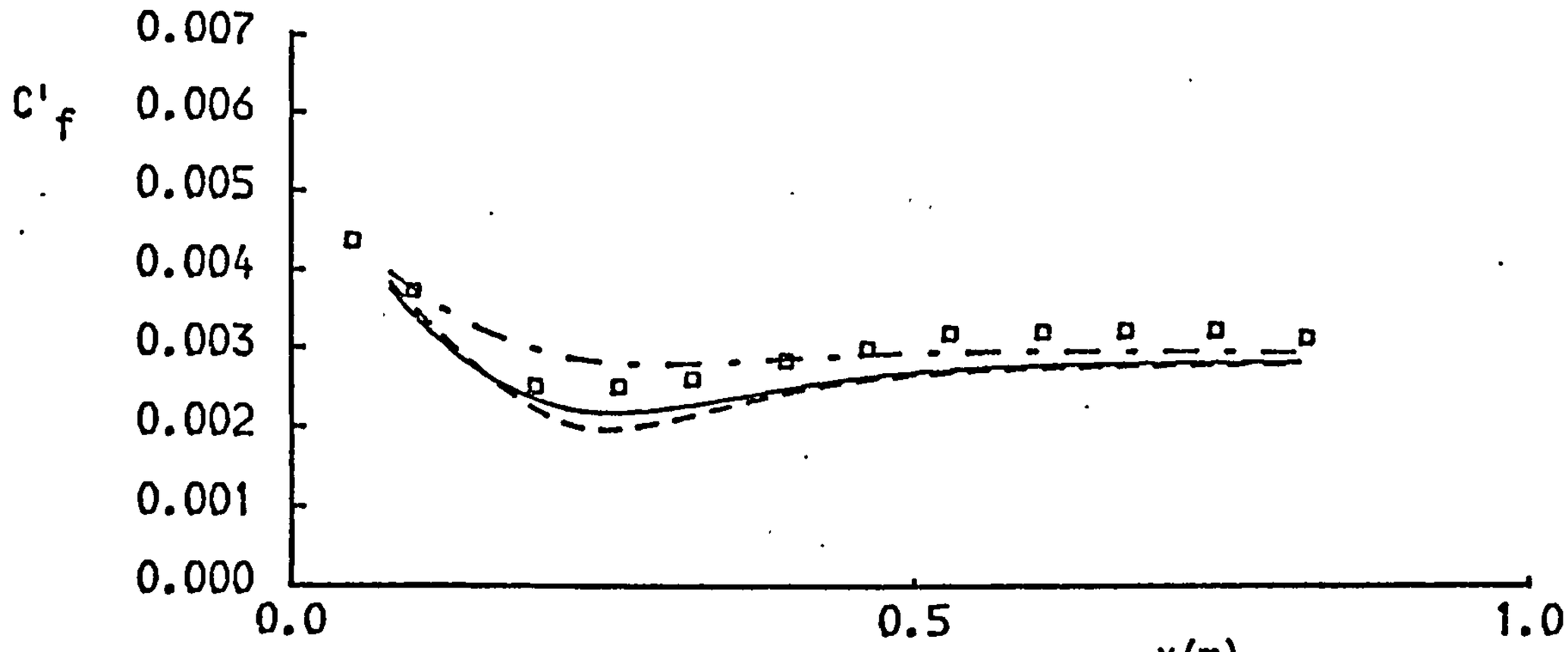

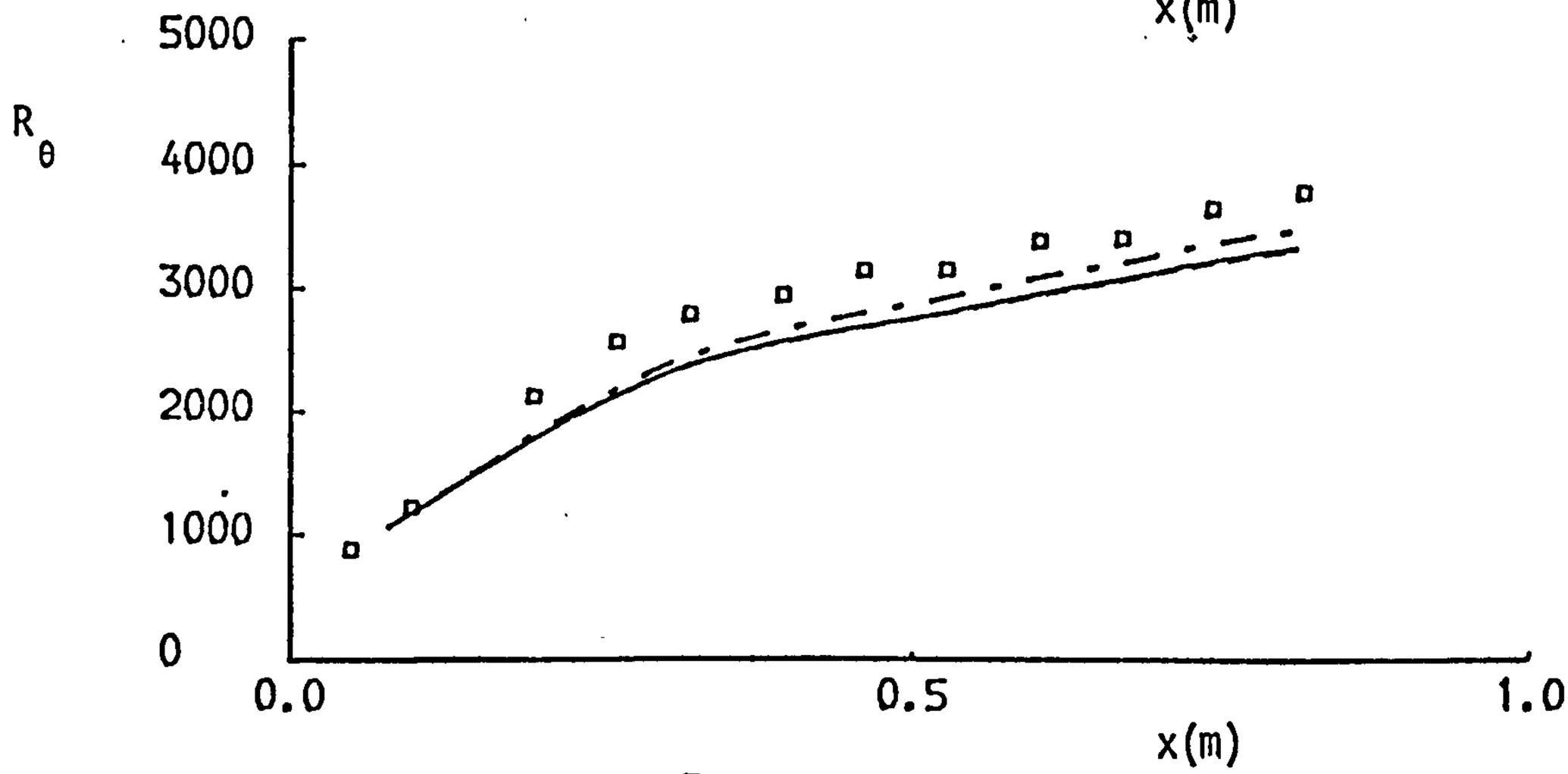

——————— Energy Method

— - — - - Entrainment Method

– – – – – – Moment of Momentum Method

FIG. 4.10 PREDICTION OF FLOW OVER A REGULARLY-ROUGH SURFACE IN A ZERO PRESSURE GRADIENT (EXPERIMENT DUE TO BETTERMAN)

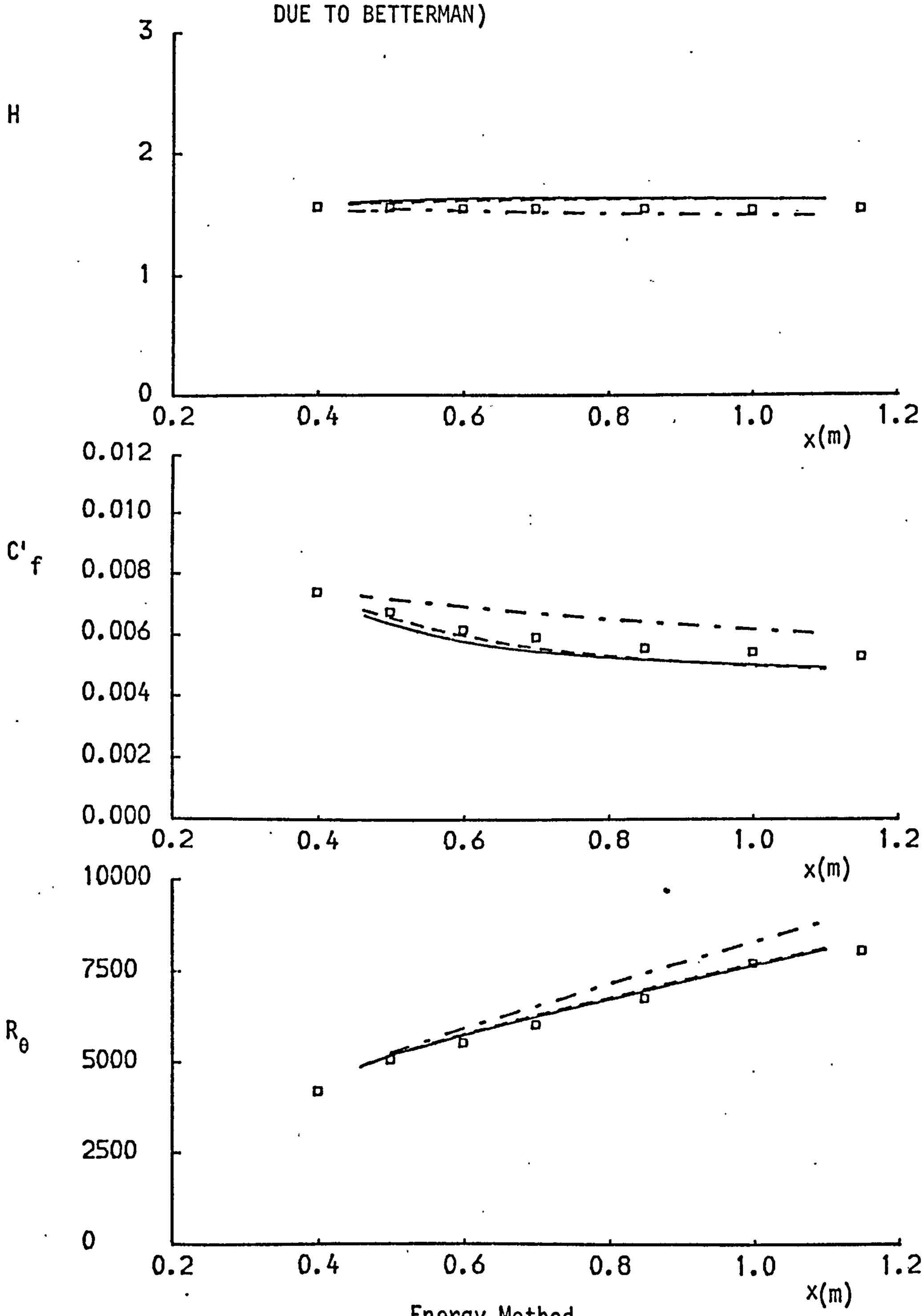

FIG. 4.11 PREDICTION OF FLOW OVER A REGULARLY-ROUGH SURFACE IN A POSITIVE PRESSURE GRADIENT (EXPERIMENT DUE TO PERRY AND JOUBERT)

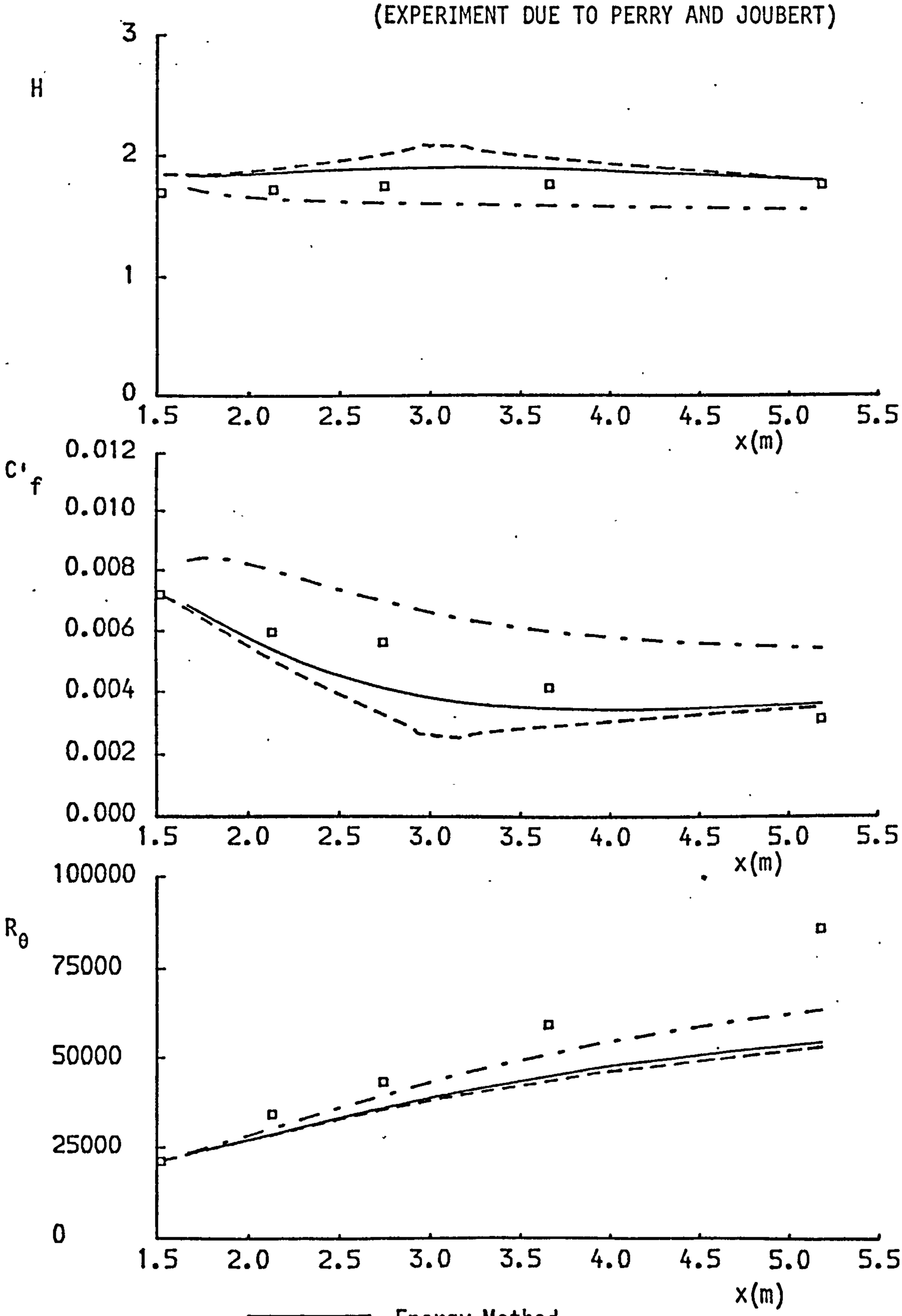

FIG. 4.12 PREDICTION OF FLOW OVER A REGULARLY-ROUGH SURFACE IN A NEGATIVE PRESSURE GRADIENT (EXPERIMENT DUE TO ARNDT AND IPPEN)

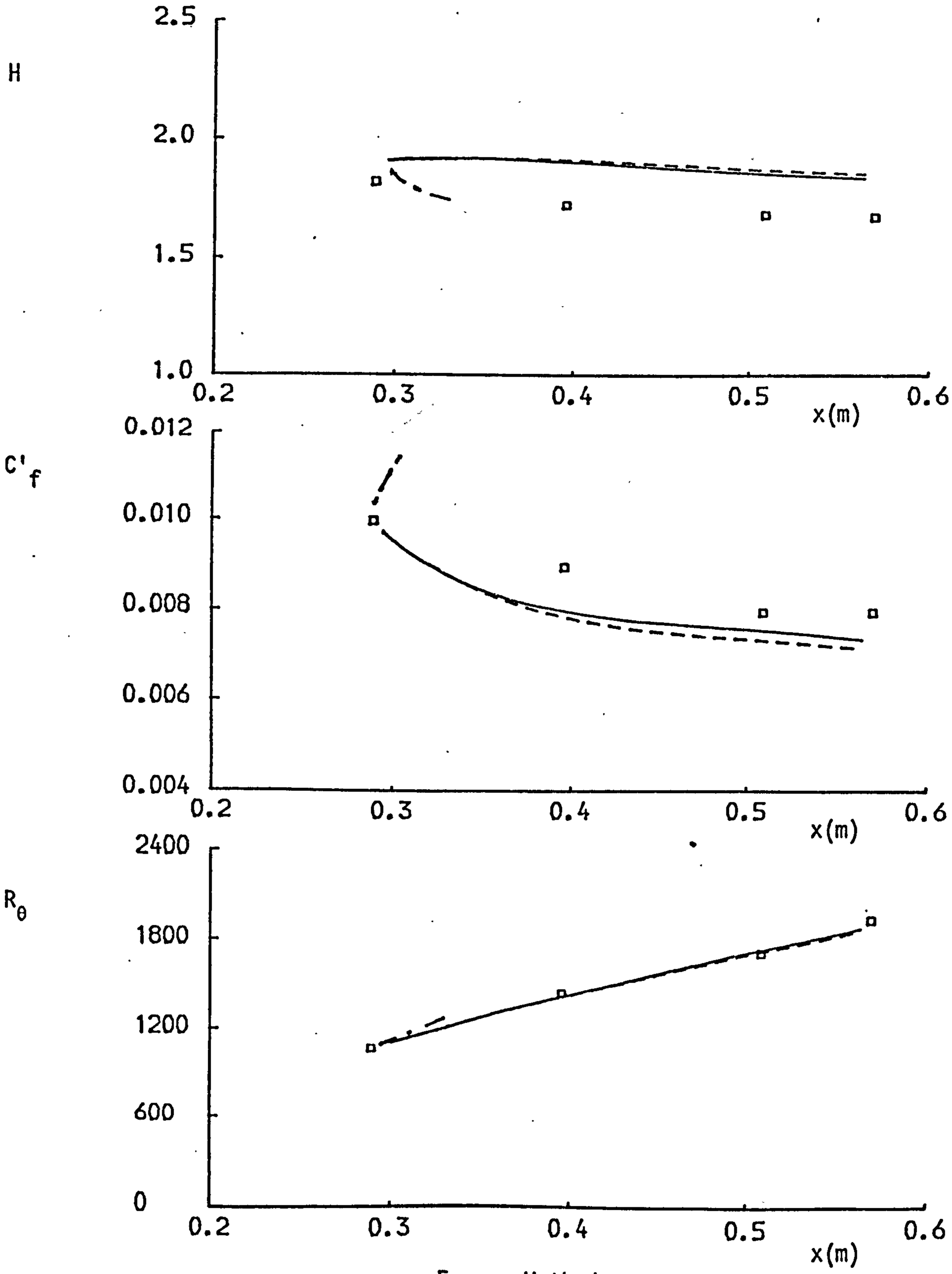

FIG. 4.13 HYPOTHETICAL VELOCITY DISTRIBUTION FOR PREDICTION OF POSITIONS OF SEPARATION

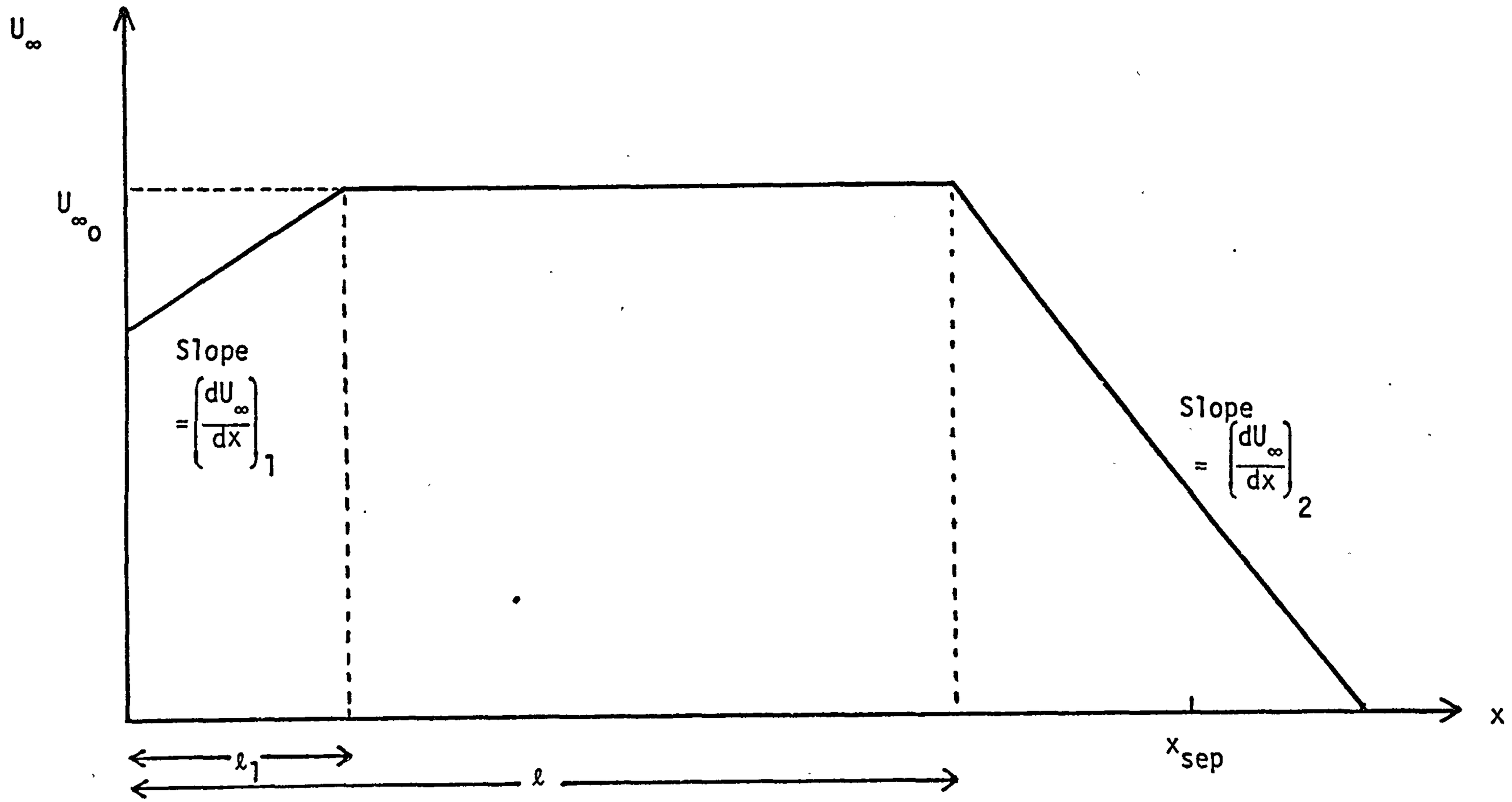

FIG. 4.14 NON-DIMENSIONAL SEPARATION DISTANCE VERSUS ROUGHNESS HEIGHT. PREDICTIONS BASED ON MEASURED ROUGHNESS FUNCTION FOR THE SURFACE R550

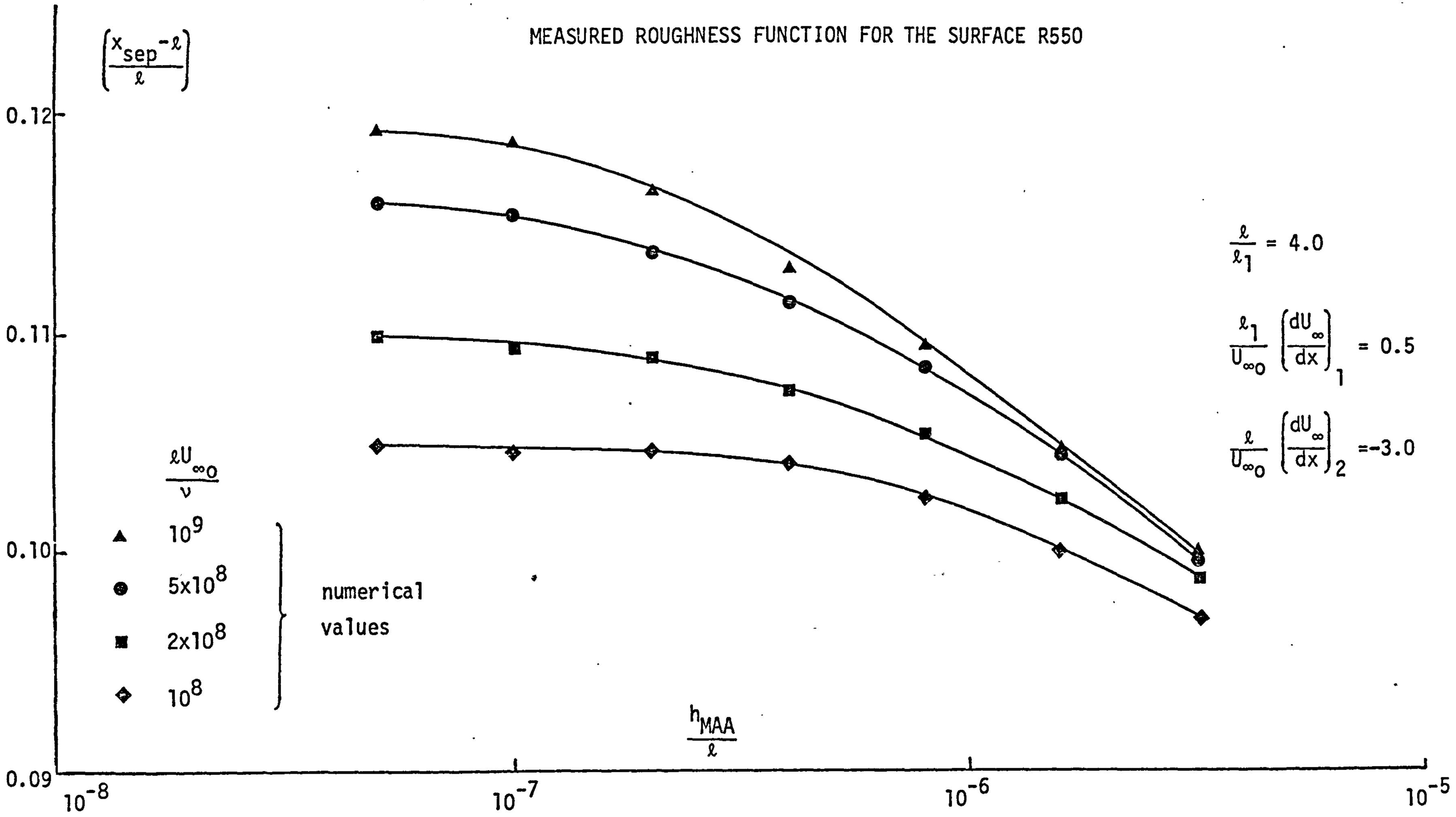

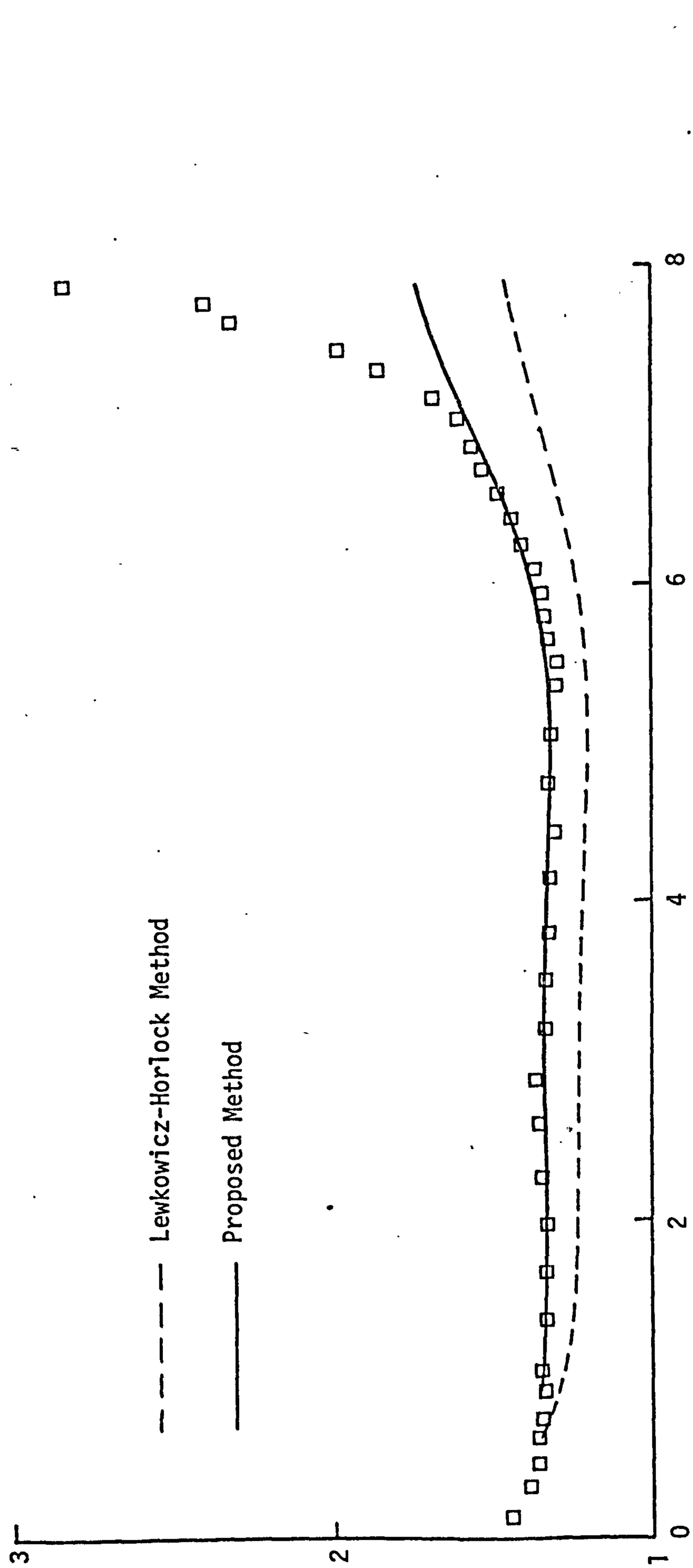

FIG. 4.15 COMPARISON OF ENERGY METHODS FOR SCHUBAUER AND KLEBANOFF 2100 FLOW

FIG. 4.16 COMPARISON OF ENERGY METHODS FOR SCHUBAUER AND KLEBANOFF 2100 FLOW

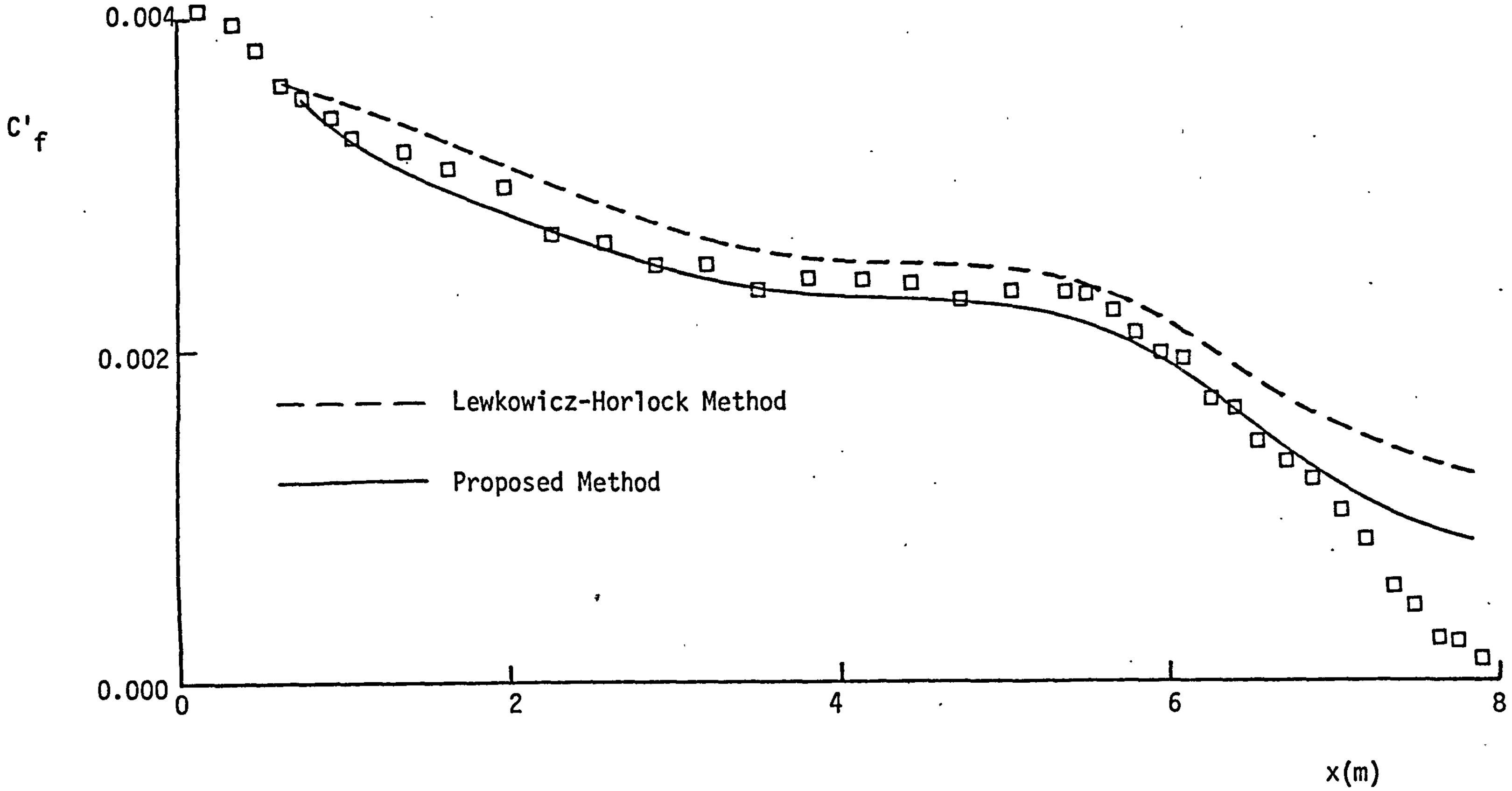

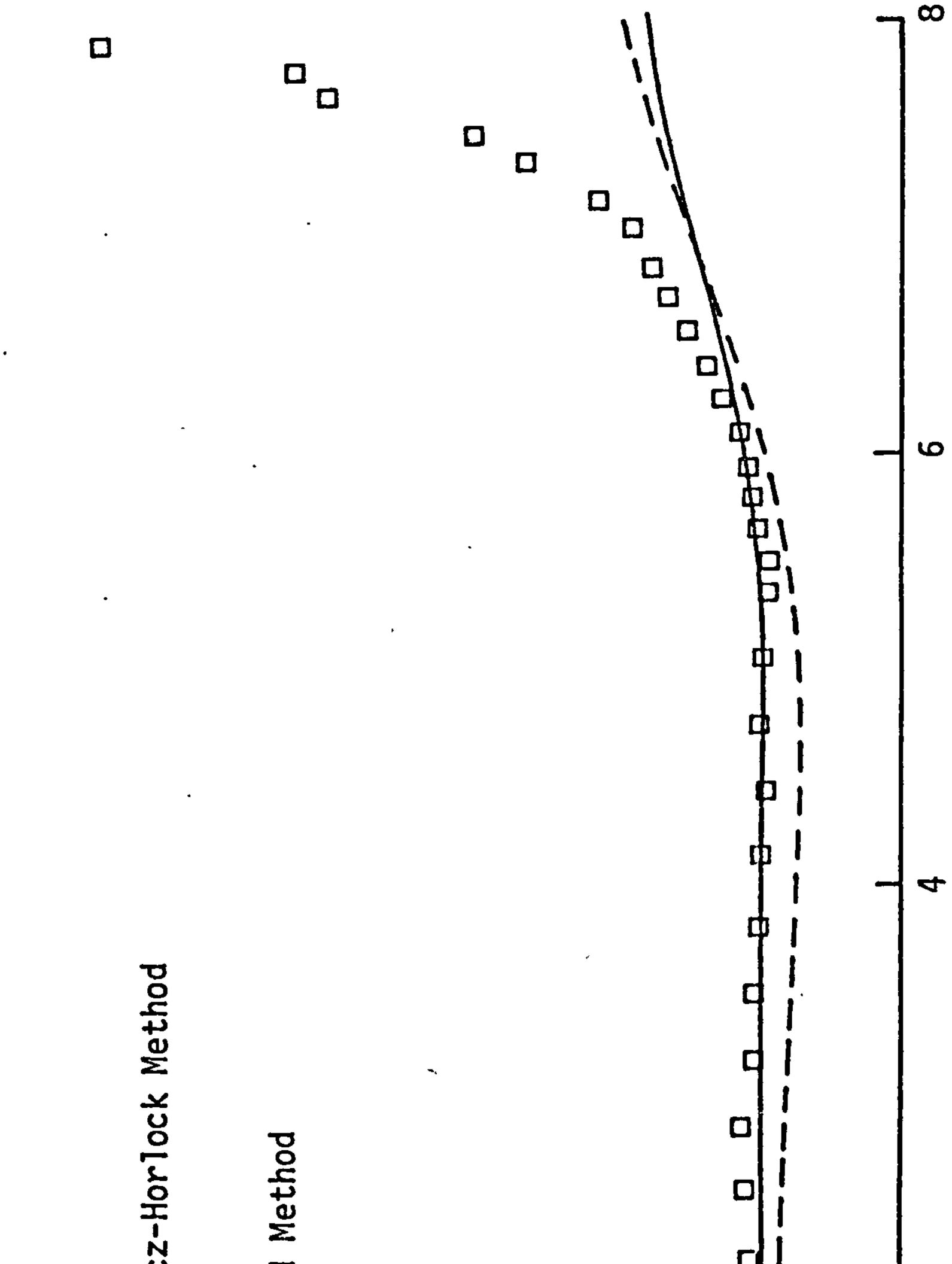

FIG. 4.17 COMPARISON OF ENTRAINMENT METHODS FOR SCHUBAUER AND KLEBANOFF 2100 FLOW

FIG. 4.18 COMPARISON OF ENTRAINMENT METHODS FOR SCHUBAUER AND KLEBANOFF 2100 FLOW

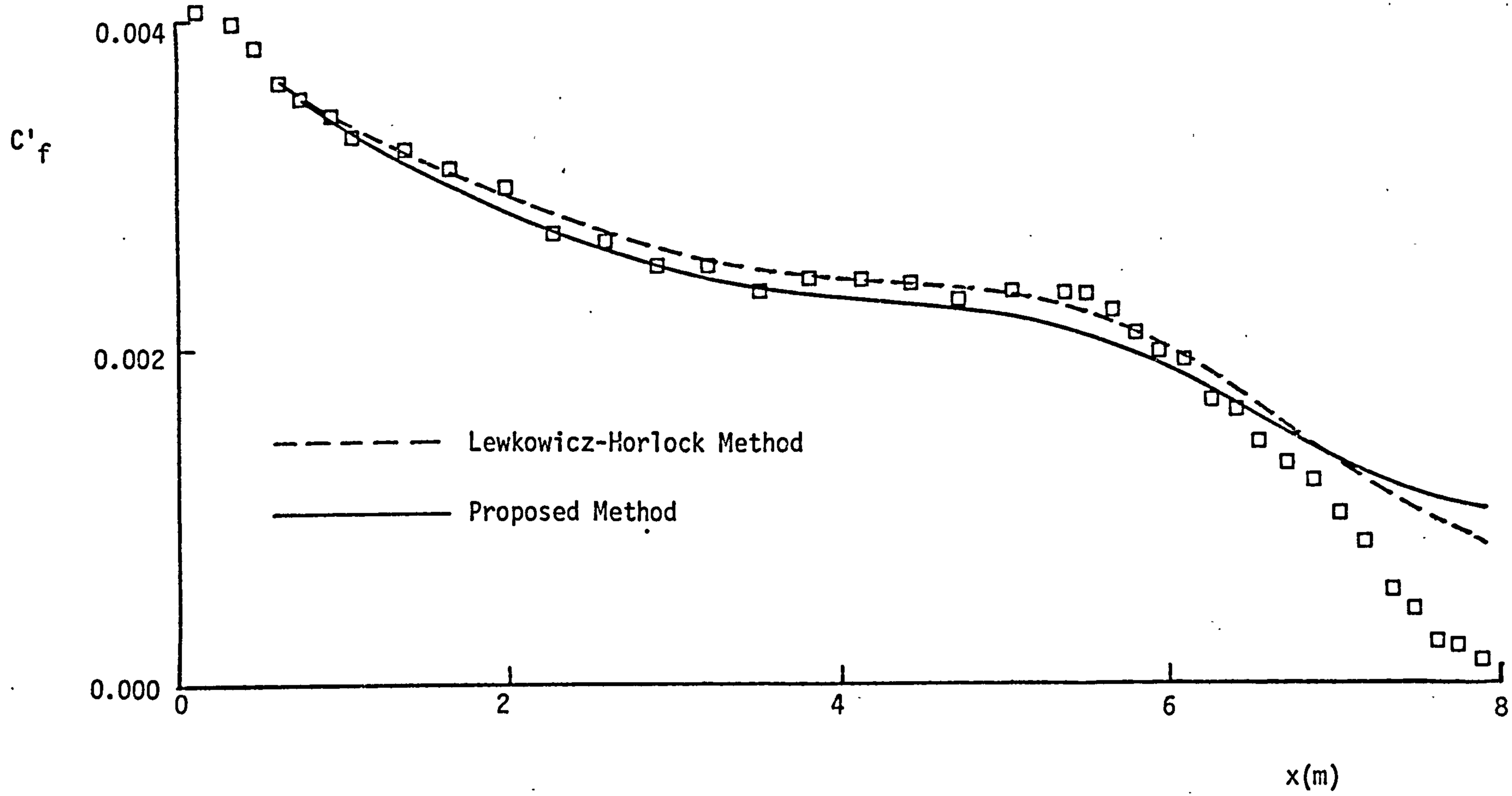

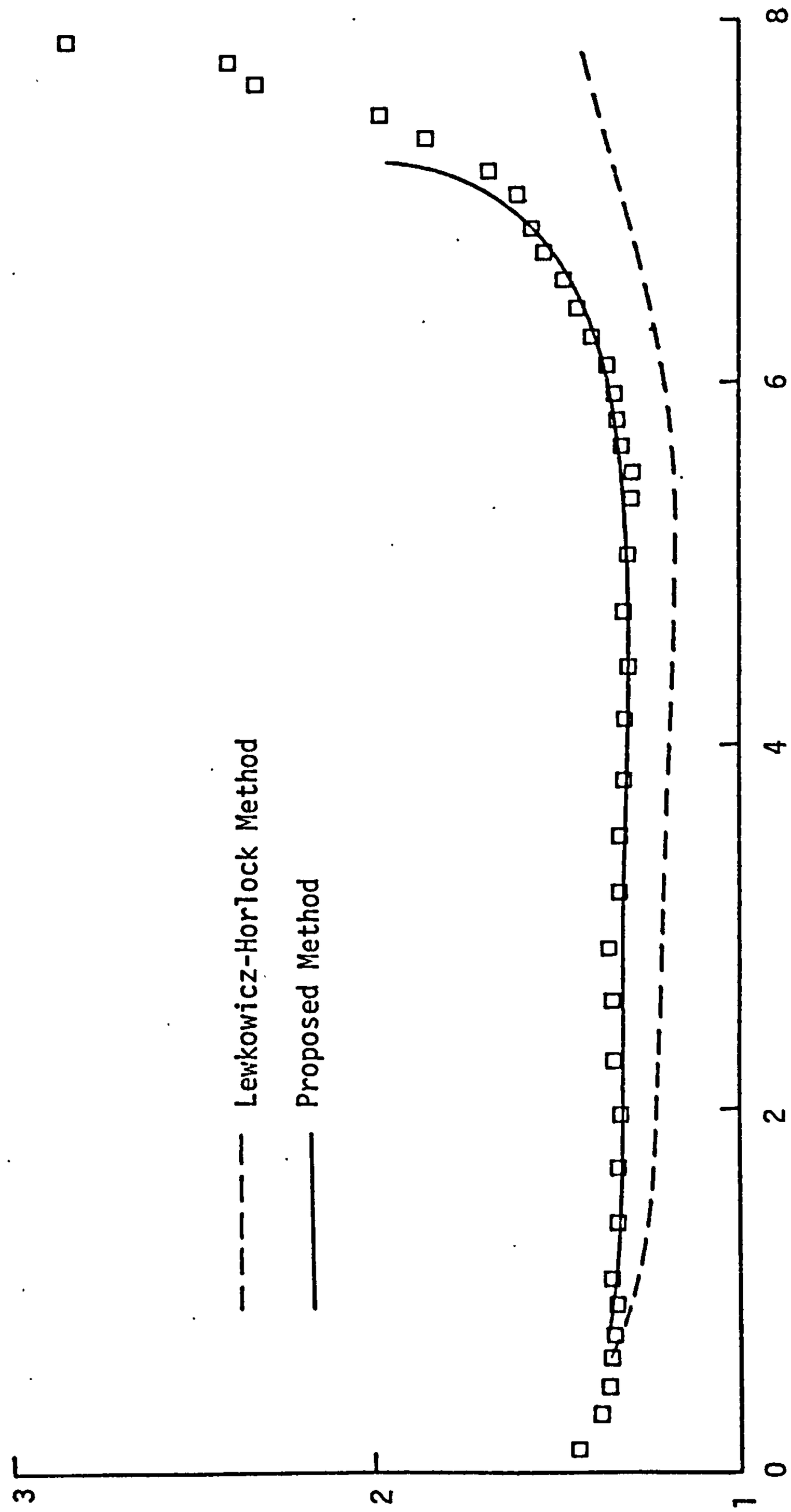

FIG. 4.19 COMPARISON OF MOMENT OF MOMENTUM METHODS FOR SCHUBAUER AND KLEBANOFF 2100 FLOW

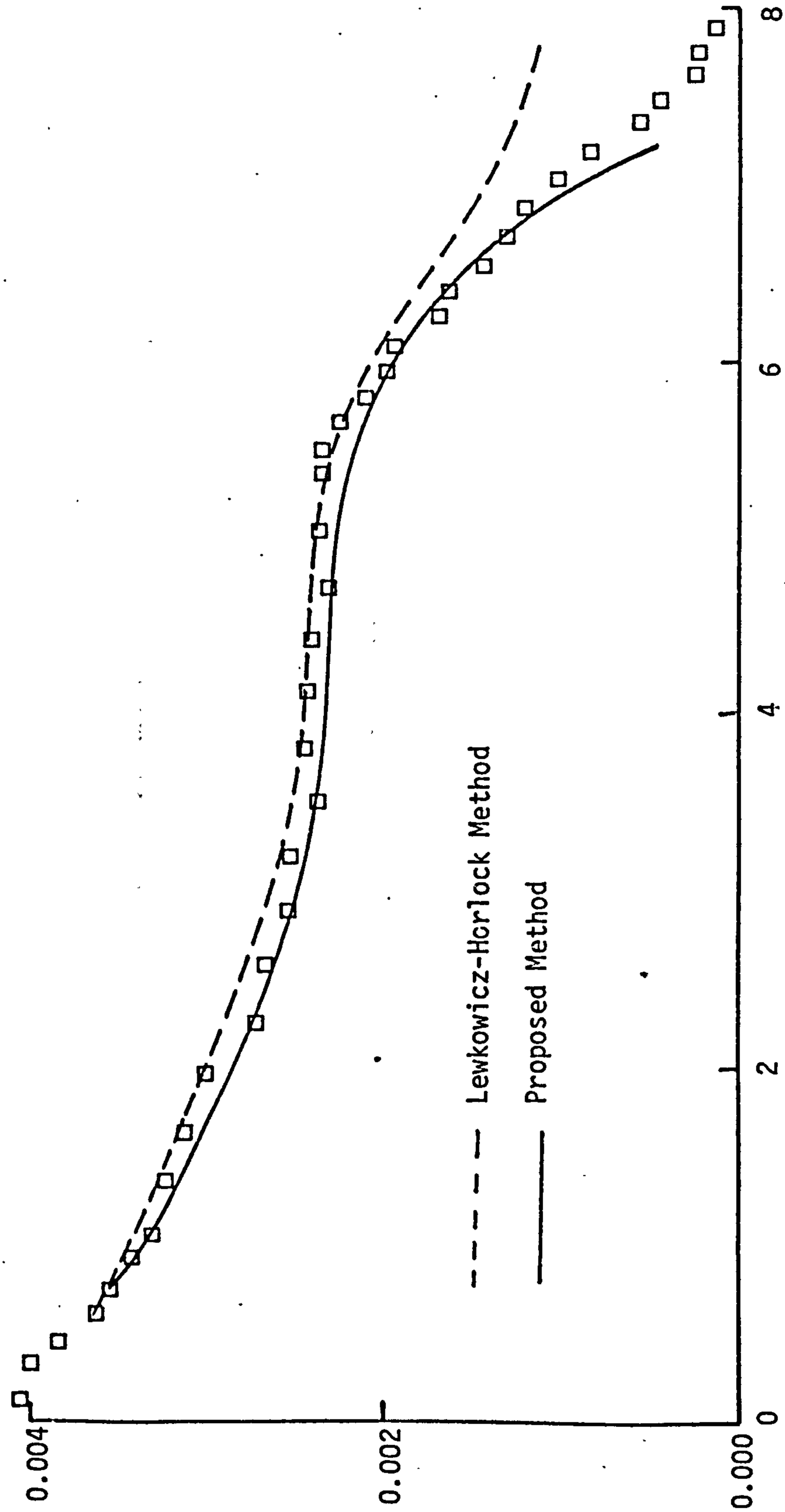

FIG. 4.20 COMPARISON OF MOMENTUM METHODS FOR SCHUBAUER AND KLEBANOFF 2100 FLOW

FIG. 5.1 CODE CONVENTION FOR SURFACE PROFILES

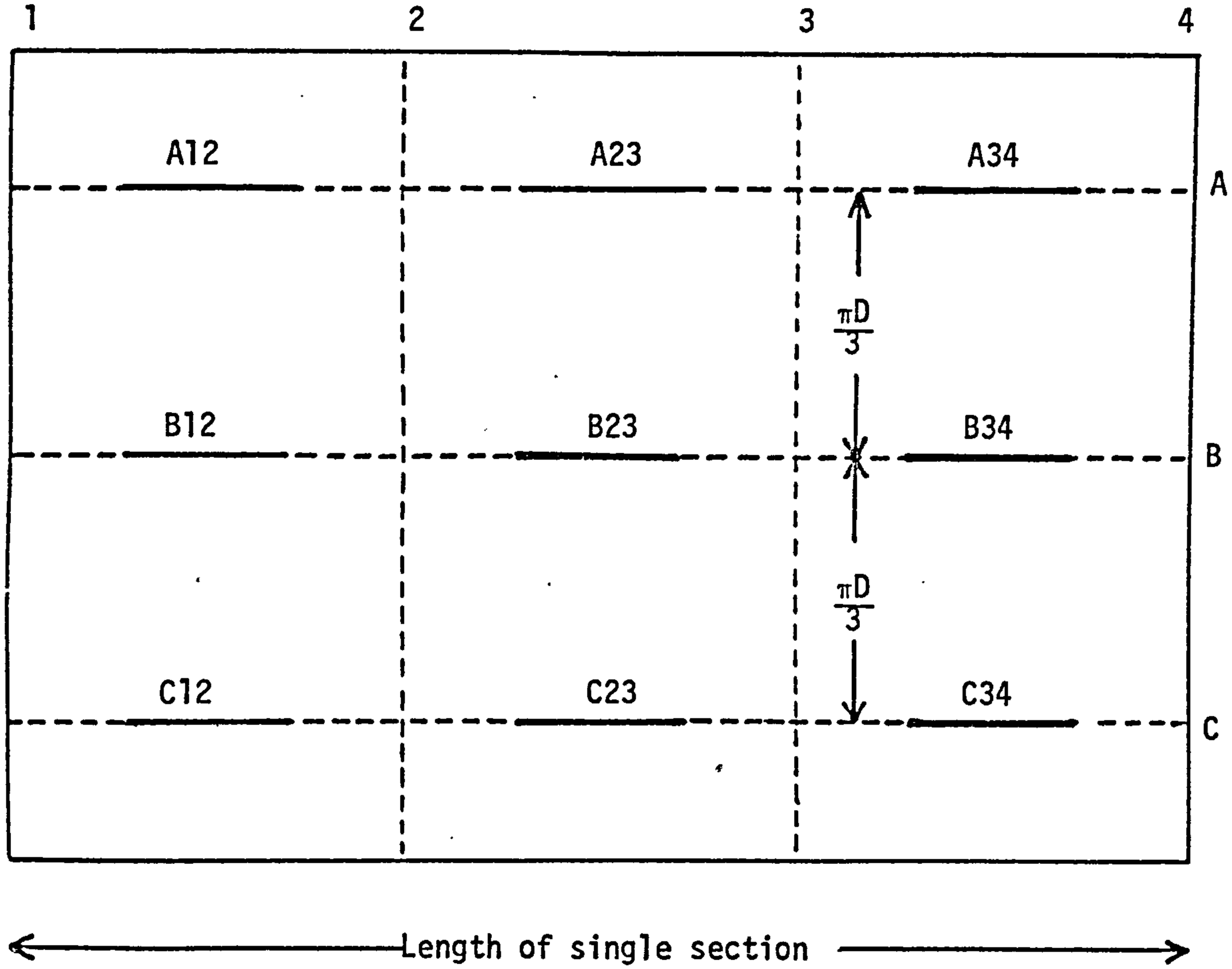

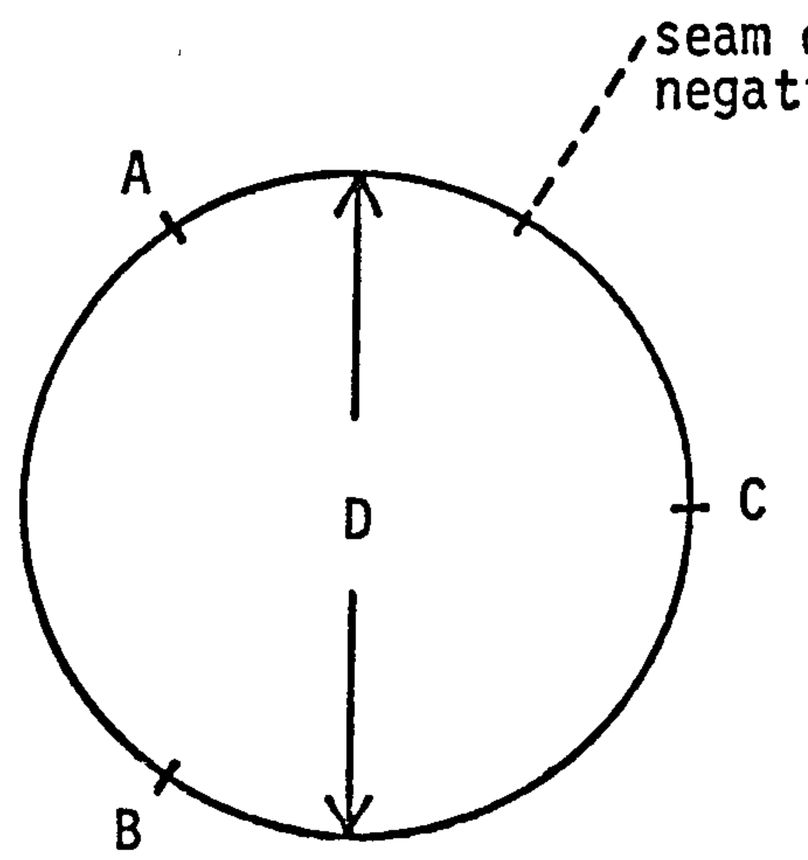

Section through pipe

FIG. 5.2 PROFILES FOR SURFACE R550

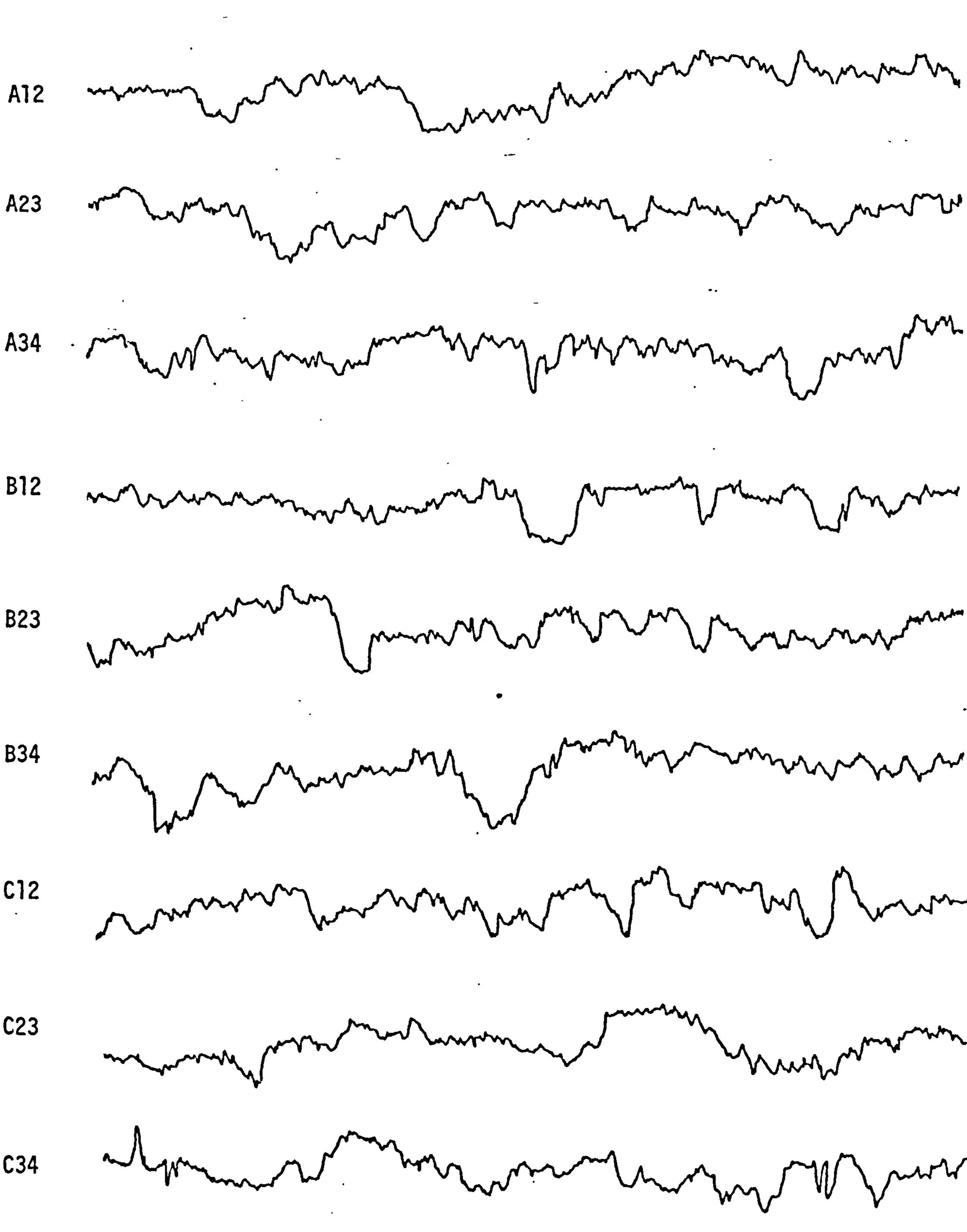

FIG. 5.3 PROFILES FOR SURFACE R420

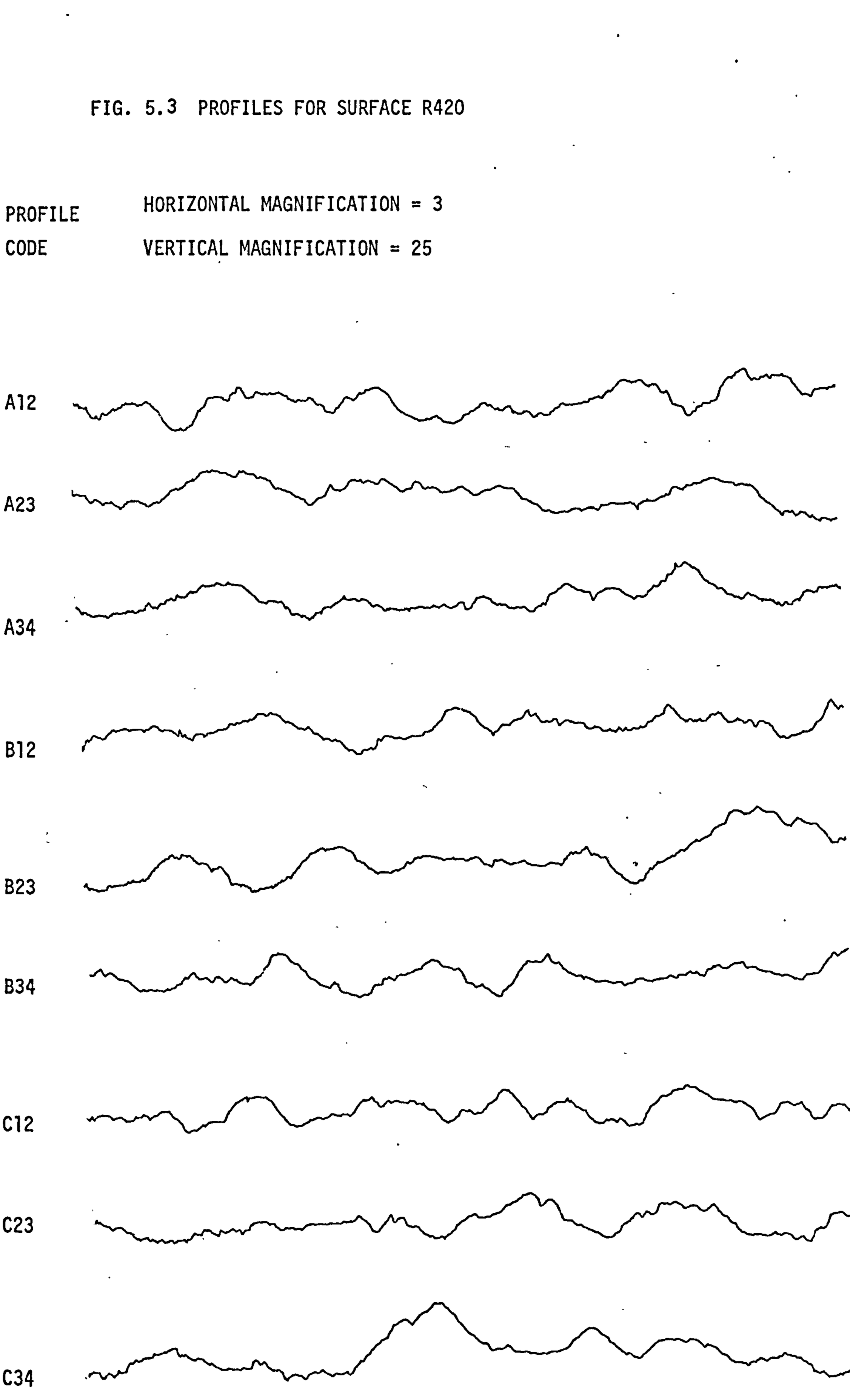

FIG. 5.4 PROFILES FOR SURFACE R345

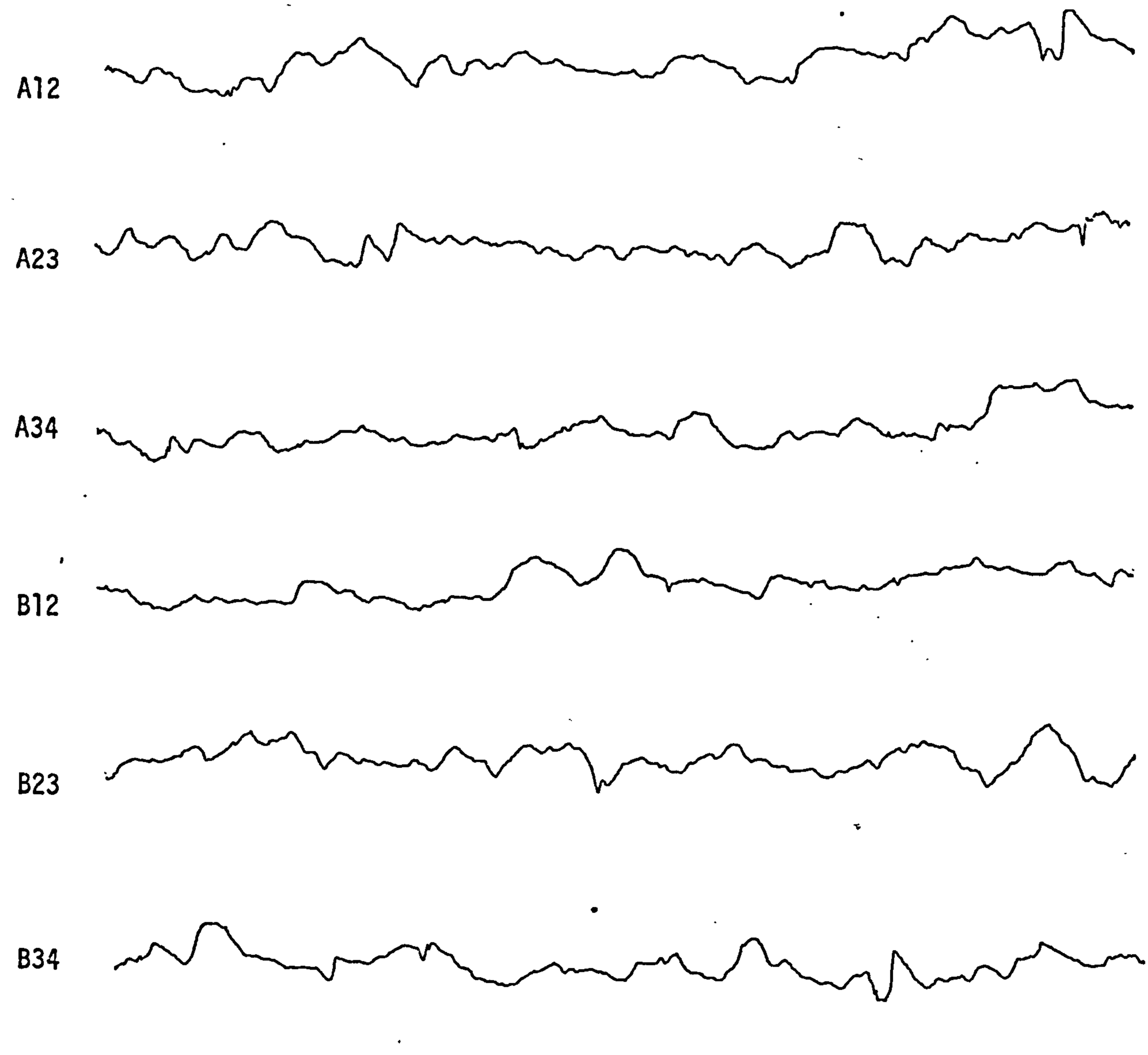

FIG. 5.5 PROFILES FOR SURFACE R253

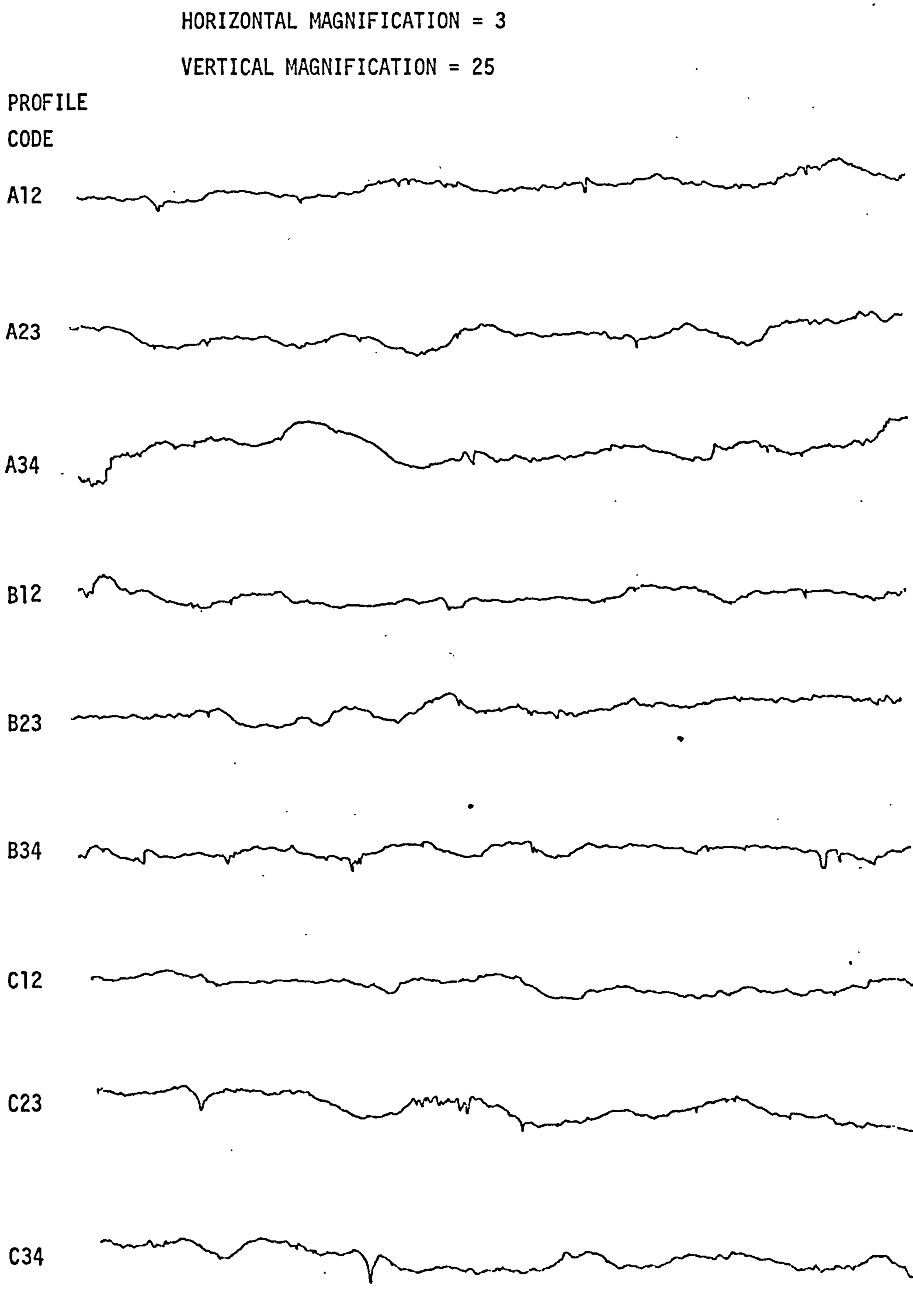

FIG. 5.6 PROFILES FOR SURFACE R173

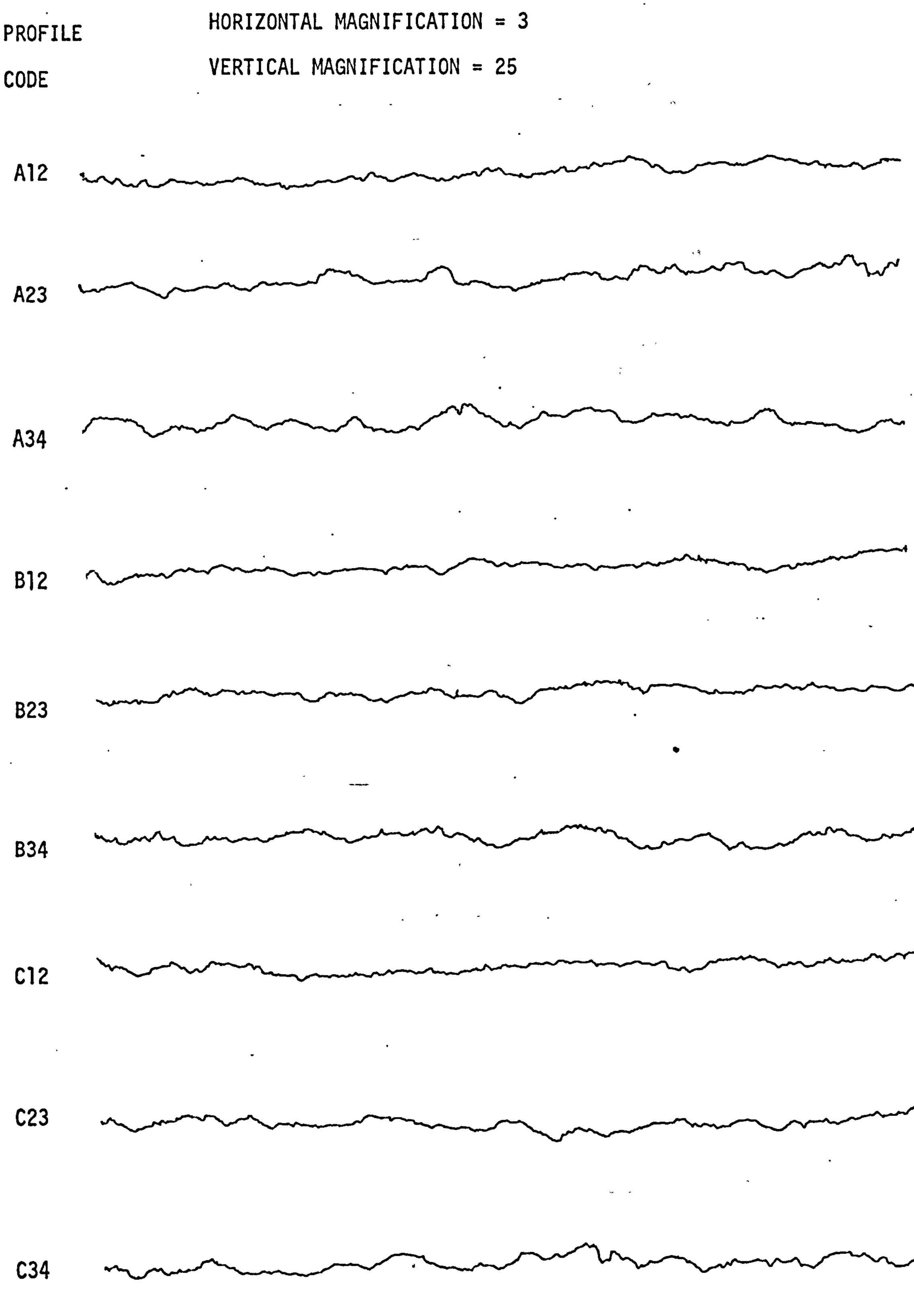

FIG. 5.7 CUMULATIVE HEIGHT DISTRIBUTION FOR THE MOST GAUSSIAN PROFILE FROM SURFACE R550

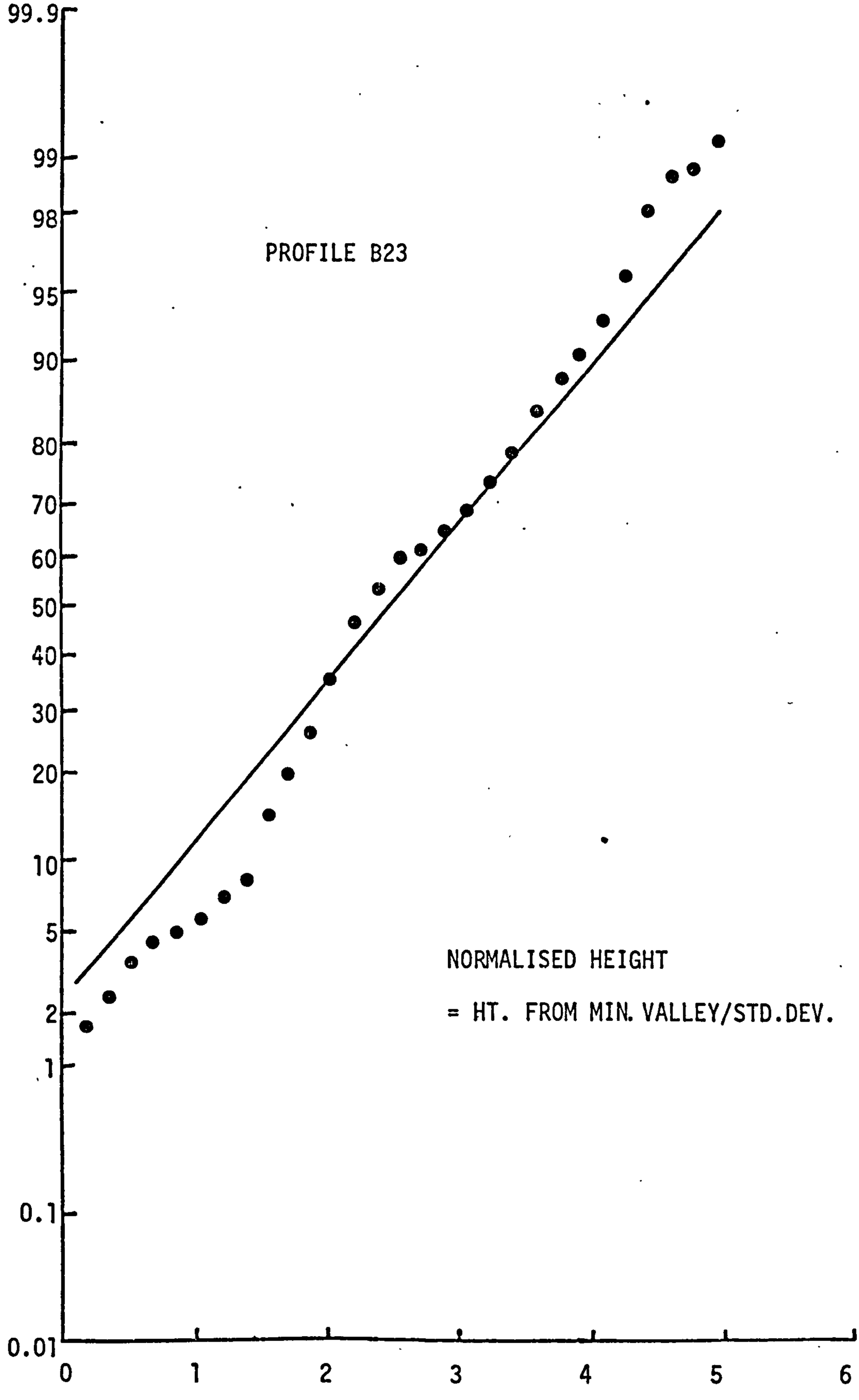

FIG. 5.8 CUMULATIVE HEIGHT DISTRIBUTION FOR THE MOST GAUSSIAN PROFILE FROM SURFACE R420

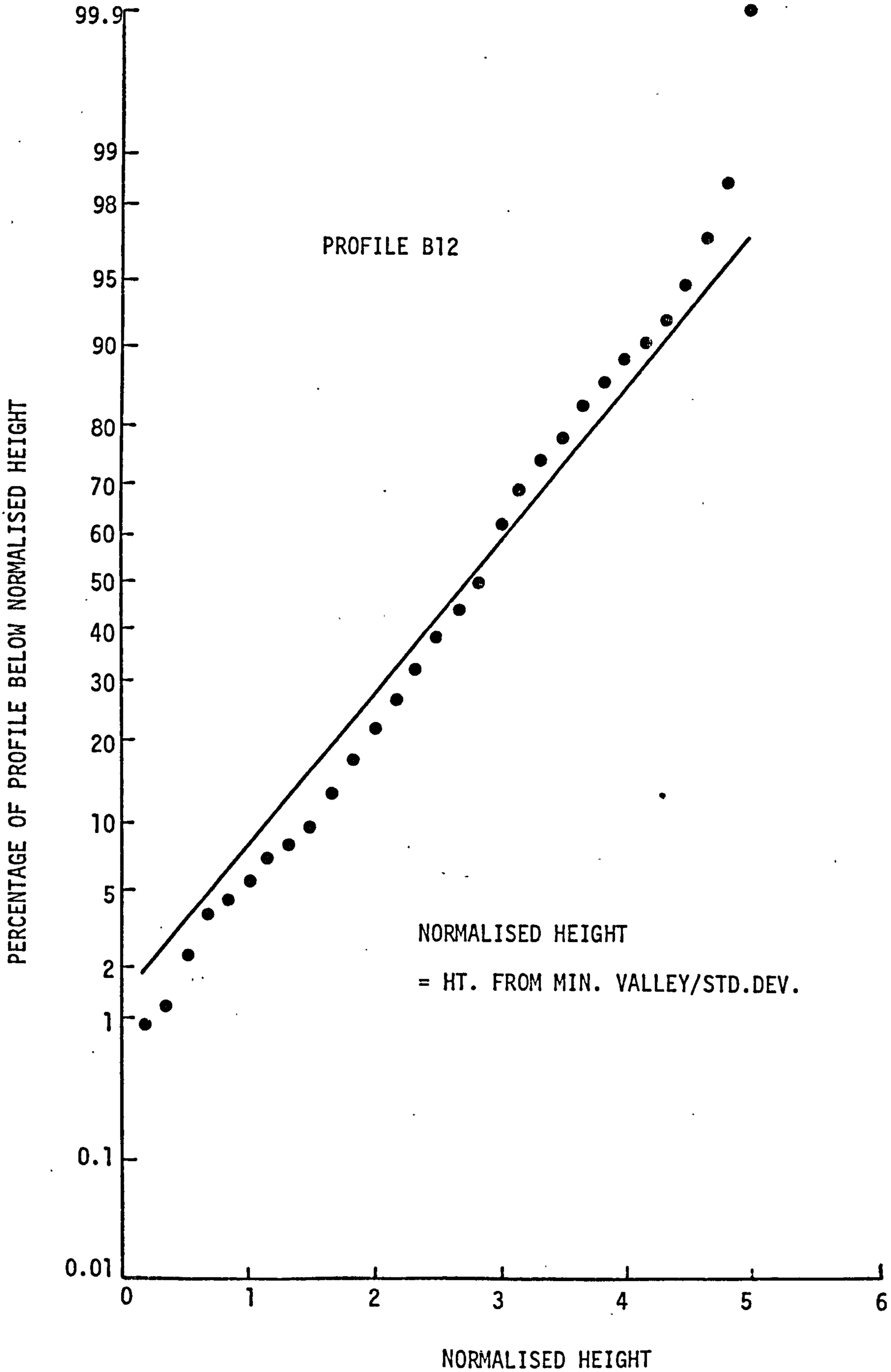

FIG. 5.9 CUMULATIVE HEIGHT DISTRIBUTION FOR THE MOST GAUSSIAN PROFILE FROM SURFACE R345

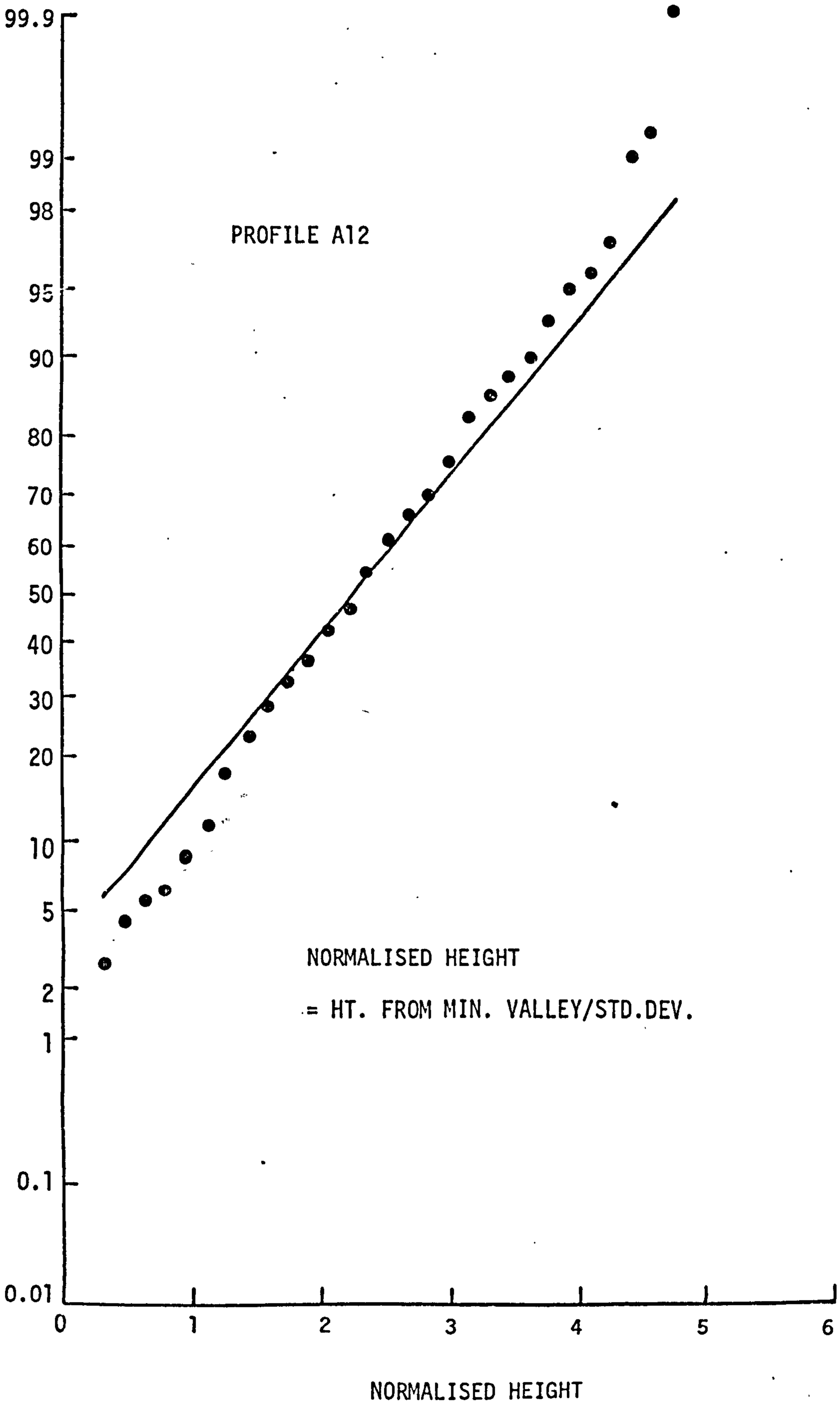

FIG. 5.10 CUMULATIVE HEIGHT DISTRIBUTION FOR THE MOST GAUSSIAN PROFILE FROM SURFACE R253

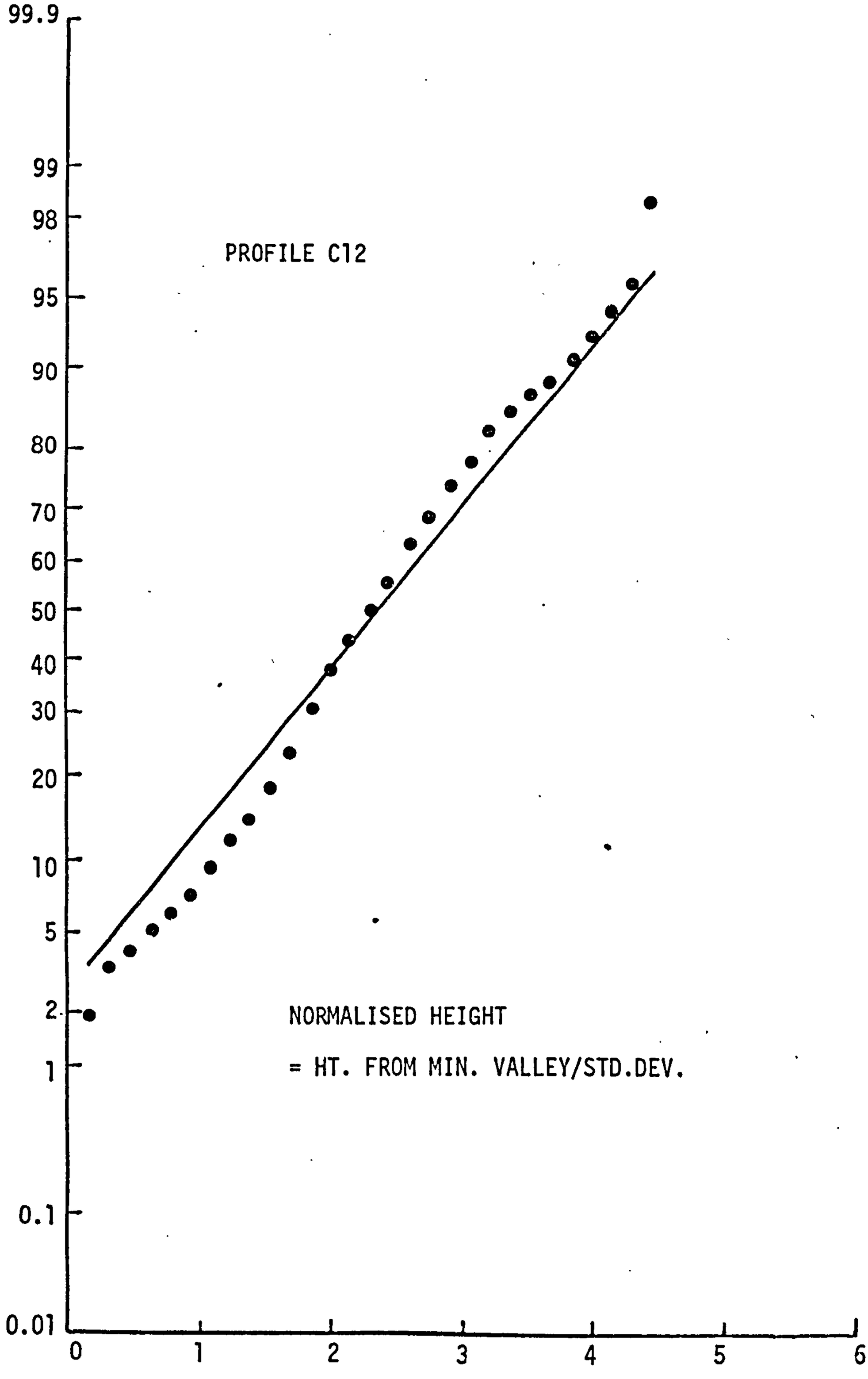

FIG. 5.11 CUMULATIVE HEIGHT DISTRIBUTION FOR THE MOST GAUSSIAN PROFILE FROM SURFACE R173

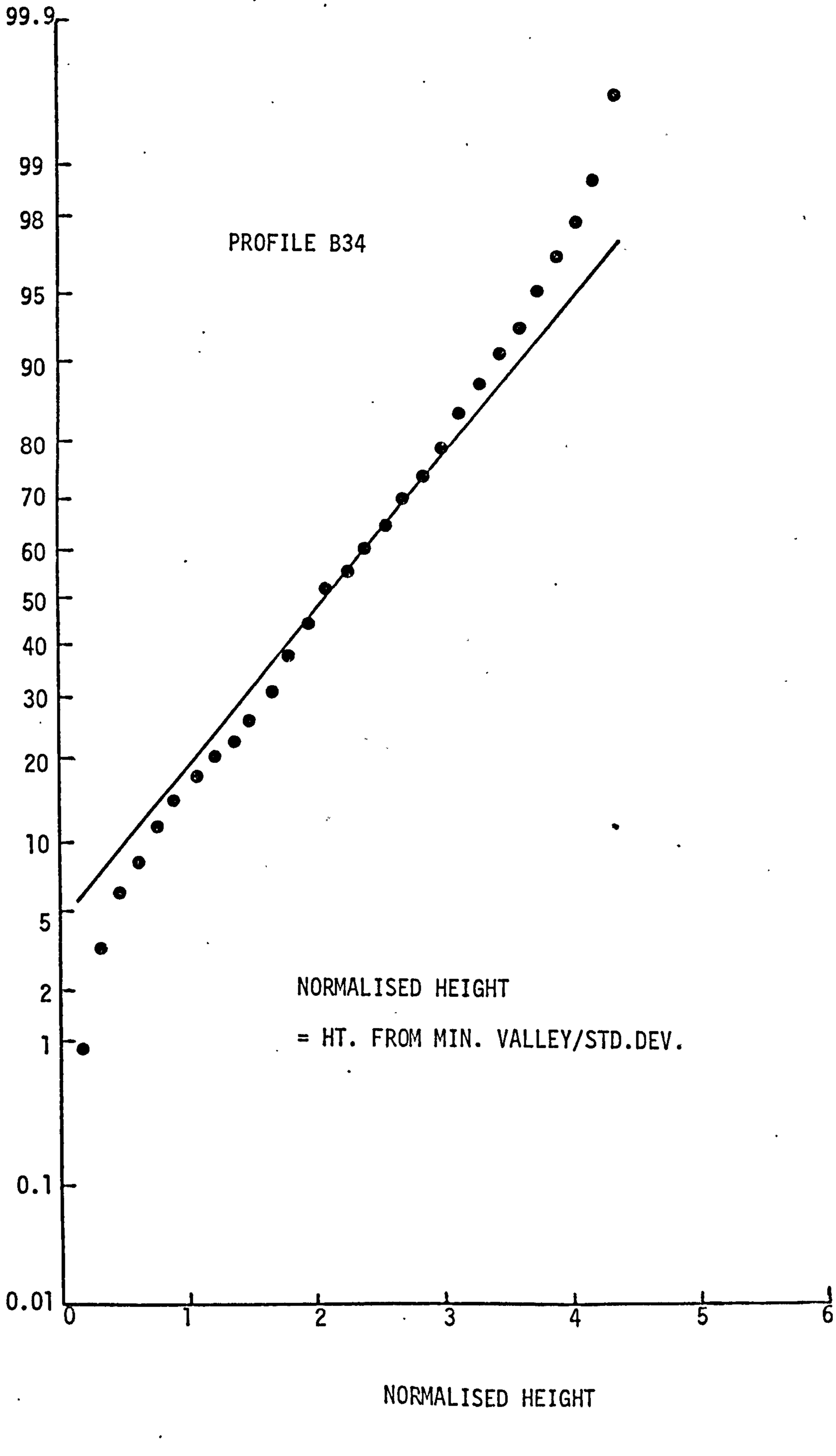

FIG. 5.12 CUMULATIVE HEIGHT DISTRIBUTION FOR THE MOST NON-GAUSSIAN PROFILE FROM SURFACE R550

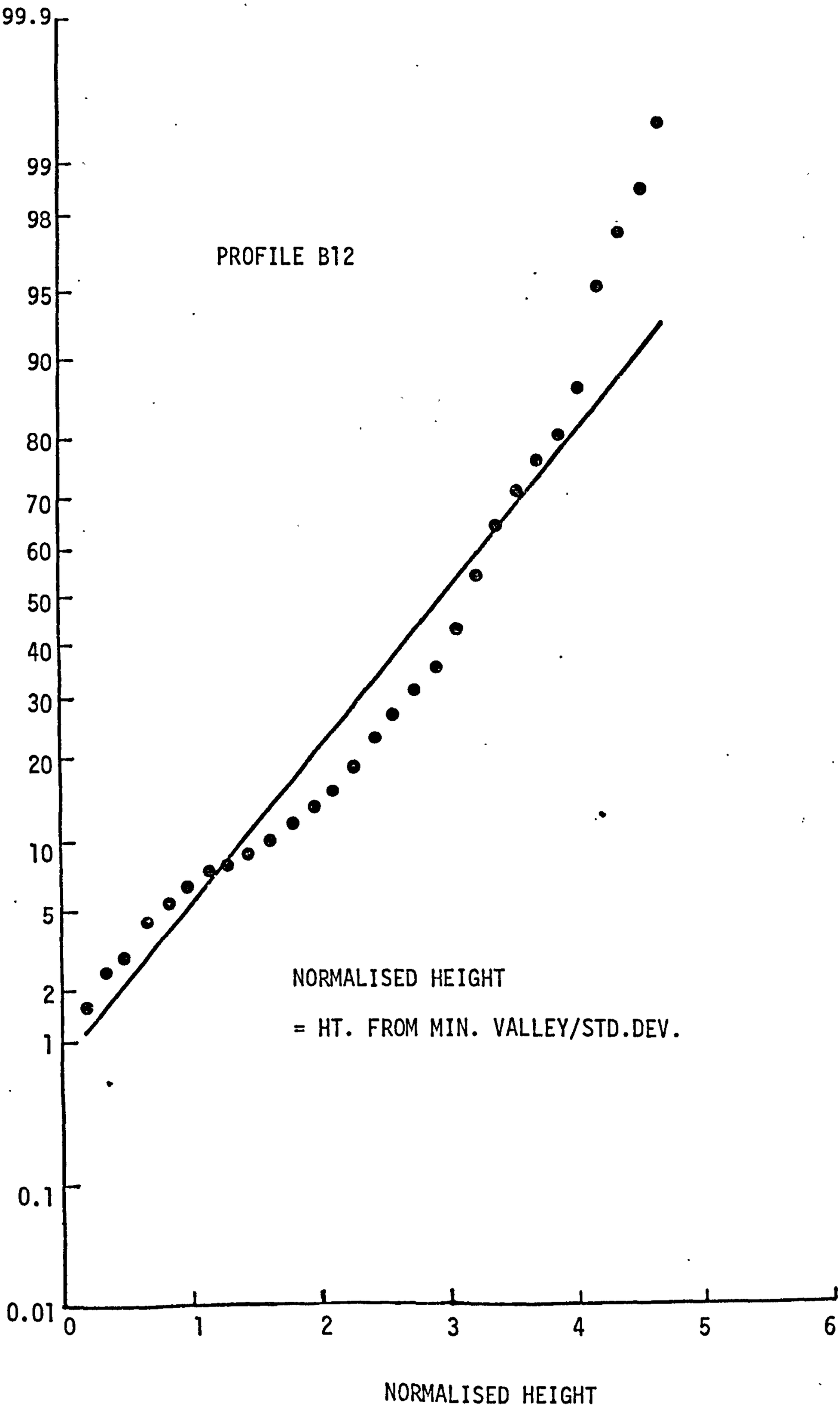

FIG. 5.13 CUMULATIVE HEIGHT DISTRIBUTION FOR THE MOST NON-GAUSSIAN PROFILE FROM SURFACE R420

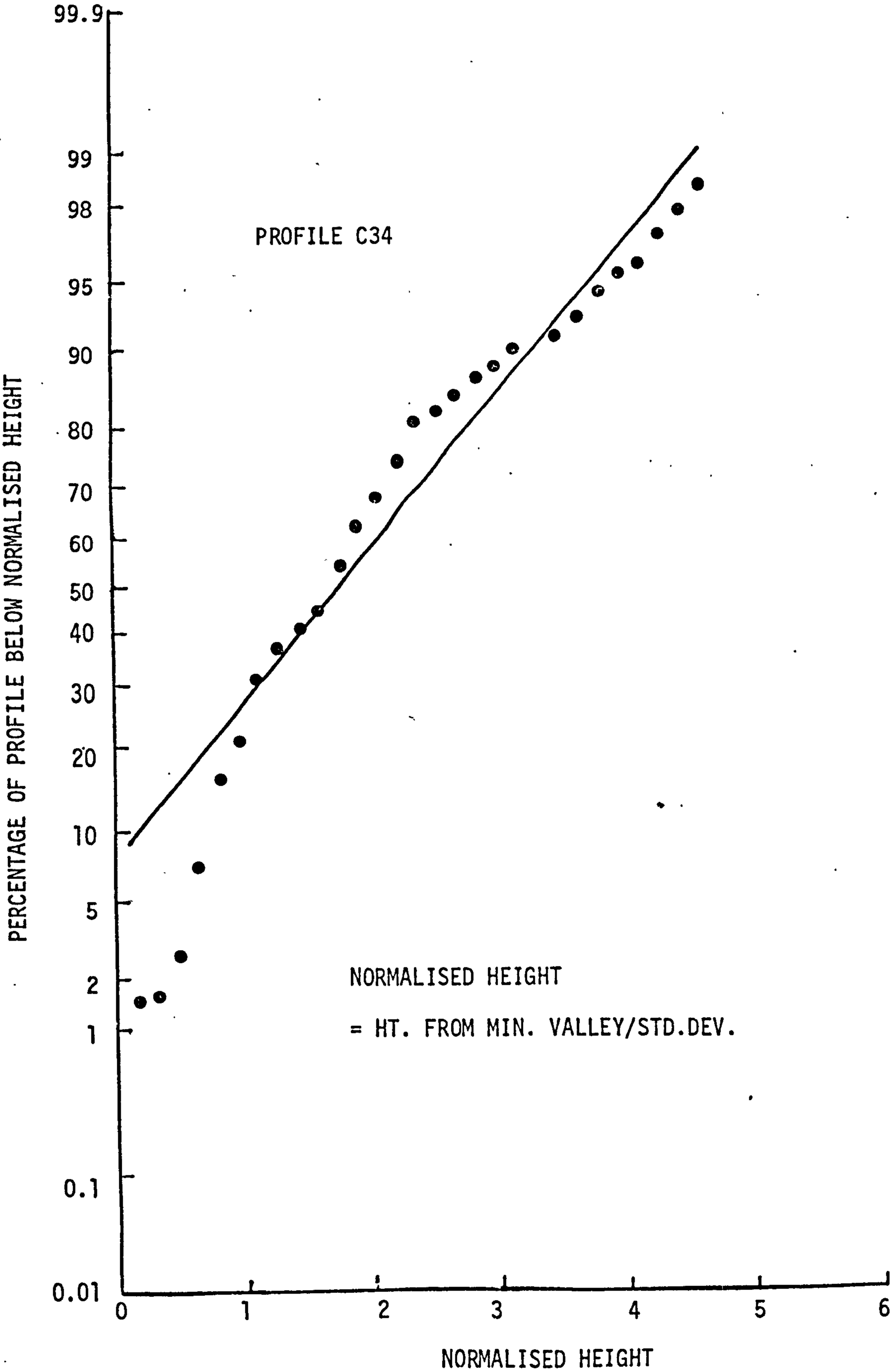

FIG. 5.14 CUMULATIVE HEIGHT DISTRIBUTION FOR THE MOST NON-GAUSSIAN PROFILE FROM SURFACE R345

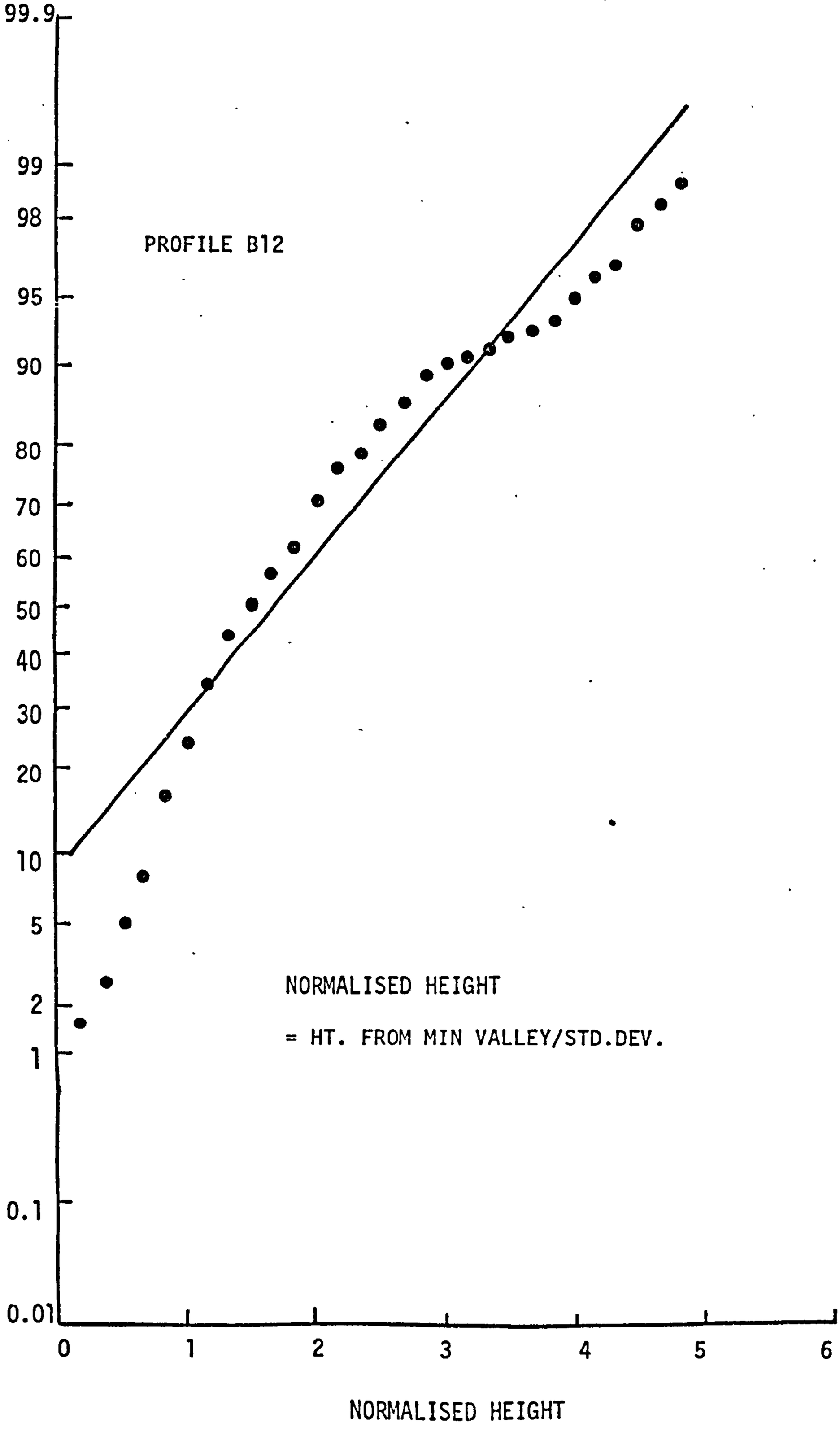

FIG. 5.15 CUMULATIVE HEIGHT DISTRIBUTION FOR THE MOST NON-GAUSSIAN PROFILE FROM SURFACE R253

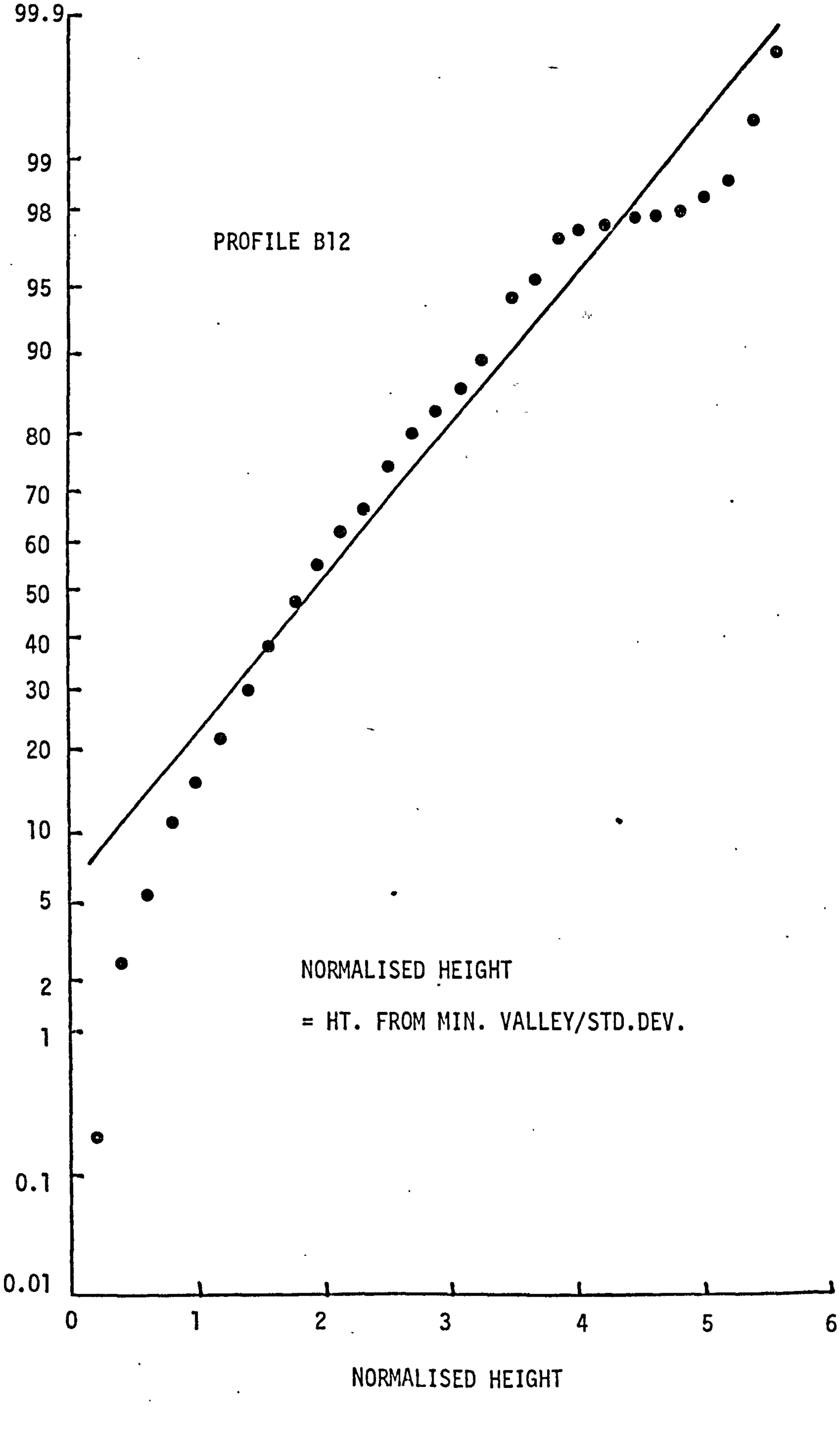

FIG. 5.16 CUMULATIVE HEIGHT DISTRIBUTION FOR THE MOST NON-GAUSSIAN PROFILE FROM SURFACE R173

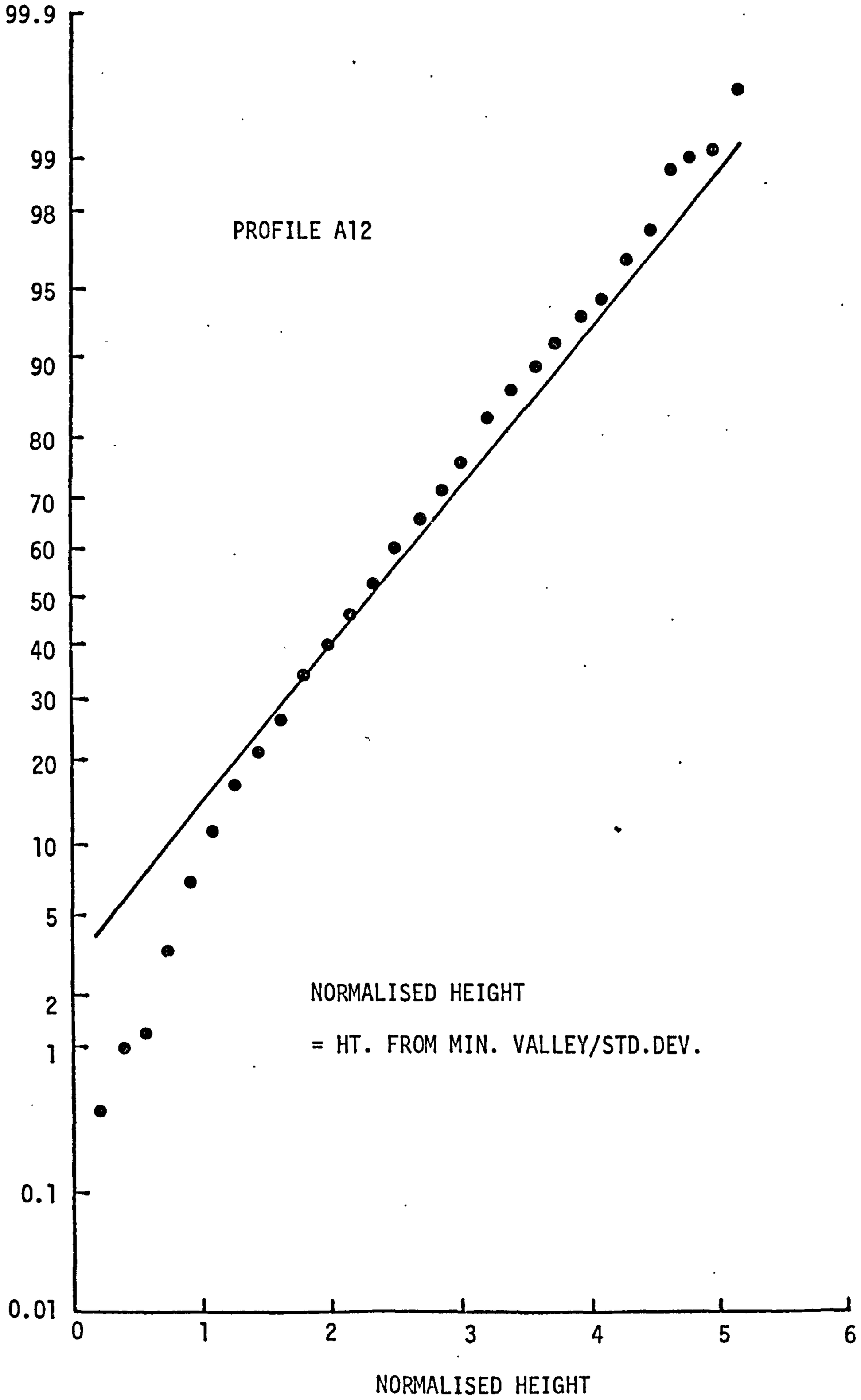

FIG. 6.1 EFFECT OF SLOPE ON FLOW OVER ROUGHNESS ELEMENT

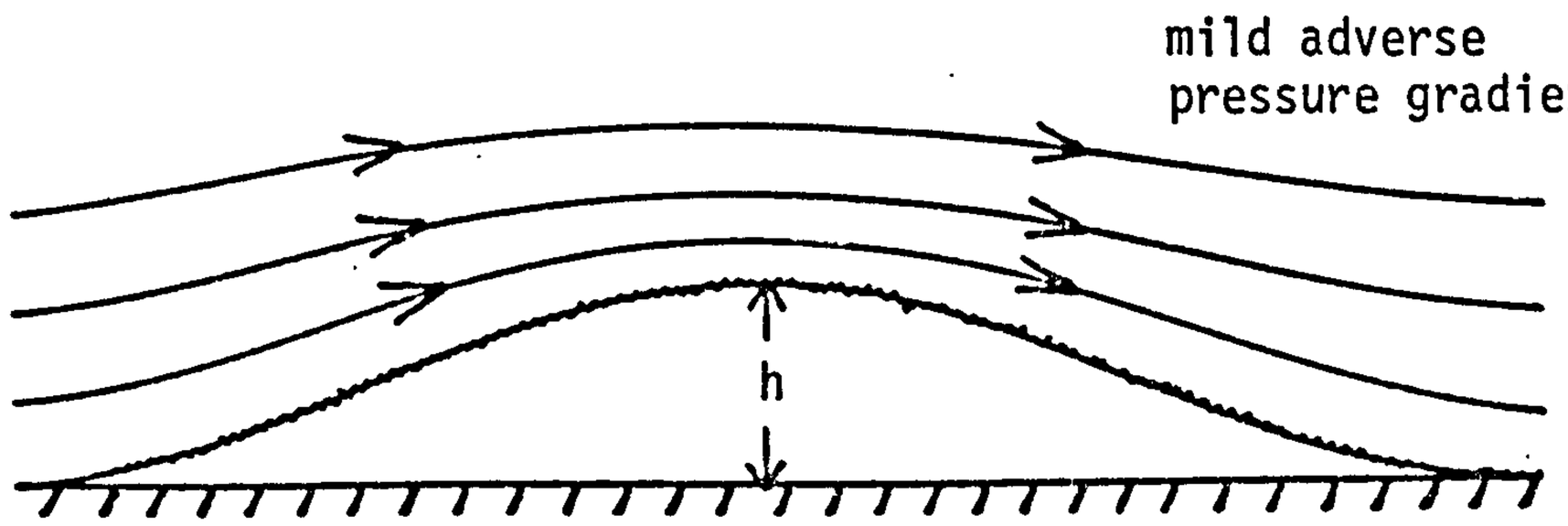

gentle slope - no separation

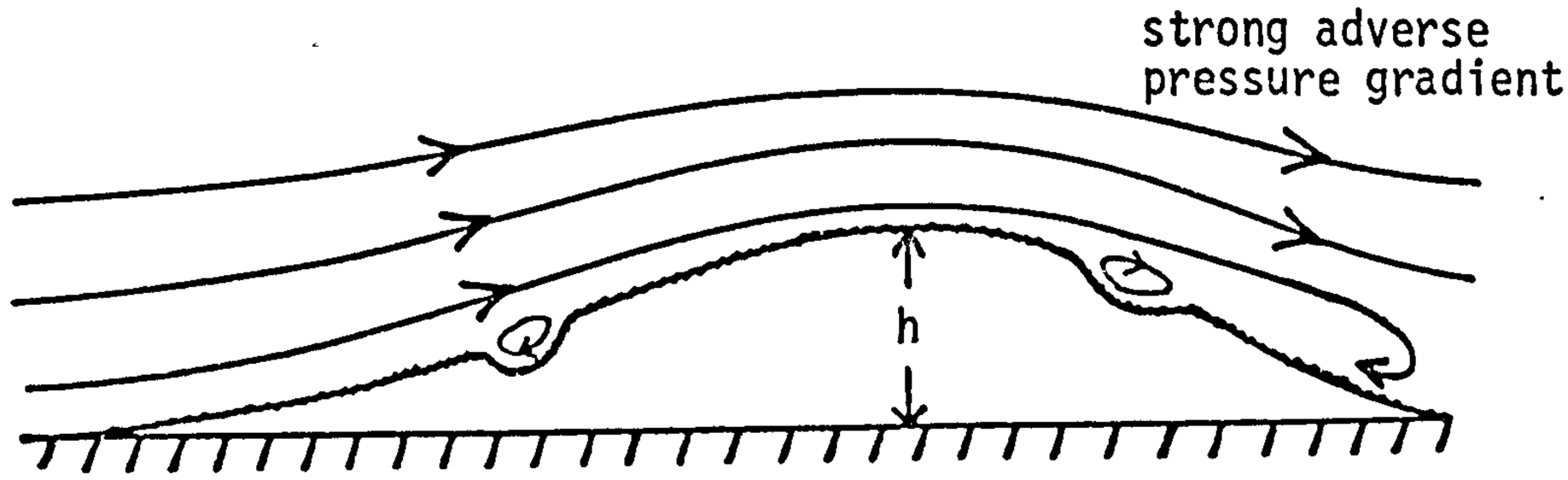

steep slope - separation bubble formed downstream of peak

FIG. 6.2 EXAMPLE OF ORIGINAL AND FILTERED WAVEFORMS FOR THE SURFACE R550 USING A 2mm CUT-OFF WAVELENGTH

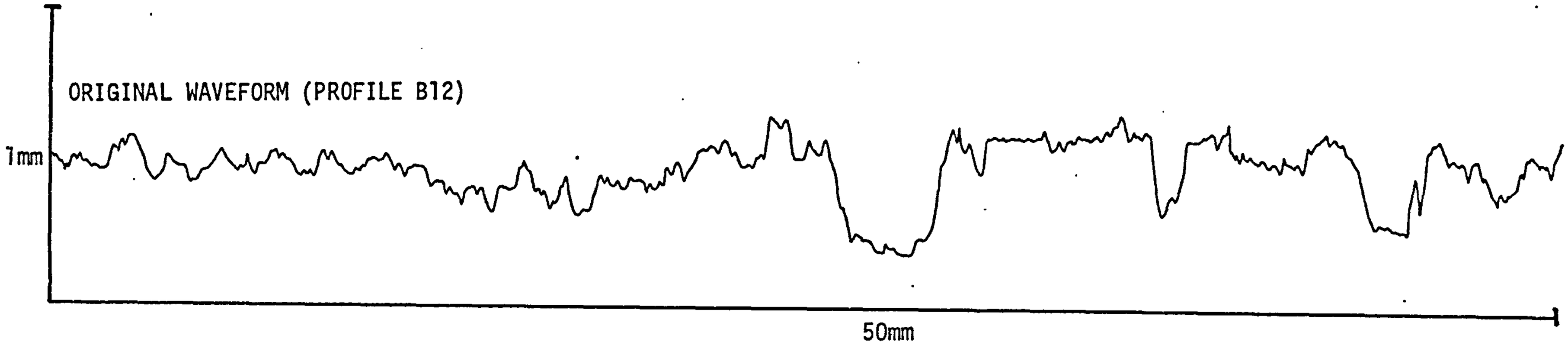

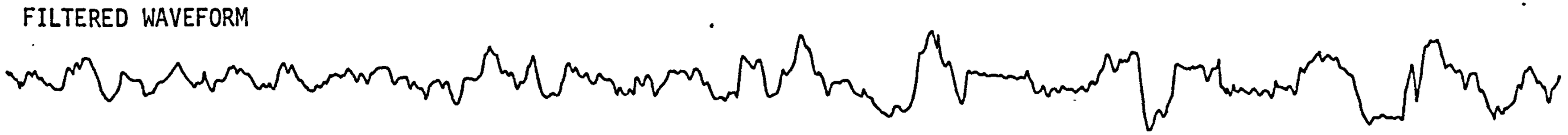

FIG. 6.3 EXAMPLE OF ORIGINAL AND FILTERED WAVEFORMS FOR THE SURFACE R420 USING A 2 mm CUT-OFF WAVELENGTH

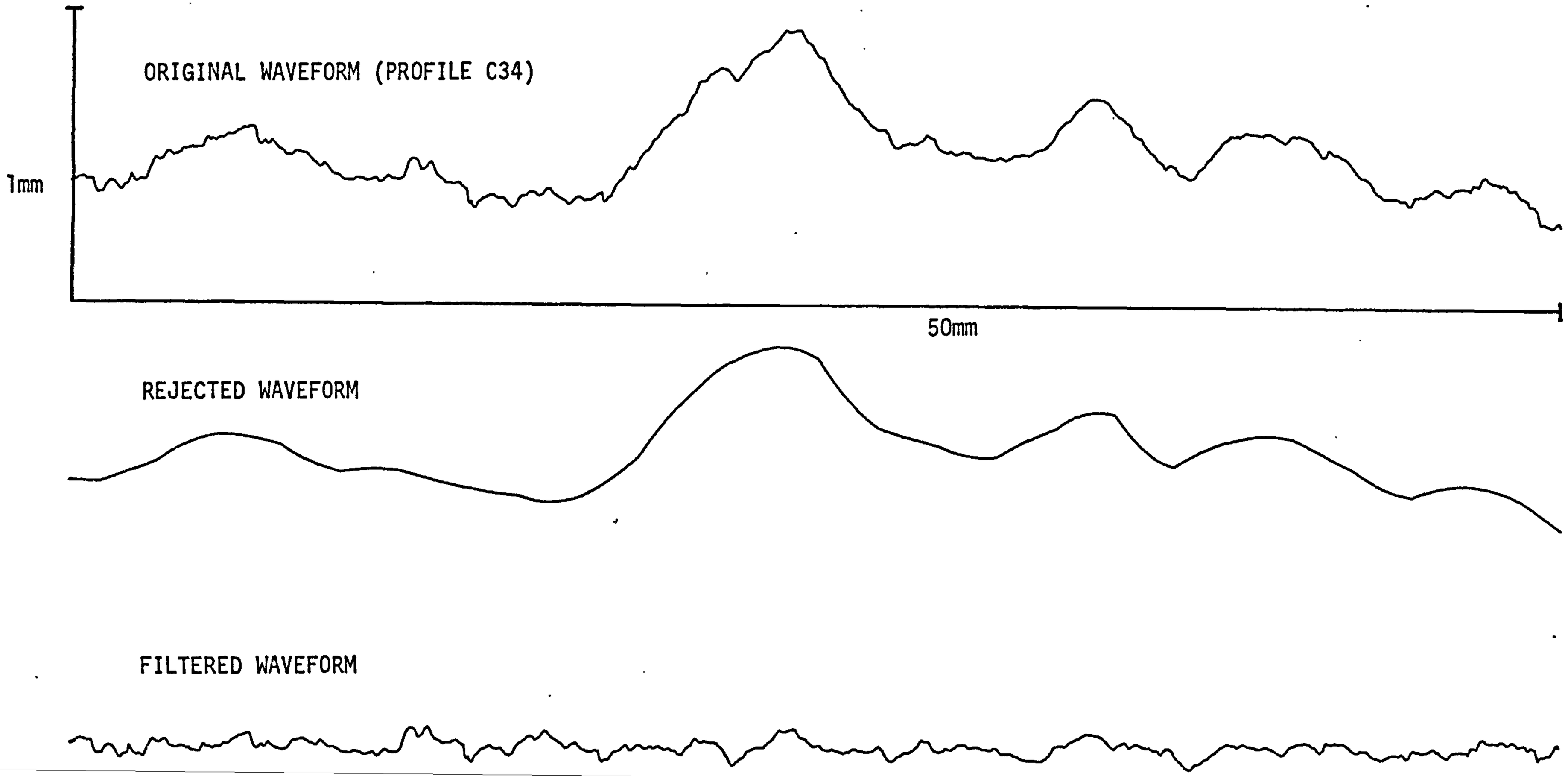

FIG. 6.4 EXAMPLE OF ORIGINAL AND FILTERED WAVEFORMS FOR THE SURFACE R345 USING A 2 mm CUT-OFF WAVELENGTH

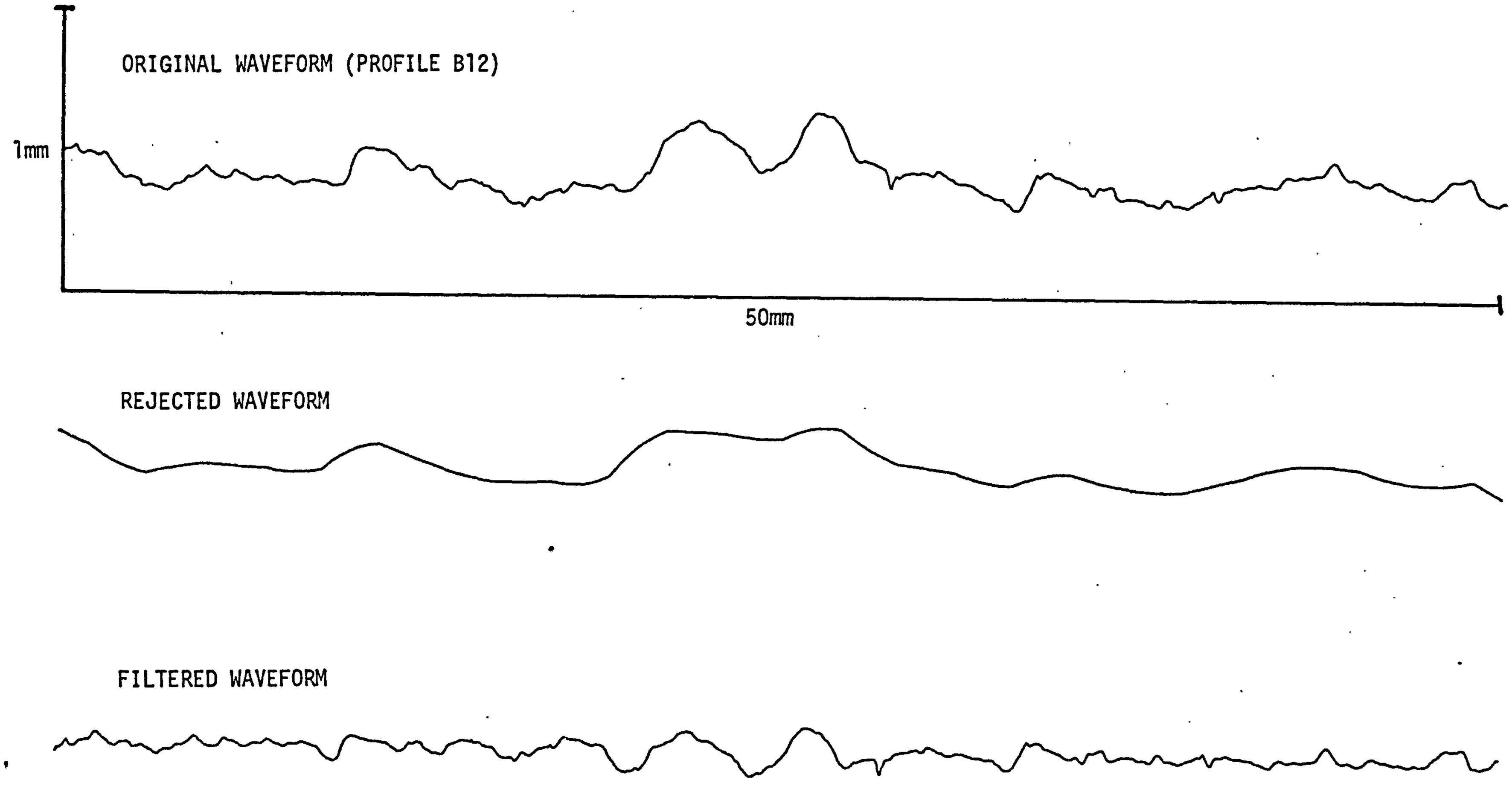

FIG. 6.5 EXAMPLE OF ORIGINAL AND FILTERED WAVEFORMS FOR THE SURFACE R253 USING A 2 mm CUT-OFF WAVELENGTH

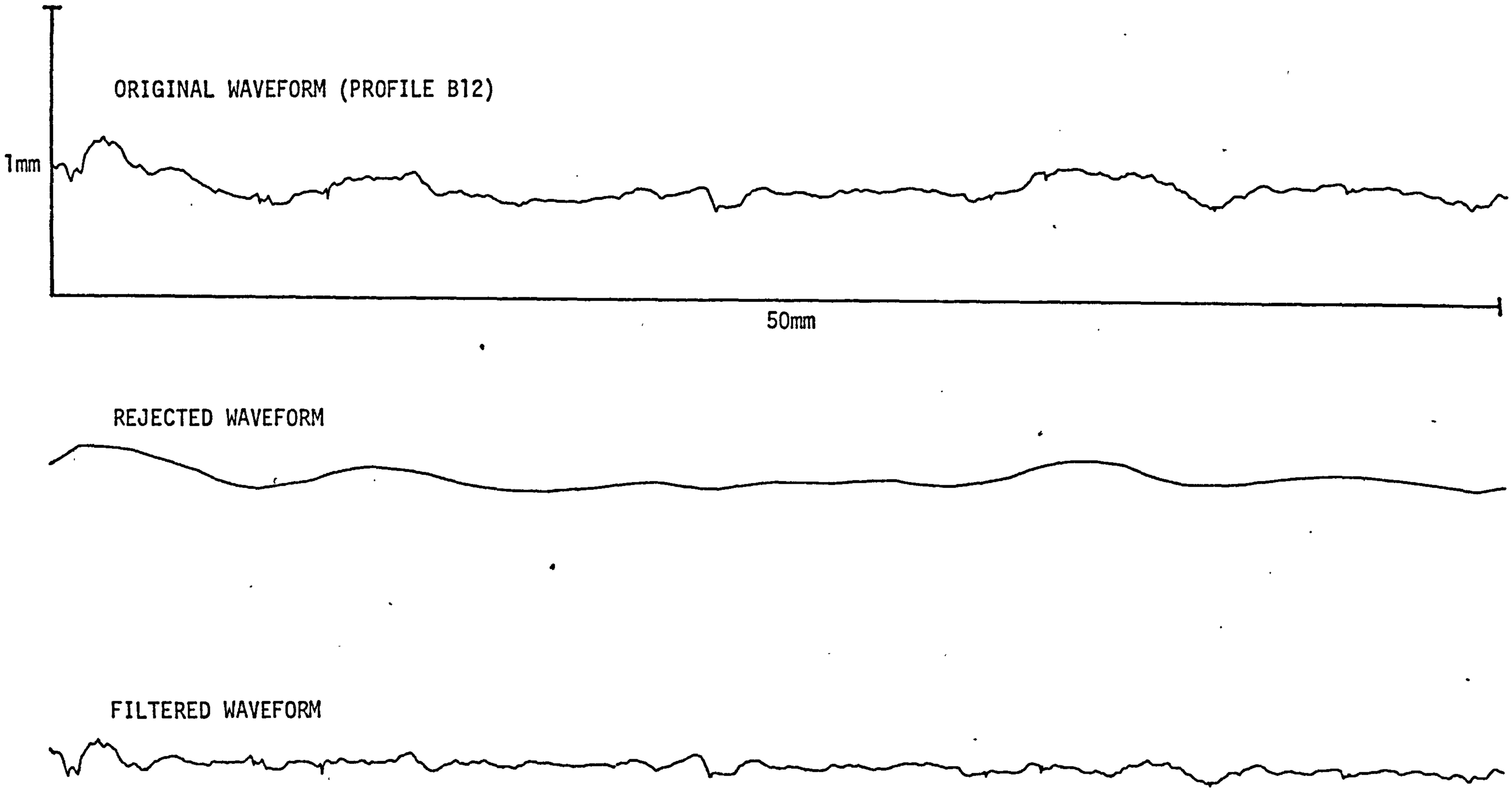

FIG. 6.6 EXAMPLE OF ORIGINAL AND FILTERED WAVEFORMS FOR THE SURFACE R173 USING A 2 mm CUT-OFF WAVELENGTH

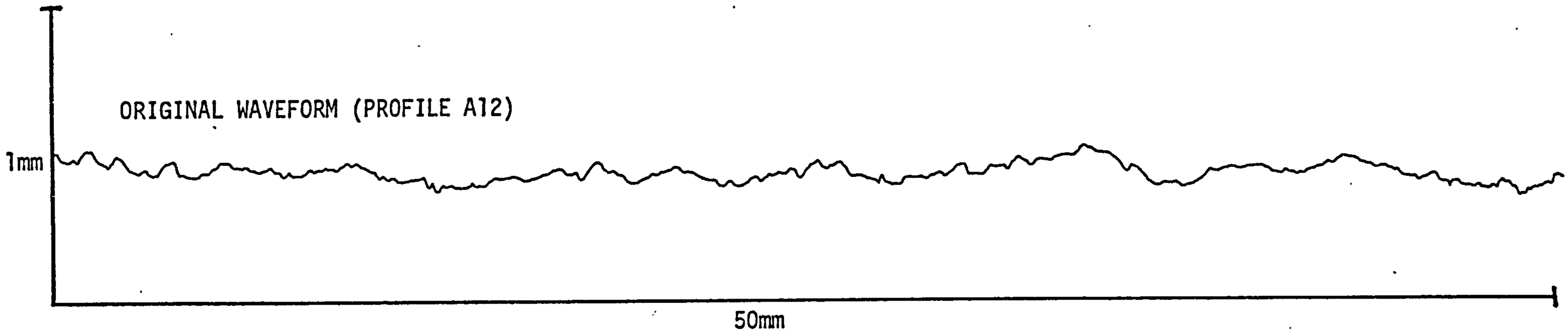

FIG. 6.7 ROUGHNESS FUNCTION $\Delta u/u_o$ VERSUS ROUGHNESS REYNOLDS NUMBER BASED ON MODIFIED ROUGHNESS HEIGHT h'

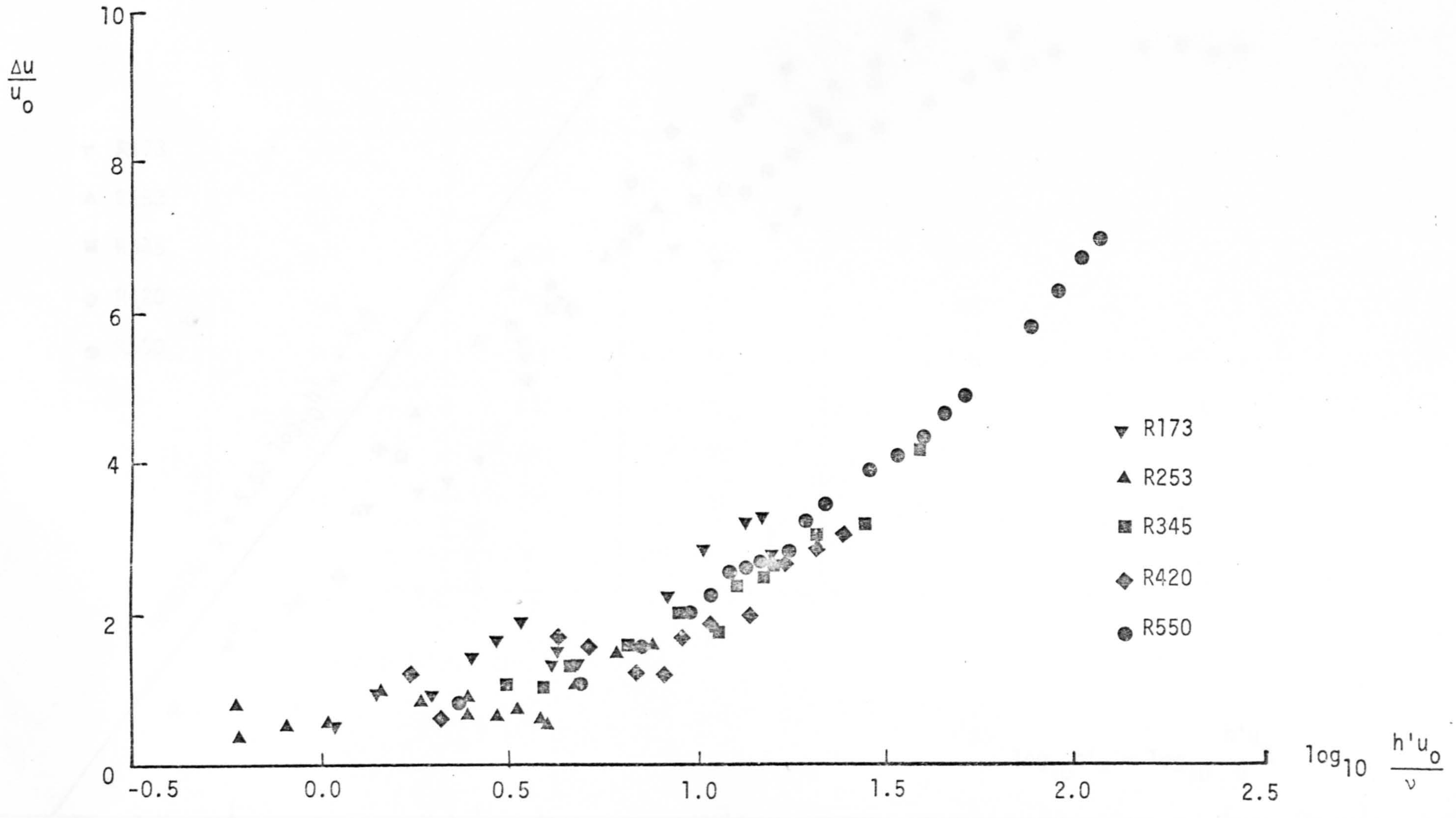

FIG. 6.8 ROUGHNESS FUNCTION χ VERSUS ROUGHNESS REYNOLDS NUMBER BASED ON MODIFIED ROUGHNESS HEIGHT h'

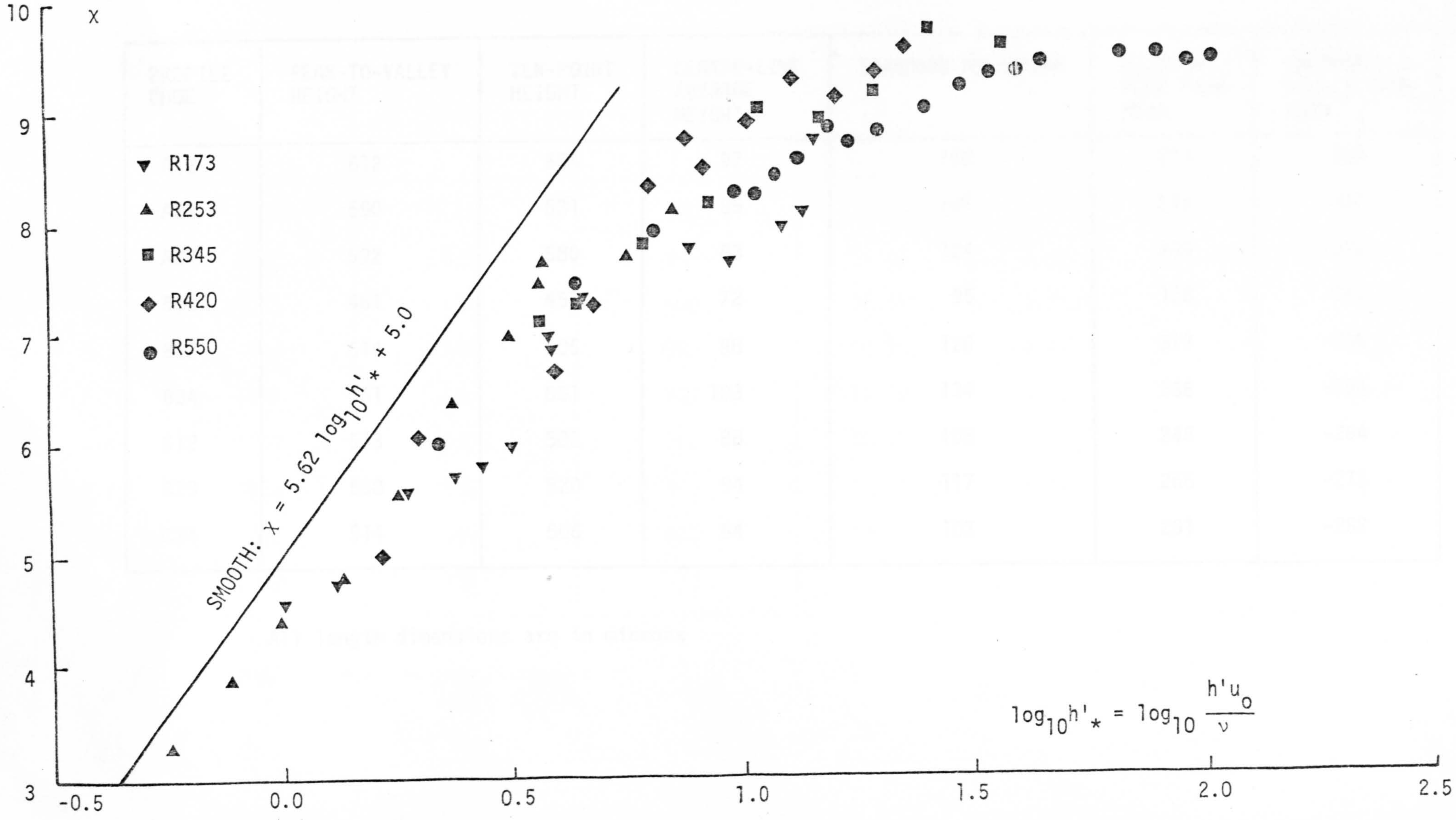

TABLE 5.1

RESULTS OF THE ANALYSIS OF THE SURFACE R550 FOR A CUT-OFF WAVELENGTH OF 50mm

PROFILE CODE	PEAK-TO-VALLEY HEIGHT	TEN-POINT HEIGHT	CENTRE-LINE AVERAGE HEIGHT	STANDARD DEVIATION	MAXIMUM PEAK FROM MEAN	MINIMUM VALLEY FROM MEAN
A12	512	504	97	118	213	-299
A23	550	531	85	107	219	-330
A34	592	580	83	104	269	-322
B12	461	453	72	95	178	-283
B23	614	605	98	120	317	-296
B34	661	651	103	134	266	-394
C12	513	502	88	106	248	-264
C23	538	520	94	117	265	-273
C34	514	506	84	103	261	-252

All length dimensions are in microns

R550 TABLE 5.1 CONTINUED.....

PROFILE CODE	CORRELATION LENGTH	AVERAGE RADIUS OF CURVATURE OF PEAKS	AVERAGE RADIUS OF CURVATURE OF VALLEYS	SLOPE^{o} FOR SAMPLING INTERVAL = 50 MICRONS	SLOPE^{o} FOR SAMPLING INTERVAL = CORRELATION LENGTH	SKEWNESS	KURTOSIS
A12	2890	1120	360	10.26	1.97	-0.70	2.65
A23	1230	460	390	10.63	3.97	-0.69	3.11
A34	1010	370	460	12.81	3.76	-0.51	3.46
B12	950	340	590	10.75	4.11	-0.99	3.74
B23	1100	690	430	11.79	4.30	0.13	2.75
B34	1440	290	360	12.42	4.08	-0.74	3.35
C12	710	250	380	13.07	6.43	-0.18	2.43
C23	2560	340	870	10.80	2.23	0.12	2.47
C34	1000	350	370	12.46	4.43	0.26	2.55

All length dimensions are in microns

TABLE 5.2

RESULTS OF THE ANALYSIS OF THE SURFACE

R420 FOR A CUT-OFF WAVELENGTH OF 50mm

PROFILE CODE	PEAK-TO-VALLEY HEIGHT	TEN-POINT HEIGHT	CENTRE-LINE AVERAGE HEIGHT	STANDARD DEVIATION	MAXIMUM PEAK FROM MEAN	MINIMUM VALLEY FROM MEAN
A12	367	363	84	95	182	-184
A23	351	342	83	94	172	-179
A34	379	373	65	81	242	-136
B12	365	362	57	73	165	-199
B23	547	542	90	114	241	-306
B34	374	367	60	76	213	-160
C12	316	315	65	79	168	-148
C23	427	422	72	89	235	-192
C34	646	641	104	136	406	-240

All length dimensions are in microns

TABLE 5.2 CONTINUED.....

PROFILE CODE	CORRELATION LENGTH	AVERAGE RADIUS OF CURVATURE OF PEAKS	AVERAGE RADIUS OF CURVATURE OF VALLEYS	SLOPE^{o} FOR SAMPLING INTERVAL = 50 MICRONS	SLOPE^{o} FOR SAMPLING INTERVAL = CORRELATION LENGTH	SKEWNESS	KURTOSIS
A12	1590	760	1040	5.31	2.92	-0.19	1.80
A23	2240	1240	1170	4.32	1.57	-0.05	1.74
A34	1850	1110	1110	4.70	2.06	0.85	3.11
B12	1620	960	950	4.65	1.99	-0.15	3.00
B23	2250	880	950	4.74	2.46	-0.10	2.88
B34	1380	1152	960	4.65	2.65	0.47	2.95
C12	1180	1180	3610	5.03	3.00	0.15	2.19
C23	2050	700	750	4.76	1.94	0.27	2.65
C34	2640	760	900	4.90	2.37	0.99	3.72

All length dimensions are in microns

TABLE 5.3

RESULTS OF THE ANALYSIS OF THE SURFACE

R345 FOR A CUT-OFF WAVELENGTH OF 50mm

PROFILE CODE	PEAK-TO-VALLEY HEIGHT	TEN-POINT HEIGHT	CENTRE-LINE AVERAGE HEIGHT	STANDARD DEVIATION	MAXIMUM PEAK FROM MEAN	MINIMUM VALLEY FROM MEAN
A12	373	369	64	79	197	-178
A23	286	283	53	65	152	-134
A34	318	315	58	73	176	-142
B12	330	325	50	66	218	-111
B23	403	382	57	71	203	-200
B34	404	402	64	81	213	-191
C12	511	504	93	114	260	-250
C23	254	244	38	47	149	-105
C34	466	459	84	106	301	-164

All length dimensions are in microns

TABLE 5.3 CONTINUED.....

PROFILE CODE	CORRELATION LENGTH	AVERAGE RADIUS OF CURVATURE OF PEAKS	AVERAGE RADIUS OF CURVATURE OF VALLEYS	SLOPE^{o} FOR SAMPLING INTERVAL = 50 MICRONS	SLOPE^{o} FOR SAMPLING INTERVAL = CORRELATION LENGTH	SKEWNESS	KURTOSIS
A12	1120	2010	2010	5.41	2.42	0.11	2.56
A23	810	1490	1490	5.92	3.27	0.18	2.42
A34	1480	930	930	4.75	2.23	0.34	2.67
B12	1380	1070	1070	3.84	1.97	1.23	4.39
B23	890	1540	1540	5.40	3.01	0.20	2.88
B34	1030	950	950	5.68	2.73	0.48	2.95
C12	1570	1450	1450	6.21	3.72	-0.13	2.48
C23	750	1270	1270	5.08	2.56	0.32	2.48
C34	2040	1160	1160	5.05	2.53	0.77	3.00

All length dimensions are in microns

TABLE 5.4

RESULTS OF THE ANALYSIS OF THE SURFACE

R253 FOR A CUT-OFF WAVELENGTH OF 50mm

PROFILE CODE	PEAK-TO-VALLEY HEIGHT	TEN-POINT HEIGHT	CENTRE-LINE AVERAGE HEIGHT	STANDARD DEVIATION	MAXIMUM PEAK FROM MEAN	MINIMUM VALLEY FROM MEAN
A12	201	184	29	37	97	-104
A23	252	248	42	53	116	-135
A34	462	454	66	87	207	-255
B12	241	226	32	41	160	-80
B23	219	214	29	38	132	-86
B34	218	212	31	38	78	-140
C12	175	173	29	38	86	-88
C23	293	268	43	55	143	-150
C34	288	249	43	51	92	-196

All length dimensions are in microns

R253 TABLE 5.4 CONTINUED.....

PROFILE CODE	CORRELATION LENGTH	AVERAGE RADIUS OF CURVATURE OF PEAKS	AVERAGE RADIUS OF CURVATURE OF VALLEYS	SLOPE^{O} FOR SAMPLING INTERVAL = 50 MICRONS	SLOPE^{O} FOR SAMPLING INTERVAL = CORRELATION LENGTH	SKEWNESS	KURTOSIS
A12	1630	2650	1470	3.77	1.03	0.23	2.72
A23	1530	2320	1160	3.65	1.71	-0.14	2.72
A34	1960	980	1360	4.55	1.54	0.15	3.60
B12	1650	1970	1400	3.08	0.92	0.89	4.16
B23	1200	1210	1140	3.89	1.18	0.21	4.00
B34	1160	890	1000	4.31	1.16	-0.44	3.18
C12	1560	1720	1800	2.78	0.90	0.11	2.87
C23	2130	4290	1110	4.14	1.31	-0.11	2.75
C34	1800	1320	1800	4.08	1.12	-0.37	2.40

All length dimensions are in microns

TABLE 5.5

RESULTS OF THE ANALYSIS OF THE SURFACE

R173 FOR A CUT-OFF WAVELENGTH OF 50mm

PROFILE CODE	PEAK-TO-VALLEY HEIGHT	TEN-POINT HEIGHT	CENTRE-LINE AVERAGE HEIGHT	STANDARD DEVIATION	MAXIMUM PEAK FROM MEAN	MINIMUM VALLEY FROM MEAN
A12	162	156	24	30	93	-68
A23	196	188	29	37	100	-95
A34	249	245	43	52	137	-112
B12	163	158	23	30	72	-90
B23	154	149	25	30	75	-79
B34	189	182	34	42	101	-88
C12	165	155	25	29	94	-71
C23	185	183	28	35	75	-109
C34	238	233	36	45	145	-92

All length dimensions are in microns

R173 TABLE 5.5 CONTINUED.....

PROFILE CODE	CORRELATION LENGTH	AVERAGE RADIUS OF CURVATURE OF PEAKS	AVERAGE RADIUS OF CURVATURE OF VALLEYS	SLOPE^{o} FOR SAMPLING INTERVAL = 50 MICRONS	SLOPE^{o} FOR SAMPLING INTERVAL = CORRELATION LENGTH	SKEWNESS	KURTOSIS
A12	1230	1740	1350	3.53	1.05	0.40	2.79
A23	860	2100	1920	3.75	1.66	0.23	3.01
A34	1320	2140	980	4.08	1.83	0.25	2.53
B12	1240	2910	1680	3.30	0.82	-0.32	3.18
B23	1200	1330	1380	3.45	1.11	0.12	2.47
B34	1470	2650	1140	4.10	1.29	0.01	2.32
C12	1300	1120	1040	3.52	1.04	0.04	2.22
C23	1260	1150	3390	3.25	1.13	-0.37	3.10
C34	1290	860	1110	4.07	1.59	0.72	3.21

All length dimensions are in microns

TABLE 6.1

RESULTS OF THE ANALYSIS OF THE SURFACE R550 FOR

DIFFERENT CUT-OFF WAVELENGTHS

Cut-off Wavelength	Peak-to-Valley Height	Ten-Point Height	Centre-line Average Height	Standard Deviation	Maximum Peak from Mean	Minimum Valley from Mean
50×10^3	551±61	539±61	90±10	112±12	249±40	-302±43
10×10^3	505±82	487±85	73±9	93±12	224±42	-281±49
2×10^3	336±84	317±81	40±7	52±10	164±43	-172±48

All length dimensions are in microns

Errors quoted are ± one standard deviation

R550 Table 6.1 Continued.....

Cut-off Wavelength	Correlation Length	Average Radius of Curvature of Peaks	Average Radius of Curvature of Valleys	Slope^{o} for Sampling Interval = 50 Microns	Slope^{o} for Sampling Interval = Correlation Length	Skewness	Kurtosis
$50x10^3$	1430±760	470±280	470±70	11.7±1.07	3.9±1.3	-0.4±0.46	2.9±0.48
$10x10^3$	920±370	720±500	650±400	11.7±1.07	4.5±1.07	-0.5±0.32	3.3±0.82
$2x10^3$	320±60	400±110	400±80	11.5±1.10	7.0±1.17	-0.2±0.16	3.5±0.52

All length dimensions are in microns

Errors quoted are ± one standard deviation

TABLE 6.2

RESULTS OF THE ANALYSIS OF THE SURFACE R420 FOR

DIFFERENT CUT-OFF WAVELENGTHS

Cut-off Wavelength	Peak-to-Valley Height	Ten-Point Height	Centre-line Average Height	Standard Deviation	Maximum Peak from Mean	Minimum Valley from Mean
$50x10^3$	420±108	415±107	76±16	94±20	225±75	-194±52
$10x10^3$	358±30	353±29	61±7	76±7	178±30	-179±24
$2x10^3$	149±23	142±20	19±3	25±3	74±13	-76±14

All length dimensions are in microns

Errors quoted are ± one standard deviation

R420 Table 6.2 Continued.....

Cut-off Wavelength	Correlation Length	Average Radius of Curvature of Peaks	Average Radius of Curvature of Valleys	Slope^{o} for Sampling Interval = 50 Microns	Slope^{o} for Sampling Interval = Correlation Length	Skewness	Kurtosis
$50x10^3$	1870±470	970±200	1270±890	4.8±0.28	2.3±0.48	0.2±0.44	2.7±0.65
$10x10^3$	1450±210	1000±250	1290±760	4.8±0.29	2.4±0.51	0.1±0.33	2.7±0.43
$2x10^3$	440±50	1090±230	1080±280	4.3±0.25	2.4±0.34	0.0±0.25	3.4±0.41

All length dimensions are in microns

Errors quoted are ± one standard deviation

TABLE 6.3

RESULTS OF THE ANALYSIS OF THE SURFACE R345 FOR

DIFFERENT CUT-OFF WAVELENGTHS

Cut-off Wavelength	Peak-to-Valley Height	Ten-Point Height	Centre-line Average Height	Standard Deviation	Maximum Peak from Mean	Minimum Valley from Mean
50×10^3	372±84	365±83	63±17	78±21	208±49	-164±47
10×10^3	350±82	343±82	52±13	66±17	182±40	-168±45
2×10^3	222±52	212±48	26±3	34±5	109±28	-113±30

All length dimensions are in microns

Errors quoted are ± one standard deviation

R345 Table 6.3 Continued.....

Cut-off Wavelength	Correlation Length	Average Radius of Curvature of Peaks	Average Radius of Curvature of Valleys	Slope^{o} for Sampling Interval = 50 Microns	Slope^{o} for Sampling Interval = Correlation Length	Skewness	Kurtosis
$50x10^3$	1230±420	1310±340	1340±400	5.3±0.70	2.7±0.54	0.4±0.40	2.9±0.61
$10x10^3$	900±250	1190±200	1450±310	5.2±0.70	3.1±0.46	0.2±0.27	3.1±0.44
$2x10^3$	390±45	1150±200	1356±510	4.9±0.68	3.3±1.25	0.0±0.25	3.9±0.79

All length dimensions are in microns

Errors quoted are ± one standard deviation

TABLE 6.4

RESULTS OF THE ANALYSIS OF THE SURFACE R253 FOR

DIFFERENT CUT-OFF WAVELENGTHS

Cut-off Wavelength	Peak-to-Valley Height	Ten-Point Height	Centre-line Average Height	Standard Deviation	Maximum Peak from Mean	Minimum Valley from Mean
50×10^3	262±85	248±83	39±12	49±16	124±42	-138±58
10×10^3	208±33	195±28	30±6	38±8	96±19	-112±33
2×10^3	132±38	117±28	12±2	16±3	52±10	-80±37

All length dimensions are in microns

Errors quoted are ± one standard deviation

R253 Table 6.4 Continued.....

Cut-off Wavelength	Correlation Length	Average Radius of Curvature of Peaks	Average Radius of Curvature of Valleys	Slope^{o} for Sampling Interval = 50 Microns	Slope^{o} for Sampling Interval = Correlation Length	Skewness	Kurtosis
$50x10^3$	1620±320	1930±1070	1360±290	3.8±0.57	1.2±0.27	0.1±0.40	3.2±0.62
$10x10^3$	1160±330	1600±680	1700±1400	3.8±0.56	1.3±0.22	-0.1±0.36	3.0±0.4
$2x10^3$	300±70	2290±1610	1770±880	3.6±0.52	2.1±0.51	-0.4±0.55	5.9±2.28

All length dimensions are in microns

Errors quoted are ± one standard deviation

TABLE 6.5

RESULTS OF THE ANALYSIS OF THE SURFACE R173 FOR

DIFFERENT CUT-OFF WAVELENGTHS

Cut-off Wavelength	Peak-to-Valley Height	Ten-Point Height	Centre-line Average Height	Standard Deviation	Maximum Peak from Mean	Minimum Valley from Mean
50×10^3	190±34	184±35	30±7	37±8	100±27	-90±15
10×10^3	166±34	160±34	25±6	32±7	87±27	-80±10
2×10^3	99±20	92±17	13±3	17±3	48±12	-52±15

All length dimensions are in microns

Errors quoted are ± one standard deviation

R173 Table 6.5 Continued.....

Cut-off Wavelength	Correlation Length	Average Radius of Curvature of Peaks	Average Radius of Curvature of Valleys	Slope^{o} for Sampling Interval = 50 Microns	Slope^{o} for Sampling Interval = Correlation Length	Skewness	Kurtosis
$50x10^3$	1240±160	1780±720	1560±750	3.7±0.34	1.3±0.34	0.1±0.34	2.8±0.38
$10x10^3$	930±140	1570±610	1530±780	3.7±0.34	1.4±0.29	0.1±0.32	2.9±0.29
$2x10^3$	350±70	1430±610	1310±380	3.5±0.27	2.0±0.26	-0.1±0.33	3.2±0.33

All length dimensions are in microns

Errors quoted are ± one standard deviation